LA-UR-93-805
c.2

LA-UR-93-805

INTRODUCTION TO LINEAR ACCELERATORS

Thomas P. Wangler

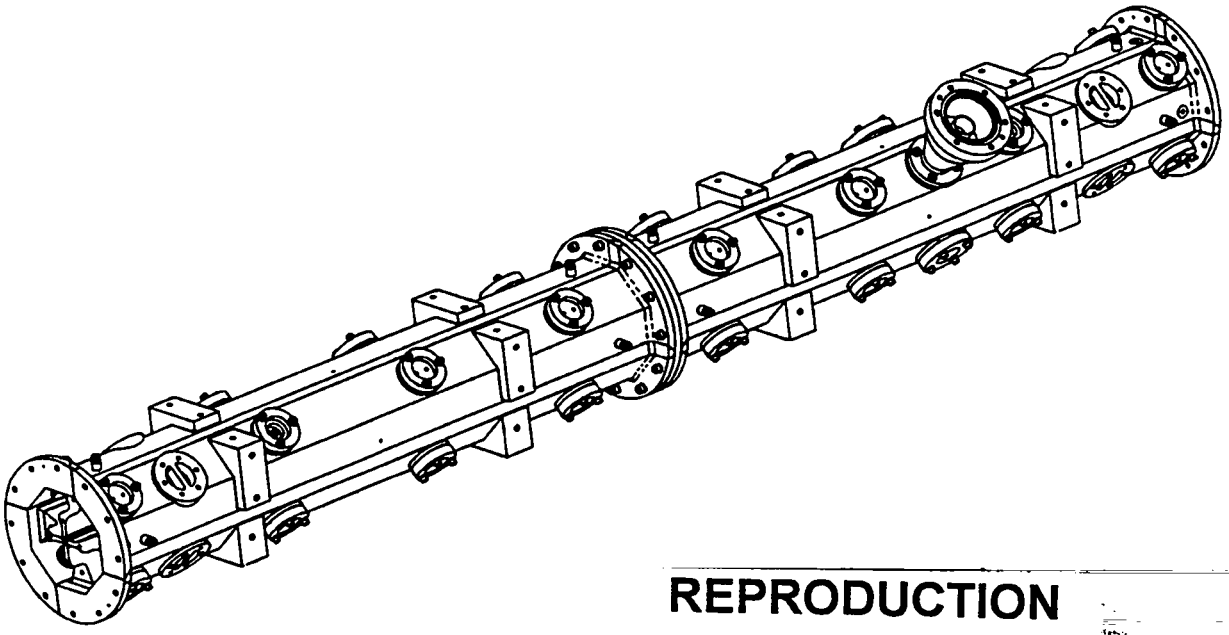

REPRODUCTION
COPY
IS-4 REPORT SECTION

LOS ALAMOS NATL. LAB. LIBS.
3 9338 00208 9992

Los Alamos
Los Alamos National Laboratory
Los Alamos, New Mexico 87545

PREFACE

The material contained here is based on my lectures on rf linear accelerators presented for the U. S. Particle Accelerator School (USPAC) at University of Texas, Austin, in January, 1992, and at Harvard University, in June, 1993. Material on linear accelerators can be found from a variety of sources, including conference proceedings, review articles, and laboratory internal reports, the very useful short course given earlier through the USPAC by G. Loew and R. Talman, Russian books on linear accelerator theory by A. D. Vlasov, and by I. M. Kapchinskiy, the large red book "Linear Accelerators", edited by P. Lapostolle and A. Septier, and some introductory material in several general books on charged particle accelerators. The field is undergoing rapid development in many areas as a result of interest in linear colliders, high-power proton linacs, the injector linac for the Superconducting Supercollider, and commercial applications. Therefore, it was clear that there was a real need for a comprehensive and systematic presentation to the physics or engineering student, who is new to the field, and it is with this objective that these notes were produced. The material is presented assuming that the student has a basic knowledge of classical and relativistic mechanics, and electromagnetism. The first chapter contains a summary and review of the prerequisite material, and it was delivered to the students prior to the first class meeting for the University of Texas course. The remaining chapters emphasize the topics of rf accelerating structures, and linac beam dynamics that are important for an introduction to the physics that underlies the subject. The principles of operation of the most common linac-accelerating structures are presented, including drift-tube linacs, coupled-cavity linacs, and the radiofrequency quadrupole (RFQ). In the area of beam dynamics we discuss focusing and defocusing effects in a linac, and the longitudinal and transverse beam dynamics both for noninteracting particles and for high-intensity beams. We discuss phase space, rms emittance, the rms-envelope equation, space-charge dominated beams, wake fields, and emittance-growth mechanisms, all of which are important for modern high-intensity linacs.

I would like to express my thanks to Mel Month, and the staff of the USPAC for their help and advice, to Margaret Dienes, who edited the lecture notes, to AT-Division at Los Alamos, including Jim Stovall, Stan Schriber, and Bob Hardekopf for their support, and to the AT-Division publications group of Carolyn Beckmann, Anita Rodriguez, and Barbara Maes. I especially want to thank my colleague Jim Billen, who helped me in presenting the courses, and who worked all the problems and helped to clarify many of the physics issues associated with the problems. Thanks to the staff members of AT-Division with whom I was able to discuss many of these topics. Putting this material together took a lot of time during evenings and weekends, and I want to thank my family, my wife Julie, and my children Mike and Anne for their patience and support.

Los Alamos, April 21, 1993 Thomas P. Wangler

INTRODUCTION TO LINEAR ACCELERATORS

Thomas P. Wangler
Los Alamos National Laboratory

TABLE OF CONTENTS

1 PRELIMINARY TOPICS AND REFERENCE MATERIAL 1

1.1 Units 1
1.2 Important Constants and Some Vector Relationships 1
1.3 Review of Relativistic Mechanics 2
1.3.1 Convenient Relativistic Conversions 3
1.4 Summary of Electromagnetic Fields and Maxwell's Equations in Vacuum 4
1.5 Cylindrical Waveguide (propagating) Modes 5
1.5.1 TE_{mn} modes 5
1.5.2 TM_{mn} Modes 6
1.5.3 Wave Velocities 7
1.5.4 Bessel Functions 7
1.6 Cylindrical Resonator (standing-wave) Modes 9
1.6.1 TE_{mnp} Modes 9
1.6.2 TM_{mnp} modes 10
1.6.3 Summary of Dispersion Relations for Cylindrical Resonators 11
1.6.4 Cavity Resonator Characteristics and Definitions 12
1.7 Equivalent Lumped Circuit Model of Cavity Resonant Mode 13
1.8 TM_{010} Cylindrical Cavity Mode 15
1.9 Coaxial Transmission Line 16
1.10 Coaxial Resonator (l/2 or half-wave Resonator) 18
1.11 Capacity-Loaded Coaxial Resonator (l/4 or quarter-wave resonator) 19
1.12 Quadrupole Lenses 20
1.13 Hill's Equation 21
1.13.1 Transfer Matrix Solution of Hill's Equation 21
1.13.2 Matrix Solution Through Piecewise Constant Elements 22
1.13.3 Phase-Amplitude Form of Solution to Hill's Equation 23
1.13.4 Transfer Matrix Through One Period 24
1.14 Thin Lens FODO Periodic Lattice 25
1.15 Problems 27

2 INTRODUCTION AND GENERAL PRINCIPLES 30

2.1 Inherent Advantages of Linear Accelerators 30
2.2 Applications 30
2.3 Overview of Linear Accelerator Technology and Operating Principles 31
2.4 Longitudinal Focusing 32
2.5 Transverse Focusing 33
2.6 Power Efficiency and Electric Breakdown 33
2.7 Accelerating Structures 34
2.8 Traveling Waves Versus Standing Waves 38
2.9 Duty Factor 39
2.10 Superconducting Linacs 39
2.11 Beam Intensity, Beam Losses, and Beam Quality 40
2.12 Summary 40

3 ACCELERATION 41

3.1 Electromagnetic Fields in a Cavity Resonator 41
3.1.1 Introduction 41
3.1.2 Axial Electric Field 42
3.1.3 Application to Uniform Cylindrical Cavity 44
3.1.4 Periodic Cavity In 0 Mode 44
3.1.5 Periodic Cavity in π Mode 46
3.1.6 Other Field Components 48
3.2 RF Acceleration in a Gap 49
3.3 Approximations for Transit-Time Factor 51
3.4 Space Harmonics in Periodic Accelerating Structures 54
3.5 Power Efficiency Figures of Merit 59
3.6 Cavity Design 61
3.7 Scaling of Cavity Parameters with Frequency 64
3.8 Problems 65

4 LINEAR ACCELERATOR STRUCTURES 67

4.1 Independently Phased Cavity Linacs 67
4.2 Wideroe Linac 69
4.3 Drift-Tube Linac 71
4.3.1 Basic Concept 71
4.3.2 Design of Drift-Tube Linacs 76
4.3.3 Summary of Drift-Tube Linacs 78
4.4 Coupled-Cavity Linacs 78
4.4.1 Basic Concept 78
4.4.2 Resonant Coupling 79
4.4.3 Coupled Oscillators Three-Oscillator Example 80
4.4.4 General Problem of N + 1 Coupled Oscillators 86
4.4.5 Coupled-Cavity Structures for Accelerators 87
4.4.6 Design of Coupled-Cavity Linacs 91
4.4.7 Relative Merits of Coupled-Cavity Linacs 92
4.5 Radiofrequency Quadrupole Linac 92
4.5.1 Introduction 92
4.5.2 Potential Function and Electric Field 94
4.6 Traveling-Wave Linacs 98
4.6.1 Overview 98
4.6.2 Constant-Impedance Structure 100
4.6.3 Constant-Gradient Structure 102
4.7 Problems 104

5 BEAM DYNAMICS 106

5.1 Longitudinal Dynamics 106
5.1.1 Introduction 106
5.1.2 Difference Equations of Longitudinal Motion for Standing-Wave Linacs 107
5.1.3 Differential Equations of Longitudinal Motion 108
5.1.4 Longitudinal Motion when Acceleration Rate is Small 109
5.1.5 Hamiltonian and Liouville's Theorem 114
5.1.6 Small Oscillations 115
5.1.7 Phase Damping 116
5.1.8 Longitudinal Dynamics of Ion Beams in Coupled-Cavity Linacs 117

5.1.9 Longitudinal Dynamics of Beams Injected into a v=c Linac 119
5.2 Transverse Dynamics 122
5.2.1 Introduction 122
5.2.2 Radial Impulse from the Equivalent Traveling Wave 123
5.2.3 Solution of Maxwell's Equations near Axis for TM Mode 124
5.2.4 Radial Impulse from Standing-Wave Field in the Gap 125
5.2.5 Electrostatic Focusing Effect in the Gap 126
5.2.6 Other Descriptions of Transverse Motion in the Gap 127
5.2.7 Quadrupole Focusing 128
5.2.8 Radial Motion for Relativistic Beams 131
5.3 Problems 132

6 MULTIPARTICLE BEAM EFFECTS 133

6.1 Beam Ellipse and Emittance 133
6.1.1 Beam Quality, Phase Space, and Emittance 133
6.1.2 RMS Beam Ellipse and RMS Emittance 135
6.1.3 Transverse Emittance 137
6.1.4 Longitudinal Emittance 138
6.1.5 Emittance Conventions 138
6.1.6 Ellipse Transformations 139
6.2 Space Charge 141
6.2.1 Introduction 141
6.2.2 Relativistic Mass and Self-Magnetic-Field Corrections 143
6.2.3 RMS Envelope Equation with Space Charge 145
6.2.4 Envelope Equation for Continuous Elliptical Beams 148
6.2.5 Envelope Equation for 3-D Ellipsoidal Bunched Beams 149
6.2.6 Equivalent Uniform Beams 151
6.2.7 Longitudinal Dynamics Including Space Charge 152
6.2.8 Longitudinal Current Limit 154
6.2.9 Transverse Dynamics with Space Charge 155
6.2.10 Matched-Beam Relationships 156
6.2.11 Transverse Current Limit 157
6.2.12 Emittance Growth from Space Charge 158
6.3 Wakefields and Emittance Growth in Electron Linacs 160
6.4 Problems 162

REFERENCES 163

BIBLIOGRAPHY 164

INTRODUCTION TO LINEAR ACCELERATORS

Thomas P. Wangler
Los Alamos National Laboratory
Los Alamos, NM 87545

1 PRELIMINARY TOPICS AND REFERENCE MATERIAL

1.1 Units

The units most commonly used in accelerator physics calculations are the SI or MKS units, with two notable exceptions.

(1) The magnetic flux density is sometimes expressed in gauss units. The conversion factor between tesla and gauss is 1 gauss = 10^{-4} tesla.

(2) Beam energy is usually given in electron volt (eV) units rather than joules. The electron volt is defined as the energy acquired by a particle with charge equal to the electron charge that has been accelerated through a potential difference of 1 volt. The conversion factor between electron volts and joules is $1.60217733 \times 10^{-19}$ joules = 1 eV.

The particle mass is usually expressed as the ratio of its rest energy to c^2 in eV/c^2 units.

1.2 Important Constants and Some Vector Relationships[1]

Some important constants are given in Table 1.1. from *Phys. Lett.* **B239** (1990).

Table 1.1 Constants

Speed of light	c	2.99792458×10^8 m/s
Electron charge	e	$1.60217733 \times 10^{-19}$ C
Electron mass	m_e	0.51099906 MeV/c^2
Proton mass	m_p	938.27231 MeV/c^2
Atomic mass unit*	u	931.49432 MeV/c^2
Permeability of free space	μ_0	$4\pi \times 10^{-7}$T-m/A
Permittivity of free space	ε_0	$8.854187817 \times 10^{-12}$ F/m
DC resistivity of room temperature copper (nominal value)	$1/\sigma$	1.7×10^{-8} W-m

*Mass of $^{12}C/12$.

Some useful differential relationships are given in Table 1.2.

Table 1.2 Differential Relationships

Cartesian coordinates	Cylindrical coordinates
	Orthogonal line elements
dx, dy, dz	$dr, r\,d\theta, dz$
	Components of gradient
$(\nabla\psi)_x = \frac{\partial\psi}{\partial x}$	$(\nabla\psi)_r = \frac{\partial\psi}{\partial r}$
$(\nabla\psi)_y = \frac{\partial\psi}{\partial y}$	$(\nabla\psi)_\theta = \frac{1}{r}\frac{\partial\psi}{\partial\theta}$
$(\nabla\psi)_z = \frac{\partial\psi}{\partial z}$	$(\nabla\psi)_z = \frac{\partial\psi}{\partial z}$
	The divergence of $\mathbf{A} = \nabla\cdot\mathbf{A}$
$\frac{\partial A_x}{\partial x} + \frac{\partial A_y}{\partial y} + \frac{\partial A_z}{\partial z}$	$\frac{1}{r}\frac{\partial(rA_r)}{\partial r} + \frac{1}{r}\frac{\partial A_\theta}{\partial\theta} + \frac{\partial A_z}{\partial z}$
	Components of curl $\mathbf{A}$
$(\nabla\times\mathbf{A})_x = \left(\frac{\partial A_z}{\partial y} - \frac{\partial A_y}{\partial z}\right)$	$(\nabla\times\mathbf{A})_r = \left(\frac{1}{r}\frac{\partial A_z}{\partial\theta} - \frac{\partial A_\theta}{\partial z}\right)$
$(\nabla\times\mathbf{A})_y = \left(\frac{\partial A_x}{\partial z} - \frac{\partial A_z}{\partial x}\right)$	$(\nabla\times\mathbf{A})_\theta = \left(\frac{\partial A_r}{\partial z} - \frac{\partial A_z}{\partial r}\right)$
$(\nabla\times\mathbf{A})_z = \left(\frac{\partial A_y}{\partial x} - \frac{\partial A_x}{\partial y}\right)$	$(\nabla\times\mathbf{A})_z = \frac{1}{r}\left(\frac{\partial(rA_\theta)}{\partial r} - \frac{\partial A_r}{\partial\theta}\right)$
	Laplacian of ψ = div grad $\psi = \nabla^2\psi$
$\frac{\partial^2\psi}{\partial x^2} + \frac{\partial^2\psi}{\partial y^2} + \frac{\partial^2\psi}{\partial z^2}$	$\frac{1}{r}\frac{\partial}{\partial r}\left(r\frac{\partial\psi}{\partial r}\right) + \frac{1}{r^2}\frac{\partial^2\psi}{\partial\theta^2} + \frac{\partial^2\psi}{\partial z^2}$

Table 1.3 contains useful vector relationships.

1.3 Review of Relativistic Mechanics[2,3]

Consider a particle of mass m and speed v. If c is the speed of light define β as

$$\beta = v / c$$

The relativistic mass factor γ is defined as $\gamma = 1/\sqrt{1-\beta^2}$.

The momentum is $\vec{p} = \gamma m \vec{v}$ The kinetic energy is $W = (\gamma - 1)mc^2$. The rest energy is mc^2 The total energy is $U = W + mc^2 = \gamma m c^2$. The nonrelativistic limit applies when $\beta << 1$. Then

$$\gamma \to 1 + \frac{\beta^2}{2}; \quad \vec{p} \to m\vec{v}; \quad W \to \frac{mv^2}{2}; \quad U \to mc^2 + \frac{mv^2}{2}.$$

Table 1.3 Vector Relationships

$$\vec{A} \cdot \vec{B} \times \vec{C} = \vec{B} \cdot \vec{C} \times \vec{A} = \vec{C} \cdot \vec{A} \times \vec{B}$$

$$\vec{A} \times (\vec{B} \times \vec{C}) = (\vec{A} \cdot \vec{C})\vec{B} - (\vec{A} \cdot \vec{B})\vec{C}$$

$$\nabla(\psi\phi) = \phi\nabla\psi + \psi\nabla\phi$$

$$\nabla \cdot (\psi\vec{A}) = \vec{A} \cdot \nabla\psi + \psi\nabla \cdot \vec{A}$$

$$\nabla \cdot (\vec{A} \times \vec{B}) = \vec{B} \cdot \nabla \times \vec{A} - \vec{A} \cdot \nabla \times \vec{B}$$

$$\nabla \times (\psi\vec{A}) = \nabla\psi \times \vec{A} + \psi\nabla \times \vec{A}$$

$$\nabla \times (\nabla \times \vec{A}) = \nabla(\nabla \cdot \vec{A}) - \nabla^2\vec{A}$$

$$\nabla \cdot \nabla \times \vec{A} = 0$$

$$\nabla \cdot \nabla\psi = \nabla^2\psi$$

$$\nabla \times \nabla\psi = 0$$

1.3.1 Convenient Relativistic Conversions

(a) *Velocity to kinetic energy:*

$$\gamma = 1/\sqrt{1-\beta^2}; \qquad W = (\gamma - 1)mc^2 .$$

(b) *Kinetic energy to velocity:*

$$\gamma = \frac{W + mc^2}{mc^2}; \;\; \beta = \sqrt{1 - 1/\gamma^2} .$$

(c) *Energy to momentum:*

$$\beta\gamma = \sqrt{\gamma^2 - 1} .$$

For small differences:

$$\delta\gamma = \gamma^3\beta\,\delta\beta, \;\; \delta\gamma = \beta\,\delta(\beta\gamma); \;\; \delta W = mc^2\delta\gamma, \;\; \delta p = mc\delta(\beta\gamma) .$$

Dynamics:

$$\vec{F} = \frac{d\vec{p}}{dt} = m\frac{d(\gamma\vec{v})}{dt}.$$

For a particle of charge q in an electromagnetic field, the Lorentz force is

$$\vec{F} = q(\vec{E} + \vec{v} \times \vec{B}).$$

1.4 Summary of Electromagnetic Fields and Maxwell's Equations in Vacuum[2-4]

Definitions:

ρ (charge density), $\vec{j}$ (current density),
$\vec{E}$ (electric field), $\vec{B}$ (magnetic-flux density), $\vec{H}$ (magnetic field).

$$\vec{B} = \mu_0 \vec{H}.$$

Maxwell's equations (differential form):

$$\nabla \bullet \vec{E} = \rho / \varepsilon_0 \quad \text{Gauss's law;}$$

$$\nabla \bullet \vec{B} = 0;$$

$$\nabla \times \vec{E} = -\partial\vec{B} / \partial t \quad \text{Faraday's law;}$$

$$\nabla \times \vec{H} = \vec{j} + \varepsilon_0 \partial\vec{E} / \partial t \quad \text{Ampere's law;}$$

$$\nabla \bullet \vec{j} = -\partial\rho / \partial t \quad \text{continuity equation.}$$

Maxwell's equations (integral form):

$$\int \vec{E} \bullet d\vec{S} = \frac{1}{\varepsilon_0}\int \rho dV \quad \text{Gauss's law;}$$

$$\int \vec{B} \bullet d\vec{S} = 0;$$

$$\int \vec{E} \bullet d\vec{l} = -\int \frac{\partial\vec{B}}{\partial t} \bullet d\vec{S} \quad \text{Faradays law;}$$

$$\int \vec{H} \bullet \vec{dl} = \int (\vec{j} + \varepsilon_0 \frac{\partial \vec{E}}{\partial t}) \bullet d\vec{S} \quad \text{Ampere's law;}$$

$$\int \vec{j} \bullet \vec{dS} = -\int \frac{\partial \rho}{\partial t} dV \quad \text{continuity equation.}$$

Wave equation:

$$\nabla^2 \vec{E} - \frac{1}{c^2}\frac{\partial^2 \vec{E}}{\partial t^2} = 0; \quad \nabla^2 \vec{H} - \frac{1}{c^2}\frac{\partial^2 \vec{H}}{\partial t^2} = 0.$$

Boundary Conditions on Conducting Walls:

At the surface of a perfect conductor, only the normal electric-field component and the tangential magnetic-field component can be nonzero.

1.5 Cylindrical Waveguide (propagating) Modes:[4,5]

1.5.1 TE_{mn} modes

The field components are given by

$$B_z = AJ_m(k_{mn}r)\cos m\theta \exp[j(\omega t - k_z z)],$$

$$B_r = -j\frac{k_z}{k_{mn}} AJ'_m(k_{mn}r)\cos m\theta \exp[(j(\omega t - k_z z)],$$

$$B_\theta = j\frac{k_z}{k_{mn}^2 r} AJ_m(k_{mn}r)\sin m\theta \exp[(j(\omega t - k_z z)],$$

$$E_z = 0 \quad , \quad E_r = \omega B_\theta / k_z \quad , \quad E_\theta = -\omega B_r / k_z .$$

$$\omega^2 / c^2 = k_{mn}^2 + k_z^2 \quad \text{dispersion relation,}$$

where $k_{mn} = x'_{mn} / a$ [defined by , $J'_m(x'_{mn}) = 0$] and $k'_z = 2\pi / \lambda_{guide}$.

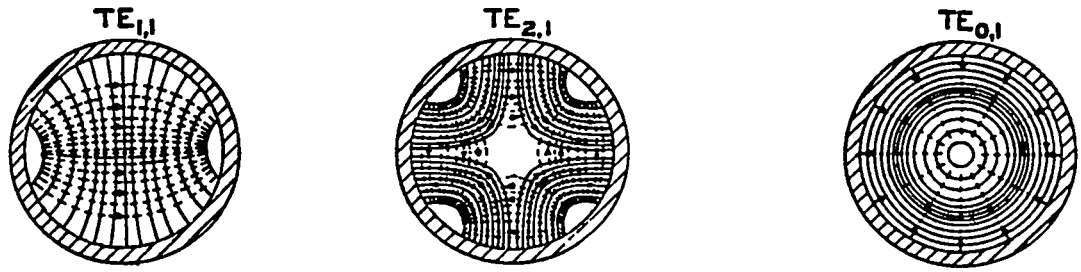

Figure 1.1. TE-mode field patterns in a circular waveguide.

1.5.2 TM_{mn} Modes

The field components are give by

$$E_z = AJ_m(k_{mn}r)\cos m\theta \exp\left[j(\omega t - k_z z)\right] ,$$

$$E_r = -j\frac{k_z}{k_{mn}} AJ'_m(k_{mn}r)\cos m\theta \exp\left[j(\omega t - k_z z)\right] ,$$

$$E_\theta = j\frac{k_z}{k_{mn}^2 r} AJ_m(k_{mn}r)\sin m\theta \exp\left[j(\omega t - k_z z)\right] ,$$

$$B_z = 0 \quad , \quad B_r = -\omega E_\theta / k_z c^2 \quad , \quad B_\theta = \omega E_r / k_z c^2 .$$

$\omega^2 / c^2 = k_{mn}^2 + k_z^2$ dispersion relation,

where $k_{mn} = x_{mn} / a$ [defined by $J_m(x_{mn}) = 0$], and $k_z = 2\pi/\lambda_{guide}$.

Nomenclature:

The subscript m (m = 0, 1, 2, ...) is the number of full period variations in θ of the field components. The subscript n (n = 1, 2, 3, ...) is the number of zeros of the axial field component in the radial direction in the range $0 < r \leq a$, (excluding r = 0).

The lowest frequency mode for a given m, n family is called the cutoff frequency. This occurs when $k_z = 0$ or $\lambda_{guide} = \infty$. Then $k = k_{mn}$, and

$$\omega_c \equiv \omega = k_{mn}c = \begin{bmatrix} x'_{mn}\, c / a \text{ for TE modes} \\ x'_{mn}\, c / a \text{ for TM modes} \end{bmatrix} .$$

Figure 1.2 shows the field pattern for the lowest TM mode.

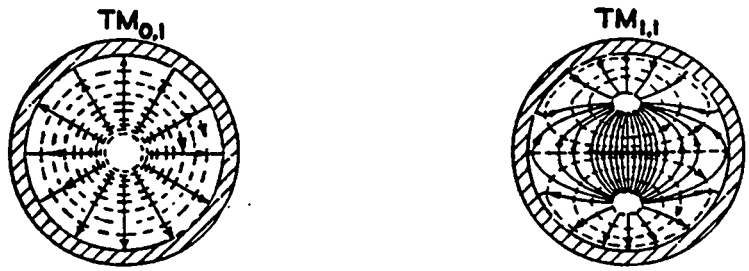

Figure 1.2. TM-mode field patterns in a circular waveguide.

1.5.3 Wave Velocities

The phase velocity is the velocity of a point of constant phase. For the waveguide modes

$$v_p = \frac{\omega}{k_z} = \frac{c}{\sqrt{1-(k_{mn}^2 c^2/\omega^2)}} > c \ .$$

The group velocity is the velocity at which the energy, consisting of a finite frequency region of the spectrum, propagates. For the waveguide modes

$$v_g = \frac{d\omega}{dk_z} = c\sqrt{1-(k_{mn}^2 c^2/\omega^2)} < c \ .$$

1.5.4 Bessel Functions

The first few Bessel functions of order m are shown in Figure 1.3. The derivatives can be easily calculated from

$$J_m'(x) = \frac{J_{m-1}(x) - J_{m+1}(x)}{2} \quad , \quad \text{and } J_0'(x) = -J_1(x) \ .$$

Fig. 1.3 contains the zeros of these functions.

The modified Bessel function is defined as

$$I_m(x) = j^{-m} J_m(jx) \ .$$

$$I_m'(x) = \frac{I_{m-1}(x) - I_{m+1}(x)}{2} \quad \text{and} \quad I_0'(x) = I_1(x) \ .$$

The first few are shown in Fig. 1.3. The expansions to lowest order of the first few Bessel functions are useful. We have

$$J_0(x) \cong 1 - x^2/4 + \ldots, \quad J_1(x) \cong x/2 + \ldots;$$

$$I_0(x) \cong 1 + x^2/4 \ldots, \quad I_1(x) \cong x/2 + \ldots .$$

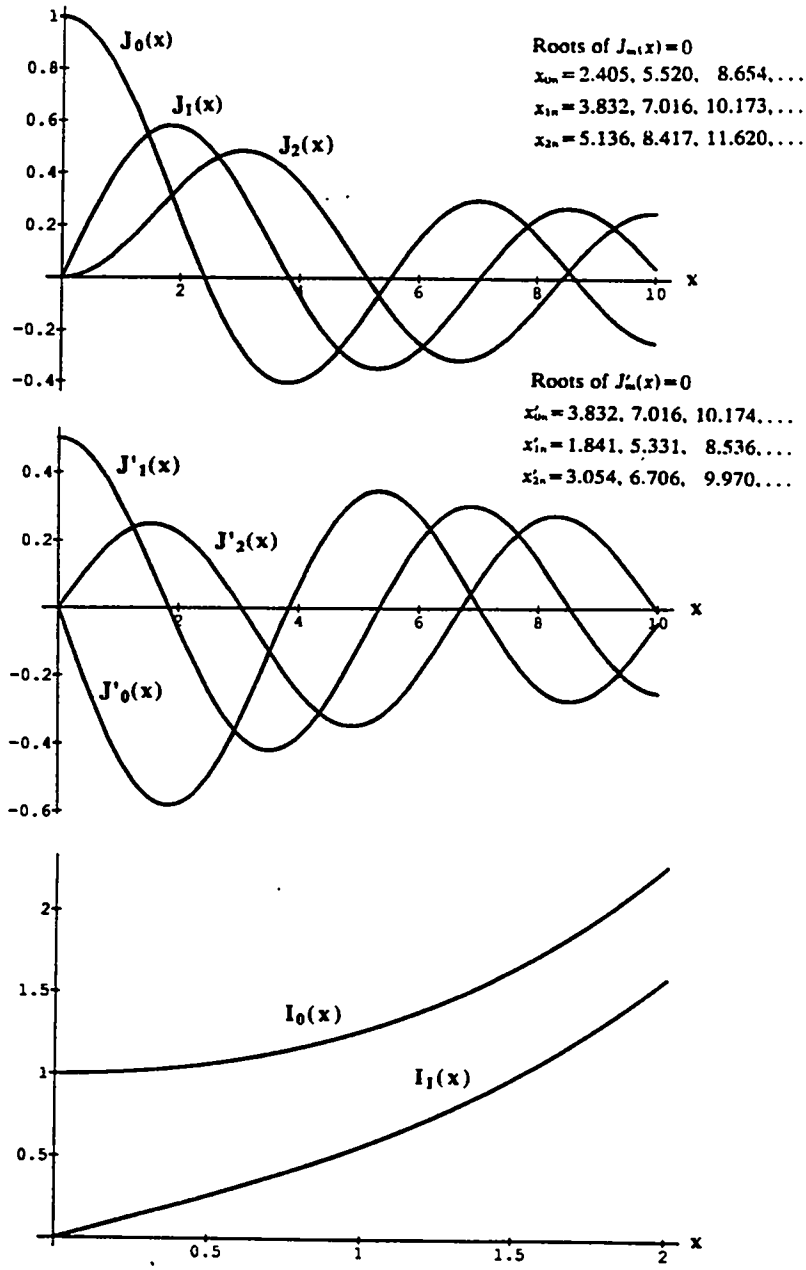

Fig. 1.3. Commonly use Bessel functions.

1.6 Cylindrical Resonator (standing-wave) Modes[4,5]

1.6.1 TE_{mnp} Modes

The field patterns for some common modes are given in Fig. 1.4 and the field components are given by

$$B_z = B_0 J_m(k_{mn} r)\cos m\theta \sin(p\pi z/\ell)\exp[j\omega t] ,$$

$$B_r = \frac{p\pi}{\ell}\frac{a}{x'_{mn}} B_0 J'_m(k_{mn} r)\cos m\theta \cos(p\pi z/\ell)\exp[j\omega t] ,$$

$$B_\theta = -\frac{p\pi}{\ell}\frac{ma^2}{x'^2_{mn} r} B_0 J_m(k_{mn} r)\sin m\theta \cos(p\pi z/\ell)\exp[j\omega t] ,$$

$$E_z = 0 ,$$

$$E_r = j\omega\frac{ma^2}{x'^2_{mn} r} B_0 J_m(k_{mn} r)\sin m\theta \sin(p\pi z/\ell)\exp[j\omega t] ,$$

$$E_\theta = j\omega\frac{a}{x'_{mn}} B_0 J'_m(k_{mn} r)\cos m_\theta \sin(p\pi z/\ell)\exp[j\omega t] .$$

$$\omega^2/c^2 = k_{mn}^2 + k_z^2 \quad \text{dispersion relation,}$$

where $k_{mn} = \frac{x'_{mn}}{a}$ (defined by $J'_m(x'_{mn}) = 0$)

and $k_z = \frac{2\pi}{\lambda_{guide}} = \frac{p\pi}{\ell}$, $p = 1,2,3,\ldots$.

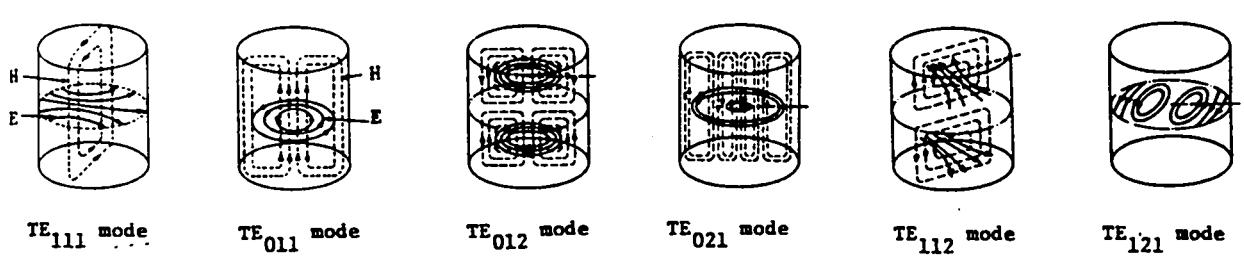

Fig. 1.4 TE-mode field patterns in cylindrical cavity resonator.

1.6.2 TM_{mnp} modes

The field patterns for some common modes are given in Fig. 1.5 and the field components are given by

$$E_z = E_0 J_m(k_{mn} r)\cos m\theta \cos(p\pi z/\ell)\exp[j\omega t] \ ,$$

$$E_r = -\frac{p\pi}{\ell}\frac{a}{x_{mn}} E_0 J'_m(k_{mn} r)\cos m\theta \sin(p\pi z/\ell)\exp[j\omega t] \ ,$$

$$E_\theta = -\frac{p\pi}{\ell}\frac{ma^2}{x_{mn}^2 r} E_0 J_m(k_{mn} r)\sin m\theta \sin(p\pi z/\ell)\exp[j\omega t] \ ,$$

$$B_z = 0 \ ,$$

$$B_r = -j\omega\frac{ma^2}{x_{mn}^2 r c^2} E_0 J_m(k_{mn} r)\sin m\theta \cos(p\pi z/\ell)\exp[j\omega t] \ ,$$

$$B_\theta = -j\omega\frac{a}{x_{mn} c^2} E_0 J'_m(k_{mn} r)\cos m\theta \cos(p\pi z/\ell)\exp[j\omega t] \ ,$$

$$\omega^2/c^2 = k_{mn}^2 + k_z^2 \ \text{dispersion relation}$$

where $k_{mn} = \frac{x_{mn}}{a}$ (defined by $J_m(x_{mn}) = 0$)

and $k_z = \frac{2\pi}{\lambda_{guide}} = \frac{p\pi}{\ell}$, $p = 0, 1, 2, \ldots$.

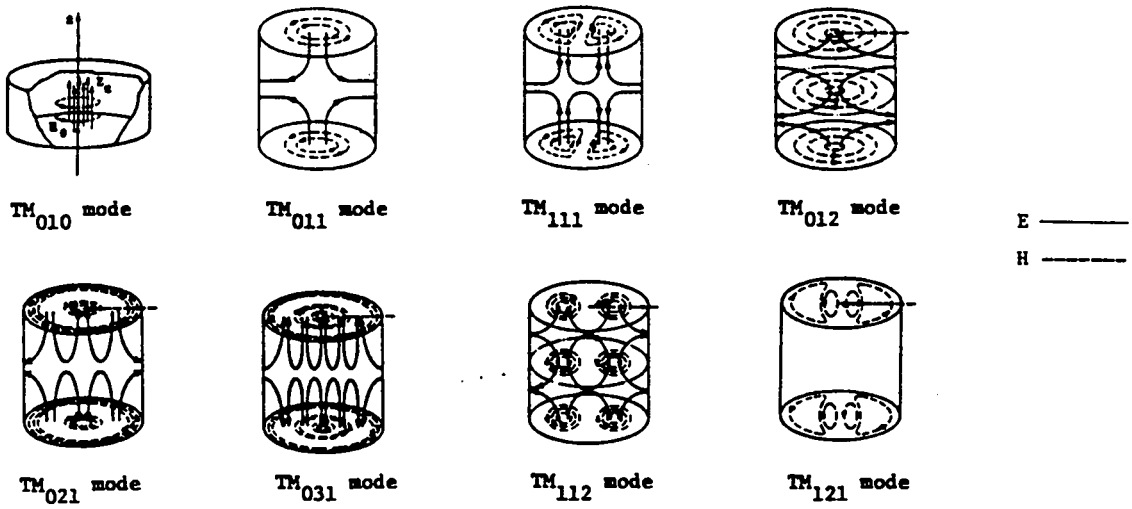

Figure 1.5 TM-mode field patterns in cylindrical cavity resonator.

1.6.3 Summary of Dispersion Relations for Cylindrical Resonators

$$\left[\frac{\omega}{2\pi}\right]^2 = \left[\frac{\omega_c}{2\pi}\right]^2 + \left[\frac{k_z c}{2\pi}\right]^2 \quad \text{where } k_z = \frac{p\pi}{\ell},$$

$$p = \begin{bmatrix} 0, 1, 2, \ldots \text{ for TM modes} \\ 1, 2, 3, \ldots \text{ for TE modes} \end{bmatrix},$$

$$\omega_c = \begin{bmatrix} x_{mn}\, c/a \text{ for TM modes} \\ x'_{mn}\, c/a \text{ for TE modes} \end{bmatrix}.$$

Nomenclature:

The subscript m (m = 0, 1, 2, ...) is the number of full-period variations in θ of the field components. The subscript n (n = 1, 2, 3, ...) is the number of zeros of the axial field component in the radial direction in the range $0 < r \leq a$ (excluding r = 0). The subscript p (p = 0, 1, 2, ... for TM, and p = 1, 2, 3, ... for TE modes) is the number of half-period variations in z of any field component.

1.6.4 Cavity Resonator Characteristics and Definitions[4-6]

Quality factor:

$$Q \equiv \omega \frac{\text{cavity stored energy}}{\text{average power dissipated}} = \frac{\omega U}{P} .$$

Stored energy:

$$U \equiv \frac{\varepsilon_0}{2} \int E^2 dV + \frac{\mu_0}{2} \int H^2 dV .$$

In the steady state for any resonant mode, the electric and magnetic stored energies oscillate in time, 90° out of phase. The total stored energy U remains constant. The time-averaged electric and magnetic energies are equal. It is usually easiest to calculate U by using either the electric or the magnetic term alone with the peak value of the field in time.

Power dissipation:

The rf currents and the ohmic losses are confined to within about a skin depth at the surface. If dS is the area element on the cavity walls, the average power dissipation per cycle is

$$P = \frac{R_s}{2} \int H^2 dS$$

where P is the average power over an rf cycle, in watts; H is the peak magnetic field at the surface in amperes per meter; dS is the surface area element in meter squared, and R_S is the rf surface resistance in ohms. For normal conducting metals

$$R_s = \frac{1}{\sigma\delta} ,$$

where σ is the dc conductivity and δ is the skin depth, given by

$$\delta = \sqrt{\frac{2}{\sigma\mu_0\omega}} .$$

Recall that $\omega = 2\pi f$ is the rf angular frequency. For superconducting niobium the rf losses are also confined to the region at the surface. For the rf surface resistance we will use the formula

$$R_s(\Omega) = 9 \times 10^{-5} \frac{f^2(\text{GHz})}{T(^\circ\text{K})} \exp\left[-\alpha \frac{T_c}{T}\right] + R_{\text{residual}} ,$$

where $\alpha = 1.83$, and $T_c = 9.2K$ is the critical temperature. $R_{residual}$ is the residual resistance, which is the result of various imperfections in the surface and typically lies in the range $10^{-8}\Omega < R_{residual} < 10^{-7}\Omega$.

Loaded and unloaded Q:

In the steady state the generator supplies the power losses in the cavity walls. If the generator also supplies power to elements external to the cavity, this should be included in the calculation of the Q. We define Q_0 as the quality factor of the cavity unloaded by the external elements. Thus

$$Q_0 \equiv \omega U / P_{cavity} \ .$$

The total (loaded) power supplied by the generator is

$$P_T = P_{cavity} + P_{external} \ .$$

If the loaded quality factor is $Q_L \equiv \dfrac{\omega U}{P_T}$,

then $\dfrac{1}{Q_L} = \dfrac{1}{Q_0} + \dfrac{1}{Q_{ext}}$ where $Q_{ext} = \dfrac{\omega U}{P_{external}}$.

1.7 Equivalent Lumped Circuit Model of Cavity Resonant Mode

A cavity mode is often represented by an equivalent parallel resonant circuit driven by a current generator (Fig. 1.6). The current driven by the generator causes a voltage across the circuit. We have

$$I(t) = I_C + I_L + I_R, \quad I(t) = C\dot{V} + \frac{\int V dt}{L} + \frac{V}{R}, \quad \frac{\dot{I}}{C} = \ddot{V} + \frac{2\dot{V}}{\tau} + \omega_0^2 V,$$

where $\omega_0^2 \equiv \dfrac{1}{LC}$ and $\tau = 2RC$.

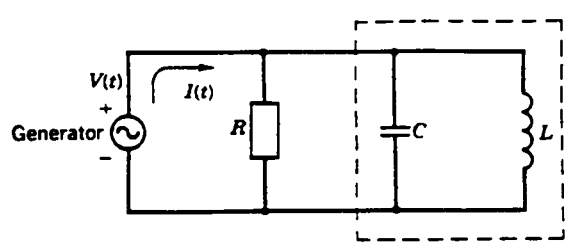

Fig. 1.6. Circuit model of cavity resonator.

This is the equation for a damped driven oscillator. We express the driving term with driving frequency ω as

$$\dot{I}/C = F_0 \cos \omega t.$$

It can be shown that if the peak voltage is V, the stored energy is

$$U = \frac{1}{2}CV^2,$$

the average power loss per cycle is $P = V^2/2R$,

and the quality factor is $Q = \frac{\omega_0 U}{P} = \frac{\omega_0 \tau}{2}$.

The steady-state solution is $V(t) = \frac{F_0 \cos(\omega t + \phi)}{\sqrt{(\omega_0^2 - \omega^2)^2 + (2\omega/\tau)^2}}$,

where $\tan \phi = \frac{2\omega/\tau}{\omega_0^2 - \omega^2}$.

This results in $\omega = \omega_0$ when $\phi = 90°$,
$\omega < \omega_0$ when $0 \le \phi < 90°$,
$\omega > \omega_0$ when $90° < \phi \le 180°$.

For fixed ω_0 and fixed t, if resonance is defined as the frequency that gives maximum amplitude, resonance corresponds to

$$\omega_r \equiv \omega^2 = \omega_0^2 - 2/\tau^2.$$

The resonant amplitude is $V_0(\omega_r) = \frac{F_0}{\frac{2\omega_0}{\tau}\sqrt{1 - \frac{1}{(\omega_0 \tau)^2}}}$.

By convention the bandwidth of an oscillator is the frequency difference $\Delta\omega$ between the half power points of the resonance response curve. This voltage is lower than the peak by $\sqrt{2}$. Thus

$$\Delta\omega \equiv 2|\omega - \omega_r| = 2/\tau = \omega_0 / Q_0.$$

Then $Q_0 = \omega_0 / \Delta\omega$.

Oscillators are classified as overdamped, critically damped, or underdamped. For a high-Q resonator we deal with the underdamped case. If at t = 0 the driving force is turned off, with the oscillator in the steady state, the voltage decays as

$$V(t) = V_0 \cos(\omega_1 \tau + \delta) \exp(-t/\tau) ,$$

where $\omega_1^2 = \omega_0^2 - 1/\tau^2, \quad \tau = 2Q_0/\omega_0$.

1.8 TM_{010} Cylindrical Cavity Mode[2-5]

Because this mode (see Fig. 1.7) is the most similar to the mode used for acceleration in linear accelerator structures, it is important to study it more closely to understand its characteristics. The nonzero field components are

$$E_z = E_0 J_0(k_{01} r) \sin(\omega t) , \quad B_\theta = \frac{E_0}{c} J_1(k_{01} r) \cos(\omega t) ,$$

with $\omega/c = k_{01} = x_{01}/a$, where $x_{01} = 2.405$. Thus the frequency is independent of the cavity length for this mode, but depends on the cavity radius a as

$$\frac{\omega}{2\pi} = \frac{k_{01} c}{2\pi} = \frac{2.405c}{2\pi a} .$$

Note that the electric and magnetic fields are 90° out of phase. The electric field maximum E_0 is at r = 0, where J_0 has its maximum. The magnetic field maximum, $B = 0.5819\ E_0/c$ is at r = 0.766a, where J_1 has its maximum. The ratio of peak magnetic to peak electric fields is

$$\frac{B_{max}}{E_{max}} = \frac{0.5819}{c} = 19.4 \frac{\text{gauss}}{\text{MV/m}} .$$

For a cavity of length ℓ and radius a the stored energy is

$$U = \frac{\pi}{2} \varepsilon_0 \ell a^2 E_0^2 J_1^2(2.405) .$$

The power dissipation on the walls is

$$P = \pi \frac{\varepsilon_0}{\mu_0} a R_s E_0^2 J_1^2(2.405)[\ell + a] .$$

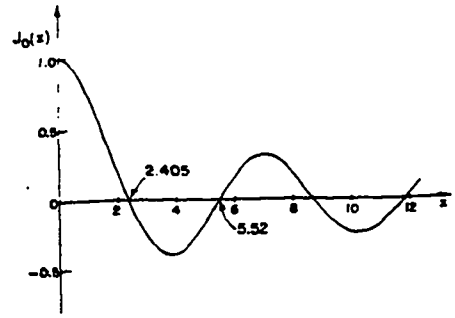

The Bessel function $J_0(x)$.

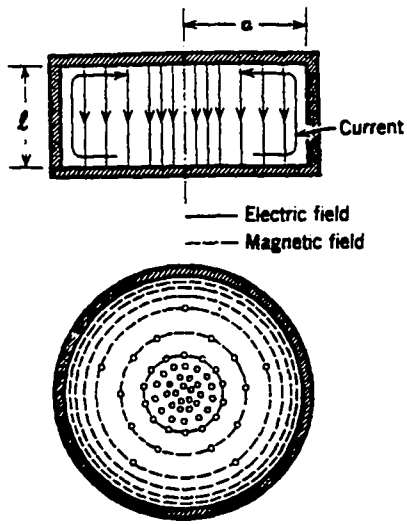

Sections through a cylindrical cavity with fields of TM_{010} mode.

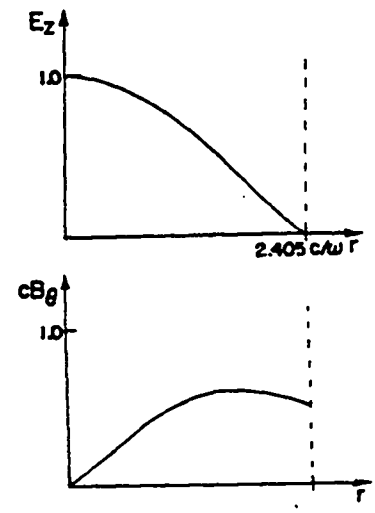

Figure 1.7 Fields for a TM010 mode of a cylindrical (pillbox) cavity resonator.

The first term comes from the losses in the cylindrical wall and the second term from those in the two end walls. The quality factor is

$$Q_0 = \frac{\omega U}{P} = \frac{\mu_0 c}{2R_s} \frac{2.405}{\left[1+\frac{a}{\ell}\right]}.$$

1.9 Coaxial Transmission Line[4,5]

We are interested in the TEM mode of a coaxial line (See Fig. 1.8). The nonzero field components are

$$B_\theta = \frac{\mu_0 I_0}{2\pi r}\exp[j(\omega t - k_z z)],$$

$$E_r = \sqrt{\frac{\mu_0}{\varepsilon_0}}\frac{I_0}{2\pi r}\exp[j(\omega t - k_z z)],$$

where I_0 is the current that flows on each conductor. The field pattern is shown in Fig. 1.9. Note that the electric and magnetic fields are in phase. The relationship between frequency and wave number is the same as in free space, $\omega = k_z c$. The capacitance per unit length between the conductors is

$$C_1 = \frac{2\pi\varepsilon_0}{\ln b/a},$$

and the inductance per unit length is $L_1 = \frac{\mu_0}{2\pi}\ln b/a$.

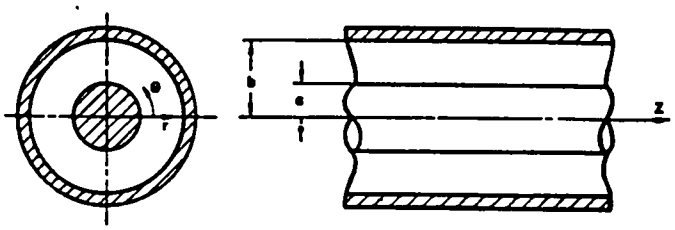

Fig. 1.8. A section of coaxial transmission line.

$$L_1 = \frac{\mu_0}{2\pi}\ln b/a .$$

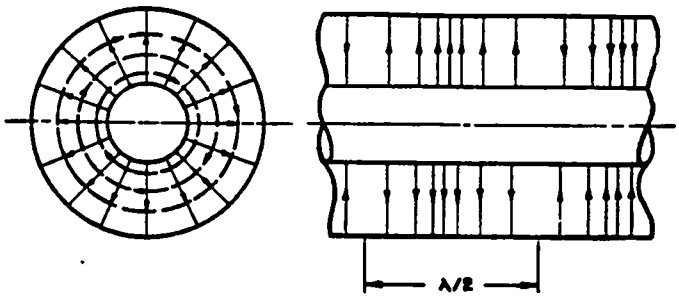

Fig.1.9. Field distribution for the principal mode in a coaxial line.

The characteristic impedance of a transmission line is the ratio of the peak voltage across the conductors to the peak current in the conductors when a traveling wave propagates along the line. The peak voltage is related to the peak electric field by

$$E_r = \frac{V_0}{r \ln b/a}.$$

Thus $V_0 = I_0 \sqrt{\frac{\mu_0}{\varepsilon_0}} \frac{\ln(b/a)}{2\pi}$.

The characteristic impedance is $Z_0 = \sqrt{\frac{\mu_0}{\varepsilon_0}} \frac{\ln(b/a)}{2\pi}$.

1.10 Coaxial Resonator (λ/2 or half-wave Resonator)[4,5]

A coaxial resonator (Fig. 1.10) is formed by placing conducting end walls on a section of coaxial line. When the section length is an integer multiple of half wavelengths, a TEM resonant standing-wave mode can exist. Resonance occurs when the boundary condition on the end walls, $E_r = 0$, is satisfied. This occurs when the conducting walls are separated by a distance

$$\ell = p\lambda/2, \quad p = 1, 2, 3, \ldots .$$

The nonzero field components are

$$B_\theta = \frac{2\mu_0 I_0}{2\pi r} \cos(p\pi z/\ell) \exp[j\omega t] ,$$

$$E_r = -2j\sqrt{\frac{\mu_0}{\varepsilon_0}} \frac{I_0}{2\pi r} \sin(p\pi z/\ell) \exp[j\omega t] ,$$

where $\omega = k_z c = \frac{p\pi c}{\ell}$, $p = 1, 2, 3, \ldots$.

The stored energy is $U = \frac{\mu_0 \ell I_0^2 \ln(b/a)}{2\pi}$

and the quality factor is $Q_0 = \frac{p\pi}{R_s} \sqrt{\frac{\mu_0}{\varepsilon_0}} \frac{\ln(b/a)}{\left[\ell\left(\frac{1}{a} + \frac{1}{b}\right) + 4 \ln \frac{b}{a}\right]}$.

. . .

The most common resonator of this type corresponds to p = 1, and is called the half-wave resonator. A full-wave resonator corresponds to p = 2.

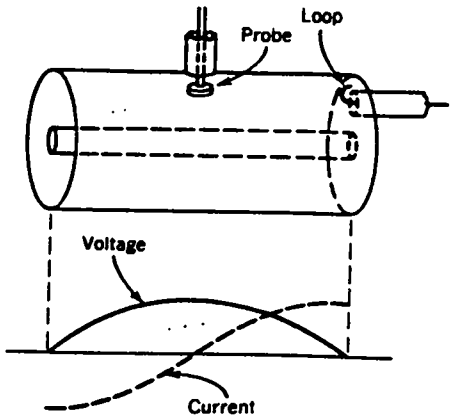

Fig. 1.10. Coaxial resonator with voltage and current standing waves.

1.11 Capacity-Loaded Coaxial Resonator (λ/4 or quarter-wave resonator)[4,5,7]

A widely used type of resonator for accelerator applications is the coaxial line terminated at one end by a short, and at the other end by a capacitance (Fig. 1.11). The transition from a coaxial line resonator to a cylindrical cavity is shown in Fig. 1.12. The capacitive termination can be accomplished in practice with a coaxial line that has, at one end, a small gap between the center conductor and a conducting end wall. To obtain the resonant frequency we use a result of transmission line theory, namely, that the impedance between conductors at a distance λ from a shorted plane is

$$Z = jZ_0 \tan(2\pi\ell/\lambda) ,$$

where Z_0 is the characteristic impedance.

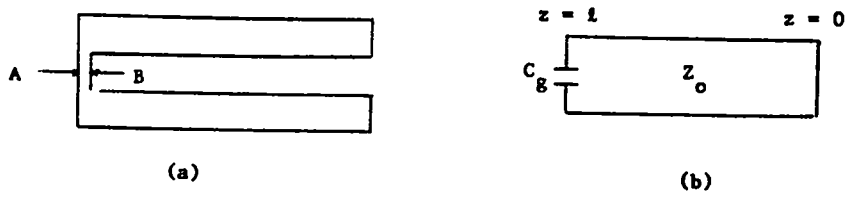

Fig. 1.11. Short gap coaxial resonator with equivalent circuit.

For $\ell < \lambda/4$, Z is positive and an inductive impedance. This is the impedance looking back into the coaxial line from the gap. A resonant mode will exist at frequency ω if a capacitance is placed across the line such that

$$1/\omega C = Z_0 \tan(2\pi\ell/\lambda) .$$

For $\omega C Z_0 << 1$, the resonant modes correspond approximately to $\ell = \lambda/4, 3\lambda/4, 5\lambda/4$, etc. As $\omega C Z_0$ increases, ℓ decreases at resonance, so that for the lowest mode $\ell < \lambda/4$. Thus the capacitive loading shortens the resonator.

Recall that the characteristic impedance of the coaxial line is

$$Z_0 = \sqrt{\frac{\mu_0}{\varepsilon_0}} \frac{\ln(b/a)}{2\pi} .$$

Thus resonance occurs when

$$\tan(2\pi\ell/\lambda) = \sqrt{\frac{\varepsilon_0}{\mu_0}} \frac{2\pi}{\omega C \ln(b/a)} .$$

Accurate design formulae for the quarter-wave resonator are given by Moreno[7].

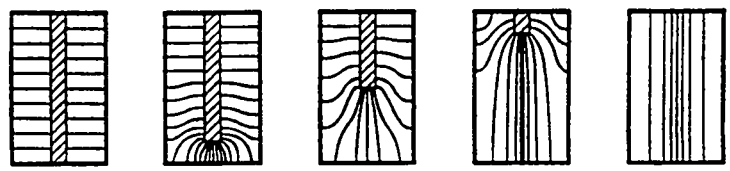

Fig. 1.12. Transition from coaxial line to cylindrical resonator, showing electric field lines.

1.12 Quadrupole Lenses

The quadrupole lens generally provides the strongest transverse focusing and is a universal feature of accelerators. The pole tips ideally have hyperbolic profiles. The quadrupole gradient is

$$G = \frac{\partial B_x}{\partial y} = \frac{\partial B_y}{\partial x} .$$

For a particle moving along the z direction with velocity v and with transverse coordinates (x,y), the Lorentz force components are

$$F_x = vG_x, \quad F_y = -vG_y .$$

If G is positive, the lens defocuses in x and focuses in y. If G is negative this polarity reverses. The two polarities are shown in Fig. 1.13. Although individual quadrupole

lenses focus in only one plane, they can be combined with both polarities in doublets, triplets, and higher multiplets to give overall strong focusing in both transverse planes.

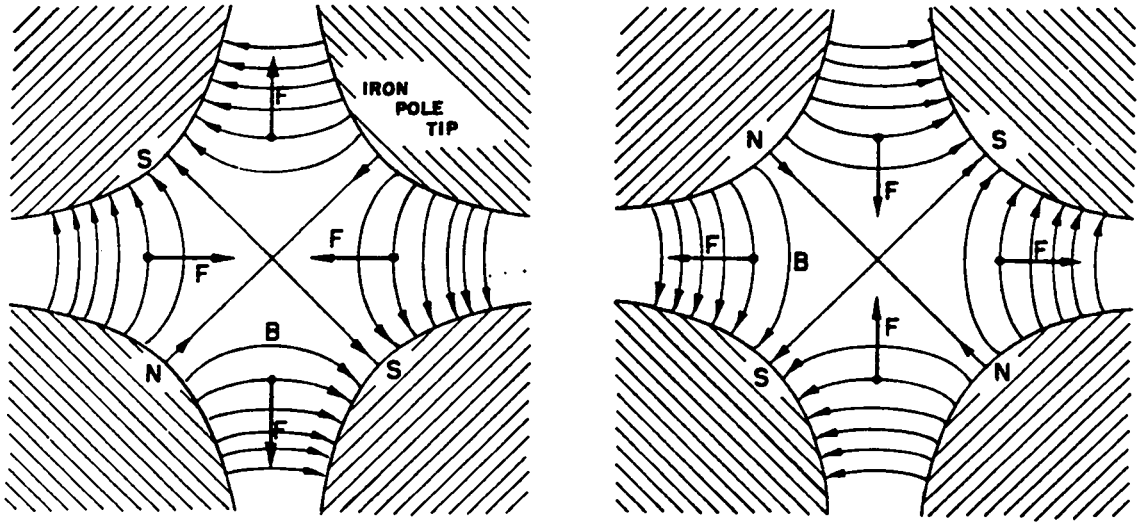

Fig.1.13. Magnetic fields in horizontal and vertical focusing quadrupole lenses.

1.13 Hill's Equation[8,9]

Beams in linear accelerators are usually focused by discrete elements that provide restoring forces, which are linear functions of the displacement from the equilibrium trajectory. The particle trajectories are then solutions of Hill's equation, which has the form

$$x'' + K(s)x = 0 \ ,$$

where s is the axial direction, x is the displacement and $x'' = d^2x/ds^2$. The divergence angle is $x' = dx/ds$. In linear accelerators the quantity K(s) is usually nearly periodic.

1.13.1 Transfer Matrix Solution of Hill's Equation

Because Hill's equation is a linear second-order differential equation, its solution can be written in matrix form. We can write

$$\begin{bmatrix} x \\ x' \end{bmatrix} = \begin{bmatrix} a & b \\ c & d \end{bmatrix} \begin{bmatrix} x_0 \\ x_0' \end{bmatrix}$$

where x_0 and x_0' are the initial displacement and divergence and x and x' are the final values. The 2×2 matrix is called a transfer matrix, and, because Hill's equation does not contain any first-derivative term, its determinant can be shown to equal unity. In

linear accelerators we will be interested in field-free drift spaces with K = 0, and in quadrupole magnets that give (transverse) focusing when K > 0 and defocusing when K < 0. Denoting the transfer matrix by R, the following results can be derived.

Drift space (K = 0) :

$$R = \begin{bmatrix} 1 & \ell \\ 0 & 1 \end{bmatrix}, \quad \text{where } \ell \text{ is the drift length.}$$

Focusing quadrupole (K > 0):

$$R = \begin{bmatrix} \cos\sqrt{K}\ell & \dfrac{\sin\sqrt{K}\ell}{\sqrt{K}} \\ -\sqrt{K}\sin\sqrt{K}\ell & \cos\sqrt{K}\ell \end{bmatrix}.$$

where ℓ is the length, and $K = \dfrac{qG}{mc\beta\gamma}$, with G as the quadrupole gradient.

Defocusing quadrupole (K < 0):

$$R = \begin{bmatrix} \cosh\sqrt{|K|}\ell & \dfrac{\sinh\sqrt{|K|}\ell}{\sqrt{|K|}} \\ \sqrt{|K|}\sin\sqrt{|K|}\ell & \cosh\sqrt{|K|}\ell \end{bmatrix}.$$

Thin lens:

$$R = \begin{bmatrix} 1 & 0 \\ \pm\dfrac{1}{f} & 1 \end{bmatrix} \quad \text{where f is the focal length.}$$

When the sign is negative this is a focusing lens, and when positive it is defocusing. The quadrupole lens approximates the thin-lens form when $\sqrt{|K|}\ell \to 0$, while $|K|\ell$ remains finite. Then for a thin-lens quadrupole,

$$\frac{1}{f} = |K|\ell = \frac{qG\ell}{mc\beta\gamma}.$$

1.13.2 Matrix Solution Through Piecewise Constant Elements

The total transfer matrix through a sequence of piecewise constant elements is obtained by taking the product of the individual R matrices, taken in the correct order. If the beam is transported through the elements 1, 2, 3, ..., n, the R matrix is R = R_n, ..., R_3, R_2, R_1.

1.13.3 Phase-Amplitude Form of Solution to Hill's Equation

When K > 0, Hill's equation is that of a harmonic oscillator. When K = K(s) we are interested in a solution to Hill's equation that has a form similar to that of a harmonic oscillator. This solution is sometimes called the phase-amplitude form of the solution and is written

$$x(s) = \sqrt{\varepsilon_1 \beta(s)} \cos(\phi(s) + \phi_1),$$

where $\beta(s)$ and $\phi(s)$ are called the amplitude and phase functions, and ε_1 and ϕ_1 are constants determined by the initial conditions. The functions $\beta(s)$ and $\phi(s)$ are related by

$$\phi(s) = \int \frac{ds}{\beta(s)} .$$

We now assume that K(s) is a periodic function of s. Then two other functions of $\beta(s)$ are defined as

$$\alpha(s) = -\frac{1}{2}\frac{d\beta(s)}{ds}, \quad \text{and} \quad \gamma(s) = \frac{1+\alpha(s)^2}{\beta(s)} .$$

The quantities $\alpha(s)$, $\beta(s)$, and $\gamma(s)$ are sometimes called Twiss parameters and sometimes Courant-Snyder parameters. These can be shown to be periodic functions with the same period as K(s). The coordinates x and x' satisfy the equation

$$\gamma(s)x^2 + 2\alpha(s)xx' + \beta(s)x'^2 = \varepsilon_1 .$$

This is the general equation of an ellipse centered at the origin of x-x' phase space, whose area is $A = \varepsilon_1/\pi$. When α is nonzero, the ellipse is tilted. Because α, β, and γ depend on s, the ellipse varies with s. But, because these parameters are periodic in s, if the coordinates lie on a particular ellipse at location s then, the coordinates at a location one full period away lie on the same ellipse. Also, it can be shown that the area of the ellipse is invariant with respect to s.

If a new set of initial conditions is chosen, ε_1 and ϕ_1 will be different. At a given location s, the new coordinates lie on a concentric, similar ellipse with the same α, β, and γ as for the first trajectory. Because ε_1 is different, the area of the new ellipse will be different, and because ϕ_1 is different, the phase or position of the new coordinates on the new ellipse will be different. The general ellipse is shown in Figure 1.14. The values of ε_1, α, β, and γ determine the projections and the intercepts on the x and x' axes.

A particle beam at any location in a focusing channel consists of a large sample of particle coordinates each on its own ellipse, each enclosing its own area, and each with its own initial phase. Each ellipse changes periodically as a function of s, and each ellipse area remains constant. At each s all the ellipses are concentric and self-similar. When K > 0, the solution reduces to that of a harmonic oscillator. Then the β function

is constant and equal to $\beta = \lambda/2\pi$, where λ is the wavelength of the oscillation. Also $\alpha = 0$, and the ellipse is always upright.

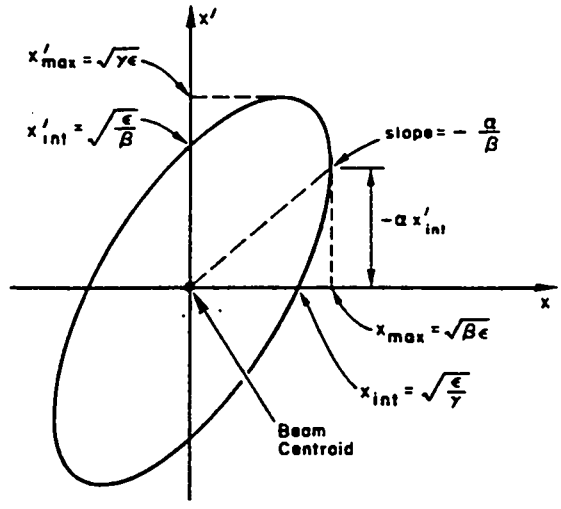

Fig. 1.14. The general ellipse and its parameters.

1.13.4 Transfer Matrix Through One Period

The general solution to Hill's equation is

$$x(s) = \sqrt{\varepsilon_1 \beta(s)}\cos(\phi(s) + \phi_1)\,,$$

$$x'(s) = -\sqrt{\varepsilon_1 / \beta(s)}\left[\alpha(s)\cos(\phi(s) + \phi_1) + \sin(\phi(s) + \phi_1)\right]\,.$$

Using this solution one can derive the transfer matrix between any two locations A and B as

$$R(A \to B) = \begin{bmatrix} \sqrt{\frac{\beta_B}{\beta_A}}(\cos\Delta\phi + \alpha_A \sin\Delta\phi) & \sqrt{\beta_A\beta_B}\sin\Delta\phi \\ \frac{-(1+\alpha_A\alpha_B)\sin\Delta\phi + (\alpha_B - \alpha_A)\cos\Delta\phi}{\sqrt{\beta_A\beta_B}} & \sqrt{\frac{\beta_A}{\beta_B}}(\cos\Delta\phi - \alpha_B \sin\Delta\phi \end{bmatrix},$$

where $\Delta\phi = \phi_B - \phi_A$. When locations A and B are corresponding points in the periodic lattice that are one period apart, $\alpha_A = \alpha_B$ and $\beta_A = \beta_B$. The transfer matrix through one full period M is then

$$P \equiv R(s \to s + P) = \begin{bmatrix} \cos\sigma + \alpha\sin\sigma & \beta\sin\sigma \\ -\gamma\sin\sigma & \cos\sigma - \alpha\sin\sigma \end{bmatrix},$$

where $\beta = \beta_A = \beta_B$, $\alpha = \alpha_A = \alpha_B$, $\gamma = \gamma_A = \gamma_B$, and $\sigma = \Delta\phi$ is the phase advance per period of every particle, each on its own trajectory ellipse. If the focusing is too strong the solution is unstable. The requirement for stability is

$$|\mathrm{Tr}\ P| < 2,$$

where Tr P is the trace of the P matrix. Generally one finds that this restricts the phase advance σ to satisfy $0 < \sigma < \pi$.

The phase advance per period σ is related to the β function by

$$\sigma = \int^P \frac{ds}{\beta(s)}.$$

This relationship unambiguously determines σ. It is also useful for getting an estimate of the average β value over the period. If β is assumed to be constant, equal to its average value, then $\langle\beta\rangle = P/\sigma$, where P is the period. Typically, if σ is equal to about 1 radian, then $\langle\beta\rangle = P$.

The above result for the P matrix is useful because it provides a simple method for obtaining the α (s), β (s), γ (s) functions, and the phase advance per period σ. By transporting two orthogonal trajectories, beginning at location s, over one full period, either by numerical integration through the specified fields or by matrix multiplication for piecewise constant elements, the transfer matrix elements can be calculated. These can then be compared with the elements of the P matrix to obtain the values of $\alpha(s)$, $\beta(s)$, $\gamma(s)$ and σ.

1.14 Thin Lens FODO Periodic Lattice

The FODO lattice structure is the most common focusing structure used in accelerators. Each period contains a single F (focusing) lens and a single D (defocusing lens) of equal strength, separated by equal drift distances of length L (Fig. 1.15). The resulting period is P = 2L. For simplicity we assume thin lenses. We summarize the results beginning at four different locations s in the period.

Case 1 Beginning at center of focusing lens:

$$P = \begin{bmatrix} 1 & 0 \\ -(2f)^{-1} & 1 \end{bmatrix} \begin{bmatrix} 1 & L \\ 0 & 1 \end{bmatrix} \begin{bmatrix} 1 & 0 \\ f^{-1} & 1 \end{bmatrix} \begin{bmatrix} 1 & L \\ 0 & 1 \end{bmatrix} \begin{bmatrix} 1 & 0 \\ (2f)^{-1} & 1 \end{bmatrix}.$$

After multiplying the matrices above and equating the result to the transfer matrix P through one period, one obtains

$$\cos\sigma = 1 - \frac{L^2}{2f^2}, \qquad \sin\frac{\sigma}{2} = \frac{L}{2f}. \qquad \beta = 2L\frac{1+\sin\sigma/2}{\sin\sigma} \qquad \alpha = 0.$$

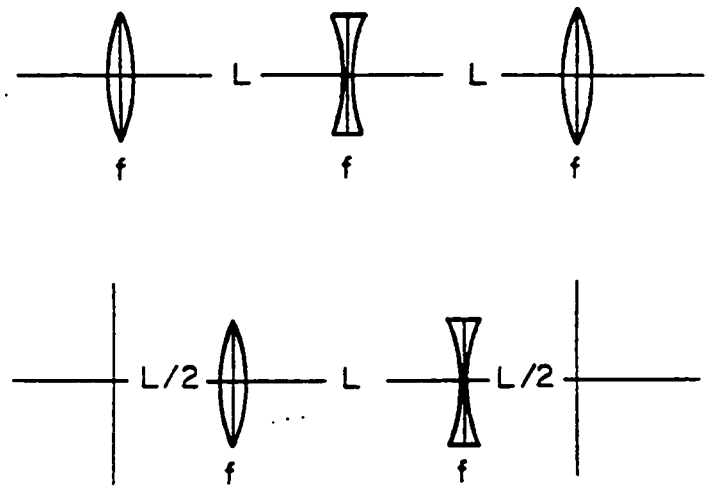

Fig. 1.15. The thin lens FODO lattice.

Case 2 Beginning at center of defocusing lens:

$$P=\begin{bmatrix}1 & 0\\ (2f)^{-1} & 1\end{bmatrix}\begin{bmatrix}1 & L\\ 0 & 1\end{bmatrix}\begin{bmatrix}1 & 0\\ -f^{-1} & 1\end{bmatrix}\begin{bmatrix}1 & L\\ 0 & 1\end{bmatrix}\begin{bmatrix}1 & 0\\ (2f)^{-1} & 1\end{bmatrix}$$

$$\cos\sigma=1-\frac{L^2}{2f^2},\qquad \sin\frac{\sigma}{2}=\frac{L}{2f},\qquad \beta=2L\frac{1-\sin\sigma/2}{\sin\sigma}\qquad \alpha=0.$$

Case 3 Beginning at center of drift after focusing lens:

$$P=\begin{bmatrix}1 & \frac{L}{2}\\ 0 & 1\end{bmatrix}\begin{bmatrix}1 & 0\\ f^{-1} & 1\end{bmatrix}\begin{bmatrix}1 & L\\ 0 & 1\end{bmatrix}\begin{bmatrix}1 & 0\\ -f^{-1} & 1\end{bmatrix}\begin{bmatrix}1 & \frac{L}{2}\\ 0 & 1\end{bmatrix}.$$

$$\cos\sigma=1-\frac{L^2}{2f^2},\qquad \sin\frac{\sigma}{2}=\frac{L}{2f},$$

$$\beta=\frac{L}{\sin\sigma}\left[2-\sin^2(\sigma/2)\right],\qquad \alpha=-\frac{2\sin(\sigma/2)}{\sin\sigma}.$$

Case 4 Beginning at center of drift after defocusing lens:

$$P=\begin{bmatrix}1 & \frac{L}{2}\\ 0 & 1\end{bmatrix}\begin{bmatrix}1 & 0\\ -f^{-1} & 1\end{bmatrix}\begin{bmatrix}1 & L\\ 0 & 1\end{bmatrix}\begin{bmatrix}1 & 0\\ f^{-1} & 1\end{bmatrix}\begin{bmatrix}1 & \frac{L}{2}\\ 0 & 1\end{bmatrix}.$$

$$\cos\sigma = 1 - \frac{L^2}{2f^2}, \qquad \sin\frac{\sigma}{2} = \frac{L}{2f}, \qquad \beta = \frac{L}{\sin\sigma}[2 - \sin^2(\sigma/2)], \qquad \alpha = \frac{2\sin(\sigma/2)}{\sin\sigma}.$$

The beta function is maximum in the focusing lens and minimum in the defocusing lens. The ratio of the beta functions in the focusing and defocusing lenses is

$$\frac{\beta_{max}}{\beta_{min}} = \frac{1+\sin(\sigma/2)}{1-\sin(\sigma/2)}.$$

If the quadrupole lens is focusing in the x plane, it is defocusing in the y plane. Therefore this ratio is also the ratio of beta functions in the same lens in the two different planes.

By comparing cases 3 and 4, in the center of the drift space, we obtain the result $\beta_x = \beta_y$ and $\alpha_x = -\alpha_y$.

It is of interest to calculate several values of σ as a function of L/f:

This is shown in Table 1.4

Table 1.4

L/f	σ
2	π
$\sqrt{2}$	$\pi/2$
1	$\pi/3$

The solution is unstable for $\sigma \geq \pi$ which means that the focal length must satisfy $f \geq L/2$.

1.15 Problems

1-1. What is the kinetic energy in units of both Joules and electron volts for an electron accelerated through a dc potential of 1 megavolt?

1-2. Find an expression for the fractional error when the nonrelativistic approximation for kinetic energy as a function of β is used. (a) At what values of β and γ does the error in kinetic energy equal 1%? (b) To what kinetic energy does this correspond, for electrons and for protons?

1-3. If the only nonzero components of the electromagnetic field in cylindrical coordinates are E_r, E_z, and B_θ, write the nonzero components of the Lorentz force for a particle of mass m and charge q moving along the z direction with velocity v.

1-4. The rate of work done by a force F acting on a particle with velocity v is $\vec{F}\cdot\vec{v}$. Using the definition of the Lorentz force and the appropriate vector relationship, derive the expression for the rate of kinetic energy gain for a particle of charge q, and show that the magnetic force does not contribute.

1-5. A commercial cylindrical waveguide has a diameter of 1.5 inches (3.81cm). (a) Identify the two modes with the lowest cutoff frequencies. (b) For both modes write the expressions for the six components of the electromagnetic field. (c) For both modes plot the dispersion relation, i.e. frequency ($\omega/2\pi$) versus wave number ($k_z = 2\pi / \lambda_{guide}$) both on the same graph.

1-6. A cylindrical resonator has a diameter of 1.5 inches (3.81 cm) and length ℓ of 1 inch (2.54 cm). (a) Calculate the resonant frequency of the TM_{010}, TM_{110}, TE_{011}, TE_{111}, and TE_{211} modes, and list in order of increasing frequency. (b) For the two lowest-frequency modes plot the dispersion relation, f (= $\omega/2\pi$) versus k_z(= $p\pi/\ell$), both on the same graph. For simplicity, label the abscissa with the longitudinal mode index p (that is, units of π/ℓ for p = 0 to p = 5. (Recall that the TE modes have no resonance at p = 0.)

1-7. Repeat the exercise of problem 6 for the same diameter resonator but with different lengths. (a) ℓ = 7.725 cm. Note the frequency of the TE_{112} mode compared to the TM_{010} mode. How did it change relative to the result of problem 6? (b) ℓ = 25.4 cm. Note that all of the first five TE_{11p} modes now lie below the TM_{010} frequency.

1-8. Calculate the rf surface resistance and skin depth of room temperature copper at 400 MHz. Use a dc resistivity $\sigma^{-1} = 1.7\times10^{-8}$ Ω-m.

1-9. Calculate the rf surface resistance of superconducting niobium at 400 MHz. Assume a residual resistance $R_{residual} = 20\times10^{-9}$ W. What is the ratio of the rf surface resistance of superconducting niobium to that of room temperature copper? (a) Assume T = 4.2 K, (b) assume T = 2.0 K.

1-10. Design a room temperature cylindrical cavity that operates in the TM_{010} mode at 400 MHz with an axial electric field E_0 = 1 MV/m, and a length $\ell = \lambda/2$, where λ is the rf wavelength in free space. (a) Calculate the length and diameter of the cavity. (b) Calculate the maximum B and H fields on the cavity wall. Where does this occur? (c) Calculate the B and H fields on the cylindrical wall. (d) Calculate the electromagnetic stored energy in the cavity. (e) Use the value of R_s from problem 8 for a room temperature copper surface to calculate the power loss P, the quality factor Q_0, and the decay time τ. (f) Repeat part (e) using R_s from problem 9 for a 4.2 K niobium surface.

1-11. Design a half-wave coaxial cavity to be used as a 100-kW resonant load at 400 MHz. To absorb the rf power, use a 20-cm-diameter stainless steel pipe as the center conductor inside a 60-cm-diameter copper cylinder with copper end walls. This type of cavity is easily cooled by flowing water through the center conductor. (a) Ignoring any effects of the coupling loop and probe, calculate the length of the cavity. (b) Assume that the room temperature surface resistance of stainless steel is 6.5 times that of copper. (From problem 8 the copper surface resistance at 400 MHz is 0.0052 Ω.) Calculate the power dissipated on the center conductor, end walls, and outer wall. (c) Calculate the cavity stored energy and the unloaded Q. (d) What is the peak power density in watts/cm^2 on the inner and outer conductors?

1-12. A quadrupole magnet of effective length $\ell = 3.25$ cm is operated at a gradient of 100 T/m, and is used for focusing a 5-MeV proton beam. Calculate the focusing strength K and the thin-lens focal length.

1-13. A 5-Mev proton is incident on the quadrupole magnet of problem 12. The initial coordinates of the proton at the entrance plane of the quadrupole are $x = 3$ mm, $x' = 0$, $y = 0$, and $y' = 0$. Calculate the final divergence angle x' at the exit plane of the quadrupole, using the following assumptions: (a) The quadrupole has constant field over the effective length and is focusing in the x plane. (b) The quadrupole has constant field over the effective length and is defocusing in the x plane. (c) The quadrupole obeys the thin-lens approximation and is focusing in the x plane.

1-14. Consider a FODO lattice composed of the same beam and quadrupoles as in problems 12 and 13. Assume the thin lens approximation is valid, and assume the center-to-center spacing of the quadrupoles is 10 cm. (a) Calculate the phase advance per focusing period s of the beam particles. (b) Calculate the Twiss parameters α, β, and γ of the trajectory ellipses in the middle of a focusing lens. (c) Repeat the Twiss parameter calculation in the middle of a defocusing lens. (d) Repeat the Twiss parameter calculation in the middle of the two drift spaces.

1-15. Assume the emittance in the x plane of the ellipse on which the largest amplitude particle lies is $\varepsilon_1 = 30$ mm-mr (3×10^{-5} m-radians). (a) Use the results of Section 1.13 (see Fig. 14), and the values of the Twiss parameters calculated in problem 14 to tabulate the projections $\sqrt{\varepsilon_1\beta}$ and $\sqrt{\varepsilon_1\gamma}$ and the intercepts $\sqrt{\varepsilon_1 / \beta}$ and $\sqrt{\varepsilon_1 / \gamma}$ at each of the four locations in problem 14, beginning at the middle of the focusing lens. How large must the aperture be in the quadrupoles so that the largest-amplitude particle is transported? (b) Use the projections and intercepts calculated in part (a) to make a rough sketch of the ellipse at each of the four locations (middle of the lenses and of the drift spaces), beginning with the middle of the thin focusing quadrupole, with the same scales for all plots.

1-16. Suppose the particle with the maximum amplitude of problem 15 has coordinates $x = \sqrt{\varepsilon_1\beta} = 3.22$ mm and $x' = 0$ at the middle of a thin focusing lens. (a) Use the transfer matrix through a period to calculate the particle coordinates x and x' at the middle of the next thin focusing lens. (b) Plot these two points on the ellipse at the thin focusing lens sketched for problem 15. The phase advance from one focusing lens to the following one was calculated for problem 14. Do the plotted coordinates look qualitatively consistent with this?

2 INTRODUCTION AND GENERAL PRINCIPLES

2.1 Inherent Advantages of Linear Accelerators

A linear accelerator (linac) produces energetic particles by acceleration in a straight line. It is also common usage to restrict the definition to devices configured as an array of low-voltage cells. Some further restrict the definition to include only accelerating structures that support time-varying electric fields. By this definition dc accelerators are excluded; these also have a linear geometry, but are usually considered as a separate category of accelerator. The electric fields for acceleration in linear accelerators have been produced by two methods: (a) the *rf linac* cells are sections of waveguide or resonant cavities that contain sinusoidally varying electromagnetic fields, usually in the UHF and microwave frequency ranges; (b) the *induction linac* cells use a pulsed current that passes through a magnetic toroid to produce a rapidly changing magnetic flux, which, by Faraday's law, induces a voltage across an accelerating gap. We will emphasize the rf linacs. However, some of the beam dynamics treatments also apply to induction linacs.

The main advantage of the linear accelerator is its capability for producing high-energy, high-intensity charged particle beams of excellent quality (small diameter and low energy spread). The main reasons for these attractive characteristics include the following. (a) Acceleration to high energies is not limited by electrical breakdown as in dc accelerators. Electric breakdown limits the maximum energy for singly charged ions in dc accelerators to several tens of MeV. (b) Strong focusing can easily be provided for containment of high intensity beams. (c) The beam traverses the structure in a single pass, and therefore repetitive exposure to error conditions causing destructive beam resonances, as in a circular machine, does not occur. This raises the current limit for acceleration of high intensity beams. (d) Because the beam travels in a straight line, there is no power loss from synchrotron radiation, which usually is a problem for high energy electron beams in circular accelerators. (e) Injection and extraction are simpler than in circular accelerators. The natural orbit of the linac is open at each end and therefore, although the beam must generally be bunched before injection, special techniques for these beam transfers are unnecessary. (f) The linac can operate at any duty factor all the way to 100% duty or CW (continuous-wave).

2.2 Applications

Here we include both existing and proposed applications. For electron linacs the present applications of most interest include: (a) Elementary particle-physics applications including electron-positron colliders (advantages are the avoidance of synchrotron radiation losses that are suffered by relativistic electrons in circular accelerators, and high beam quality); (b) high quality electron beams for free-electron lasers; (c) pulsed neutron sources for nuclear physics and material sciences; and (d) x-ray sources for radiotherapy.

For proton sources the main applications include (a) injectors to high energy synchrotrons for elementary particle physics; (b) meson production for nuclear physics; (c) CW spallation neutron sources for materials studies, breeding of nuclear fuel, transmutation of nuclear wastes, or new fission reactor concepts; (d) CW neutron sources for materials studies related to fusion reactors; and (e) medical applications such as boron neutron-capture therapy.

There are also linacs for heavy ions, whose applications include (a) linacs for nuclear physics research; (b) ion implantation for semiconductor technology; and (c) 10-GeV linacs for heavy-ion-driven inertial-confinement fusion.

2.3 Overview of Linear Accelerator Technology and Operating Principles

The accelerator structure is driven by an rf generator, which injects high frequency electromagnetic energy through a transmission line or waveguide. Because the accelerator uses a sinusoidally varying electric field for acceleration, particles can either gain or lose energy depending on their phase relative to the crest of the wave. Therefore the accelerator must provide an electric field with the correct phase relationship relative to the beam to maintain acceleration along its length. Also, to provide acceleration for all the particles, the beam is grouped into bunches as shown in Fig. 2.1, that are nominally separated longitudinally by one period of the electromagnetic field oscillations (rf period).

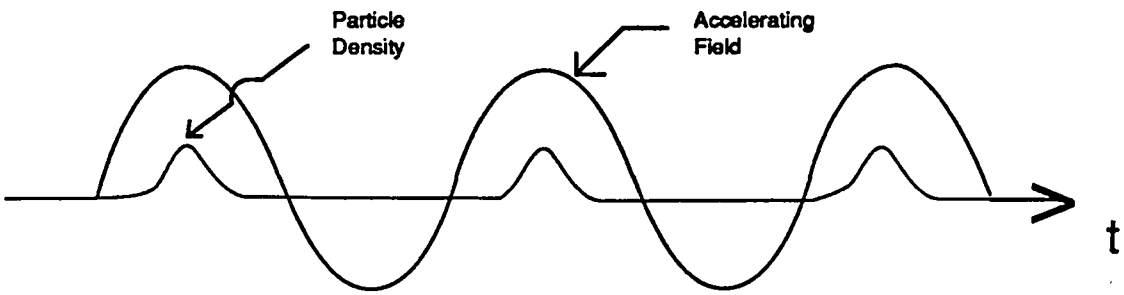

Fig. 2.1. Beam bunches in an rf linac.

Two approaches have been used.

(a) *Traveling-wave structures*, where the accelerator functions as a waveguide in which the injected electromagnetic wave travels with a phase velocity equal to the beam velocity along the entire length. The beam particles gain energy continuously from the longitudinal electric component of the wave, depending on their phase relative to the crest. The wave propagates with attenuation because of the ohmic losses in the structure walls, and beam loading if the current is high, and after a certain distance the remaining power is absorbed in a load, whose impedance is matched to the characteristic impedance of the guide.

(b) *Standing-wave structures*, which are resonant cavities that contain one or more accelerating cells. If the frequency of the injected wave matches the resonant frequency of the cavity, a characteristic standing-wave pattern is built up, as a result of reflections of the injected wave from the ends of the cavity. The correct phase relationship of the field relative to the beam is determined either by phasing of the rf sources that drive the different cavities, or by using multicell cavities where definite phase relationships exist between adjacent cells. Again, the longitudinal electric field component provides the accelerating force. The standing-wave pattern described above also may be pictured as a linear combination of two equal-amplitude traveling waves going in opposite directions. In this view the forward wave is synchronous with the beam and causes acceleration.

In most (but as we will see not all) cases the backward wave is not synchronous and produces no net average force on the particles.

In both the traveling- and standing-wave cases the beam and the electromagnetic waves are in synchronism, and this device is called a synchronous accelerator. We will say more later about these two approaches.

2.4 Longitudinal Focusing

The replacement of a standing wave with an equivalent traveling wave provides a unifying principle that allows discussion of both structure types in the language of traveling-wave accelerating structures. Accelerators for particles whose velocities are significantly less than the velocity of light are generally designed to produce a given velocity gain per cell. Particles with the correct initial velocity will continue to gain the right amount of energy to match the speed of the wave. For a field amplitude above a certain threshold, there will be two phases for which the velocity gain is equal to the design value, one earlier and the other later than the crest, as shown in Fig. 2.2.

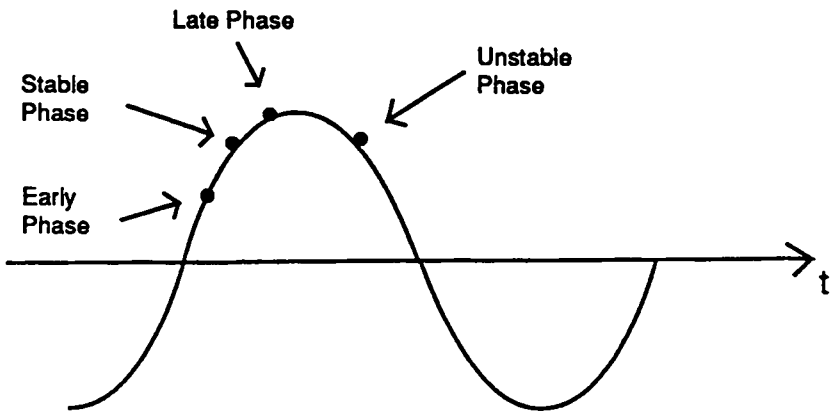

Fig. 2.2. Stable and unstable phases.

The earlier phase is called the synchronous phase and is the stable point. It is the stable point because nearby particles that arrive earlier than the synchronous phase experience a smaller accelerating field, and particles that arrive later will experience a larger field. This provides a longitudinal restoring force that keeps the nearby particles oscillating about the stable phase, and provides phase focusing or phase stability. The particle with the correct initial velocity at the stable phase is called the synchronous particle, and it maintains exact synchronism with the traveling wave. More detailed analysis shows that there is a range for stability, within which the particles oscillate about the synchronous phase, at a frequency that is slow compared to the rf frequency. The bunch is composed of the stable particles, which on the average maintain synchronism with the wave and gain energy at the design rate. The stable region is called the "bucket" in common accelerator terminology. As the particles approach relativistic velocities, the velocity approaches the speed of light independent of energy, and the phase oscillations slow down. All particles regardless of their energy begin to maintain a nearly constant phase relative to the traveling wave.

2.5 Transverse Focusing

Longitudinal focusing for particles injected near the synchronous phase on the leading edge of the wave is essential for beams of high intensity. However, rf transverse fields also act on these particles as shown in Fig. 2.3, and it can be proven from general principles that the particles experience transverse defocusing forces. Earnshaw's theorem states that in the frame of reference moving with the beam, the force component in at least one of the three dimensions is defocusing. Since the particles experience a restoring force in the longitudinal direction, they must experience defocusing forces in the transverse direction. Furthermore, the injected beam always has a finite transverse velocity spread, and the beam particles exert repulsive Coulomb or space-charges forces on each other. To obtain even moderate beam currents, some provision for transverse focusing must be provided. The most successful solutions to the focusing problem have been (a) to include separate magnetic quadrupole or solenoid focusing lenses, and (b) to invent accelerating structures that provide quadrupole focusing from the rf transverse electric fields. The rf electric focusing is superior at low velocities to the magnetic focusing, because the magnetic force is proportional to the particle velocity.

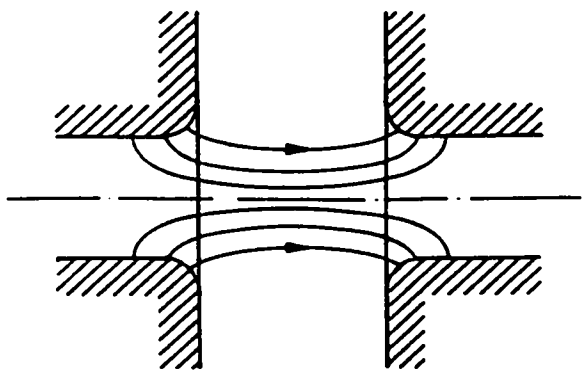

Fig. 2.3. Electric field lines in an accelerating gap.

2.6 Power Efficiency and Electric Breakdown

Because the linac is generally used as a single-pass device, the accelerator- structure length and ohmic power consumption in the cavity walls become disadvantages, especially when used for acceleration of particles to high energies. To shorten the accelerator for a given energy gain, it is necessary to raise the longitudinal electric field. This implies that the accelerating structures must be designed to avoid high surface fields that are limited by electric breakdown. Furthermore, the total power dissipation in the accelerator for a given energy gain increases in inverse proportion to the length. This means that the accelerating structures must be designed for high power efficiency. For high-duty-factor operation the average power density from losses on the cavity walls can produce challenging cooling requirements for the conventional copper-cavity technology. An approach that has become increasingly successful in recent years is the use of superconducting niobium cavities, which we discuss later.

2.7 Accelerating Structures

We return to the question of how to design an accelerating structure to provide the required synchronous acceleration with good power efficiency. There have been several solutions. First, an array of short independent cavities excited in a TM_{010} mode (see Fig. 2.4) can be used, each driven by its own generator and each phased to provide continuous acceleration along the entire length. This solution is commonly used for superconducting heavy-ion linacs, where its main advantages include (a) flexibility to vary the synchronous velocity profile for a wide range of ions of different charge and mass, by changing the phasing of the cavities, and (b) flexibility to optimize the amplitude settings of the cavities, depending on their performance levels.

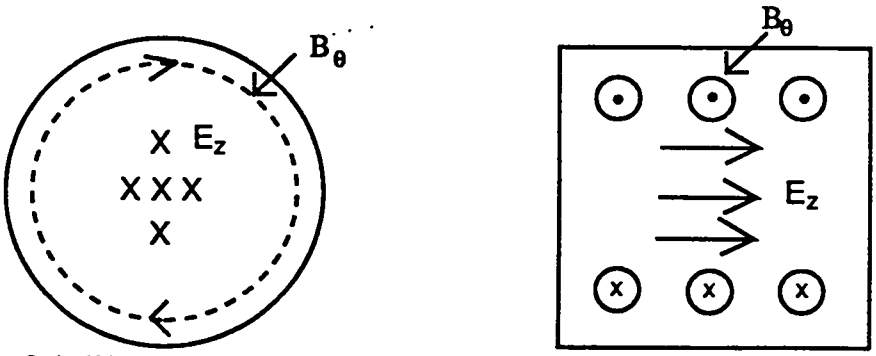

Fig. 2.4. Electric and magnetic fields in a cylindrical-cavity TM_{010} mode.

A significant disadvantage of the independent cavity approach is the operational complexity of setting the phases and amplitudes of each cavity, especially for a long accelerator. Attractive alternative solutions are to use a waveguide accelerating structure, supporting a TM_{01} traveling wave, or to use an electromagnetic standing-wave multicell cavity consisting of coupled cells in excited TM_{010} resonant modes (the phase relationships between adjacent cells is fixed within the cavity). Both have been used.

The traveling-wave structure has been used for the 50-GeV electron linac at SLAC. The most straightforward method would be to inject a TM_{01} electromagnetic wave into a cylindrical waveguide. However, this approach cannot provide continuous acceleration because the phase velocity always exceeds the velocity of light. A more complicated structure is required to lower the phase velocity. At SLAC, to accelerate electrons to high energies, the structure consists of a cylindrical guide with a periodic array of conducting disks with axial holes (Fig. 2.5). The net propagation of the wave down the structure depends on the constructive interference of the incident wave and the reflected waves from the disks. The electrical characteristics of this disk-loaded waveguide structure will be described in more detail later.

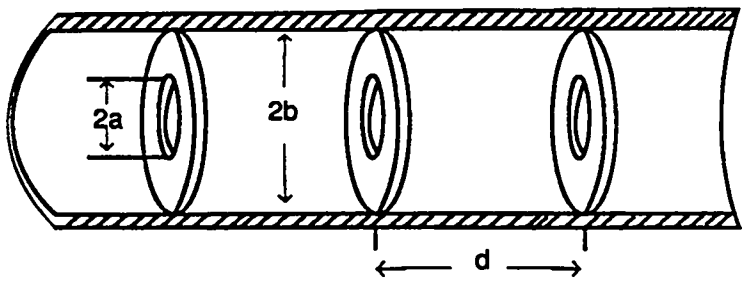

Fig. 2.5. Iris-loaded traveling-wave structure.

The other method, which has been widely used for both electron and ion applications, is to excite a standing wave in a multicell or coupled cavity array, which is driven by a single rf generator. This method has the advantage that it avoids power dissipation in the load, and therefore under most conditions (the exceptions will be discussed later) gives higher efficiency. The disk-loaded structure can be operated in this manner, but the optimization for maximum efficiency would result in choices of the geometry different from those used for traveling-wave operation. The electrical characteristics of the structure are described in terms of the mode spectrum of the coupled TM_{010} resonant cells (Fig. 2.6). For n cells there are n structure modes, each characterized by the distribution of amplitudes and phases from cell to cell along the structure. The frequency spectrum of these modes is centered about the frequency of the TM_{010} mode, unperturbed by the coupling. The frequency width of this group of modes increases in proportion to the strength of the coupling. The lowest frequency corresponds to the mode where all cells have the same amplitude and phase. The modes are identified by the phase advance from cell to cell; this lowest mode is called the 0 mode. For the highest frequency mode all cells have the same amplitude, but adjacent cells are π out of phase. In the middle of the frequency range is the $\pi/2$ mode (Fig. 2.7), in which the excitation of a sequence of four cells at a given time is as follows: cell 1, excited cell; cell 2, zero amplitude (unexcited) cell; cell 3, excited cell π out of phase with respect to the first cell; and cell 4, zero amplitude (unexcited) cell.

The efficiency of standing-wave structures in the 0 mode or π mode is maximum, a result that can be related to the the fact that for these modes both the forward and backward traveling waves with the same phase velocity as the beam contribute to the acceleration, instead of only the forward waves. But mode interference from nearby modes is greatest for 0 and π modes, which results in an extreme sensitivity of the field distribution to beam current and mechanical tolerances. The sensitivity increases with the number of cells. The solution to this problem, which has made standing-wave operation very attractive from most points of view, has been the development of resonant coupling. In this solution the structure is operated electrically in the $\pi/2$ mode, where the mode spacing is maximum, but the geometry is arranged so the unexcited cells take up no longitudinal space along the accelerator. Because the beam experiences the fields of the excited cells in a π-mode sequence, the efficiency remains high.

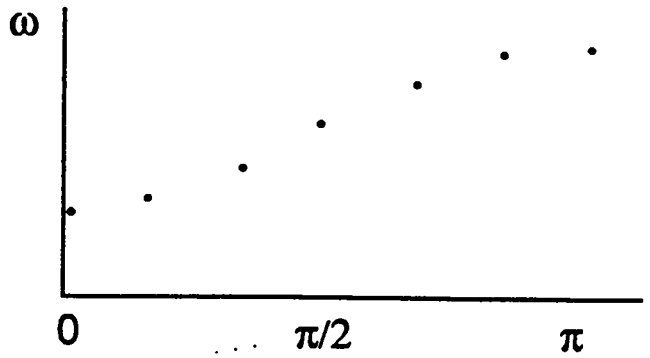

Fig. 2.6. Normal-mode spectrum of a chain of seven coupled oscillators plotted as frequency versus phase-advance per cell. The frequency width of the spectrum is related to the strength of the cell-to-cell coupling.

(a)

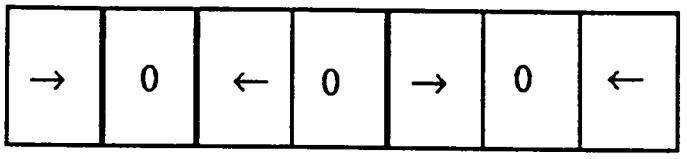

(b)

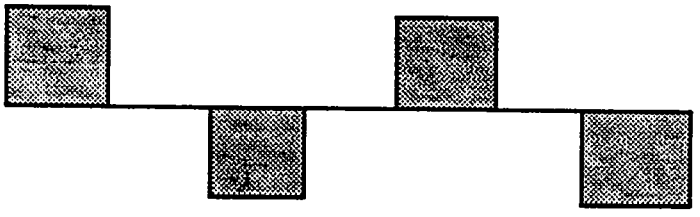

Fig. 2.7. Chain of seven coupled cavities in a π/2 mode. The longitudinal electric field direction in each cell is shown by (a) arrows and zeros, and (b) a histogram.

One example is the side-coupled linac where the unexcited cells are placed off axis, and the excited or accelerating cells are on axis and spaced by half an rf period (π mode). The side-coupled structure is used in LAMPF to accelerate the proton beam from 100 to 800 MeV. Another example is the on-axis coupled structure, where the coupling cells are squeezed along the axis, so the distance between the centers of adjacent excited (accelerating cells) is half an rf period (π mode). In all these cases, transverse focusing can be provided by quadrupole lenses between the tanks. At high energies the transverse focusing requirements are usually relaxed, and this arrangement usually is adequate. The coupled-cavity linac structures are used for electrons and protons in the velocity range above about 0.4 of the speed of light. This corresponds to kinetic energies near 50 keV for electrons (the typical injection energy from an electron gun), and near 100 MeV for protons.

The internal geometry of the cells is usually modified from the cylindrical or pillbox shape by introducing nose cones onto the end walls around the beam axis. The noses produce a capacitive effect, concentrating the electric field at the midplane of the cell and along the axis. This concentration near the midplane increases the acceleration rate for a given power dissipated and therefore improves the efficiency. A parameter called the transit-time factor is commonly used as a measure of the effectiveness of the field in producing acceleration. A disadvantage of nose cones is that the peak surface electric field is increased, which increases the probability of electrical breakdown. Another undesirable effect at high intensity can arise from increased excitation of high-order modes from the beam.

At high velocities the p-mode structure generally gives higher efficiency than the 0-mode structure operating at the same frequency. This is a due to the smaller gap and improved transit-time effect with two accelerating cells or gaps per rf period in the π mode, compared to the one longer cell per rf period in the 0 mode. But at lower velocities, as the cells become shorter, the number of end walls per unit length increases, and the total power dissipation on the end walls dominates. To improve the efficiency at low velocities, it becomes attractive to operate in the 0 mode. As we will see, it is even possible to remove the end walls without significantly perturbing the fields, which removes the contribution of power losses from the end walls of each cell. The nose cones become drift tubes, which are supported mechanically by cylindrical stems. This type of structure is the TM_{010} Alvarez drift-tube linac (Fig. 2.8), which is universally used to accelerate protons and other ions in the velocity range from about 0.04 to 0.4 of the speed of light.

The transverse focusing requirements, which are increasingly important at low velocities, are provided by magnetic quadrupole lenses mounted within the drift tubes. The internal space within the drift-tube structure is therefore very efficiently used, either for accelerating gaps or for focusing lenses. The drift-tube structure is not used for electrons in this velocity range because the electrons are so light that they are already beyond this velocity region at injection from the dc electron gun. This property results in a much simpler linac configuration for electrons than for protons and heavier ions, which need additional linac structures for the low-velocity region.

The newest accelerating structure for the very-low-velocity region is the radio-frequency quadrupole (RFQ), shown in Fig. 2.9. An electric quadrupole mode is excited in a cavity resonator loaded with four conducting rods or vanes, placed symmetrically about the beam axis. The RFQ electric field provides strong transverse electric focusing, which is an important requirement for low-velocity protons and

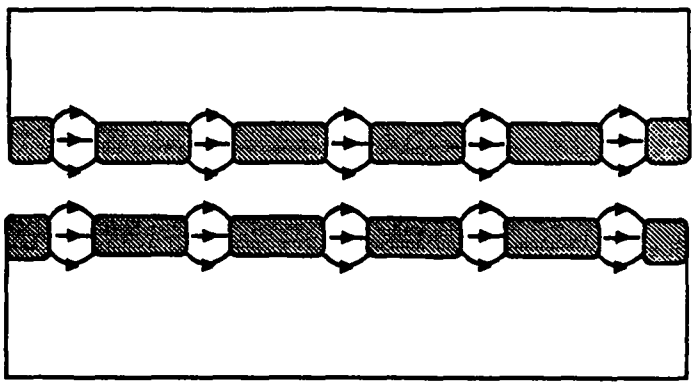

Fig. 2.8. Alvarez drift-tube linac structure.

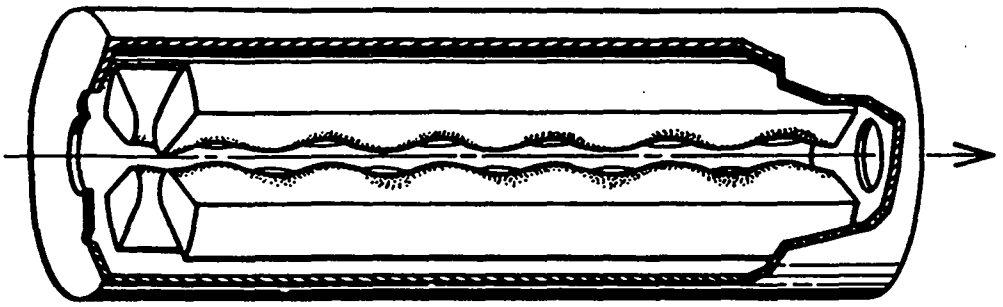

Fig. 2.9. The radiofrequency quadrupole (RFQ).

heavier ions. Both 4-rod and 4-vane structures have been used, and acceleration is obtained by introducing a longitudinal modulation pattern on these four elements to create an array of accelerating cells. The RFQ cell structure bunches, with high capture efficiency, a continuous or dc injected beam, and then accelerates the beam to high enough energies for injection into the low-velocity end of the drift-tube linac. The overall result is improvement of the focusing throughout the low-velocity region between about 0.01 and 0.07 or more of the speed of light.

2.8 Traveling Waves Versus Standing Waves

When the pulse length is long or the application calls for continuous or CW operation, the standing-wave structures can be designed for greater efficiency. The traveling-wave structure always wastes power in the load at the output end. For short pulse applications the traveling-wave structures may give greater efficiency than standing-wave structures for two reasons. (1) In a traveling-wave accelerator the steady state field distribution is established when the energy has propagated along the length of the structure in a single pass, a filling time of l/v_g, where v_g is the group velocity. In the standing-wave structure the field distribution is built up by successive reflections. Generally the filling time is less in the traveling-wave structure. If the beam is injected only after the structure has reached a steady state, the power dissipated in the cavity walls during the filling represents wasted energy. For long-pulse applications,

where the energy loss during the fill time is small compared to the total energy loss, this effect is inconsequential. But for short-pulse applications, where it represents a large fraction of the power loss per pulse, the traveling-wave structure is more efficient. (2) For pulses very much shorter than the natural time constant of the structure, most of the incident power from the generator is reflected. This reflected power is dissipated in a load external to the structure. This effect contributes further to the poor initial power efficiency of the standing-wave structure.

2.9 Duty Factor

The duty factor is the fraction of time during which the accelerator is in an active mode. One can speak of one duty factor for the rf energy, and another duty factor for the beam. Because of the finite time for the structure to fill with electromagnetic energy, the rf duty factor can never be smaller than the beam duty factor. In discussing this issue one must distinguish between micropulses and macropulses. As discussed earlier, the linac pulse train consists of a sequence of rf buckets separated by an rf period, each of which can contain a bunch of particles. These particle bunches are called micropulses. When the rf generator is pulsed, with a period long compared to the rf period, the generator pulses are called macropulses.

There is no fundamental reason why a linear accelerator cannot be continuously driven by the rf generator. This corresponds to 100% duty factor or a continuous mode (commonly termed continuous wave or CW). The choice to pulse the rf generator rather than operate it continuously depends on several issues. One important issue is rf efficiency. If the application requires a small average current, most of the power from the rf generator is not delivered to the beam but is lost in the structure walls in the CW operating mode. Instead, if the accelerator is operated in a pulsed mode and the current per rf bucket is increased in inverse proportion to the duty factor, then more fractional power is delivered to the beam. Another important advantage for pulsed operation is that the peak surface electric field attainable is generally larger for shorter pulses. If high accelerating fields are required, pulsed operation is preferred.

The main application of longer pulses or CW operation is for high average currents. The effects from space charge, wakefields, and other intensity-dependent phenomena are functions of the intensity in a micropulse. These effects can be reduced by spreading the total beam charge over more rf buckets, as is done in longer-pulse or CW operation.

2.10 Superconducting Linacs

A technical approach that has become increasingly successful in recent years is to use superconducting niobium cavities. This allows high-field operation at 100% duty factor, resulting in shorter linacs. Overall power dissipation is low, and cooling requirements are relaxed. The use of rf superconductivity provides many benefits for high-field CW operation, but also presents new issues to be addressed. The superconducting systems are more complex because of the need to use cryogenic techniques. Electric-field limitations arise from field-emission-induced electron loading, and magnetic-field limitations from the presence of normal-conducting impurities. High performance also requires great attention to cleanliness during fabrication and handling of the cavities.

2.11 Beam Intensity, Beam Losses, and Beam Quality

As the beam intensity increases some additional beam-dynamics effects begin to degrade the performance. Eventually these effects limit the beam current. The main intensity limitations result from (a) the repulsive space-charge forces, which are usually most important at low velocities, and (b) the excitation by the beam of high-order deflecting modes, which eventually cause a beam-breakup instability for relativistic beams. The space-charge force causes additional defocusing and, because it is generally nonlinear, it produces distortions in the particle distribution in phase space and creates a diffuse halo surrounding the main core of the beam. The halo contributes to beam loss that causes radioactivity in the accelerating structure, increasing the difficulty of maintaining of the facility and reducing its availability. For applications requiring high average beam current, control of the halo and beam losses becomes an important design requirement.

Many high-intensity applications also require high beam quality. For example, a small output focal spot or small output energy spread requires good beam quality. This restricts the maximum contribution of the nonlinear forces (from both the space charge and the external fields) and of fields from high-order modes (wakefields) induced by the beam.

Solutions for reducing these effects can significantly influence the design choices for accelerator parameters such as frequency, aperture, and focusing characteristics, and for cavity geometry. Also important is beam matching into the accelerating structures.

2.12 Summary

The discussion can be summarized by identifying the two main topics of importance for the study of linear accelerators.

(1) Accelerator Structures:

The accelerating-structure (waveguide or resonant cavity) geometry and mode must provide (a) a longitudinal electric-field for acceleration, (b) synchronism with the beam, (c) stable field distribution, and (d) good power efficiency.

(2) Beam Dynamics

The linac must provide sufficient longitudinal and transverse focusing for good transmission and good beam quality.

3 ACCELERATION

3.1 Electromagnetic Fields in a Cavity Resonator

3.1.1 Introduction

We consider a resonant cavity, which consists of a linear, periodic sequence of accelerating cells. We are interested in the properties of a TM_{010}-like standing-wave mode ($B_z = 0$) in which the fields have rotational symmetry about the beam axis. Two standing-wave modes are commonly used for linacs, as shown in Fig. 3.1. One is the 0 mode, in which the field has the same sign in all gaps and there is one accelerating gap per axial period L (field period = L). The other is the π mode (we include the $\pi/2$ mode, where, in accelerating structures, there is still a phase shift of π between sequential accelerating cells), where the field on axis reverses from one gap to the next. The π mode has two accelerating gaps per axial period L (field period = 2L).

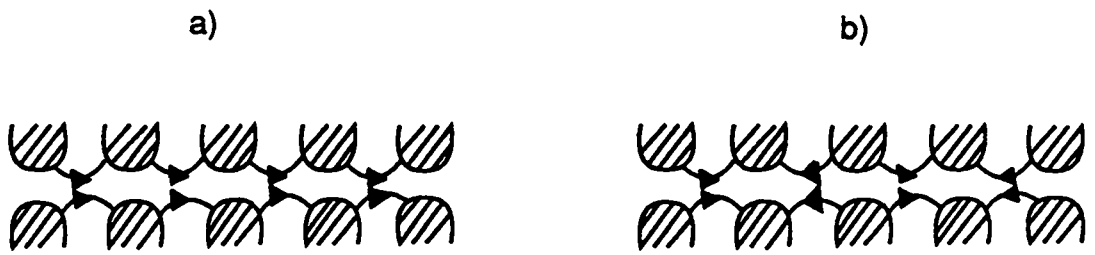

Fig. 3.1. Electric-field directions in accelerating gaps, (a) 0 mode and (b) π mode.

To treat both cases, we will assume the fields have a period 2L, as shown in Fig. 3.2. By restricting our treatment to the region near the beam axis, we are limiting the solutions to those that are finite at r = 0, but we will not impose any specific radial boundary conditions at the walls of the cavity. Furthermore we are neglecting fields from the beam charges and currents. The only nonzero components will be E_z, E_r, and B_θ.

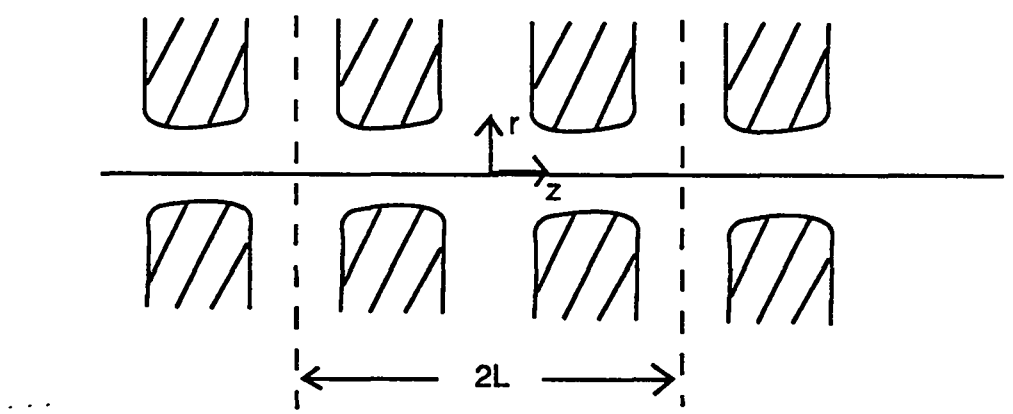

Fig. 3.2. Linear periodic sequence of accelerating cells.

3.1.2 Axial Electric Field

We express the electric-field component along the beam axis as

$$E_z(r,z,t) = E(r,z)\cos\omega t\,,$$

where $\quad E(r,z) = E(r,z+2L)\,.$

We can express E(r,z) as a Fourier series in z. We will take the origin of the coordinate system at the center of a cell and assume E is an even function about the origin. Then we can use only the cosine series to obtain

$$E(r,z) = \frac{a_0(r)}{2} + \sum_{m=1}^{\infty} a_m(r)\cos\frac{m\pi z}{L}\,,$$

and $\quad a_m(r) = \frac{1}{L}\int_{-L}^{L} E(r,z)\cos\frac{m\pi z}{L}dz\,.$

We substitute this solution for E_Z into the wave equation:

$$\frac{\partial^2 E_z}{\partial z^2} + \frac{1}{r}\frac{2E_z}{2r} + \frac{\partial^2 E_z}{\partial r^2} - \frac{1}{c^2}\frac{\partial^2 E_z}{\partial t^2} = 0.$$

We obtain

$$\cos\omega t\sum_{m=0}^{\infty}\cos\frac{m\pi z}{L}\left[\frac{d^2 a_m(r)}{dr^2} + \frac{1}{r}\frac{da_m(r)}{dr} + K_m^2 a_m(r)\right] = 0\,,$$

where $\quad K_m^2 = \left[\frac{2\pi}{\lambda}\right]^2\left[1-\left(\frac{m\lambda}{2L}\right)^2\right].$

The sign of K_m can be either positive or negative. In what follows we will define K_m as $\sqrt{|k_m^2|}$ If we apply the orthogonality relation to the cosine function for each m, we see that the differential equation in brackets for each m must vanish individually. Then, if we define $x_m^2 \equiv K_m^2 r^2$, we can write

$$x_m^2\frac{d^2 a_m}{dx_m^2} + x_m\frac{da_m}{dx_m} + x_m^2 a_m = 0\ .$$

This is the Bessel function of order zero or the modified Bessel function of order zero, depending on the sign of K_m^2. The solutions are

$$a_m(r) = A_m J_o(K_m r), \text{when } K_m^2 > 0,$$

and

$$a_m(r) = A_m I_o(K_m r), \text{when } K_m^2 < 0.$$

The expression for the z-component of the electric field is

$$E_z(r,z,t) = \left[\frac{a_0(r)}{2} + \sum_{m=1}^{\infty} a_m(r)\cos\frac{\pi m z}{L}\right]\cos\omega t.$$

Some additional insight comes by substituting a trigonometric identity for the product of cosines. We obtain

$$E_z(r,z,t) = \frac{a_0(r)\cos\omega t}{2} + \sum_{m=1}^{\infty}\frac{a_m(r)}{2}\left[\cos\left(\omega t - \frac{m\pi z}{L}\right) + \cos\left(\omega t + \frac{m\pi z}{L}\right)\right].$$

This equation describes the standing-wave pattern as a sum of forward and backward traveling waves. These waves are sometimes called space harmonics. The wave numbers of the mth wave are

$$K_m = \pm\, m\pi/L \ ,$$

where the signs correspond to forward and backward waves. The corresponding phase velocities are

$$\beta_m = \frac{\omega}{k_m c} = \pm\frac{2L}{m\lambda}.$$

For a linear accelerator one of these waves will be synchronous with the accelerated particles. The effect of all other waves on the beam averages to zero because they do not maintain a specific phase relationship with the beam.

These space-harmonic waves are of course generally not identical with the traveling-wave eigenmodes of the waveguide (evaluated near the beam axis). For example, in a drift-tube structure, each of the eigenmodes must have a vanishing field within the drift tubes (at least for the lower-frequency eigenmodes which are below the cutoff frequency in the drift tube). The eigenmodes act on the beam only in the gaps. The individual space harmonics are nonzero inside the drift tubes and act continuously on the beam. Each set of waves is a complete orthogonal set, and each traveling-wave eigenmode is an infinite sum of the space-harmonic components. The Fourier sum given above describes this field pattern. The distinction, and the differences between these two sets of waves, should be made clear. The only space harmonic that on average can contribute energy to the beam is the synchronous forward wave. But this is not necessarily true for the eigenmode waves. For example, in the π mode both the forward and backward eigenmodes contribute equally to the acceleration of the beam, because these waves act on the beam only in the gaps, where they can always interfere constructively at the time the beam arrives. Nevertheless, the space-harmonic

expansion will be very useful for providing a general analysis, as we will see. We now examine several cases of interest.

3.1.3 Application to Uniform Cylindrical Cavity

The equation for E_z reduces to the solution for the uniform cylindrical (pillbox) cavity when $L \to \infty$. Then we obtain $K_m = 2\pi/\lambda, k_m = 0, \text{and} \beta_m = \pm\infty$. The solution is

$$E_z(r,z,t) = A J_0(2\pi r/\lambda)\cos\omega t .$$

This is the familiar TM_{010} mode of the cylindrical cavity. Because the phase velocity of the traveling wave is infinite, there can be no synchronism with the beam particles, and the uniform cylindrical cavity is not suitable for continuous acceleration.

3.1.4 Periodic Cavity In 0 Mode

We now consider the application of these results to an Alvarez drift-tube linac. By symmetry, the integrals for the a_m coefficients vanish for all odd m values. (The period of the field pattern is L, and harmonics of the form L/p are present, where p = 0, 1, 2, 3, etc. The wavelength of the mth harmonic in the Fourier expansion is $\lambda_m = 2L/m$. Therefore, the terms with m/2 equal to an integer are the only nonzero terms, leaving only m = 0, 2, 4, ...) Since it is convenient to let n = m/2, the nonzero terms are labeled n = 0, 1, 2, ... Then we have

$$E_z(r,z,t) = \left[\frac{a_0(r)}{2} + \sum_{n=1}^{\infty} a_n(r)\cos\frac{2\pi nz}{L}\right]\cos\omega t ,$$

and
$$E_z(r,z,t) = \frac{a_0(r)\cos\omega t}{2} + \sum_{n=1}^{\infty}\frac{a_n(r)}{2}\left[\cos\left(\omega t - \frac{2\pi nz}{L}\right) + \cos\left(\omega t + \frac{2\pi nz}{L}\right)\right],$$

The phase velocity of the nth harmonic is $\beta_n = \dfrac{\omega}{k_n c} = \pm\dfrac{L}{n\lambda}$.

The radial index is $K_n^2 = \left[\dfrac{2\pi}{\lambda}\right]^2\left[1 - \left(\dfrac{n\lambda}{L}\right)^2\right]$.

If we require the phase velocity β_n of the nth traveling wave to equal the particle velocity β, we must have $L = n\beta\lambda$. This is physically possible for all values of $n > 0$.

The usual choice for the synchronous wave is n = 1, which gives a period $L = \beta\lambda$ and corresponds to the $L = \beta\lambda$ Alvarez drift-tube linac. The choice n = 2 is sometimes made, especially when more space is needed for focusing quadrupole magnets, which must fit within the drift tubes. This is called the $2\beta\lambda$ Alvarez drift-tube linac.

. . .

We now look more carefully at the n = 1, $L = \beta\lambda$ case. We obtain

$$\beta_n = \pm\, \beta/n \quad \text{and} \quad K_n^2 = \left[\frac{2\pi}{\lambda}\right]^2 \left[1 - \left(\frac{n}{\beta}\right)^2\right].$$

For $\beta < 0$ this results in $K_n^2 < 0$ for all n except n = 0. The solution for E_z can be written as

$$E_z(r,z,t) = \left[\frac{A_0 J_0(2\pi r/\lambda)}{2} + \sum_{n=1}^{\infty} A_n I_0(K_n r)\cos\frac{2\pi n z}{\beta\lambda}\right]\cos\omega t\,,$$

where $$A_n = \frac{2}{L I_0(K_n r)}\int_{-L/2}^{L/2} E(r,z)\cos\frac{2\pi n z}{\beta\lambda}dz\,, \quad n = 1,2,3,\ldots$$

and $$A_0 = \frac{2}{L J_0(2\pi r/\lambda)}\int_{-L/2}^{L/2} E(r,z)dz\,.$$

The particles experience the field of the synchronous wave, which is

$$E_{z1}(r,z,t) = \frac{A_1}{2} I_0(K_1 r)\cos\left(\omega t - \frac{2\pi z}{\beta\lambda}\right)\,,$$

where $$K_1^2 = \left[\frac{2\pi}{\lambda}\right]^2\left[1 - \left(\frac{1}{\beta}\right)^2\right] = -\left[\frac{2\pi}{\gamma\beta\lambda}\right]^2,$$

$$K_1 = \sqrt{|K_1^2|} = 2\pi/\gamma\beta\lambda, \text{and}\, \gamma = 1/\sqrt{1-\beta^2}\,.$$

Example: <u>*Square-Wave Field Distribution*</u>

We assume that the electric field at the drift-tube bore (r = a) is constant within the gap and zero within the metallic walls (Fig. 3.3). We assume $L = \beta\lambda$. Thus

$$E(r=a,z) = \begin{Bmatrix} E_g, & 0 \le |z| \le g/2 \\ 0, & g/2 < |z| \le L/2 \end{Bmatrix}.$$

We evaluate the integral for the A_n at r = a, where $E = E_g$ in the gap region. This gives the results

$$A_0 = \frac{2E_g g}{L J_0(2\pi a/\lambda)}\,, \quad A_n = \frac{2E_g}{I_0(K_n a)}\frac{\sin(n\pi g/\beta\lambda)}{n\pi}, n = 1,2,3,\ldots$$

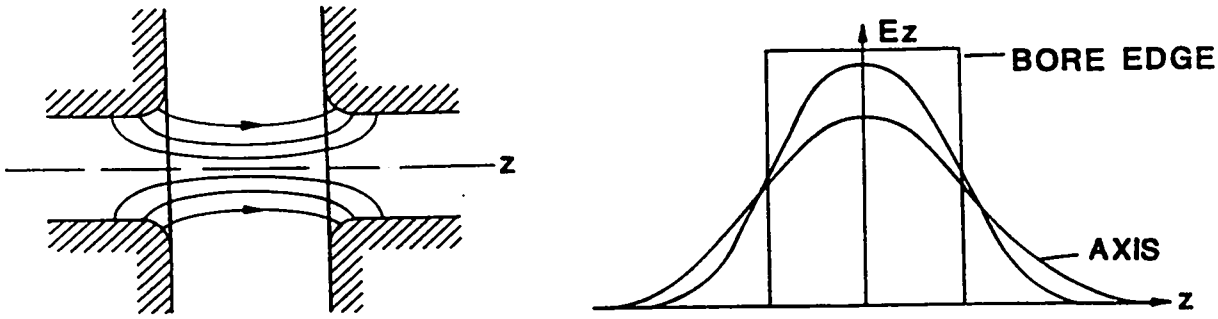

Fig. 3.3. Electric field distribution across the gap.

Later we will see that E_g can be related to the average axial field. The above expressions allow us to estimate the relative sizes of the terms. A typical value of $g/\beta\lambda$ is 1/4. We see that the coefficients decrease with n as $1/I_0(K_n a)n$, which is at least as fast as 1/n.

3.1.5 Periodic Cavity in π Mode

Now we consider the π mode and π/2 mode, where one complete period of the field distribution on axis contains two accelerating gaps with an alternating sign of the field. Examples include the coupled-cavity linacs and the Wideroe linac.

Examination of the symmetry of the a_m expressions reveals that the a_m vanish for all even m values. (The period of the field pattern is 2L, and all odd harmonics can be present. The wavelength of the mth harmonic in the Fourier expansion is $\lambda_m = 2L/m$. Therefore, the terms with m an odd integer are the only nonzero terms, leaving only m = 1, 3, 5, ...) Since it is convenient to let n = (m-1)/2, the nonzero terms are labeled n = 0, 1, 2, ... Then we have

$$E_z(r,z,t) = \sum_{n=0}^{\infty} a_n(r)\cos\frac{2\pi(n+1/2)z}{L}\cos\omega t\,,$$

and

$$E_z(r,z,t) = \sum_{n=0}^{\infty}\frac{a_n(r)}{2}\left[\cos\left(\omega t - \frac{2\pi(n+1/2)z}{L}\right) + \cos\left(\omega t + \frac{2\pi(n+1/2)z}{L}\right)\right].$$

The phase velocity of the nth harmonic is $\beta_n = \dfrac{\omega}{k_n c} = \pm\dfrac{L}{(n+1/2)\lambda}$.

The radial index is $K_n^2 = \left[\dfrac{2\pi}{\lambda}\right]^2\left[1-\left(\dfrac{(n+1/2)\lambda}{L}\right)^2\right]$.

If we require the phase velocity β_n of the nth traveling wave to equal the particle velocity β, we must have $L = (n+1/2)\beta\lambda$. This is physically possible for all values of n (n = 0, 1, 2, ...).

The choice of synchronous wave for the coupled-cavity linacs and the Wideroe linac is n = 0, which gives a period $L = \beta\lambda / 2$. We obtain

$$\beta_n = \pm\beta / (2n+1) \quad \text{and} \quad K_n^2 = \left[\frac{2\pi}{\lambda}\right]^2 \left[1 - \left(\frac{(2n+1)}{\beta}\right)^2\right].$$

If $\beta < 1$ these are always negative, and the modified Bessel functions are used. The solution for E_Z can be written as

$$E_z(r,z,t) = \sum_{n=0}^{\infty} A_n I_0(K_n r) \cos\frac{2\pi(2n+1)z}{\beta\lambda} \cos\omega t,$$

where $$A_n = \frac{2}{L I_0(K_n r)} \int_{-L/2}^{L/2} E(r,z) \cos\frac{2\pi(2n+1)z}{\beta\lambda} dz.$$

On average the particles experience the field of the synchronous wave, which is

$$E_{z0}(r,z,t) = \frac{A_0}{2} I_0(K_0 r) \cos\left(\omega t - \frac{2\pi z}{\beta\lambda}\right),$$

where $$K_0^2 = \left[\frac{2\pi}{\lambda}\right]^2 \left[1 - \left(\frac{1}{\beta}\right)^2\right] = -\left[\frac{2\pi}{\gamma\beta\lambda}\right]^2,$$

$$K_0 = \sqrt{|K_0^2|} = 2\pi / \gamma\beta\lambda \quad \text{and} \quad \gamma = 1\sqrt{1-\beta^2}.$$

Note that the form of the synchronous traveling wave is the same for the π mode as for the 0 mode. Note also that if the structure is designed for $\beta = 1$, $K_0 = 0$, and because $I_0(0) = 0$, there is no radial variation for the synchronous wave.

Example: Square-Wave Field Distribution

We assume that the electric field at the drift-tube bore (r = a) is constant within the gap and zero outside within the metallic walls. We assume $L = \beta\lambda/2$. Thus

$$E(r=a,z) = \begin{Bmatrix} E_g, & 0 \le |z| \le g/2 \\ 0, & g/2 < |z| \le L/2 \end{Bmatrix}.$$

We evaluate the integral for the A_n at r = a, where $E = E_g$ in the gap region. This gives the result

$$A_n = \frac{4E_g}{I_0(K_n a)} \frac{\sin[(2n+1)\pi g/\beta\lambda]}{(2n+1)\pi}, \qquad n = 0, 1, 2, \ldots .$$

A typical value of $g/\beta\lambda$ is 1/4. We see that the coefficients decrease with n as $1/[I_0(K_n a)(2n+1)]$.

3.1.6 Other Field Components

Now we return to the other field components. We recall the general expression for the z-component of the electric field:

$$E_z(r,z,t) = \left[\frac{A_0 J_0(2\pi r/\lambda)}{2} + \sum_{m=1}^{\infty} A_m I_0(K_m r)\cos\frac{\pi m z}{L}\right]\cos\omega t.$$

An E_r component is derived from Gauss's law in the absence of charge ($\rho = 0$):

$$\nabla\cdot\vec{E} = \frac{1}{r}\frac{\partial(rE_r)}{\partial r} + \frac{\partial E_z}{\partial z} = 0.$$

Then

$$E_r = -\frac{1}{r}\int^r dr\, r\frac{\partial E_z}{\partial z}.$$

We use the relationship

$$\int^x dx\, x I_0(x) = x I_1(x),$$

to obtain

$$E_r(r,z,t) = \left[\sum_{m=1}^{\infty} A_m \frac{m\pi}{K_m L} I_1(K_m r)\sin\frac{\pi m z}{L}\right]\cos\omega t.$$

To obtain B_θ we use Ampere's law for zero current ($\vec{j} = 0$) and evaluate the radial component of

$$\nabla\times\vec{B} = \frac{1}{c^2}\frac{\partial\vec{E}}{\partial t} \qquad \text{or} \qquad \frac{\partial B_\theta}{\partial z} = -\frac{1}{c^2}\frac{\partial E_r}{\partial t},$$

to obtain

$$B_\theta(r,z,t) = \left[-\frac{\omega}{c^2}\sum_{m=1}^{\infty}\frac{A_m}{K_m} I_1(K_m r)\cos\frac{\pi m z}{L}\right]\sin\omega t.$$

The remaining components can be shown to be zero. We assumed that $B_Z = 0$, because we assumed a TM solution. This fact, together with requiring that the solutions be finite at $r = 0$, is sufficient to prove that B_r and E_θ are zero.

3.2 RF Acceleration in a Gap

The beam is acted upon by the E_z, E_r and B_θ fields in the TM_{010} mode. The equations of motion are

$$\frac{dp_z}{dt} = q[E_z(r,z)\cos(\omega t+\phi) + v_r B_\phi(r,z)\sin(\omega t+\phi)],$$

and

$$\frac{dp_r}{dt} = q[E_r(r,z)\cos(\omega t+\phi) - v_z B_\phi(r,z)\sin(\omega t+\phi)] + F_{ex} \quad ,$$

where F_{ex} is any external radial field that might be applied for focusing. Exact results can be calculated by numerical integration of these equations using measured or calculated fields.

The following treatment allows us to see some of the general properties of the motion without a detailed numerical integration. We will define two important parameters, the average axial field and the transit-time factor. We begin by expressing the longitudinal electric field seen by a particle on the axis with velocity v, passing through an accelerating gap, such as that shown in Fig. 3.4, as

$$E_z(r=0,z,t) = E(0,z)\cos[\omega t(z)+\phi],$$

where $\quad t(z) = \int_0^z dz / v(z)$

is the time the particle is at position z. By these definitions, at time t = 0 the particle is at the origin where z = 0, and the phase of the field relative to the crest is ϕ.

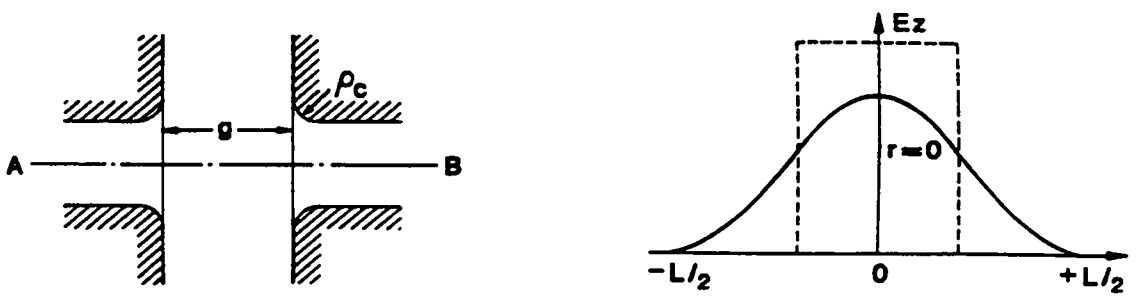

Fig. 3.4. Geometry and field distribution across the gap.

The energy gain of the particle of charge q traveling over a distance L is

$$\Delta W = q\int_{-L/2}^{L/2} E(0,z)\cos(\omega t(z)+\phi)dz\,.$$

Generally we assume that the length L is chosen large enough to include all the field in the gap, i.e. that the field at $z = \pm L/2$ has fallen to zero. The use of a trigonometric identity allows us to write the energy gain as

$$\Delta W = q\int_{-L/2}^{L/2} E(0,z)[\cos\omega t\cos\phi - \sin\omega t\sin\phi]dz\,.$$

It is customary to express this result in terms of the spatial average of the accelerating field. We can write

$$\Delta W = qE_0TL\cos\phi,$$

where we have introduced the spatial average of the accelerating field, defined by

$$E \equiv \frac{1}{L}\int_{-L/2}^{L/2} E(0,z)dz\,,$$

and a quantity we call the transit-time factor, defined by

$$T \equiv \frac{\int_{-L/2}^{L/2} E(0,z)\cos\omega t(z)dz}{\int_{-L/2}^{L/2} E(0,z)dz} - \tan\phi\frac{\int_{-L/2}^{L/2} E(0,z)\sin\omega t(z)dz}{\int_{-L/2}^{L/2} E(0,z)dz}\,.$$

The above equation for the energy gain is an important result that we will use frequently. The phase ϕ is 0 if the particle arrives at the origin when the field is at a crest. It is negative if the particle arrives earlier than the crest, and positive if it arrives later. This phase convention differs from the one generally used in the literature for circular accelerators (where the crest corresponds to 90°). Maximum acceleration occurs when $\phi = 0$, which is often the choice for relativistic electrons. But we will see that for nonrelativistic particles, where phase focusing is important, it is necessary to operate with negative phases.

The quantity E_0L is the voltage gain that would be experienced by a particle passing through a dc field equal to the field in the gap at time $t = 0$. This voltage does not depend on the length L if L includes (essentially) all of the field in the gap. But the value of E_0 does depend on L. Thus if we consider two different definitions of L, both of which contain all the field in the gap, this will result in two different E_0 values. Therefore when a value of E_0 is quoted for a cavity, it is important to specify the corresponding length L. The transit-time factor measures the ratio of the energy gained in the time-varying rf field to that in a dc field of voltage $E_0L\cos\phi$; it is a measure of the reduction in the energy gain caused by the sinusoidal time variation of the field in the gap. The phase and the transit-time factor depend on the choice of the origin. We can simplify the transit-time factor, and remove its dependence on the phase, by choosing the origin at the electrical center, as we will do soon.

We note that the transit-time factor definition requires that the integral of the field over the distance L be nonzero. A TM_{011} cavity mode (with a node in E_z at the center) is an example for which the integral of the axial field is zero. Of course the transit-time

factor does not have to be used to calculate the energy gain, but it could still be used if the cavity is separated into two accelerating gaps, which are analyzed separately.

Usually E(z) is at least approximately an even function about the geometric center of the gap region. Let us choose to put the origin at the electrical center of the gap, defined by

$$0 = \int_{-L2}^{L/2} E(0,z)\sin\omega t(z)dz\,.$$

When E(z) is an even function, the electrical center and the geometric center coincide. Then the transit time factor becomes

$$T = \frac{\int_{-L/2}^{L/2} E(0,z)\cos\omega t(z)dz}{\int_{-L/2}^{L/2} E(0,z)dz}\,.$$

Then the transit-time factor becomes the average of the cosine factor experienced by the particle, weighted by the field. The transit-time factor increases when the field is more localized longitudinally near the origin, where the cosine factor is largest. Thus, the larger the gap between drift tubes, or the more the field penetrates into the drift tubes, the smaller the transit-time factor.

In many cases the change of particle velocity in the gap is small compared to the initial velocity. If we ignore the velocity change, we have

$$\omega t \approx \omega z/v = 2\pi/\beta\lambda\ ,$$

where $\beta = v/c$ and $\beta\lambda$ is recognized as the distance the particle travels in an rf period. The transit-time factor becomes

$$T = \frac{\int_{-L/2}^{L/2} E(0,z)\cos(2\pi/\beta\lambda)dz}{\int_{-L/2}^{L/2} E(0,z)dz}\,.$$

3.3 Approximations for Transit-Time Factor

We will obtain approximate expressions for the transit-time factor which show how it depends on parameters such as the gap length and the aperture radius. The first approximation for T assumes that $E(0,z) = E_{g0}$ is constant over a gap of length g, and falls to zero outside the gap (Fig. 3.5). This would be the exact result for a simple TM_{010} pillbox cavity of length g in the limit that the beam-aperture radius is vanishingly small. Then $E_0 = E_{g0}L/g$ and the above integral for T gives

$$T = \left[\frac{\sin\pi g/\beta\lambda}{\pi g/\beta\lambda}\right].$$

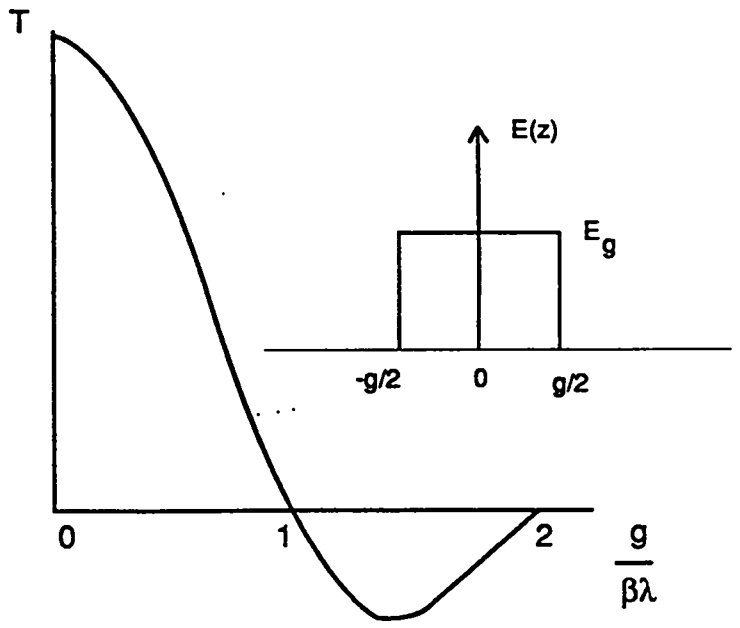

Fig. 3.5. Transit-time factor for square-wave electric-field distribution.

This form for T is the same for both 0-mode and π-mode structures, and it represents the effect of the field variation during the finite transit time of the particle through the gap. T = 1 when $g/\beta\lambda = 0$, and T = 0 when $g/\beta\lambda = 1$ (one rf period). In this range, as the gap increases, the transit-time factor decreases. When $g/\beta\lambda = 1/4$, T = 0.9, which is still quite large. At $g/\beta\lambda = 1/2$, $T = 2/\pi \approx 0.64$. We can see from these numbers that without a drift tube to decrease the gap in the drift-tube linac, we would have $g/\beta\lambda = 1$ and T = 0. For a coupled-cavity linac, where $g/\beta\lambda = 1/2$, the value of T can be increased above T = 0.64 by adding nose cones, as described later.

A better approximation for T can be obtained for the Alvarez drift-tube linac (0 mode), if we take into account the penetration of the field into the bore hole of the drift tube. This field penetration further reduces T because it reduces the concentration of the field near the center of the gap. We now assume that the electric field at the drift-tube bore (r = a) is constant within the gap and zero outside the gap, within the metallic walls (see Fig. 3.3). This is a more realistic approximation than the one above, because it does not constrain the axial field to vanish at the end of the gap. Thus

$$E(r=a,z)=\begin{Bmatrix} E_g, & 0\le|z|\le g/2 \\ 0, & g/2<|z|\le L/2 \end{Bmatrix}.$$

The Fourier coefficients are

$$A_n=\frac{2}{LI_0(K_n r)}\int_{-L/2}^{L/2}E(r,z)\cos\frac{2\pi nz}{\beta\lambda}dz\,,\quad n=1,2,3,\ldots$$

and $$A_0 = \frac{2}{LJ_0(2\pi r/\lambda)}\int_{-L/2}^{L/2} E(r,z)dz .$$

The average axial field and transit-time factor are

$$E_0 \equiv \frac{1}{L}\int_{-L/2}^{L/2} E(r=0,z)dz ,$$

and $$T = \frac{\int_{-L/2}^{L/2} E(0,z)\cos(2\pi/\beta\lambda)dz}{\int_{-L/2}^{L/2} E(0,z)dz} .$$

The A_0 coefficient can be evaluated from the integral expression by setting $r = 0$ and using the definition of E_0. We immediately obtain $A_0 = 2E_0$, using $J_0(0) = 1$. We can also calculate A_0 by evaluating the integral at $r = a$, where $E = E_g$ in the gap region. The result is

$$A_0 = \frac{2E_g g}{LJ_0(2\pi a/\lambda)}$$

Equating the two expressions for A_0, we have a relation between E_g and E_0:

$$E_g = E_0 \frac{L}{g} J_0(2\pi a/\lambda) .$$

Next, we evaluate the integral for $n = 1$ at $r = 0$, and by inspection we see that $A_1 = 2E_0T$. Thus the transit time-factor is proportional to the $n = 1$ (synchronous wave) coefficient of the Fourier series. We obtain all the Fourier coefficients by evaluating the integrals at $r = a$,

$$A_n = \frac{2}{LI_0(K_n a)}\int_{-g/2}^{g/2}\left[\frac{E_0 L}{g} J_0(2\pi a/\lambda)\right]\cos\frac{2\pi nz}{\beta\lambda}dz ,$$

or

$$A_n = \frac{2E_0 J_0(2\pi a/\lambda)}{I_0(K_n a)}\frac{\sin m\pi g/\beta\lambda}{n\pi g/\beta\lambda} , \quad n = 1,2,3,\ldots .$$

The $n = 1$ coefficient is

$$A_1 = \frac{2E_0 J_0(2\pi a/\lambda)}{I_0(K_1 a)}\frac{\sin \pi g/\beta\lambda}{\pi g/\beta\lambda} ,$$

Then by comparing this result to $A_1 = 2E_0T$, we find the more accurate expression for the transit-time factor:

$$T = \frac{J_0(2\pi a/\lambda)}{I_0(K_1 a)}\left[\frac{\sin(\pi g/\beta\lambda)}{\pi g/\beta\lambda}\right],$$

where usually the factor $J_0(2\pi a/\lambda) \approx 1$ and is neglected in the literature. Recall that

$$K_1 = \sqrt{|K_1^2|} = 2\pi/\gamma\beta\lambda .$$

The Bessel-function factors account for the field penetration into the drift-tube bore holes. The Bessel function I_0 increases as its argument $K_1 a$ increases, and T decreases. This treatment does not apply to the π-mode cavity because the boundary condition inside the shorter drift tube, where the field reverses sign, must be taken into account.

3.4 Space Harmonics in Periodic Accelerating Structures

We now present a more general approach to the description of the fields, which applies to both standing-wave and traveling-wave structures. First we will make some preliminary comments about traveling-wave accelerators. Traveling-wave accelerators are also built as periodic structures. The periodic structure can be designed to reduce the phase velocity to the velocity of light (or less), but this cannot be done for the uniform waveguide with conducting boundaries. The traveling-wave structure that is used at SLAC and throughout the world to accelerate relativistic electrons is a periodic structure, known as the disk-loaded or iris-loaded cylindrical waveguide. Later we will return to a discussion of this structure and how a periodic structure reduces the phase velocity. For now we will discuss the accelerating field.

In a lossless uniform waveguide, the axial field distribution for the TM_{01} mode is written in exponential notation as

$$E_z(r,z,t) = EJ_0(Kr)e^{j(\omega t - k_0 z)}.$$

This describes a wave propagating in the +z direction, with wavenumber $k_0 = 2\pi/\lambda_{guide}$, where λ_{guide} is the wavelength in the waveguide.

The phase velocity of the wave is $v_p = \dfrac{\omega}{k_0 c}$.

The uniform waveguide has a dispersion relation (Fig, 3.6) given by

$$\omega^2 = (Kc)^2 + (k_0 c)^2 ,$$

where K is the cutoff wavenumber for the TM_{01} mode. The cutoff angular frequency is $\omega_c = Kc$. Then the phase velocity can be expressed as

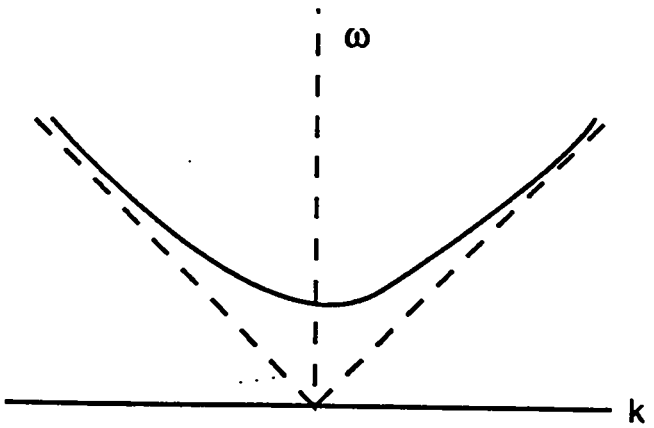

Fig. 3.6. Dispersion curve (Brillouin diagram) for uniform waveguide.

$$v_p = \frac{c}{\sqrt{1-(Kc)^2/\omega^2}} > c .$$

One might guess that introducing elements to make this a periodic structure (Fig. 3.7) might perturb this field distribution by introducing a periodic modulation of the amplitude of the wave, giving a form

$$E_z(r,z,t) = E_d(r,z)e^{j(\omega t - k_0 z)} ,$$

where $E_d(r,z)$ is a periodic function with the same period d as the structure. This is indeed the correct solution as can be shown from Floquet's theorem, which states that in a steady-state propagating mode the fields at two different cross sections that are separated by one period differ only by a complex constant. In this case the complex constant is $e^{jk_0 d}$.

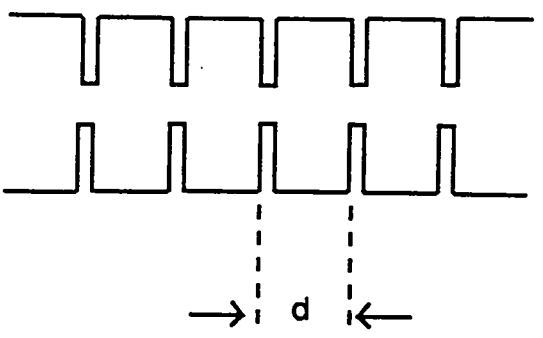

Fig. 3.7. Periodic structure.

Because $E_d(r,z)$ is periodic, it can be expanded in a Fourier series as

$$E_d(r,z) = \sum_{n=-\infty}^{\infty} a_n(r) e^{-j2\pi nz/d} .$$

If we require this solution for $E_z(r,z,t)$ to satisfy the wave equation, as we did earlier in this section, we find that

$$a_n(r) = E_n J_0(K_n r) ,$$

where $\quad K_n^2 = (\omega / c)^2 - (k_0 + 2\pi n / d)^2 .$

Recall that when $K_n^2 < 0$ we must use $I_0(K_n r)$ in place of $J_0(K_n r)$. Then the general solution for the field may be written as

$$E_z(r,z,t) = \sum_{n=-\infty}^{\infty} E_n J_0(K_n r) e^{j(\omega t - k_n z)} .$$

where we define the wavenumber for the nth space harmonic as

$$k_n = k_0 + \frac{2\pi n}{d} .$$

The phase velocity for the nth space harmonic is

$$\beta_n = \frac{\omega}{k_n c} = \frac{\beta_0}{1 + (n\beta_0 \lambda / d)} .$$

The expression for the field describes an infinite series of traveling waves, each with the same frequency but with different wavelengths, and each with a constant amplitude E_n independent of z (see Fig. 3.8). The waves for $n > 0$ travel in the +z direction and are called forward waves; those for $n < 0$ are backward waves traveling in the -z direction. When forward and backward waves with the same phase velocity have equal amplitude there is a standing wave. The terms of this Fourier series are called space harmonics, and any steady-state field distribution in a periodic structure for either propagating or standing waves can be expressed with this series.

We now describe the acceleration of a particle in the periodic structure. On axis the traveling-wave field is

$$E_z(0,z,t) = e^{j\omega t} \left\{ E_0 e^{-jk_0 z} + \sum_{n=1}^{\infty} \left[E_n e^{-j(k_0 + 2\pi nz/d)} + E_{-n} e^{-j(k_0 - 2\pi nz/d)} \right] \right\} .$$

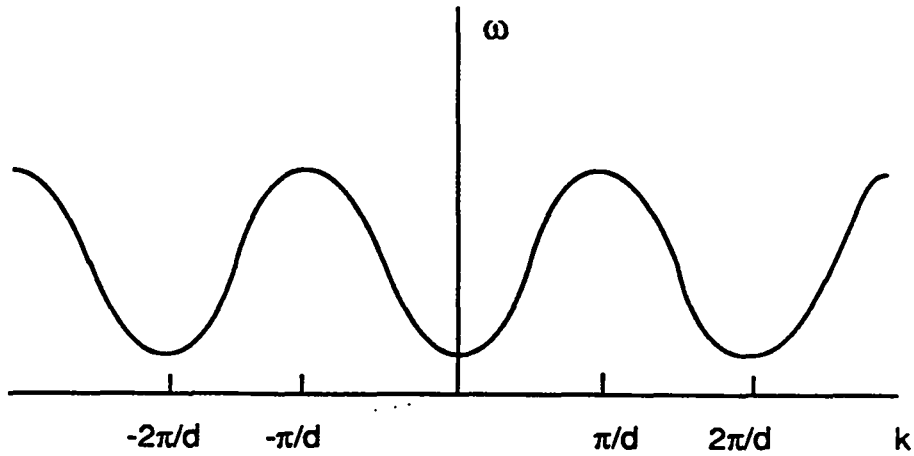

Fig. 3.8. Dispersion curve of lowest passband of a periodic waveguide.

Now consider the effect of this field on a particle with velocity β, which is at the origin $z = 0$ (an arbitrary position in the waveguide) at time $t = t_0$, when the phase relative to the wave crest is $\phi_0 = \omega t_0$. We can write $t = z/\beta c + t_0$, and we note that

$$\omega t - k_0 z = \frac{2\pi z}{\beta\lambda} - \frac{2\pi z}{\beta_0\lambda} + \phi_0 .$$

Periodic structures not only form an infinite number of propagating space harmonics with different phase velocities but also have a dispersion relation different from that of the uniform waveguide, and the phase velocity of the principal n=0 wave is also changed. One finds that it is possible to reduce the phase velocity to match the particle velocity. For small periodic perturbations, one expects that the principal n=0 wave, which is the only wave with nonzero amplitude in a perfectly uniform guide, will have the largest amplitude. Therefore we consider an example, where we assume that $\beta_0 = \beta$, which means the particle and the $n = 0$ wave are synchronous. We introduce the notation $\beta_s = \beta_0 = \beta$ for the velocity of the particle and the wave to indicate that they are synchronous. Then the field experienced by the particle is obtained by substituting the above relation into $E_z(r,z,t)$, which yields

$$E_z(0,z,t = z/\beta c + t_0) = e^{j\varphi_0}\left\{E_0 + \sum_{n=1}^{\infty}[E_n e^{-j2\pi nz/d} + E_{-n} e^{+j2\pi nz/d}]\right\}.$$

The energy gain of the particle as it travels over a period d, experiencing the force of the wave, is

$$\Delta W = q\int_0^d E_z(0,z,t = z/\beta c + t_0)dz = qe^{j\phi_0}E_0 d ,$$

where we used $\int_0^d e^{\pm j2\pi nz/d} dz = 0$.

Taking the real part of the exponential we have

$$\Delta W = qE_0 d \cos\varphi_0 .$$

Since this result is general, it must apply to a standing-wave field in an accelerating gap, for which we have already derived an expression. This expression has the same form, except that it has no transit-time factor. This is to be expected because for the equivalent traveling wave the acceleration is continuous. Then the amplitude E_0 for the equivalent traveling wave must be associated with E_0T in the standing-wave expression. Also, the phase ϕ_0 for the equivalent traveling wave in the above expression must be associated in the standing-wave case with ϕ_s, the phase of the field when the synchronous particle is at the center of the gap.

We see that only the n = 0 space harmonic, which has the same phase velocity as the particle, contributes to the energy gain of the particle. The other space harmonics are needed to satisfy boundary conditions, but do not contribute to the energy gain because they are nonsynchronous with the particle. For most structures the synchronous space harmonic component is n = 0. An exception is the Alvarez drift-tube linac structure, where $d = n\beta_S\lambda$, the guide wavelength $\beta_S\lambda$ is infinite, and the synchronous space harmonic is the nth term. Usually n = 1, which corresponds to the conventional $1\beta_S\lambda$ drift-tube linac.

In the treatment given above we have not allowed for the increase of the particle velocity. Because of this the accelerating structures for nonrelativistic particles are not exactly periodic. The cells lengths are graded to allow for the increase of the particle velocities, and therefore we can describe these structures as quasiperiodic.

The result above is a very powerful one. In a periodic structure, regardless of whether the field is a standing wave or a traveling wave, the effect on the beam is equivalent to replacing the actual field distribution with that of an equivalent traveling wave with a uniform amplitude and with the same phase velocity as the particle. The average effect of the other waves can be ignored. Even when the structure is not exactly periodic, this result is a good approximation if the fractional energy gain of the particle is not large and the amplitude and phase velocity of the wave vary slowly with axial position.

In general then the accelerating field of the equivalent traveling wave, taking into account the radial field is

$$E_z(r,z,t) = E_0 I_0(Kr)\cos\phi ,$$

where $K = \dfrac{2\pi}{\gamma_s\beta_s\lambda}$, and $\phi = \omega t - \dfrac{2\pi}{\lambda}\int^z \dfrac{dz}{\beta_s(z)}$.

We have already shown that Maxwell's equations with cylindrical symmetry can be used to obtain expressions for the other nonzero field components. The radial field is obtained from

$$E_r = -\frac{1}{r}\int^{z}\frac{\partial E_z}{\partial z} r\,dr\,,$$

and for the magnetic field we use $B_\theta = -\frac{1}{c^2}\frac{\partial E_r}{\partial t}$.

We also need the identity $\int^{x} I_0(x)x\,dx = x\,I_0(x)$.

From this we obtain the radial electric field $E_r = -\gamma_s E_0\, I_1(Kr)\sin\phi$,

and the azimuthal magnetic field $B_\theta = -\frac{\gamma_s\beta_s}{c}E_0 I_1(Kr)\sin\phi$,

In summary the equivalent traveling-wave field components are

$$E_z = E_0\, I_0(Kr)\cos\phi, \quad E_r = -\gamma_s\, E_0\, I_1\,(Kr)\sin\phi\ , \text{ and } \quad B_\theta = -\frac{\gamma_s\beta_s}{c}E_0 I_1(Kr)\sin\phi\,,$$

where K and ϕ are defined above.

Near the beam axis, where $Kr \ll 1$ we have

$$E_z = E_0\cos\phi\ , \quad E_r \equiv -\frac{\pi r}{\beta_s\lambda}E_0\sin\phi\,, \quad \text{and} \quad B_\theta = -\frac{\pi r}{c\lambda}E_0\sin\phi\,.$$

When the fractional energy gain per rf period is large, as is sometimes the case at low velocities, it is better to solve the equations of motion numerically through the exact field distributions rather than to use the equivalent traveling-wave approximation.

3.5 Power Efficiency Figures of Merit

Power is dissipated from resistive losses in the walls of the cavity to maintain the fields. We will introduce shunt impedance parameters which are commonly used in linac terminology. The figure of merit for stored energy U per unit power loss P in the cavity walls is the quality factor defined by

$$Q = \omega U/P\ .$$

But for accelerators we often want to maximize the energy gain per unit power dissipation. Our efficiency figure of merit measures how effective the cavity is in producing an axial electric field per unit power loss. The shunt impedance per cavity r_s has units of ohms or megohms, and is defined by

$$r_s \equiv V_0^2 / P$$

where $V_0 = E_0L$ is the peak axial voltage for a cavity of length L and average axial field E_0. (We note that sometimes one finds a factor of 2 in the denominator for this definition, so be careful.) Note that r_S is independent of the excitation level of the cavity because the power loss is proportional to the square of the field.

The peak energy gain of a particle occurs when $\phi = 0$, and may be written as

$$\Delta W_{\phi=0} = qE_0LT = q\sqrt{(r_sT^2)P}\,.$$

We define an effective shunt impedance $r = r_ST^2$ that includes the transit-time factor. Then

$$r \equiv r_sT^2 = \left[\frac{\Delta W_{\phi=0}}{q}\right]^2 \frac{1}{P} = \frac{[E_0TL]^2}{P}\,.$$

This parameter in ohms measures the efficiency for delivering energy to a particle per unit power loss. The effective shunt impedance r is usually of more interest for accelerators than r_S.

Both r and r_S increase linearly with the length of the cavity. For long cavities we prefer to use a figure of merit that is independent of both the field level and the cavity length; thus we characterize a power efficiency per unit length rather than per cavity. The shunt impedance Z per unit length is simply

$$Z \equiv \frac{r_s}{L} = \frac{E_0^2}{P/L}\,.$$

The effective shunt impedance per unit length measures the acceleration efficiency per unit length and is

$$ZT^2 = \frac{r_sT^2}{L} = \left[\frac{\Delta W_{\phi=0}}{qL}\right]^2 \frac{1}{P/L}\,.$$

For a cavity with constant E_0T along its length

$$ZT^2 = \frac{(E_0T)^2}{P/L}\,.$$

The units of shunt impedance per unit length and effective shunt impedance per unit length are usually given in megohms per meter. Especially for normal-conducting cavities, one of the main objectives in cavity design is to choose the geometry to maximize effective shunt impedance or effective shunt impedance per unit length. A derived parameter which many find useful for cavity design is the ratio of effective shunt impedance to Q, often called r over Q, which is

$$\frac{r}{Q} = \frac{(V_0 T)^2}{\omega U} .$$

We see that r/Q measures the efficiency of acceleration per unit stored energy, and is independent of the power. It is a function of the cavity geometry and is independent of the surface properties that determine the power losses.

If the rf generator is matched to the cavity structure then all the incident rf power goes into the structure. It will be dissipated in the cavity walls and some will go into the beam that is being accelerated. The beam power P_B is easily calculated from

$$P_B = I\Delta W ,$$

where I is the beam current and ΔW is the energy gain. The total power is $P_T = P + P_B$ and the efficiency of the structure is

$$\varepsilon_S = P_B/P_T$$

The overall system efficiency must also include the efficiency of the rf generator, which is the ratio of the rf power delivered to the accelerator to the total ac power used. This efficiency usually lies in the range from about 50% to nearly 70%.

3.6 Cavity Design

Cavity designers generally use computer programs like SUPERFISH that numerically solve Maxwell's equations with the specified boundary conditions. The procedures depend on the constraints of the problem. Suppose the objective is to maximize the effective shunt impedance of a single cavity. If we begin with a simple pillbox cavity for reference, adding nose cones centered on the beam axis allow us to reduce the gap and raise the transit-time factor (Fig. 3.9). The nose creates a region of more localized electric field near the beam axis and concentrates the magnetic field near the outer regions of the cavity. In drift-tube linac cells the nose takes the form of a drift tube, and its shape is limited by the requirement that it must hold a focusing quadrupole magnet. If the gap between drift tubes is too small, then the voltage gain, for either a given axial electric field or a given stored energy, becomes small. Also the capacitance between the opposite noses increases at small gaps, increasing the ratio of wall current to axial voltage. Some prefer to optimize in steps. First, the gap and geometry of the nose cones can be choosen to maximize the r/Q parameter to increase the energy gain per unit stored energy. Then, the geometry of the outer walls can be adjusted to maximize Q, thus minimizing the power dissipation per unit stored energy. This latter procedure usually leads to a spherical shape for the outer wall, which corresponds to the smallest surface area for a given volume.

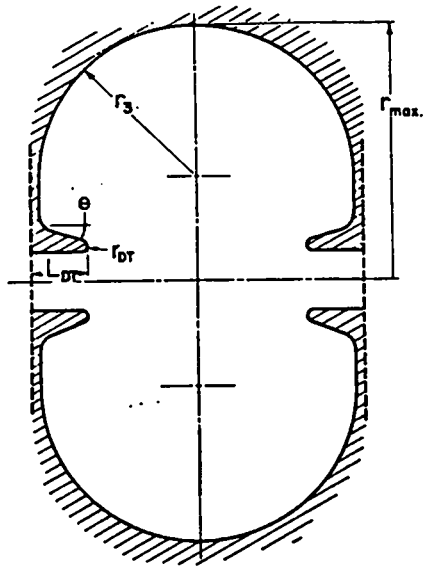

Fig. 3.9. Cross section of cavity with nose cones and spherical outer wall.

In superconducting cavities, the rf power efficiency may not be as important as other requirements such as minimizing the peak surface fields, which limit the performance. The spherical or elliptical cavity shape (without nose cones), shown in Fig. 3.10, is now the universally accepted choice for a high-β superconducting cavity shape because of its low peak surface field to E_0 ratios, its lack of strong multipacting levels, and practical advantages during chemical processing.

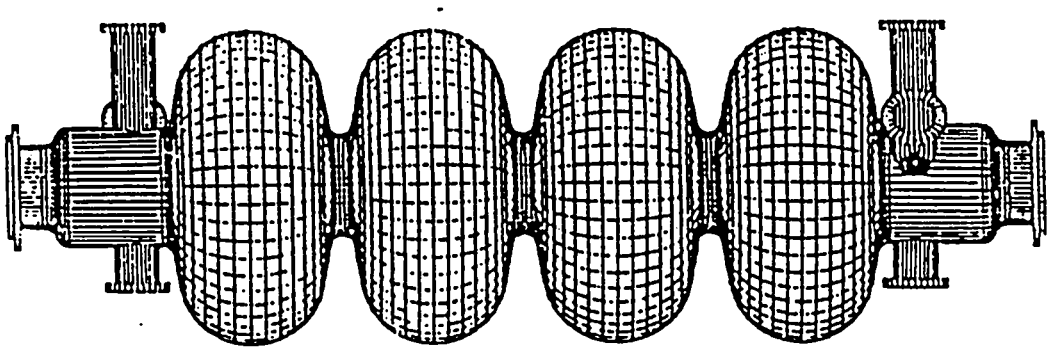

Fig. 3.10 Cross section of elliptical cavity used for superconducting applications at CERN.

The peak surface electric field and magnetic field are often important in cavity design. In room temperature cavities, too large a peak surface electric field can result in electric breakdown. For a cavity with nose cones or drift tubes, a typical ratio of peak surface electric field E_s to average axial field E_0, is $E_s/E_0 = 6$, whereas the ratio is unity for a pillbox cavity. The Kilpatrick criterion is often used as a design guideline for

room temperature cavities. A frequency-dependent "Kilpatrick" formula sometimes used is

$$f(\mathrm{MHz}) = 1.64\,E_K^2 \exp(-8.5 / E_K)\,,$$

where E_K is the Kilpatrick field in units of MV/m, and the rf frequency is f. To use the formula one must invert the expression; this can be done easily by iterative solution. One finds that E_K varies roughly as $f^{0.4}$ for frequencies in the hundred-MHz range. The peak surface electric field can exceed E_K, and reliable performance can be obtained especially in clean vacuum systems and for short pulses (< ~1 ms). The ratio of peak surface electric field E_s to the Kilpatrick field E_K is often called the bravery factor b. For long-pulse (>1 ms) accelerators, a typical bravery factor lies in the range $1 < b = E_s/E_K < 2$.

In superconducting cavities large electric fields cause field emission, which produces electrons in the cavity volume that absorb rf energy and create additional power losses. The surface magnetic fields result in surface currents that produce resistive heating. Therefore, for room temperature structures, cooling requirements restrict the peak magnetic field (average power densities of about 20 watts/cm^2 can begin to produce cooling difficulties in drift-tube linacs). Also, superconducting cavities will quench and make a transition to normal conducting when the critical magnetic field is exceeded. This field depends on temperature, and is near B = 0.2 T in the range of operating temperatures from about 2 to 4.2 K. In practice the presence of normal-conducting impurities lowers this limit. Few designers of superconducting cavities would exceed about B = 0.1 T. The ratio of peak surface magnetic field to average axial field E_0 is 19 G/MV/m for a pillbox cavity. This value is still typical in spherical cavity cells, but it can increase by a factor of 2 to 3, especially on drift tubes of drift-tube linac cells.

The aperture radius is usually chosen to satisfy the beam-dynamics requirements for good transmission. The aperture being too large results in reduced transit-time factor and increased power loss. It also can cause larger peak surface electric fields.

Introducing nose cones increases the local electric field and the surface charge; this can be described as increasing the capacitance and is called capacitive loading. Introducing rods or stems that carry a net rf current increases the local magnetic flux and is called inductive loading. These methods of loading a cavity with reactive circuit elements can be used to reduce the outer diameter of the cavity, to make the structures easier to handle. This idea is especially useful for very low-frequency structures and is widely used for heavy-ion accelerating structures. Consider the cavity as a lumped-circuit oscillator with resonant frequency $\omega = (LC)^{-1/2}$. In the lumped-circuit picture the inductance in a pillbox cavity is associated with currents flowing on the outer walls, which create a magnetic flux that circulates azimuthally about the axis. The cavity radius determines the area in which the flux circulates; therefore the inductance increases with the radius. For a cavity at a given frequency, capacitive or inductive loading implies a reduced outer wall inductance and therefore a reduced radius. Loading has some disadvantages: capacitive loading generally increases the power loss for a given accelerating field, and inductive loading increases the local magnetic field and the power density. It sometimes results in structures with complicated 3-D geometries, whose properties are more difficult to calculate.

3.7 Scaling of Cavity Parameters with Frequency

Consider a cavity structure with fixed accelerating field E_0. How do the structure parameters vary with frequency? Suppose we scale all transverse cavity dimensions with wavelength or as f^{-1}. Of course the cell lengths of a multicell structure are proportional to $\beta\lambda$ and also would scale as f^{-1}, but the total length for a given energy gain is independent of frequency if E_0 and the energy gain ΔW are fixed. Therefore assume that the diameter, gap, radial aperture, and cell length are scaled as f^{-1}. How do the other parameters behave? If E_0 and ΔW are fixed then all other fields are fixed. Then we have $T \propto f^0$, $E \propto f^0$, $B \propto f^0$, $\Delta\Omega \propto f^0$, length $\propto f^0$, surface area $\propto f^{-1}$, cavity volume $\propto f^{-2}$, and stored energy $\propto f^{-2}$. Surface-resistance and power loss scaling depends on whether the structure is normal or superconducting. In what follows we will ignore the residual resistance term in the superconducting rf resistance (a good approximation at high frequency). We find the rf surface resistance scales as

$$R_s \propto \begin{Bmatrix} f^{1/2} & \text{normal conducting} \\ f^2 & \text{superconducting} \end{Bmatrix}.$$

The rf power losses are not zero in the superconducting case. They are caused by normal-conducting electrons that are present at any finite temperature. Although these losses are small in terms of rf power, they affect the requirements for cryogenic refrigeration and must be taken into account.

The rf power dissipation scales as

$$P = \frac{R_s}{2}\left|\frac{B}{\mu_0}\right|^2 dA \propto \begin{Bmatrix} f^{-1/2} & \text{normal conducting} \\ f & \text{superconducting} \end{Bmatrix}.$$

Thus higher frequency gives reduced power losses for normal-conducting structures but increased power losses for superconducting ones.

The Q scales as

$$Q = \frac{\omega U}{P} \propto \begin{Bmatrix} f^{-1/2} & \text{normal conducting} \\ f^{-2} & \text{superconducting} \end{Bmatrix}.$$

The effective shunt impedance per unit length scales as

$$ZT^2 = \frac{E_0 T^2 L}{P} \propto \begin{Bmatrix} f^{-1/2} & \text{normal conducting} \\ f^{-1} & \text{superconducting} \end{Bmatrix}.$$

Like the power, the shunt impedance improves at higher frequencies for normal-conducting structures and at lower frequencies for superconducting structures.

The ratio ZT^2/Q scales as

$$\frac{ZT^2}{Q} \propto \begin{Bmatrix} f^1 & \text{normal conducting} \\ f^1 & \text{superconducting} \end{Bmatrix}.$$

This is the same for normal and superconducting, as it should be, since this is a figure of merit that is independent of the surface properties.

3.8 Problems

3-1. Consider a cylindrical pillbox cavity of length L operated in a TM_{014} mode. Complete the following steps to determine whether one can use this mode to achieve synchronous acceleration at each antinode. (a) Sketch the wave pattern for E_z versus z. Express the spacing between adjacent antinodes as a function of the cavity length. How many antinodes are there? (b) Express a synchronism requirement by equating the spacing between adjacent antinodes to the distance the particle travels in one half an rf period. This should relate the cavity length L to $\beta\lambda$. (c) But the cavity length and λ are already related by the dispersion relation. Write the dispersion relation and evaluate it for the TM_{014} mode. Substitute the synchronism condition from part b. Solve for β, and determine the range of allowed β values. Can one use this mode to achieve synchronous acceleration at each antinode?

3-2. Consider a 2.5-cm-long TM_{010} pillbox cavity that is resonant at 400 MHz and is excited with an axial electric field of $E_0 = 2$ MV/m. Suppose a proton with an initial kinetic energy of 5 MeV is accelerated along the axis of the cavity and arrives at the center when the phase of the field is 30° before the crest. (a) Ignoring the effects of the aperture, and assuming the velocity β remains constant at its initial value, calculate the transit-time factor. (b) Calculate the final energy of the particle as it leaves the cavity. Also calculate the fractional change in the velocity.

3-3. Consider a room temperature TM_{010} pillbox cavity that is resonant at 400 MHz with an axial electric field $E_0 = 1$ MV/m and a length $\lambda/2$ where λ is the rf wavelength. Assume the cavity accelerates relativistic electrons. (a) Use the power loss formula for the pillbox cavity from the reference material to calculate the rf power dissipated in the walls. (b) Ignoring the effects of the apertures calculate the transit-time factor. (c) Calculate the shunt impedance, the effective shunt impedance, and the effective shunt impedance per unit length. (d) Calculate the energy gain of an electron with synchronous phase $\phi = 0$.

3-4. Consider a room temperature 10-m long electron linac with synchronous phase $\phi = 0$, that accelerates the beam from nearly zero kinetic energy to 100 MeV. Suppose the effective shunt impedance per unit length is $ZT^2 = 50$ MΩ/m. (a) Assuming the power delivered to the beam is negligible, how much rf power is required? (b) Repeat part (a) assuming the accelerator length is 100 m.

3-5. Use the definition of effective shunt impedance per unit length and the expression for energy gain in a cavity to show that the resistive power loss for fixed energy gain and fixed ZT^2 is proportional to E_0T. For a 100-MeV room temperature electron linac with synchronous phase $\phi = 0$, and $ZT^2 = 50$ MΩ/m, plot the curve of power (MW) required versus E_0T (MV/m).

3-6. Suppose you have to design a TM_{010} pillbox cavity with a constant axial electric field, but you are free to choose the length. If the cavity is too short the voltage gain across it is small; if it is too long the transit-time factor is small. (a) Ignoring the effect of the beam aperture, find the ratio of length to $\beta\lambda$ that maximizes the energy gain

for the cavity. (b) At this length, what is the transit time factor? (c) Show that a zero-length cavity is required to maximize the energy gain per unit length. (In practice you would be limited by peak-surface electric fields.)

3-7. Derive expressions for r, r/Q, and ZT^2 for a cylindrical pillbox cavity in a TM_{010} mode. (Use the analytic expressions for the pillbox cavity already given in the reference material, and leave the formulas in terms of T.)

3-8. Calculate numerical values for r, r/Q, and ZT^2 for a cylindrical pillbox cavity in a TM_{010} mode, assuming a room temperature cavity for acceleration of relativistic electrons. Assume a cavity resonant frequency of 400 MHz and a cavity length of $\lambda/2$. Use the formula for transit-time factor and ignore the aperture factor.

3-9. Suppose we want to design a CW room temperature drift-tube linac to accelerate a 100-mA proton beam from 2.5 to 20 MeV. Assume we can purchase 350-MHz klystron tubes of 1-MW capacity each for the rf power. Suppose we run the SUPERFISH cavity code and obtain the following results for all β values: $T = 0.8$, $ZT^2 = 50\ M\Omega/m$, and $E_S/E_0 = 6$. Let us choose to restrict the peak surface electric field at a bravery factor $b = E_S/E_K = 1$. For adequate longitudinal acceptance we choose the synchronous phase $\phi = -30°$. (a) Calculate the average axial field E_0. (b) Calculate the length of the linac assuming it consists of a single tank. (c) Calculate the structure power (power dissipated in the cavity walls), the beam power, and the total rf power required (assuming the klystron generator is matched to the cavity structure with the beam present). (d) What is the structure efficiency (ratio of beam power to total rf power)? Assuming a generator efficiency of 60%, what is the overall rf efficiency (ac power to beam power)? (e) How many klystrons do we need?

3-10. For largest effective shunt impedance (highest power efficiency), we prefer high frequencies for room temperature linacs. But if the frequency is too large, the radial variation of beam parameters may become intolerable. Choose the linac frequency for the cases below, by using the criterion that at the injection energy the accelerating-field variation with radius over the beam aperture must not exceed 10%. Assume for all cases that the radial aperture a = 1 cm for acceptable transmission through the entire accelerator. Assume that $E_z(r) \propto I_0(2\pi r / \gamma\beta\lambda)$, and use the approximation $I_0(x) = 1 + x^2/4$. Choose the linac frequency for the following injection conditions for the structure phase velocity: (a) electron linac near 200 keV (use $\beta\gamma = 1$, or $\beta = 0.707$ instead of $\beta = 1$ which is really used), (b) proton linac at 750 keV ($\beta = 0.04$), (c) proton linac at 3 MeV ($\beta = 0.08$), (d) proton linac near 100 MeV ($\beta = 0.4$).

. . .

4 LINEAR ACCELERATOR STRUCTURES

4.1 Independently Phased Cavity Linacs

Linacs composed of arrays of independent cavities, each containing only one or two accelerating gaps, have been used mainly for heavy ions for nuclear physics research. Well-known examples include the high energy section of the UNILAC linac at GSI, Darmstadt, and the ATLAS superconducting linac at Argonne (see Fig. 4.1).

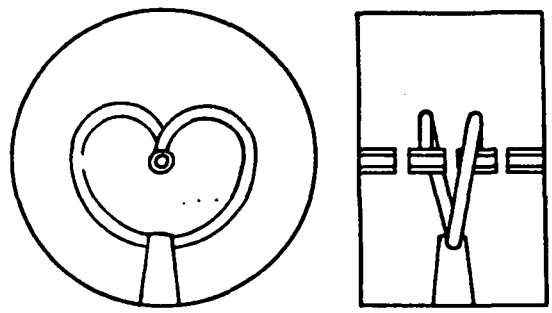

Fig. 4.1. Split-ring resonator used at the ATLAS superconducting linac at Argonne.

Each cavity is driven by a separate rf generator and can be phased independently. This system provides maximum flexibility for acceleration of a large range of ions of different charge-to-mass ratios and different velocities because each cavity phase can be adjusted to maximize the acceleration for the injected beam, within that cavity's performance limitations. The transit-time factor of a short cavity has a broad velocity acceptance, which further contributes to the flexibility. The cavity structure used at UNILAC is a single-gap cavity operating in a TM_{010} mode and has been optimized for high ZT^2.

The cavities used for very low velocities are often TEM coaxial-type structures, such as quarter-wave and half-wave resonators, loaded at the end by a drift tube. Examples are shown in Figure 4.2; different shapes for the inner conductor can be used, such as the spiral, to reduce the transverse dimensions of the cavity. Typically, a single resonator element is contained within a cylindrical cavity, and it gives two accelerating gaps with opposite polarity. The spacing between the gap centers is designed to equal $\beta_S\lambda/2$, where β_S is the synchronous velocity and λ is the rf wavelength, so that the synchronous particle travels between the two points in half an rf period.

We can analyze the acceleration in these two-gap cavities using the same approach as in the preceding section. We choose the origin at the center of the cavity (see Fig. 4.3), and we assume that the particle has a constant velocity through the cavity. It is convenient to express the time dependence of the field using the sine rather than the cosine, as

$$E_z(r,z,t) = E(r,z) \sin(\omega t + \phi).$$

For an arbitrary particle of velocity β, we write $\omega t = 2\pi z / \beta\lambda$. This is consistent with the phase convention used before because the synchronous particle has its maximum acceleration when it arrives in the center of both gaps at $\phi = 0$ (at the crest).

The energy gain is $\Delta W = q\int_{-L/2}^{L/2} E(0,z)\sin(2\pi z / \beta\lambda + \phi)dz.$

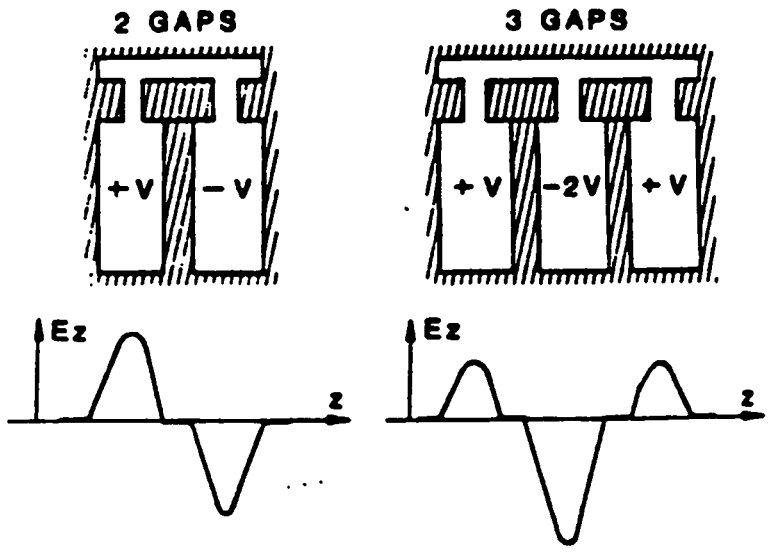

Fig. 4.2. Two- and three-gap cavities.

If we use a trigonometric identity and assume E(0,z) is an odd function about the origin, then

$$\Delta W = q\cos\phi\int_{-L/2}^{L/2} E(0,z)\sin(2\pi z/\beta\lambda)dz.$$

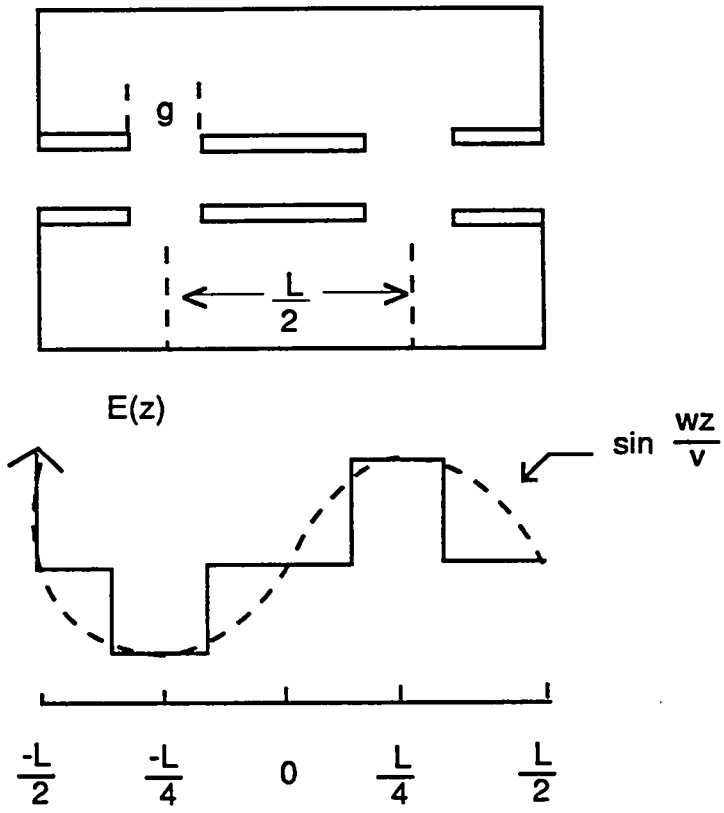

Fig. 4.3. Two-gap π-mode cavity.

The spatial average of the axial field, when E(0,z) is an odd function, is zero. But, the spatial average of the field when the field changes sign while the particle is in the center of the cavity is not a very useful quantity. Instead, we define

$$E_0 = \frac{1}{L}\int_{-L/2}^{L/2} |E(0,z)| dz.$$

Then the energy gain is $\Delta W = qE_0 T\cos\phi\, L$,

where $$T = \frac{\int_{-L/2}^{L/2} E(0,z)\sin(2\pi z/\beta\lambda)dz}{\int_{-L/2}^{L/2} |E(0,z)|dz}$$

Example: Square-Wave Field Distribution in Both Gaps.

We consider a two-gap cavity with gap length g and center-to-center gap spacing $\beta_S\lambda/2$, where β_S is the synchronous velocity. For the transit-time factor we obtain

$$T = \frac{\sin \pi g/\beta\lambda}{\pi g/\beta\lambda} \sin\frac{\pi\beta_s}{2\beta}.$$

The first factor in T is the usual gap factor, which depends on the particle β value. The second factor is associated with the degree of synchronism of the particle. Only when $\beta = \beta_S$ is this factor unity, indicating perfect synchronism. The synchronism factor reduces the range of β over which T is large. If the above exercise is carried out for an increasing number of gaps, the transit-time factor becomes a narrower function of β. If the same multicell cavity is to be used to accelerate particles over a large velocity range, the number of cells per cavity must be kept small.

4.2 Wideroe Linac

Linac energy gain requirements are usually for many MeV. They can be met by an array of single-cell cavities that can be independently phased, but this requires an rf drive into each cavity, and the setting of each cavity's phase and amplitude. This is an acceptable solution for some cases, especially for heavy-ion linacs, where it provides the flexibility needed for acceleration of a wide range of particles with different charge-to-mass ratios and different energies. For acceleration of a single particle species at a fixed input energy, it is simpler to use a multicell cavity, where the relative phasing between cells is determined by the structure geometry and the cavity mode. A multicell structure requires fewer rf drives and simplifies the operation. We will discuss in more detail the multicell structures, beginning with the Wideroe linac.

The Wideroe linac was the first successful linear accelerator, and it is still used for acceleration of low-velocity heavy ions. The beam moves within an array of hollow cylindrical electrodes to which an rf voltage is applied (Fig. 4.4). Acceleration takes place only in the gaps between the electrodes. The characteristic property of the Wideroe linac is that the voltages applied to successive electrodes alternate in sign. Therefore, half the electrodes are at a negative potential and half at a positive potential relative to ground. The electric field reverses in successive gaps, making the Wideroe linac a π-mode standing-wave structure. The linac is designed so that the synchronous particle travels from the center of one gap to the center of the next in half an rf period, making the cell lengths equal to $\beta_S\lambda/2$.

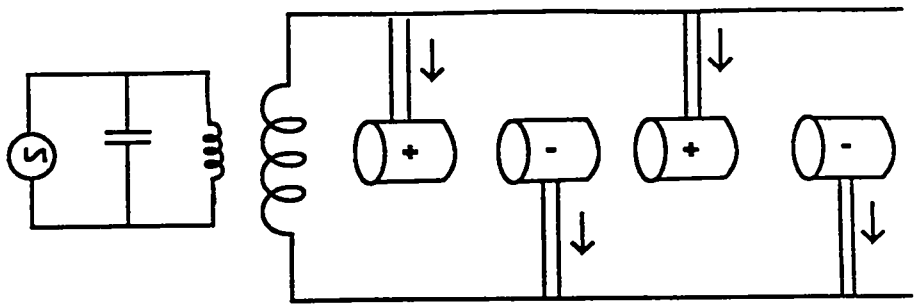

Fig. 4.4. Wideroe or Sloan-Lawrence lumped-circuit structure.

The Wideroe structure is used for particles with velocity below about β=0.03, for which a relatively low-frequency structure (< 100 MHz) is needed. An example is the 27-MHz Wideroe at the UNILAC linac at GSI, Darmstadt. The main advantage of this structure is that it can be fabricated with practical transverse dimensions, whereas a drift-tube linac, based on the TM_{010} cylindrical cavity mode, would have a transverse radius >3 m at 27 MHz.

In principle, the voltages can be supplied to the electrodes by alternately connecting them to two conductors parallel to the beam line and driven by a high-frequency oscillator. At these high frequencies, however, where the accelerator length is comparable to or larger than the rf wavelength, the voltage will vary along the conductors. In this case the two conductors of a quarter-wave resonator can be used to charge the electrodes. Because the voltage on the quarter-wave structure varies as sin $2\pi z/\lambda$, higher average accelerating fields can be obtained by bending the low-voltage end away from the beam axis, and attaching the electrodes only to the high-voltage end. This results in an array of bent quarter-wave resonator sections, which can be joined end to end and loaded with drift tubes. These structures are shown in Fig. 4.5.

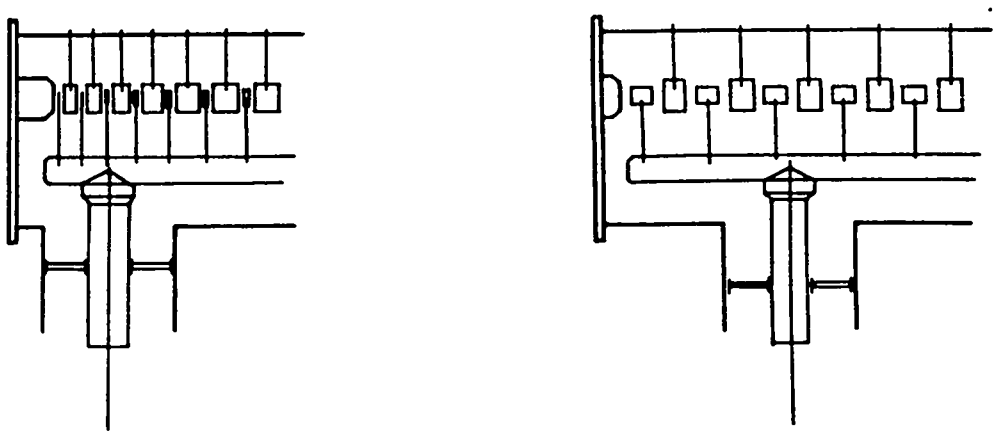

(a) (b)

Fig. 4.5. Wideroe or Sloan-Lawrence coaxial-line structure.
(a) Low-energy structure; (b) medium-energy structure.

Focusing can be provided by installing quadrupole magnets within the electrodes, provided there is enough space. One common arrangement to create the necessary space is to use a π-3π mode configuration, in which long electrodes containing quadrupoles are alternated with short, empty electrodes. The spacing between gaps alternates from $\beta_s\lambda/2$ to $3\beta_s\lambda/2$, which accounts for the name π-3π.

As the particle velocity increases, the electrode spacing increases; if the voltage between electrodes is constant, the accelerating fields will decrease. After the particle velocity reachs a few tenths of the speed of light, a higher-frequency Alvarez drift-tube linac will provide better power efficiency.

4.3 Drift-Tube Linac

4.3.1 Basic Concept

Suppose we want to accelerate the beam to high energies with a long TM_{010} pillbox cavity. We have seen that if the cavity is made longer than the distance a particle travels in half an rf period ($\beta\lambda/2$), the transit-time factor becomes very small, and the acceleration becomes inefficient. If the cavity length equals the distance a particle travels in one rf period ($\beta\lambda$), the transit-time factor is zero and the particle is decelerated as much as it is accelerated. The solution used by Alvarez et al. is to install hollow conducting drift tubes along the axis into which the electric field does not penetrate (Fig. 4.6). This creates field-free regions which shield the beam when the electric field would decelerate the beam, and concentrates the field in the gap region to increase the transit-time factor. The drift tubes divide the cavity into cells of nominal length $\beta\lambda$. As the energy increases the cell lengths also increase. Each drift tube is charged oppositely at each end, and the fields in all cells are in phase, as they are in the unperturbed TM_{010} cavity. This arrangement of the cell accelerating fields is referred to as the 0 normal mode or 0 mode, where the zero refers to the cell-to-cell phase difference at a fixed time.

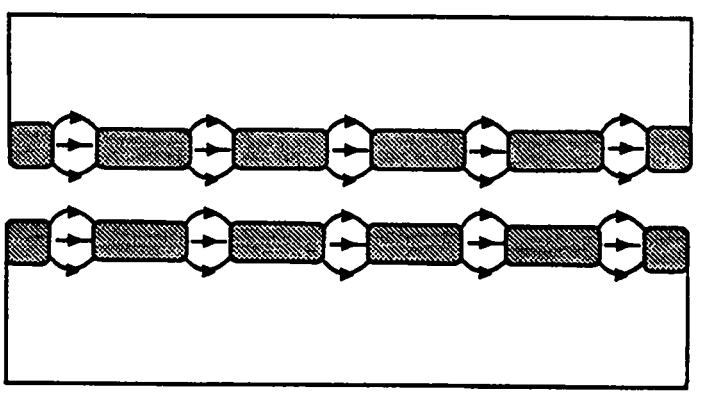

Fig. 4.6. Alvarez drift-tube linac cavity.

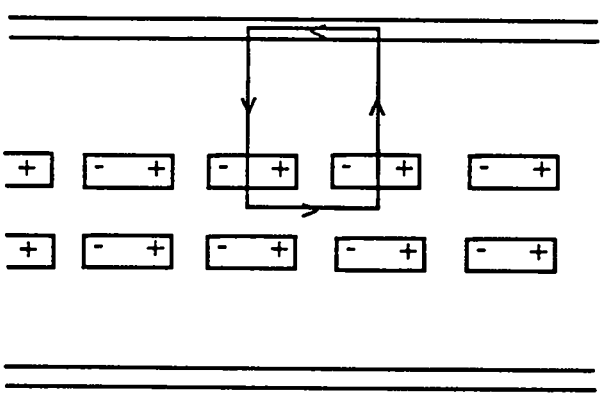

Fig. 4.7. Integration path for evaluating Faraday's law in a drift-tube linac.

We next show a very interesting and important result, that the value of the average axial field E_0 for a cell is related to the magnetic flux per unit length contained within the cell. We will apply Faraday's law, assuming an approximately periodic cavity, to the region shown in Figure 4.7. We evaluate

$$\oint \vec{E} \bullet d\vec{\ell} = -\frac{\partial}{\partial t}\int \vec{B} \bullet d\vec{A}.$$

By symmetry $E_r = 0$ along paths 2 and 4. Also $E_z = 0$ along path 3 inside the conductor. The only nonzero result is along path 1, given when the field is maximum as

$$\int_1 \vec{E} \bullet d\vec{\ell} = E_0 \beta\lambda.$$

The integral on the right side is $-\frac{\partial}{\partial t}\int \vec{B} \bullet d\vec{A} = -j\omega\Phi$,

where Φ is the magnetic flux, given by $\Phi = \int B_\theta \; drdz$.

Therefore the magnitudes of the left and right sides are related by $E_0\beta\lambda = \omega\Phi$.

The cell length is $\beta\lambda$; therefore E_0 is proportional to the magnetic flux per unit length of the cell. If the cavity is tuned so that the magnetic flux per unit length is the same for all cells, then E_0 is the same for all cells in the structure. The relative magnetic fields can be easily measured from a standard perturbation technique through holes in the outer wall and it is possible to tune the cells to obtain the same B_θ near the wall. If the cavity radius is constant along the length, and the cavity has the same radial distribution of B_θ for all cells, then the magnetic flux per unit length and E_0 will be the same for all cells, regardless of their length. In practice the conditions can be approximately obtained and the drift-tube linac has a constant E_0 for each cell rather than a constant voltage across each cell (as does a Wideroe linac). The voltage across each cell varies with the cell length $\beta\lambda$, because $V_0 = E_0\beta\lambda$. The behavior is similar to that of a voltage divider, where there is a fixed voltage across the whole structure, given by E_0L, where L is the length of the structure. The cell voltages are determined by the fraction of the length occupied by each cell.

The drift tubes are supported mechanically by stems, which can be either above or below the drift tubes. The currents flow longitudinally on the outer walls and on the drift tubes, and are everwhere in phase (see Fig. 4.8). There is no net charge on the drift tubes. The drift-tube space is generally used to install focusing quadrupole magnets. There is no net current on the stems, but, because of the time-varying magnetic fields on the surface of the stems, eddy currents produce power dissipation. Although E_0 may be the same for all cells, the peak electric field in the gaps and the peak surface electric field will vary, depending on the gap length and other details of the cell geometry. If desired, the structure can also be tuned so that E_0 is not constant.

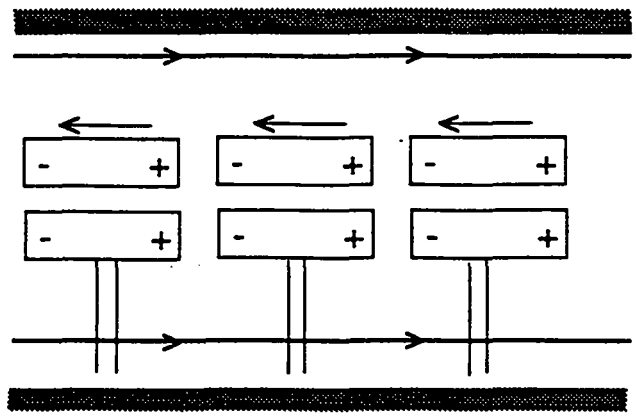

Fig. 4.8. Charges and currents in a drift-tube linac.

Adding the drift tubes makes the cavity look somewhat like a coaxial resonator especially when the gaps are small. Conduction current flows on each drift tube and becomes displacement current in the gaps. The magnetic field outside the drift-tube radius falls off with increasing radius, as in a coaxial line. Typical radial profiles of magnetic and electric fields are shown in Fig. 4.9. The electric field lines are shown in Fig. 4.10.

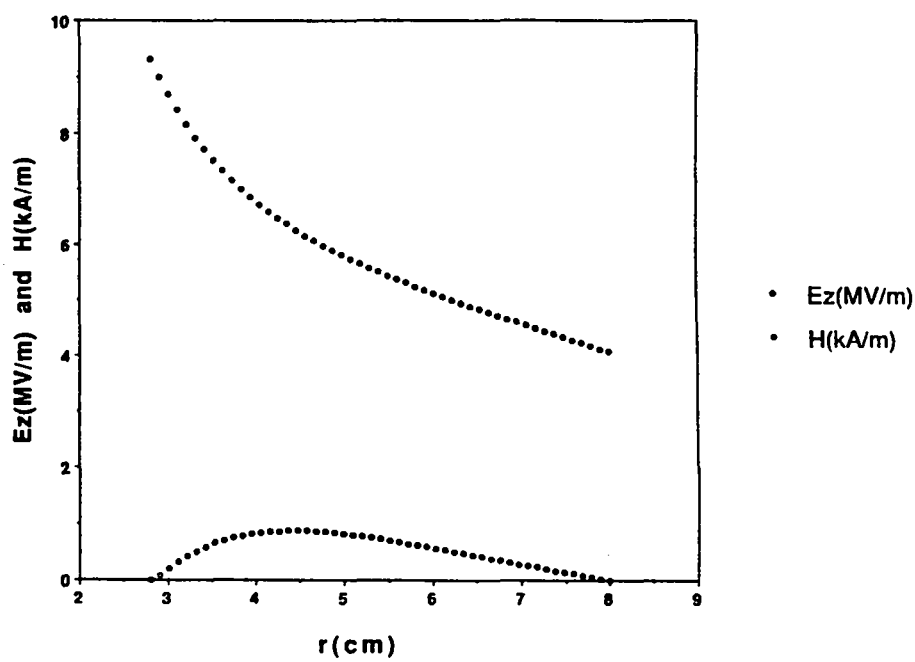

Fig. 4.9. Typical magnetic and electric fields versus radius in a drift-tube linac in the transverse plane passing through the center of a drift tube. The average axial electric field in the cell is 2.2-MV/m.

Another useful way of describing the DTL is as an array of cavity cells. In fact, if a conducting plane, perpendicular to the cavity axis was inserted at the electrical center of each drift tube, where, by symmetry, the electric field has only a longitudinal z component, the field pattern would be undisturbed and the cell resonant frequencies would be unchanged. Such conducting cell end walls are undesireable because they dissipate power. They are useful conceptually for visualizing the cells as individual cavities. Each effective cavity can be thought of as a lumped circuit consisting of the drift-tube capacitors and the inductance associated with a current loop from one

drift tube to the cylindrical outer wall and back to the other drift tube. However, this lumped-circuit model is not good enough for an accurate quantitative analysis of the structure properties, which requires use of a numerical code such as SUPERFISH. The lumped-circuit picture often remains useful for qualitative understanding. It would predict an approximate capacitance from the parallel plate formula of $C_0 = \varepsilon_0 \pi d^2 / 4g$ and an inductance of $L_0 = \mu_0 L \ln[(D-d)/2] / 2\pi$. The geometry parameters are the gap g, cell length L, drift tube diameter d, and tank diameter D. The resonant frequency of the cell is given in this model by $\omega_0^2 = 1 / L_0 C_0$.

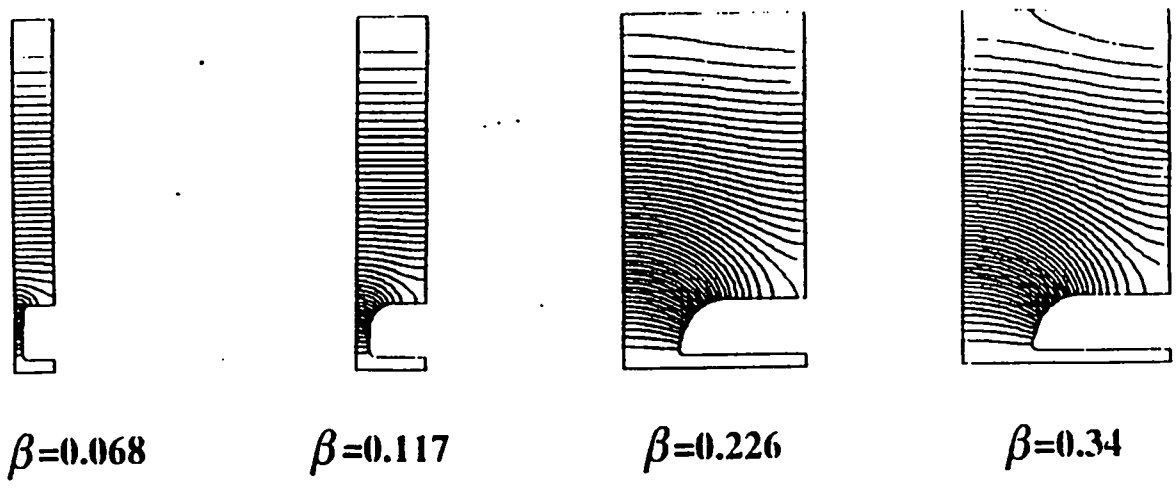

Fig. 4.10. Electric field lines shown in half cells of a drift-tube linac as calculated in the program SUPERFISH.

Consider the electric field pattern calculated by SUPERFISH as a function of particle velocity β, as shown in Figure 4.10. At low β the electric field lines concentrate on the front face of the drift tube. As β increases, the cell length increases, and the lumped-circuit model predicts that the inductance should increase if d and D remain constant. To keep the resonant frequency the same, the capacitance must decrease. If the gap increases with the cell length, the model predicts an unchanged frequency. But at higher β the pictures show that more field lines terminate on the outer diameter of the drift tube. It becomes harder to reduce the capacitance of the drift tubes by increasing the gap, and larger gaps are required to compensate for the increasing cell lengths. As energy increases, the larger gaps per unit cell length cause the transit-time factor and the effective shunt impedance to become small. We will see that eventually the coupled-cavity structures become more efficient than the DTL.

Figure 4.11 shows some parameters as a function of β for the Fermilab DTL, and Table 4.1 lists parameters for the Los Alamos (LAMPF) 200-MHz DTL. Fermilab uses nine tanks to accelerate the proton beam from 0.75 to 200 MeV, and LAMPF uses four tanks to accelerate the proton beam from 0.75 to 100 MeV. The effective shunt-impedance information in Table 4.1 shows the trend of decreasing effective shunt impedance versus β.

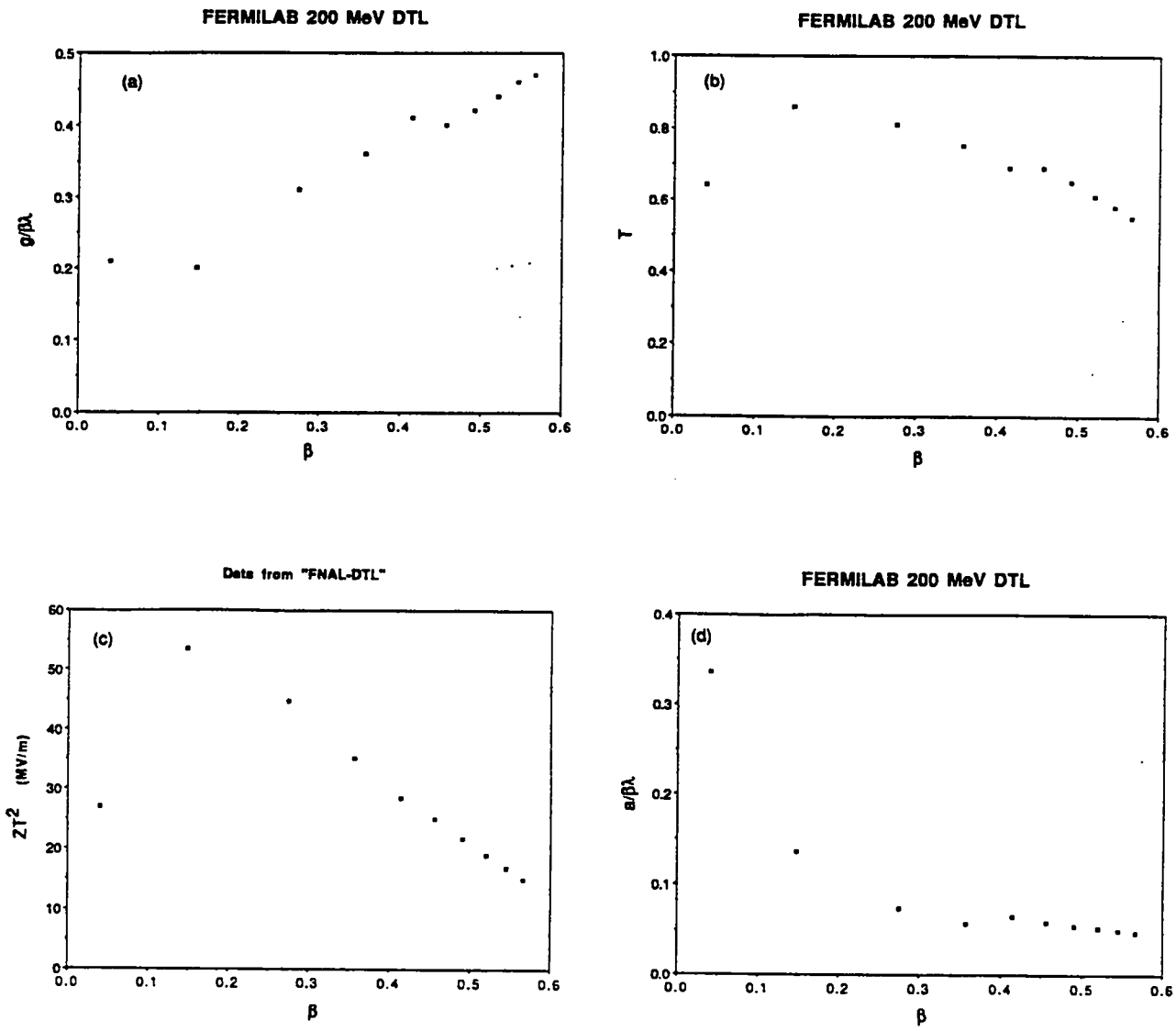

Fig. 4.11 Parameters plotted versus β for the 200-MeV proton drift-tube linac at FERMILAB: (a) gap length per βλ, (b) transit-time factor, (c) effective shunt impedance, and (d) radial aperture per βλ.

Table 4.1 Drift-Tube Linac Parameters for fhe LAMPF Proton Accelerator

	Tank 1	Tank 2		Tank 3	Tank 4
Cell No.	1 to 31	32 to 59	60 to 97	98 to 135	136 to 165
Energy in (MeV)	0.75	5.39		41.33	72.72
Energy out (MeV)	5.39	41.33		72.72	100.00
Δ energy (MeV)	4.64	35.94		31.39	27.28
Tank length (cm)	326.0	1968.8		1875.0	1792.0
Tank diameter (cm)	94.0	90.0		88.0	88.0
D. T. diameter (cm)	18.0	16.0		16.0	16.0
D. T. corner radius (cm)	2.0	4.0		4.0	4.0
Bore radius (cm)	0.75	1.0	1.5	1.5	1.5
Bore corner radius (cm)	0.5	1.0		1.0	1.0
G/L	0.21-0.27	0.16-0.32		0.30-0.37	0.37-0.41
Number of cells	31	66		38	30
Number of quads	32	29	38	20	16
Quad gradient (KG/cm)	8.34-2.46	2.44-1.89	1.01-0.87	0.90-0.84	0.84-0.83
Quad length (cm)	2.62-7.88	7.88	16.29	16.29	16.29
E_0 (MV/m)	1.60-2.30	2.40		2.40	2.50
φ_s (deg)	-26°	-26°		-26°	-26°
Power (MW)	0.305	2.697		2.745	2.674
Intertank space (cm)	15.90	85.62		110.95	--

Total length including intertank spaces = 6174.281 cm. (202 ft. 6.819 in.)

A $2\beta\lambda$ linac has twice the cell period, or one accelerating gap per $2\beta\lambda$. The linac may be designed this way to provide longer drift tubes so there is more room for quadrupole focusing magnets (inside the drift tubes). We have already seen that the average axial electric field is determined by the magnetic flux per unit length, and this is still true for the $2\beta\lambda$ linac.

We would then expect the ratio of surface magnetic field on the outer wall to E_0 would be unchanged if we exchange our $1\beta\lambda$ drift tubes for the $2\beta\lambda$ variety. However, for the same diameters of tank and drift tube, the longer cells will have twice the inductance and therefore will require half the capacitance, compared with the $1\beta\lambda$ case. This means the transit-time factor and effective shunt impedance, will be smaller for the $2\beta\lambda$ than the $1\beta\lambda$ linac. Therefore if you have a choice you will always choose the $1\beta\lambda$ structure over the $2\beta\lambda$ to obtain better efficiency.

The modern drift-tube linac also uses posts of electrical length $\lambda/4$ to provide resonant coupling between the cells (see Fig. 4.12). This is desirable to make the field distribution less sensitive to errors, and to eliminate phase shifts between cells resulting from the power flow away from the drive point. We will say more later about this resonant coupling.

4.3.2 Design of Drift-Tube Linacs

The drift-tube linac is separated into an array of cells, each of which extends from the center of one drift tube to the center of the next, and contains one accelerating gap. The DTL is a synchronous accelerator, where a particle arrives at each gap at the right time (phase) to gain a specified energy kick. The particle maintaining this synchronism is called the synchronous particle,

and the corresponding phase and energy at each cell are called the synchronous phase and energy. The linac is designed for continuous acceleration of the synchronous particle.

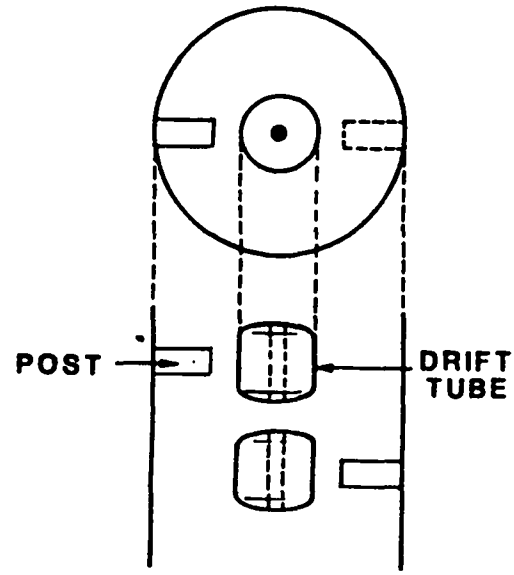

Fig. 4.12. Drift-tube linac with post couplers for field stabilization.

For simplicity we assume that the synchronous particle always arrives at the electrical center of each cell at the same phase of the electric field (same synchronous phase). For a $1\beta\lambda$ linac with constant synchronous phase, the synchronous particle travels from the center of a drift tube to the center of the gap in one half an rf period, and continues to the center of the next drift tube in the next half period. When particle velocities are increasing, the length of each cell must increase to maintain the synchronism. This length depends on the synchronous particle velocity β_S, which depends on the energy gain in each cell. But the energy gain in each cell depends on the electric field, and on the length of the cell. Consequently, the cell design requires a method of successive approximation.

First, the cell geometry at each average β_S must be chosen. This is generally done based on the criterion of maximum effective shunt impedance, consistent with (1) obtaining the correct resonant frequency, (2) allowing room within the drift tubes for quadrupole focusing lenses, and (3) keeping the peak surface electric and magnetic fields within the technological limits (determined by electric breakdown and drift-tube cooling requirements). The fields, the power, the transit-time factor for the synchronous particle (with constant velocity within a cell), and the shunt impedance calculations are usually done by codes like SUPERFISH. This procedure results in an optimum cell geometry in which the gap length, drift-tube shape, and tank diameter are determined. Because of the energy gain in the accelerating gap, the gap is always displaced toward the low-energy end of the cell. Fortunately, the field calculations relative to the gap are nearly independent of the precise location of the accelerating gap in the cell. Therefore, the SUPERFISH calculation can be done for an equivalent symmetric cell, which has the same length and geometry as the real cell, but has the gap in the geometric center of the cell. Only the field distribution and the figures of merit that do not depend on the magnitude of the field, need to be determined by this calculation.

After the electrical properties of the cells of different β_S have been calculated, the positions of the gap centers must be determined. This requires calculations that allow for the change of β_s in the cell. Furthermore, the calculations depend on the magnitude of the average accelerating field E_0 and on the synchronous phase ϕ_s. The choice of E_0 is important because it affects the accelerator length, the power dissipation, and the probability of electric breakdown. The choice of

position of electrical centers of successive gaps and the successive cell lengths still must be determined by numerical integration of the synchronous particle trajectory. A simple algorithm for integrating through the cell that often gets fairly accurate results is called the drift-kick-drift method. In this approximation the particle is assumed to drift at constant velocity β_{s1} from the center of the drift tube to the center of the gap, where it receives the acceleration as an impulse, after which it drifts at the new constant velocity β_{s2} to the center of the next drift tube. This process is repeated cell after cell until the particle reaches the desired final energy. The drift distances are $x_1 = \beta_{s1}/2$ and $x_2 = \beta_{s2}/2$, and the total cell length is $L = x_1 + x_2$. The energy gain at the center of the gap is $\Delta W_s = qE_0T(\beta_s)\cos\phi_s L$.

This calculation may be continued from cell to cell until the final energy is reached. Then the total length and power can be calculated. Similar methods are used in the widely used drift-tube linac design code, PARMILA (Phase And Radial Motion In Linear Accelerators), to lay out the gap locations and cell lengths.

The drift-tube linac is usually configured in independent tanks, each with its own rf drive. The tank lengths are determined mainly by the power available from the rf generator and by the mechanically constaints.

4.3.3 Summary of Drift-Tube Linacs

The drift-tube linac is used exclusively for accelerating protons and heavier ions. In the velocity region of $\sim 0.1 < \beta < 0.4$, it is generally unmatched in performance compared to other structures. It is not used for electrons because the injection velocity from a dc electron gun is usually higher than this velocity range. Its advantages include (1) an open structure without cell end walls, resulting in highest ZT^2 for $\sim 0.1 < \beta < 0.4$, (2) focusing quadrupoles within the drift tubes, providing strong focusing and permitting high current limits for long tanks. Its disadvantages are that (1) T and ZT^2 decrease significantly at high β values as gap lengths increase; (2) T and ZT^2 decrease at low β for fixed aperture as fields penetrate into drift tubes; and (3) focusing vanishes at low β where drift tubes are too short to hold the quadrupoles of adequate length.

4.4 Coupled-Cavity Linacs

4.4.1 Basic Concept

The coupled-cavity linac (CCL) consists of a linear array of resonant cavities, coupled together to form a multicell accelerating structure (Fig. 4.13). CCLs are used for acceleration of higher velocity beams of electrons and protons in the velocity range of about $0.3 < \beta < 1.0$. The individual cavities are also called cells, and each usually operates in a TM_{010}-like standing-wave mode. The overall standing-wave mode of the whole structure is one normal mode of the coupled-oscillator system, where specific relationships between the amplitudes and phases for adjacent cells are specified. Most of the structures provide two accelerating gaps per $\beta\lambda$ and in its simplest form the arrangement of the cell-to-cell fields is referred to as the π mode, where the π refers to the cell-to-cell phase difference at a fixed time. However, the most common arrangement in modern linacs is the $\pi/2$ normal mode, which will be discussed later. There are many examples of this type of structure, which use either electric or magnetic coupling between cells.

Here we restrict the discussion to standing-wave operation. For traveling waves the structure would be used as a periodically loaded waveguide rather than as an array of coupled standing-wave oscillators, and we will return to the traveling-wave structure later. To understand CCLs, we must understand the properties of an array of coupled oscillators. Probably the most significant advantage of this type of accelerator is called resonant coupling, which we will now discuss.

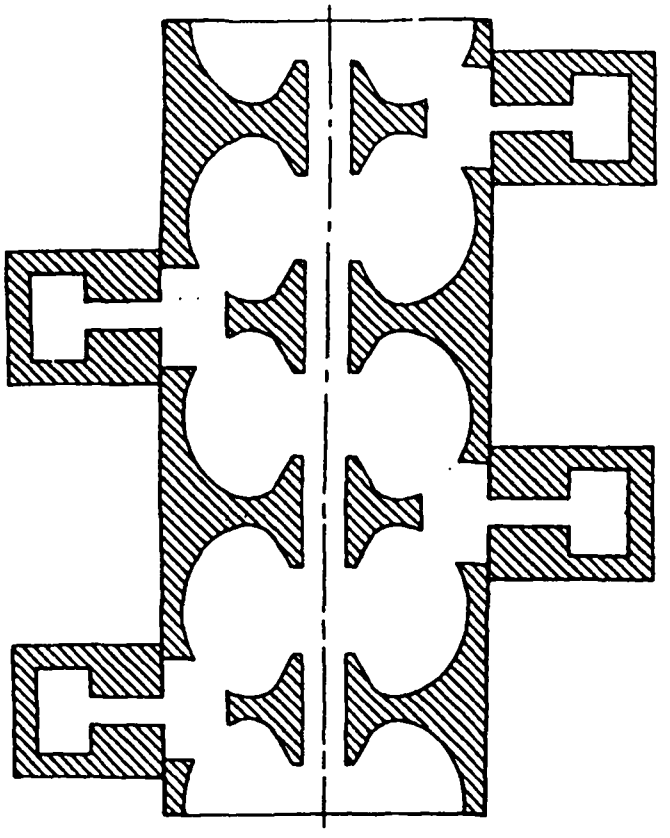

Fig. 4.13. Side-coupled linac structure as an example of a coupled-cavity linac structure. The cavities on the beam axis are the accelerating cavities. The cavities on the side are nominally unexcited and stabilize the accelerating-cavity fields against perturbations from fabrication errors and beam loading. This cell-to-cell field pattern is known as the $\pi/2$ mode.

4.4.2 Resonant Coupling

The general approach of designing standing-wave accelerating tanks by including unexcited oscillators in the array for overall field stabilization is called resonant coupling. To explain this, we must discuss the properties of a linear chain of coupled oscillators. We describe the problem of N coupled electrical oscillators shown in Figure 4.14. The coupling between oscillators is assumed to be magnetic, through the mutual inductances. Without any coupling there are N independent oscillators. This treatment can also serve as a model for a chain of cavity resonators if each cavity resonates in the same cavity mode, such as a TM_{010} mode, which is well separated in frequency from the other cavity modes (the criterion for adequate separation will become clear later). There will be N coupled states or normal modes of the system, each with a characteristic resonant frequency and a characteristic pattern of the relative amplitudes and phases for the different oscillators. In the case of real cavity resonators, where the individual oscillators have many modes, each cavity mode begets a family of N normal modes that occcupies a frequency band near the resonant frequency of an isolated oscillator. The greater the coupling, the larger the band width of the family of normal modes.

The properties of these N normal modes can be determined by solving an eigenvalue problem. This is done in the following way. Kirchoff's law is applied to the N circuits, and the sum of the voltages around each loop is set to zero. The resulting N simultaneous equations are solved for the eigenfrequencies and the corresponding eigenvectors. The eigenvector components give the distribution of currents in the oscillators for each normal mode. Many general details of the

behavior of such a system can be deduced from our coupled-circuit model, including the characteristics of the normal modes, the nature of the dispersion relation, the effects of errors in the frequencies of the oscillators, and the effects of power losses. We anticipate the applicability of this model to a chain of coupled cavities, and we will often refer to the eigenvectors as the fields, instead of currents.

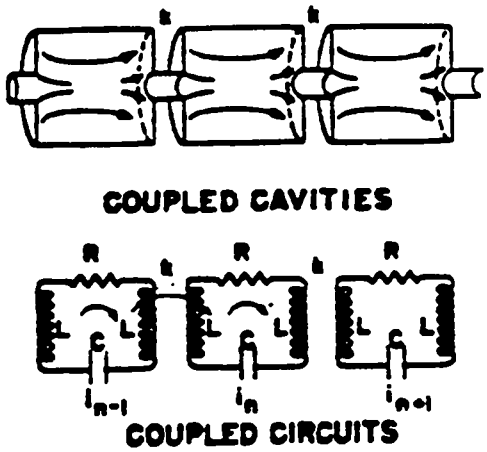

Fig. 4.14. Chains of coupled cavities and coupled circuits.

4.4.3 Coupled Oscillators: Three-Oscillator Example

We will discuss this problem in more detail using the terminology of reference 10. To get a better feeling for the physics before discussing the general problem, we present the results for the chain of three coupled oscillators, as shown in Figure 4.15.

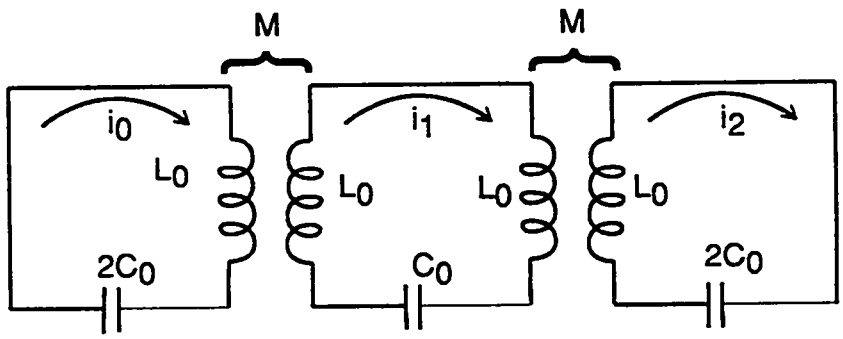

Fig. 4.15. Three coupled oscillators.

This three-oscillator system consists of one central oscillator with mutual inductances on each side for coupling to each of the end cells. The end oscillators have only half the inductance of the middle oscillator, but have twice the capacitance to give equal resonant frequencies. The end oscillators are called half cells. (In an accelerator they would correspond to half-length cells with conducting planes inserted at the center plane of symmetry.) The circuit equations may be written, by summing the voltages around each circuit, as

$$x_0\left[1-\frac{\omega_0^2}{\Omega^2}\right]+x_0k=0,\ \text{oscillator}\ n=0,$$

$$x_1\left[1-\frac{\omega_0^2}{\Omega^2}\right]+(x_0+x_2)\frac{k}{2}=0,\ \text{oscillator}\ n=1,$$

$$x_2\left[1-\frac{\omega_0^2}{\Omega^2}\right]+x_1k=0,\ \text{oscillator}\ n=2.$$

The normalized currents are $x_n = i_n\sqrt{2L_0}$, k is the coupling constant, ω_0 is the resonant frequency of the individual (uncoupled) oscillators, and Ω is the frequency of a normal mode. The details of the solution of the eigenvalue problem can be found in refererence 11. The circuit equations can be put into matrix form and can be written as

$$LX_q=\frac{1}{\Omega_q^2}X_q,$$

where L is the matrix operator, a function of the cavity frequency and the coupling constant k; X_q is the eigenvector whose elements are the currents or fields x_n; and $1/\Omega_q^2$ is the eigenvalue. For the case with no power losses, the three normal-mode eigenfrequencies Ω and the normalized eigenvectors X_n (whose components are the x_n) in order of increasing mode frequency are as follows.

(a) *Mode 0* (called the 0 mode because all oscillators have zero relative phase difference).

$$\Omega_0=\frac{\omega_0}{\sqrt{1+k}},\qquad X_0=\begin{bmatrix}1\\1\\1\end{bmatrix},$$

where the elements of the normalized eigenvector give the relative fields in each oscillator.

(b) *Mode 1* (the $\pi/2$ mode)

$$\Omega_1=\omega_0,\qquad X_0=\begin{bmatrix}1\\0\\-1\end{bmatrix}$$

(c) *Mode 2* (called the π mode, and has the highest frequency).

$$\Omega_2 = \frac{\omega_0}{\sqrt{1-k}}, \quad \text{and} \quad x_2 = \begin{bmatrix} 1 \\ -1 \\ 1 \end{bmatrix}.$$

The bandwidth including these three normal modes is approximately $\delta\omega \approx \omega_0 k$. The eigenvector components for each mode number q can be summarized in the following compact and more general form. For N + 1 coupled oscillators, where in this case N + 1 = 3, we can write (explicitly showing the time dependence) the eigenvector elements in the qth normal mode as

$$X_{q,n} = \cos\frac{\pi q n}{N} e^{j\Omega_q t}, \qquad n = 0,1,2\,(\text{oscillator}), \text{ and } q = 0,1,2\,(\text{mode}).$$

This form describes a standing wave, but it can also be expressed in terms of forward and backward traveling waves as

$$X_{q,n} = \cos\frac{\pi q n}{N} e^{j\Omega_q t} = \frac{e^{j(\Omega_q t - \pi q/N)} + e^{j(\Omega_q t + \pi q/N)}}{2}$$

The quantity $\pi q/N$ is the phase advance of the traveling waves per oscillator, where in this case for three oscillators, N = 2. The eigenfrequencies may be expressed as

$$\Omega_q = \frac{\omega_0}{\sqrt{1 + k\cos(\pi q / N)}}, \qquad q = 0,1,2\,(\text{mode}).$$

Note that the phases of adjacent oscillators in the 0 and π modes either are the same or reverse. The $\pi/2$ mode is different because it has an unexcited oscillator. We will see later that the $\pi/2$ mode has unusual properties that make it very attractive for the operating mode of an accelerating structure.

For coupled accelerator cavities it is important to determine the effects of resonant frequency errors for the individual cavities. To study the effects of frequency errors, perturbation theory can be used. The errors are contained in a perturbation matrix P, which when added to the unperturbed L matrix gives the corrected L matrix. The first-order eigenvector corrections are calculated from the series

$$\Delta X_q = \sum_{q \neq r} a_{qr} X_r,$$

where the X_r are the unperturbed eigenvectors, and the amplitudes are

$$a_{qr} = \frac{[X_q P X_r]}{\frac{1}{\Omega_r^2} - \frac{1}{\Omega_q^2}}$$

This shows that the effect of the errors is to create a new eigenvector, which is approximately the old unperturbed eigenvector, with corrections that come from adding or mixing contributions from all the other unperturbed eigenvectors. The amount by which the other eigenvectors are mixed depends on a matrix element X_q P X_r, and increases as the unperturbed eigenvalues (or

frequencies) become more closely spaced. This is an important result, to which we will return later. If all three frequencies are different, it is convenient to choose the unperturbed frequency ω_0 based on an average over the end cell eigenvalues. We define $\delta\omega_0$ as the frequency error of the end cells relative to ω_0 and $\delta\omega_1$ is the frequency error of the middle cell. Now we show the results through first order in the fractional frequency errors for both the 0 and π modes. For the $\pi/2$ mode, the first-order theory gives a nonzero correction only for the field in the middle oscillator. Therefore, for the $\pi/2$ mode we have carried out the calculations through second order. The results for the three modes, perturbed by oscillator frequency errors are as follows.

(a) *The 0 mode, valid through first order.*

$$\Omega_0 = \frac{\omega_0}{\sqrt{1+k}}\sqrt{1-\delta\omega_1/\omega_0}\ ,$$

$$X_0 = \begin{bmatrix} 1+\dfrac{1+k}{2k}\left\{\dfrac{\delta\omega_1}{\omega_0}-4\dfrac{\delta\omega_0}{\omega_0}\right\} \\ 1-\dfrac{1+k}{2k}\dfrac{\delta\omega_1}{\omega_0} \\ 1+\dfrac{1+k}{2k}\left\{\dfrac{\delta\omega_1}{\omega_0}+4\dfrac{\delta\omega_0}{\omega_0}\right\} \end{bmatrix}.$$

(b) *The $\pi/2$ mode, valid through second order.* (Note that the second-order terms appear in the eigenfrequency and in the first and third elements of the eigenvector.)

$$\Omega_2 = \frac{\omega_0}{\sqrt{1-4(\delta\omega_0/\omega_0)^2}}\ ,$$

$$X_1 = \begin{bmatrix} 1+\dfrac{4}{k^2}\dfrac{\delta\omega_1}{\omega_0}\dfrac{\delta\omega_0}{\omega_0}-\dfrac{2}{k^2}\left(\dfrac{\delta\omega_0}{\omega_0}\right)^2 \\ -\dfrac{2}{k}\dfrac{\delta\omega_0}{\omega_0} \\ -1+\dfrac{4}{k^2}\dfrac{\delta\omega_1}{\omega_0}\dfrac{\delta\omega_0}{\omega_0}+\dfrac{2}{k^2}\left(\dfrac{\delta\omega_0}{\omega_0}\right)^2 \end{bmatrix}.$$

(c) *The π mode, valid through first order.*

$$\Omega_2 = \frac{\omega_0}{\sqrt{1-k}}\sqrt{1-\delta\omega_1/\omega_0} \ ,$$

$$X_2 = \begin{bmatrix} 1-\frac{1-k}{2k}\left\{\frac{\delta\omega_1}{\omega_0}-4\frac{\delta\omega_0}{\omega_0}\right\} \\ -1-\frac{1-k}{2k}\frac{\delta\omega_1}{\omega_0} \\ 1-\frac{1-k}{2k}\left\{\frac{\delta\omega_1}{\omega_0}+4\frac{\delta\omega_0}{\omega_0}\right\} \end{bmatrix} .$$

First we see that, compared with the unperturbed case, the magnitudes of the eigenvector elements have changed but they are all real. If we express the perturbed eigenvectors as

$$X_{q,n} = Ae^{j\phi}\cos\frac{\pi qn}{N}e^{j\Omega_q t} \ ,$$

the $Ae^{j\phi}$ factor corresponds to the ratio of the elements of the perturbed to the unperturbed eigenvectors. The above results show that, for resonant frequency errors, the amplitudes A are generally no longer unity but the phases are still $\phi = 0$.

The presence of first-order corrections to the elements of the eigenvectors for the 0 and π modes shows that the field distributions for these modes are sensitive to resonant frequency errors in the individual oscillators. Such errors result in field nonuniformity, which increases with the fractional error in the frequencies and decreases with increasing coupling strength k. By contrast, the effect of such frequency errors for the $\pi/2$ mode appears as a first-order correction only to the middle (nominally unexcited) oscillator. The errors affect the outer (nominally excited) cells only in second order. Therefore the field in the excited cells in the $\pi/2$ mode is very insensitive to frequency errors. We will describe later how this insensitivity can be used beneficially in accelerator structures.

Next we look at the steady-state solution with oscillator resistive power losses included and we ignore the oscillator frequency errors. Because energy will be dissipated, we need to supply this energy with generators for a steady-state solution. For simplicity, we assume the quality factor Q is the same for all three oscillators. It is useful to consider the case where the only generator is in the end oscillator n = 0. If the driving frequency is a normal-mode frequency, that normal mode will be excited and the fields will be approximately proportional to the corresponding eigenvector elements. We obtain the following results in lowest order for the fields, after normalizing the results to the field in the driven oscillator (n = 0).

(a) *0 mode*

$$X_0 = \begin{bmatrix} 1 \\ \exp\left\{-j\frac{3\sqrt{1+k}}{kQ}\right\} \\ \exp\left\{-j\frac{4\sqrt{1+k}}{kQ}\right\} \end{bmatrix} .$$

(b) *π/2 mode* (second-order term kept for third oscillator.)

$$X_1 = \begin{bmatrix} 1 \\ \frac{1}{kQ}\exp\left\{j\frac{\pi}{2}\right\} \\ -1+\frac{2}{(kQ)^2} \end{bmatrix}$$

(c) *π mode*

$$X_2 = \begin{bmatrix} 1 \\ -\exp\left\{j\frac{3\sqrt{1-k}}{kQ}\right\} \\ \exp\left\{j\frac{4\sqrt{1-k}}{kQ}\right\} \end{bmatrix} .$$

We have expressed the field elements as an amplitude times the phase factor. If we express the perturbed normalized eigenvectors as

$$X_{q,n} = Ae^{j\phi}\cos\frac{\pi qn}{N}e^{j\Omega_q t} ,$$

the $Ae^{j\phi}$ factor corresponds to the ratio of the values with losses to the unperturbed lossless values. The above results show that, when losses are included, the amplitudes A are not changed to lowest order. We see that the losses produce a relative phase shift ϕ between adjacent oscillators in both the 0 and π modes, which increases as the Q decreases and decreases with increasing coupling strength k. This is sometimes called the power flow phase shift, because it is associated with the flow of power per unit stored energy away from the generator through the oscillator chain. In the general case of N+1 oscillators, the power-flow phase shift from the drive point to the oscillator at the end of the chain n cells away is $\Delta\varphi = n^2\sqrt{1-k}/(kQ)$. This phase-shift increases in proportion to the square of the number of oscillators. But in the $\pi/2$ mode, power losses do not produce this phase shift. Instead, they produce an excitation of the middle (nominally unexcited) oscillator that is 90 degrees out phase with the fields in the excited oscillators. There is only a second-order amplitude droop between the two excited oscillators. This is called the power-flow droop and usually is of little consequence. So far we have separated the effect of the frequency errors from that of the power losses. In the general case both effects will occur together. The resulting normalized eigenvector will have the form

$$X_{q,n} = A_{q,n} \cos \frac{\pi q n}{N} e^{j(\Omega_q t + \phi_{q,n})},$$

where, to lowest order, the deviations from unity of the amplitude $A_{q,n}$ increase with the oscillator resonant frequency errors. The power-flow phase shift $\phi_{q,n}$ increases with decreasing Q of the resonators. Both effects decrease with increasing coupling strength k.

In summary, the three-coupled-oscillator problem illustrates the sensitivity of the 0 and π modes to oscillator frequency errors. Such errors produce distortions of the nominally uniform field amplitudes. Power flow along the oscillator chain in the lossy case causes relative phase shifts between adjacent oscillators. We have also seen, for the $\pi/2$ mode, an insensitivity of the field amplitudes and phases for those oscillators that are excited in the unperturbed case.

4.4.4 General Problem of N + 1 Coupled Oscillators

Now that we have looked in some detail at the results for three coupled oscillators, we will summarize the general results for N + 1 coupled oscillators.[12] In the general case there are N - 1 identical internal oscillators each of which is magnetically coupled to two adjacent oscillators, one on each side, and there is a "half" oscillator on each end, for a total of N + 1 coupled oscillators (Fig. 4.16).

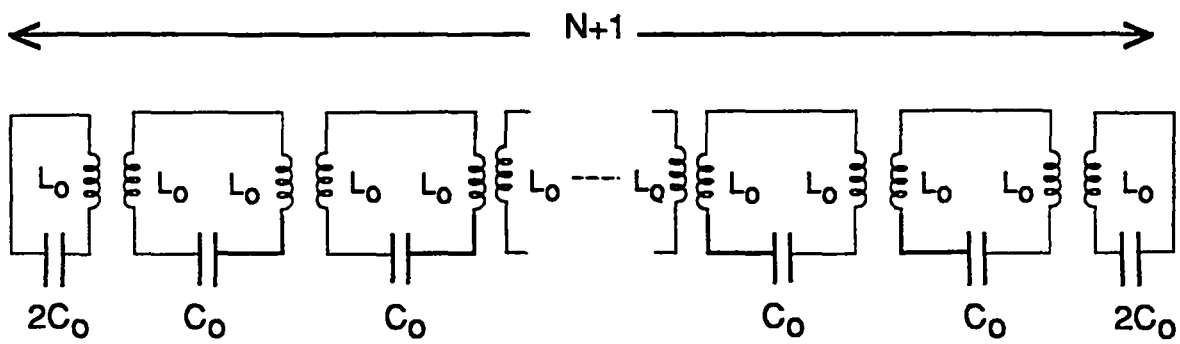

Fig. 4.16. N + 1 coupled oscillators.

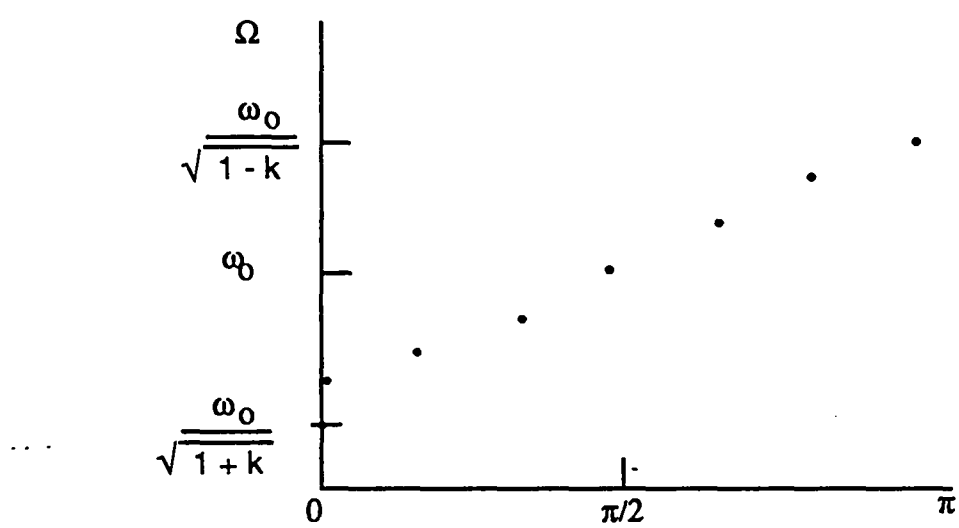

Fig. 4.17. Normal-mode spectrum of coupled oscillator system with seven oscillators.

The eigenvector elements in the qth normal mode are

$$X_{q,n} = \cos\frac{\pi q n}{N} e^{j\Omega_q t}, \qquad \begin{array}{l} n = 0,1,..,N \text{ (oscillator)}, \\ \text{and } q = 0,1,.,N \text{ (normal mode)}. \end{array}$$

The quantity $\pi q/N$ is the phase advance per oscillator of the corresponding traveling waves. The eigenfrequencies may be expressed by the dispersion relation (Ω versus $\pi q/N$) as

$$\Omega_q = \frac{\omega_0}{\sqrt{1 + k\cos(\pi q / N)}}.$$

This relationship is shown in Fig. 4.17. The coupling constant is k, and the resonant frequency of the individual cavities is ω_0. Now there are N + 1 normal modes centered at ω_0. The bandwidth of this family of normal modes may be defined as $\Omega_N - \Omega_0 = \omega_0[(1-k)^{-1/2} - (1+k)^{-1/2}] \cong \omega_0 k$.

As the number of normal modes increases, the bandwidth is fixed at $k\omega_0$, and the modes become more closely spaced. This creates two problems. First, when power losses are included, each normal mode has a width which is approximately $\Delta\omega = \omega / Q$. If the mode width is larger than the spacing to the nearest normal mode, the normal modes will overlap, and the generator will excite both modes rather than only the desired one. Second, as described earlier, perturbations resulting from frequency errors produce corrections to each eigenvector. The corrections are made in perturbation theory by adding some fraction of each of the other unperturbed eigenvectors. The contribution from each mode to this correction depends on the frequency spacing of the modes. For a given set of oscillator errors, modes that are closer together cause larger perturbations to the fields than modes that are farther apart. Therefore, small mode spacings must be avoided. The frequency spacing between the π mode and the next-nearest-mode is small because the π mode is at a point on the dispersion curve where the slope is zero. When $k << 1$ this spacing is

$$\frac{\delta\Omega}{\Omega} = k\left[\frac{\pi}{2N}\right]^2.$$

For the $\pi/2$ mode, however, this spacing is larger (for $N > 2$), and for $k << 1$ the spacing is given by

$$\frac{\delta\Omega}{\Omega} = k\left[\frac{\pi}{2N}\right].$$

This illustrates another advantage of the $\pi/2$ mode, namely, that the mode spacing is greater than for the other normal modes. The advantages described above for three coupled oscillators have nothing to do with the normal mode spacing, but result from the symmetric central position of the $\pi/2$ mode in the mode spectrum. For the $\pi/2$ mode the perturbation-theory contributions from the nearest frequency modes cancel, leaving only second-order terms.

4.4.5 Coupled-Cavity Structures for Accelerators

We have seen that the coupled-cavity system has a spectrum of normal modes, and that the spectrum becomes more closely spaced as the number of cells increases. This can create a problem of controlling the uniformity of the field distribution in the desired mode. This problem becomes more serious when the mode-spacing decreases, because small frequency errors allow the nearby normal modes to exert a large influence on the actual perturbed field distribution.

The coupled oscillator problem, studied above, revealed the following properties of an array of cavities in standing-wave operation in modes other than $\pi/2$ mode. When frequency errors are present, the field distribution is sensitive to these errors. If power is transmitted from the drive point to replace power dissipated in cavity walls or delivered to the beam, there is a (power-flow) phase shift from cell to cell. This phase shift could be compensated by shifting the gap centers, but the shift depends on the beam current (increasing current means decreasing Q), and the compensation would be correct only for a single beam current. These problems may not be serious and the π mode can be used, if the coupling strength k is large enough or the number of cells is small enough. Otherwise the $\pi/2$ mode is usually the best solution.

We have seen that the $\pi/2$ normal mode of a chain of coupled oscillators has unique properties. We can make use of this normal mode if we can devise a suitable geometry, satisfying a synchronous condition for the particles, and resulting in good acceleration efficiency (high shunt impedance). To ensure synchronism in the $\pi/2$ normal mode in a periodic array of cavities, one can choose the cavity lengths so that the spacing between sequential *excited* cavities is $\beta\lambda/2$ (half an rf period). This gives the configuration shown in Figure 4.18a, which contains four equal-length cavities on axis in a space of length $\beta\lambda$. It provides two excited accelerating cells per $\beta\lambda$ as does the π-mode structure, and includes two unexcited cells. However, this configuration does not generally lead to efficient acceleration. With the fields concentrated in only half of the cells for the $\pi/2$ mode, the net power dissipation is larger than that for the π mode, where all cells can contribute to produce the same energy gain.

A better solution has been to make a biperiodic chain, in which the accelerating cavity geometry and lengths are chosen for improved shunt impedance, and the unexcited cavities, also called coupling cavities, have a different shape and are tuned to the same uncoupled resonant frequency. The two most popular geometries have been the on-axis coupled structure (Figure 4.18b), where the coupling cavities occupy a smaller axial space than the accelerating cavities, and the side-coupled cavity (Figure 4.18c), where the coupling cavities are completely removed from the beam line. For both geometries the coupling cavities are usually coupled magnetically to the accelerating cavities. The magnetic coupling is through slots cut in the outer wall. Both solutions retain the unique properties of the $\pi/2$ mode of the periodic cavity chain and provide the flexibility for obtaining the high shunt impedance that is characteristic of the π mode. The biperiodic cavity chain can also be analysed using the coupled-circuit model. This model shows that to recover the $\pi/2$-mode properties, another step is required. To see this, we give the results for a biperiodic array for 2N (coupling) cavities with frequency ω_c, which alternate with 2N +1 accelerating cavities with frequency ω_a. The dispersion relation is

$$k^2 \cos^2 \frac{\pi q}{2N} = \left[1 - \frac{\omega_a^2}{\Omega_q^2}\right]\left[1 - \frac{\omega_c^2}{\Omega_q^2}\right], \quad q = 0,1,\ldots,2N,$$

where k is the coupling constant between the nearest neighbors, and Ω_q is the mode frequency for normal-mode q (see Fig. 4.19). The quantity $\pi q/2N$ is the phase advance per cavity of a traveling wave. The $\pi/2$ normal-mode corresponds to q = N. The dispersion relation for the $\pi/2$ mode has two solutions, $\Omega_q = \omega_a$ and $\Omega_q = \omega_c$. This is clarified by plotting the dispersion relation, where the $\pi/2$ point is seen to have a discontinuity unless $\omega_a = \omega_c$. There are two branches, which are called the lower and upper passbands. Between is the stopband, within which there are no normal-mode solutions. The discontinuity can be removed by tuning all cavities to have the same frequency so that $\omega_a = \omega_c$.

. . .

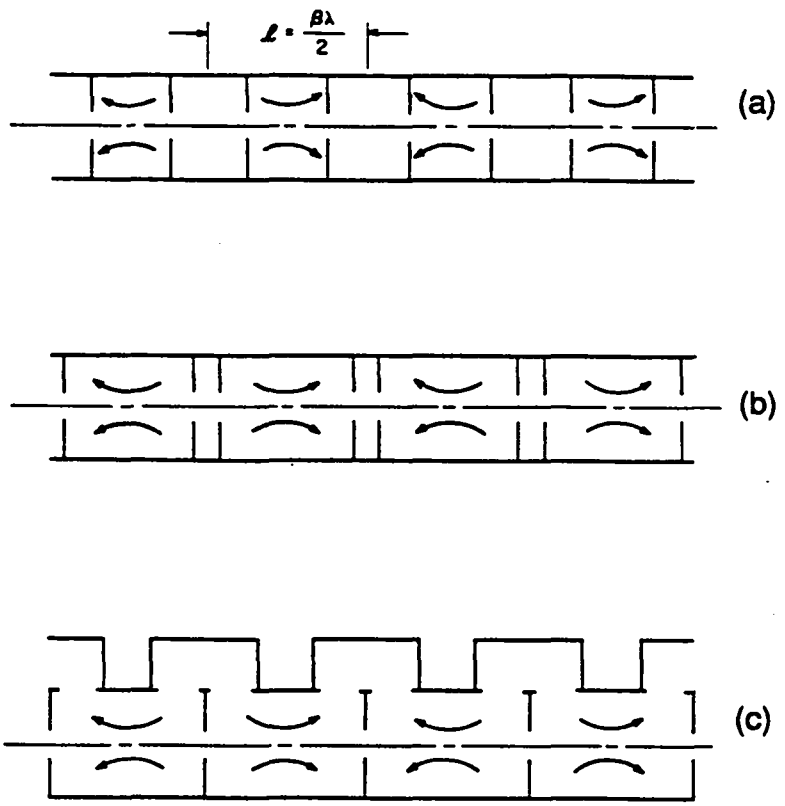

Fig.4.18. $\pi/2$-mode operation of a cavity resonator chain: (a) periodic structure in $\pi/2$ mode, (b) biperiodic on-axis coupled-cavity structure in $\pi/2$ mode, and (c) biperiodic side-coupled cavity in $\pi/2$ mode.

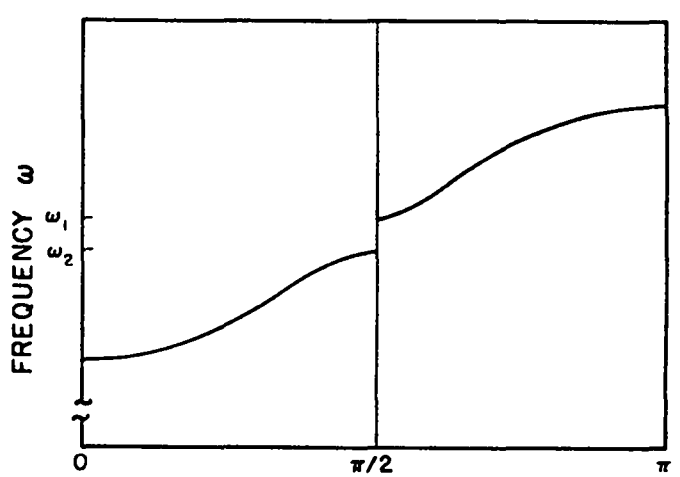

Fig. 4.19. Dispersion curve of biperiodic structure.

After this tuning the two passbands are joined at the $\pi/2$ mode, and the dispersion curve at this point is changed to have a nonzero slope. Again, with no losses and no frequency perturbations, there are excited cells separated by unexcited cells just as for the case of a $\pi/2$ mode in a periodic array. We number the even cavities or excited cavities 2n, and the odd or unexcited cavities 2n+1,

where n = 0, 1, 2, . . ., etc. The quality factor for the excited (accelerating) cavities is Q_a and for the unexcited (coupling) cavities it is Q_c. The total number of cavities is odd, and the end boundary conditions are defined by half-cell accelerating cavities.

We now state the general results for power-flow phase shift and power-flow droop. We assume that the drive is located in cavity 2m and that the results will be valid for coupling cells with $n < m$ and for accelerating cells with $n \leq m$. Thus the index n begins at an end cell, where n = 0, and advances the drive cell located at 2n = 2m.

The frequency difference between the coupling and accelerating cavities, $\delta\omega = \omega_c - \omega_a$, is also the width of the stopband in this approximation. The field in accelerating cavity 2n is given (to second order) relative to the field X_{2m} in the drive cavity (also an accelerating cavity) as

$$X_{2n} \cong (-1)^{n-m} X_{2m} \left[1 - \frac{2(m^2 - n^2)}{k^2 Q_a Q_c} + j \frac{4(m^2 - n^2)}{k^2 Q_a} \frac{\delta\omega}{\omega_a} \right].$$

The second and third terms in the bracket are power-flow correction terms and are both of second order. The second is called the power-flow droop and the third is the power-flow phase shift. Both vary quadratically with n as n decreases from the drive point. The result may also be written as

$$X_{2n} \cong (-1)^{n-m} X_{2m} \left[1 - \frac{2(m^2 - n^2)}{k^2 Q_a Q_c} \right] \exp\left[j \frac{4(m^2 - n^2)}{k^2 Q_a} \frac{\delta\omega}{\omega_a} \right].$$

When the structure is tuned to close the stop band $\delta\omega = 0$, and the power flow-phase shift vanishes. The amplitude of the accelerating cells is largest at the drive cell, where n = m, and is smallest at the end cell n = 0.

The field in coupling cavity 2n+1 has a first-order term which is

$$X_{2n+1} \cong (-1)^{n-m} X_{2m} \left[j \frac{2n+1}{kQ_a} \right],$$

or

$$X_{2n+1} \cong (-1)^{n-m} X_{2m} \left[\frac{2n+1}{kQ_a} \right] \exp(j\pi/2).$$

The amplitude of the coupling cells is largest at the coupling cell adjacent to the drive cell (n = m − 1) and smallest at the end cell (n = 0). Note that to first order Q_c does not affect the coupling-cell amplitude.

The application of the formulas we have presented is sometimes confusing because of the cavity numbering. We will present an example that is intended to clarify the notation. Consider a 9-cell structure with 5 accelerating cells and 4 coupling cells. The end cells are numbered 2n = 0 and 2n = 8. If the drive cell is the middle cell, it is numbered 2m = 4, or m = 2. The results above are valid for cells 0 through 4, or n = 0, n = 1, and n = m = 2. The fields are symmetric with respect to the drive cell in this case, but in general, to get the results for cells with n > m, one can renumber the cells to count from the other end towards the drive point and then apply the formulas for these cells, using the new numbering.

The general approach of designing standing-wave accelerating tanks by using nonexcited oscillators as coupling elements for field stabilization is called resonant coupling. We have seen how this can take the form of $\pi/2$-mode operation in periodic and biperiodic cavity chains. It is also used for stabilization of the fields in the drift-tube linac (DTL), where the resonant coupling elements are the $\lambda/4$ posts called post couplers. The DTL is usually described as a 0-mode coupled-

cavity chain, with cells that are resonantly coupled by the posts. Even without the posts, the cells are strongly coupled because of the open geometry.

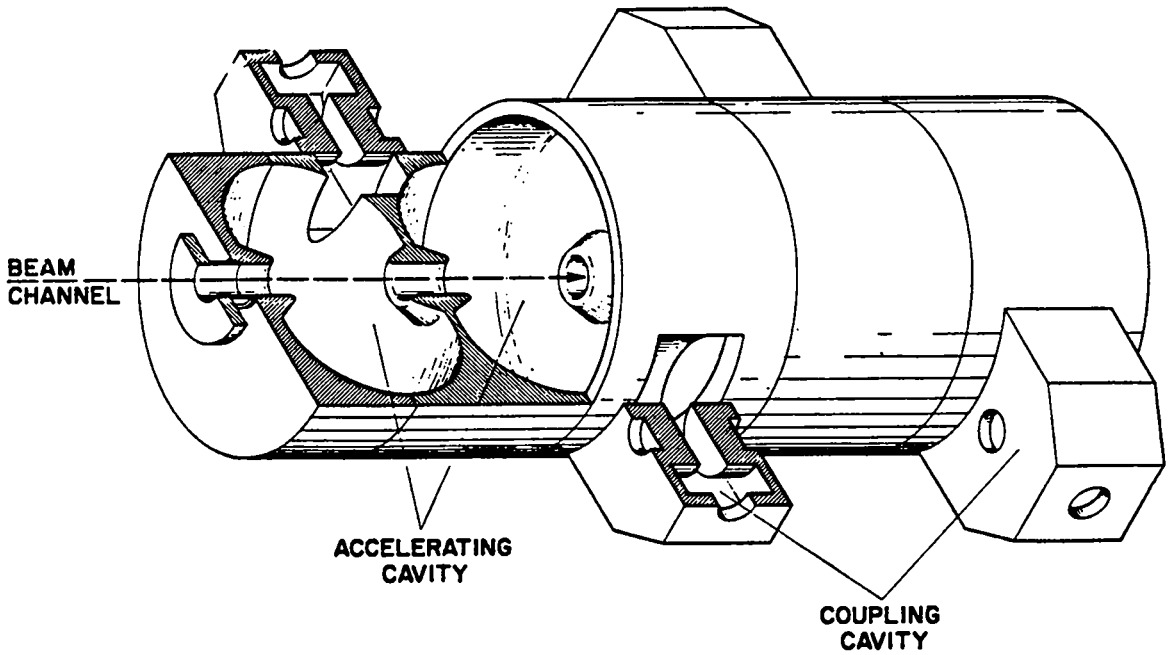

Fig. 4.20. The side-coupled structure at the Los Alamos LAMPF proton linac.

4.4.6 Design of Coupled-Cavity Linacs

The basic accelerating unit of the CCL is the multicell tank, usually consisting of identical accelerating cells and identical coupling cells. The side-coupled structure at Los Alamos is shown in Fig. 4.20. The simplification of identical length cells is possible because the velocity change in a high-beam-velocity CCL tank is much smaller than in a DTL, which generally accelerates lower velocity particles. The end cavities are not built as half cells, even though in our treatment it is convenient to model them this way. To build a cavity as a half cell, it would be necessary to place a conducting plane at the center of the cavity to provide a perfect reflecting symmetry. But a real accelerator cavity needs a beam aperture, which would destroy the perfect symmetry, and means that special tuning would be still required for this cell. Consequently, there is no real advantage in using half cells. In practice full cells are used at each end. These cells are different because they couple to a coupling cavity only on one side, and must be designed and tuned for the correct frequency.

The cell lengths are equal to $\beta_d\lambda/2$, where β_d represents an average design velocity for the beam in that tank. The cell design is then somewhat different from that for a DTL. With constant-length cells, the synchronous phase must be $\phi_s = -\pi/2$, which corresponds to no acceleration for the true synchronous particle and no increase in cell lengths. However, the design particle is injected at a specific phase near the crest of the wave. The design-particle injection phase is chosen so that the phase of the design particle advances to a maximum positive value in the first half of the tank and then decreases back to its initial (injection) value in the second half. In practice the phase changes are usually rather small within a tank, and the design particle is usually called the synchronous particle even though, strictly speaking, it is not. For relativistic electrons the value of β_d can be set to unity. The effect of phase oscillations is often negligable. Of course in the lowest velocity tank, where the electrons are not fully relativistic, phase motion will occur. We will discuss the beam dynamics in more detail in the next chapter.

The length choice for the CCL tanks results from a compromise among several factors. For protons the requirement for focusing usually sets a limit on the tank length, because a focusing element must be placed at the end of a tank and the spacing of focusing elements can affect the overall focusing strength. Two tanks can still be coupled together by means of a specially excited cavity called a bridge coupler, which is located off the beam line to make room for the quadrupole. The bridge cavity is usually magnetically coupled to the end cells of the two adjacent tanks. A combination of separate tanks coupled together by the bridge couplers and driven by one rf generator is usually called an rf module. One other consideration in setting the length of a multitank module is that the power-flow droop effect in the $\pi/2$ mode must not significantly affect the field distribution.

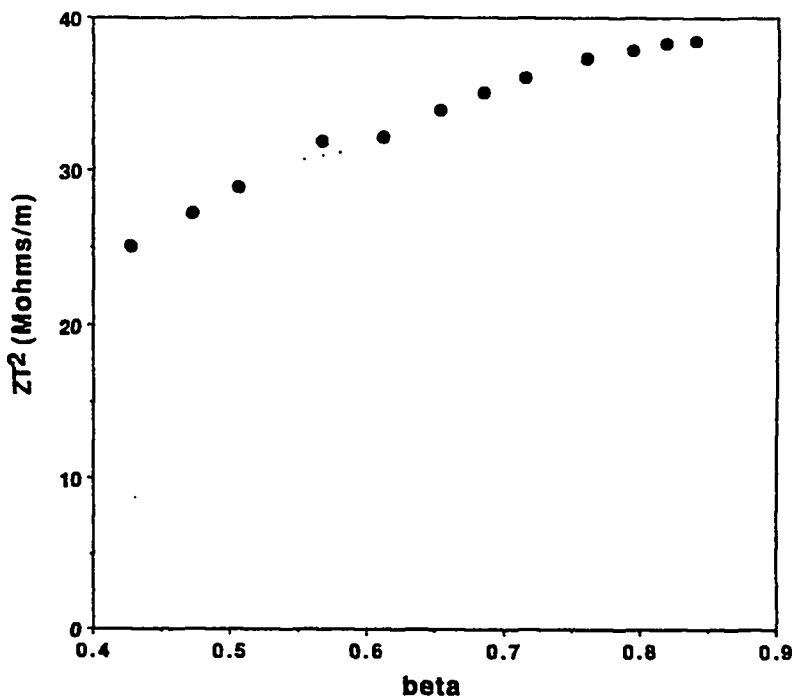

Fig. 4.21. Effective shunt impedance for the LAMPF side-coupled linac as a function of velocity.

4.4.7 Relative Merits of Coupled-Cavity Linacs

A CCL cell is only half as long as a DTL cell at the same velocity, and therefore for the same diameter has about half the inductance. The capacitance must be twice as large, which means the gap spacing is reduced (especially since the CCL nose cones are usually not as large as the DTL drift tubes). The smaller gap is beneficial because it raises the transit-time factor. This must be weighed against another property: unlike DTL cells, CCL cells have end walls, on which additional power is dissipated. The effective shunt impedance increases as a function of β, as shown in Figure 4.21. For low velocities the wall-power-loss effect favors the more open DTL structure, whereas at higher velocities the transit-time factor effect favors the CCL. In proton linacs the transition between these two regimes occurs near 100 MeV, which is the transition energy for the LAMPF proton linac.

4.5 Radiofrequency Quadrupole Linac

4.5.1 Introduction

The radiofrequency quadrupole (RFQ) accelerator is a new type of linear accelerator that is

especially suited to the acceleration of low-velocity ion beams. Properly designed RFQ accelerators can be used alone to accelerate high-current, low-emittance beams, or they can be designed to inject such beams into other types of accelerators, such as a DTL or a synchrotron. A high-energy ion accelerator system uses several types of accelerating structures. However, all high-energy beams start at low-velocity, and the low-velocity genesis of the beam is an important factor for overall accelerator performance. The popularity of the RFQ accelerator is a result of its special capability in this low-velocity region.

To introduce the ideas that led to the RFQ accelerator, we first discuss the nature of the problems of accelerating low-velocity ion beams. An essential feature of all ion linacs is the use of phase focusing. If an ion bunch traverses an accelerating gap while the voltage is rising, the particles at the tail of the bunch, which traverse the gap later, will receive a higher energy gain than the earlier particles at the head of the bunch. In this way the bunched character of the beam is maintained, and the longitudinal effects of space-charge repulsion are counteracted. However, the use of phase focusing inherently produces transverse defocusing forces that must be counteracted by extrinsic means. These so-called rf defocusing forces are stronger for low-velocity particles.

Furthermore, the transverse space-charge repulsion must be overcome, if high-intensity beams are to be accelerated. For high-current beams, nonlinear space-charge forces will rapidly and irreversibly cause transverse-emittance growth unless strong counteracting focusing forces are applied. If a DTL is used for the first linac structure, where the focusing is provided by magnetic quadrupoles installed in the drift tubes, the mechanical requirements establish a minimum cell length, which implies a minimum injection energy between about 0.5 and 1 MeV for protons. Prior to the introduction of the RFQ, the beam was accelerated to this energy by a dc Cockcroft-Walton injector, and was bunched by a system of properly phased rf cavities. This bunching increased the instantaneous current, which produced an even higher focusing requirement at the DTL input, where high focusing strength is especially difficult to obtain. The RFQ accelerator was developed to address these low-velocity problems.

Many of the problems are traceable to the use of the velocity-proportional magnetic force for transverse focusing of the beam. Use of the velocity-independent electric force is an attractive alternative, and one possibility is to use the rf electric fields for focusing. Several earlier concepts were proposed, but the RFQ accelerator in its modern form was proposed by Kapchinskiy and Teplyakov[13] in 1969. They proposed the shaping of four poles to introduce longitudinal accelerating fields while retaining inherent transverse electric-quadrupole fields for focusing. Figure 4.22 shows an RFQ accelerator based on a four-vane rf resonator. The pole-tip modulations that produce the accelerating fields are shown. If the amplitude of these modulations is increased to raise the accelerating fields, the focusing fields are decreased but the quadrupole purity of the focusing is retained.

Figure 4.23 shows a short section of an RFQ accelerator that uses the four-vane cavity resonator to excite the poles. Radiofrequency currents flow radially in the four quadrants resulting in + − + − polarities on the poles at a given time, which thus produces a quadrupole focusing or defocusing force in a given transverse plane. One-half cycle later, the forces reverse sign to produce an overall focusing effect. The focusing force at a given time is spatially continuous along the z axis. If the pole tips have constant radius, only a velocity-independent focusing force is produced. In Figure 4.23 the pole tips have a sinusoidal-like radius variation, with the x-plane variations shifted in z by one-half period from those of the y plane. This pole-tip modulation produces longitudinal electric fields in addition to the transverse focusing fields.

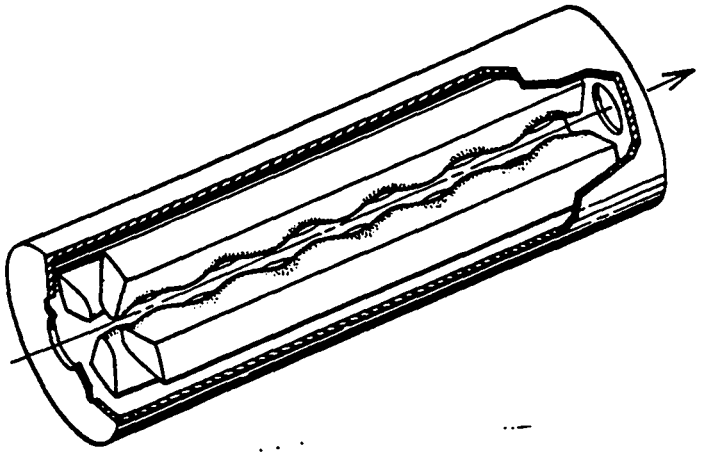

Fig. 4.22. Schematic drawing of an RFQ accelerator section. The four poles are excited with quadrupole-mode rf voltages to focus the beam. The pole-tip shape is modulated to produce longitudinal electric fields that accelerate low-velocity ions.

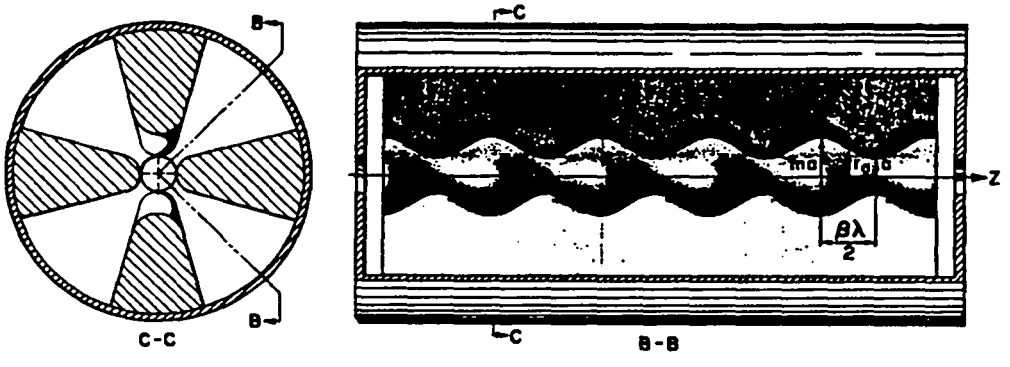

Fig. 4.23. Two schematic views of an RFQ accelerator element. The unit cell of length $\beta_s\lambda/2$ is shown along with the minimum radius a, the maximum radius ma, and r_0 defined later in the text.

4.5.2 Potential Function and Electric Field

The pole-tip geometry and the beam dynamics analysis for the RFQ accelerator are easily understood by using an analytic formulation for the rf electric fields. The electric fields are concentrated in the small volume near the four pole tips, whose dimensions are much smaller than the rf wavelength; to a good approximation, the spatial dependence of the electric field is determined as a solution of Laplace's equation with quadrupolar boundary conditions. The general solution in cylindrical coordinates for an idealized periodic RFQ structure can be expressed as an infinite Fourier-Bessel series. The analysis is greatly simplified by choosing the pole-tip geometry so that only the two lowest-order terms are significant. Then the potential function is written in cylindrical coordinates (r,ψ,z) and as a function of time t as follows:

$$U = \frac{V}{2}\left[X\left(\frac{r}{a}\right)^2 \cos 2\Psi + AI_0(kr)\cos kz\right]\sin(\omega t + \phi),$$

where V is the peak value for the time-varying potential difference between adjacent pole tips, a is

the minimum aperture radius in the cell, and ω is the angular frequency of the rf fields. If we choose $t = 0$ when a particular particle is at the beginning of the unit cell, then ϕ (called the particle phase) is the corresponding phase of the field at that time. The quantity $I_0(kr)$ is the Modified-Bessel function of order zero, and $k = 2\pi/\beta_S\lambda$, where β_S is the ratio of the velocity of the synchronous particle to the speed of light, and λ is the rf wavelength. The quantities A and X are called the acceleration and focusing efficiencies and are given by

$$A = \frac{m^2 - 1}{m^2 I_0(ka) + I_0(mka)} \ , \ X = 1 - A I_0(ka) \ ,$$

where $m \geq 1$ is the modulation parameter shown in Figure 4.23. From the gradient of the potential, the standing-wave electric field components are obtained:

$$E_r = -\frac{XV}{a^2} r \cos 2\psi - \frac{kAV}{2} I_1(kr) \cos kz \ ,$$

$$E_\psi = \frac{XV}{a^2} r \sin 2\psi \ , \ E_z = \frac{kAV}{2} I_0(kr) \sin kz \ ,$$

each multiplied by $\sin(\omega t + \phi)$. When $m = 1$, the acceleration efficiency $A = 0$, the focusing efficiency $X = 1$, and the RFQ becomes a pure electric-quadrupole transport channel with transverse electric-field components only, with field lines as shown in Figure 4.24. As m increases, A increases and X decreases, and a longitudinal electric-field component is produced (see Fig. 4.25).

The electric-quadrupole strength, which is represented by the terms in the expressions for the field that contain the focusing efficiency X, does not depend on z and varies sinusoidally in time. One can maintain the same quadrupole focusing strength in every unit cell by varying the parameters such that XV/a^2 is held fixed. The second term in the expression for E_r is the rf-defocus field that gives radial defocusing for a negative phase angle ϕ in the range $-90°$ to $0°$, where acceleration and longitudinal focusing are simultaneously obtained. The dynamics without space charge can be analyzed, and overall stability of the transverse particle motion is obtained for parameter values within definite limits. In the approximation that the velocity change over the unit cell can be ignored, the energy gain for a particle with velocity β can be calculated by replacing $t = z/\beta c$ and integrating the expression for E_z over the unit cell. For the on-axis synchronous particle with charge q, the energy gain is $\Delta W_S = qE_0 T \ell \cos \phi_S$, where $E_0 = 2AV/\beta_S\lambda$ is the space-average longitudinal field on axis, $T = \pi/4$ is the transit-time factor, $\ell = \beta_S\lambda/2$ is the cell length, and ϕ_S is the phase of the synchronous particle (phase of the field at $t = 0$). In addition, it can be shown that stable longitudinal motion can be obtained for nonsynchronous particles, just as in a conventional linac. Acceleration occurs for all particles contained within a phase-stable bucket, defined in longitudinal phase space by a separatrix trajectory.

Ideally, pole-tip geometries are derived from the $\pm V/2$ isopotential surfaces of the potential function. The transverse cross sections are approximate hyperbolae; at $z = \beta_S\lambda/4$, half way through the unit cell, the RFQ has exact quadrupolar symmetry, and the x and y pole tips have a radius equal to $r_0 = aX^{-1/2}$. In practice, the vane-tip contours must deviate from the ideal shape to control the peak surface electric field and for ease in machining. The properties of different pole-tip geometries have been calculated numerically including pole tips with (a) circular cross section with the same transverse radius of curvature throughout the cell, proportional to r_0, and (b) sinusoidal longitudinal profiles. Pole tips with constant transverse radius of curvature offer advantages of reduced peak surface electric field and capacitance independent of longitudinal position, a property

that is beneficial for tuning the RFQ cavity. For a circular transverse pole-tip geometry with no longitudinal modulations, the peak surface electric field occurs not at the pole tip but at the point where the poles have minimum separation. The field at the pole tip is V/r_0, and the peak surface electric field $E_S = \alpha V/r_0$, where $\alpha = 1.36$ for unmodulated vane-tips, when the vane-tip radius of curvature is equal to r_0. For modulated poles, the value of α is modified by the values of both the transverse and longitudinal radii of curvature.

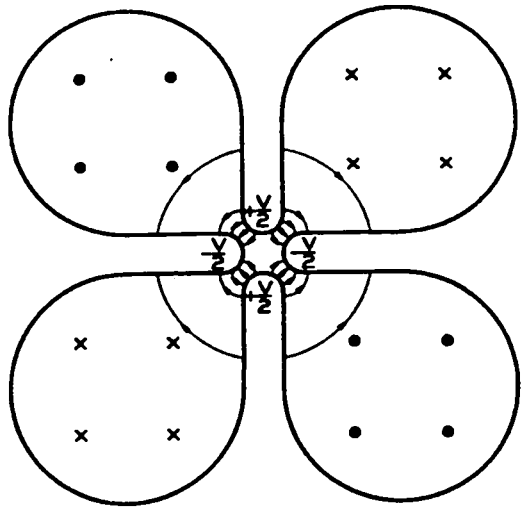

Fig. 4.24. Field lines in a four-vane RFQ cavity with unmodulated pole tips. The electric field lines lie in the transverse plane, and the magnetic field is in the longitudinal direction.

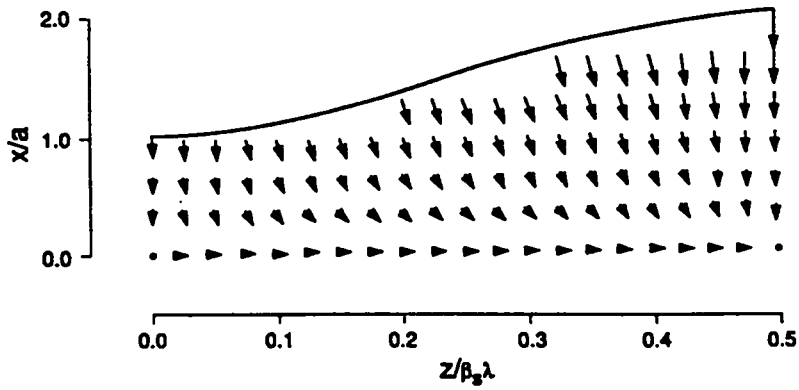

Fig. 4.25. Electric field vectors in the x-z plane ($\psi = 0$) for an RFQ unit cell with $a/\beta_s\lambda = 0.1$ and m=2. This shows how pole-tip modulation creates a longitudinal electric field component.

For a low-velocity linac like the RFQ, adiabatic bunching of the beam becomes a practical design option. This allows a dc beam to be introduced into the RFQ and to be bunched over many spatial periods, while the beam is contained transversely by the electric-quadrupole forces. At first, the rate of energy gain is low, but it gradually increases during the bunching operation and reaches a final value of typically a few MeV per nucleon per meter. In this way, the bunching forces can be programmed in a manner that holds the average bunch length constant. Adiabatic bunching allows a very large fraction of the RFQ input dc beam to be captured and converted into stable bunches that can be accelerated to the final energy without excessive emittance growth. Also, the adiabatic bunching delays the bottleneck for beam-current limit to the end of the buncher, where typically the beam energy has been increased by a factor of 5 to 10. These effects contribute to the high-current capability of the RFQ accelerator. The low emittance growth, resulting from the strong focusing,

together with the high-current capacity combine to produce high-brightness beams. Adiabatic bunching at higher ion velocities is too costly in the length of the accelerator required. Having solved the low-velocity focusing problem, adiabatic bunching can be used in the low-velocity range, which reduces the length requirements.

One possible solution for adiabatic bunching was proposed by Kapchinskiy and Teplyakov,[13] called the "gentle buncher". In their method, the longitudinal small-oscillation angular frequency at zero current and the spatial length of the separatrix are held constant. These constraints result approximately in an invariant longitudinal charge-density distribution and fixed bunch length, while accelerating and bunching in phase (time). This procedure is intended to reduce those space-charge effects, such as transverse emittance growth, that are correlated with longitudinal compression of the beam bunch. To obtain high capture efficiency, without an unacceptably long RFQ, one can introduce an initial bunching section, called a shaper, with values of A and ϕ_s that vary linearly along the RFQ, at the expense of some emittance growth associated with beam compression. This procedure results in a two-stage buncher, where the relative lengths of the two sections are chosen to achieve the best balance between beam emittance and transmission requirements versus length and rf power losses. The beam bunch usually reaches its minimum phase extent at the end of the gentle buncher. If r_0 is held constant, which keeps the capacitance independent of longitudinal position for easier cavity tuning, the aperture a will decrease as m increases along the RFQ. For these reasons, the space-charge and acceptance limits typically do not occur for the dc beam at the input but, instead, at the end of the gentle buncher. After bunching in phase, an accelerator section can be added that maintains a relatively high value of A at small $|\phi_s|$.

The remaining problem of radially matching the time-independent input beam into the varying acceptance associated with the time-dependent focusing fields in the RFQ requires an input radial matching section. The present solution is to taper the poles at the input to the RFQ so that the focusing strength changes from almost zero to its full value over a distance of several focusing periods. A particular time-independent set of ellipse parameters at the input to the radial matching section, which depends on the beam current, provides a good match for all phases. Quadrupole symmetry is maintained throughout this section (no pole-tip modulation). A typical RFQ pole-tip shape is shown in Fig. 4.26.

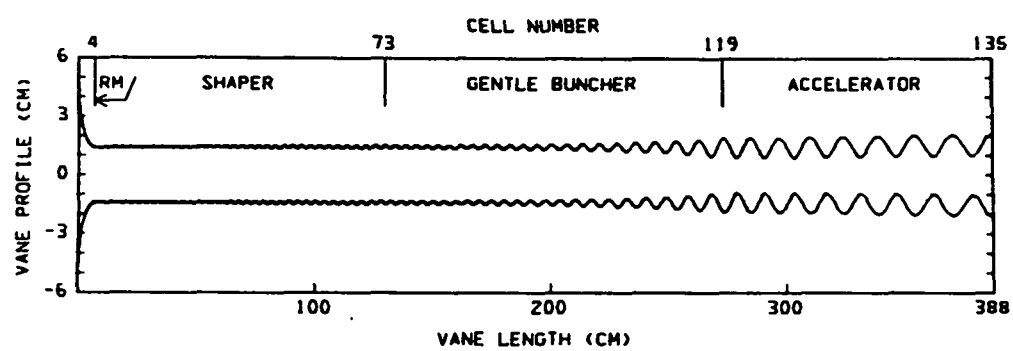

Fig. 4.26. Pole-tip shape in the x-z plane of an RFQ. The extent of the radial matching (RM) section, the shaper, the gentle buncher, and the acceleration sections are shown.

A computer program called PARMTEQ (Phase and Radial Motion in Transverse Electric Quadrupoles) is used to analyze the beam dynamics of the RFQ linac. PARMTEQ generates an RFQ linac and an input particle distribution, and performs beam dynamics calculations through the RFQ including the space-charge forces, using a particle-in-cell method.

In a practical RFQ accelerator, a method must be found for exciting the four poles to produce the desired standing-wave electric field distribution. RFQ accelerators have been built using a variety of resonant cavities. The four-vane structure, described earlier, has been the most popular, and is best suited for the higher frequencies, above about 150 MHz.

4.6 Traveling-Wave Linacs

4.6.1 Overview

We will describe the usual accelerating system for a traveling-wave linear accelerator for relativistic electrons. This accelerating structure is the disk-loaded or iris-loaded waveguide, which consists of a periodic array of cells as shown in Fig. 4.27. The apertures allow for the passage of both the beam and the traveling electromagnetic wave. The mechanism by which the disks reduce the phase velocity to that of the particles is interference of the waves reflected from the disks. Each disk produces reflections of any incident wave. The interference between the incident and all the reflected waves produces a resultant wave with a new phase velocity. The most useful practical tool for analysis of the physics is the dispersion or Brillouin diagram (plot of ω versus $k = n\pi/d$, where d is the period). Without periodic loading by the disks, the dispersion curve has the shape of a hyperbola, (Fig. 4.28) and the phase velocity, $v_p = \omega/k$, is always greater than the speed of light.

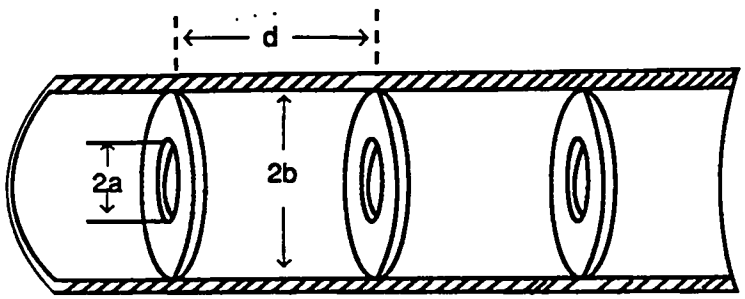

Fig. 4.27. Iris(disk)-loaded traveling-wave structure.

With periodic loading the curve is modified in the following way. As k moves away from zero, the curve initially follows the hyperbola corresponding to the uniform guide. As k increases further, it flattens out and approaches zero slope (zero group velocity) at $k = \pi/d$. Every point on the dispersion curve for the periodic structure lies below the curve for the uniform guide (Fig. 4.29), which implies a smaller phase velocity. Because electron velocities are so near the speed of light, the structure can be designed to have a phase velocity equal to the speed of light. An interesting result of this choice is that the guide wavelength becomes equal to the free-space wavelength, and the radial wavenumber for the synchronous ($n = 0$) wave becomes $K_0 = 0$. This means that the accelerating field becomes independent of radial position within the beam aperture.

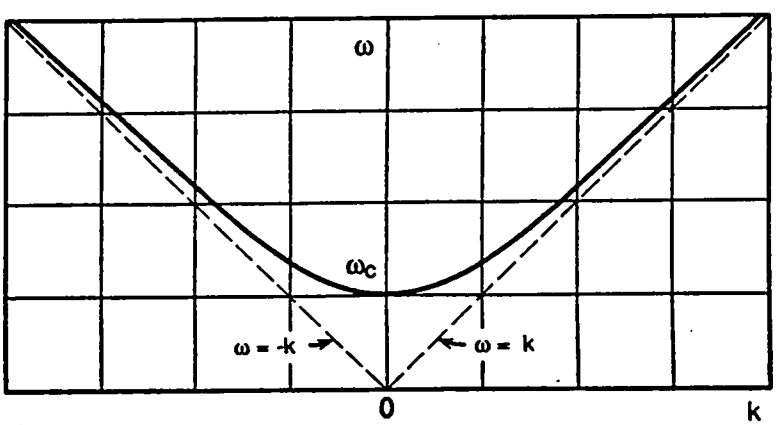

Fig. 4.28. Dispersion curve for a uniform waveguide.

The rf energy is input at equally spaced intervals along the accelerator and flows along the beam direction. The energy is attenuated by the losses on the walls and by the beam loading. At the end of the section the energy is delivered to an external load.

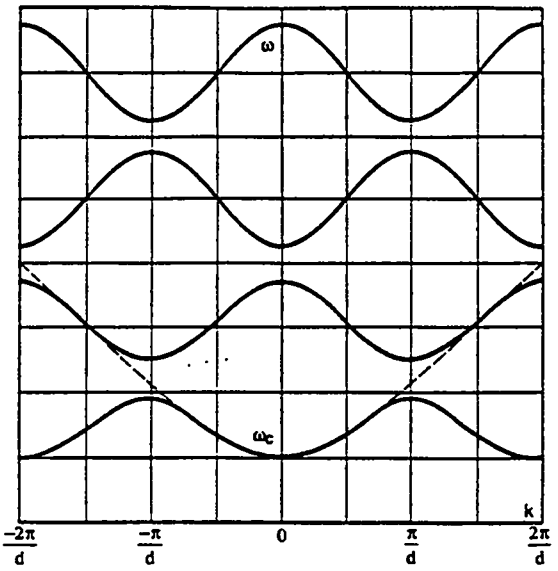

Fig. 4.29. Dispersion curve for a periodically loaded waveguide.

We will now discuss how the structure parameters can be chosen to achieve the design objectives. The frequency choice involves many considerations. A particularly relevant figure of merit for a traveling-wave accelerator is the ratio of the squared accelerating field divided by the stored energy per unit length. This ratio is of interest because the traveling-wave accelerator accelerates the beam in proportion to the accelerating field, after which most of the stored energy is delivered to and dissipated in a load. The ratio scales with frequency as ω^2. There are many other issues that affect the frequency choice (discussed in detail by Neal[14]), including power efficiency, maximum electric field strength, beam-current limit, and the number of power sources and feeds required, The choice at SLAC and many other traveling-wave linacs has been 2.856 GHz.

The disk thickness is not a critical parameter, and is chosen large enough for good mechanical strength and good tolerance for electrical breakdown. The disk separation is chosen for maximum shunt impedance per unit length. If the disks are too far apart, the amplitude of the synchronous harmonic is reduced relative to the other harmonics. If they are too close, the power loss on the disks becomes significant. The radius b of the waveguide and the aperture radius a determine the phase velocity of the synchronous wave. The radius a also determines the rate of energy flow and the group velocity, which is a very important parameter affecting the energy attenuation rate and the power efficiency. There is an optimum group velocity; its selection is described below. After a is selected, the value of b can be chosen to obtain the correct phase velocity.

To discuss the selection of the group velocity, we introduce some important relationships between the accelerating field amplitude E_a for the traveling wave, the stored energy per unit length U, and the energy flow P_w in the TM_{01} wave. The energy flow is obtained by integrating the Poynting vector over the aperture, and is

$$P_w = \int_0^a E_r H_\theta 2\pi r\, dr ,$$

where a is the radial aperture. The resistive power loss per unit length is $-dP_w/dz$. The quality factor is

where a is the radial aperture. The resistive power loss per unit length is $-dP_w/dz$. The quality factor is

$$Q = \frac{\omega U}{-dP_w / dz} .$$

The shunt impedance per unit length is

$$r_L = \frac{E_a^2}{-dP_w / dz} .$$

This quantity was called ZT^2 in our previous discussion. The group velocity is the velocity at which a modulation of the wave amplitude propagates, and is given by the slope of the dispersion curve. It can be shown that it is also the energy-flow velocity for a medium with normal dispersion, where the phase velocity increases with increasing frequency. Then we may write

$$P_w = v_g U .$$

Eliminating U from the equation for Q yields a differential equation for energy flow

$$\frac{dP_w}{dz} = -\frac{\omega P_w}{Q v_g} .$$

We define the attenuation per unit length as $\alpha_0 = \omega / 2Qv_g$.

Then $dP_w / dz = -2\alpha_0 P_w$.

4.6.2 Constant-Impedance Structure

We consider a structure whose parameters are uniform, independent of z. The relation between E_a and P_w can be expressed by eliminating dP_w/dz from the equations for Q and r_L. This yields

$$E_a^2 = \frac{\omega r_L}{Q v_g} P_w .$$

Since the energy flow is proportional to the square of the field, substituting into the differential equation for P_w gives

$$\frac{dE_a}{dz} = -\frac{\omega E_a}{2Q v_g} = -\alpha_0 E_a .$$

For a structure in which α_0 is uniform, the differential equations have an exponential decay solution. .

$$E_a(z) = E_0 e^{-\alpha_0 z} , \; P_w(z) = P_0 e^{-2\alpha_0 z} .$$

At the end of the section of length L, we have

At the end of the section of length L, we have

$$E_a(L) = E_0 e^{-\tau_0} \ , \ P_w(L) = P_0 e^{-2\tau_0} \ ,$$

where

$$\tau_0 = \alpha_0 L = \frac{\omega L}{2Qv_g}$$

is the attenuation of the section. The energy gain of a synchronous particle riding at the crest of the wave is

$$\Delta W = q\int_0^L E_a(z)dz \ \text{ or } \ \Delta W = qE_0 L \frac{\left(1-e^{-\tau_0}\right)}{\tau_0} \ .$$

Now use the relation between the input power and field

$$E_0^2 = 2r_L \alpha_0 P_0 \ ,$$

to obtain the result $\Delta W = q\sqrt{2r_L P_0 L}\dfrac{\left(1-e^{-\tau_0}\right)}{\sqrt{\tau_0}}$.

How can the energy gain over a given section of length L and for a given input power be maximized? Clearly, the shunt impedance per unit length must be maximized. Also τ_0 should be chosen to give a maximum ΔW. The maximum occurs when

$$\tau_0 = \omega L / 2Qv_g = 1.26 \ .$$

If L is fixed and Q is known, this result determines the optimum group velocity. If v_g is too small, the attenuation of the wave is too great, and if v_g is too large, the initial accelerating field for a given input power is too small. How can the group velocity be controlled? The answer is by adjusting the radial aperture a. For the TM_{01} mode near the axis, the fields E_r and H_θ are proportional to r, and

$$P_w = \int_0^a E_r H_\theta 2\pi r\, dr \propto a^4 \ .$$

The stored energy per unit length is given by the integral of the square of the field over the cross-sectional area and is independent of a. Therefore, for the group velocity we also obtain

$$v_g = \frac{P_w}{U} \propto a^4 \ .$$

The value of τ_0 also affects the filling time of the waveguide, which is calculated as the time for the energy to propagate from the input to the output end of the guide. Thus

$$t_F = \frac{L}{v_g} = \tau_0 \frac{2Q}{\omega} \ .$$

Therefore, one may choose the value of τ_0 to be less than the optimum for maximum energy gain, to reduce the filling time.

4.6.3 Constant-Gradient Structure

Another approach is to taper the waveguide so that the accelerating field $E_a = E_0$ is constant over the section. Then α_0 is no longer constant. What is the required dependence of the function $\alpha_0(z)$? We assume that the radii a and b will be varied to change the group velocity along the structure, and that these variations cause only negligable changes in Q and r_L. As before we may write

$$dP_w / dz = -2\alpha_0(z)P_w .$$

Then

$$\int_{P_0}^{P_L} \frac{dP_w}{P_w} = -2\int_0^L \alpha(z)\, dz ,$$

where P_L is the energy flow at the end of the section. Integrating this we obtain

$$P_L = P_0\, e^{-2\tau_0} ,$$

where the total attenuation is $\tau_0 \equiv \int_0^L \alpha_0(z)\, dz$.

From the relation $E_a^2 = -r_L \dfrac{dP_w}{dz}$,

we conclude that for E_a to be constant, so must dP_w/dz. Then $P_w(z)$ must be linear in z, i.e.

$$P_w(z) = P_0 + \frac{P_L - P_0}{L} z .$$

Substituting the result for P_L, we have

$$P_w(z) = P_0 \left[1 - \frac{z}{L}(1 - e^{-2\tau_0})\right] .$$

Therefore, for constant field, the energy flow decreases linearly with z.

Now we want an expression for $\alpha_0(z)$. We first differentiate the above expression

$$\frac{dP_w}{dz} = -\frac{P_0}{L}(1 - e^{-2\tau_0}) .$$

Then we use $dP_w/dz = -2\alpha_0(z)P_w$, and solve for α_0. This gives

The group velocity is $v_g(z) = \frac{\omega}{2Q\alpha_0(z)} = \frac{\omega L}{Q}\frac{\left[1-(z/L)(1-e^{-2\tau_0})\right]}{(1-e^{-2\tau_0})}$

The group velocity required for a constant accelerating field decreases linearly with z, with the same slope as P_W. This implies that the stored energy per unit length, like the accelerating field, is constant.

The energy gain in the section is simply

$$\Delta W = q\int_0^L E_a(z)dz = qE_0L.$$

The relation between the accelerating field and the energy flow is

$$E_0^2 = -r_L\frac{dP_L}{dz} = \frac{r_L P_0}{L}(1-e^{-2\tau_0}) \ .$$

Eliminating E_0 from the energy gain expression gives

$$\Delta W = q\sqrt{r_L P_0 L\left(1-e^{-2\tau 0}\right)}.$$

Both expressions for the energy contain the factor $r_L P_0 L$. High shunt impedance per unit length is desirable. For a given energy gain, the input power required is inversely proportional to the length of the section. In the constant-gradient case the optimum τ_0 is infinite, corresponding to losing all the energy in the structure. In practice not much more energy is gained by letting τ_0 exceed unity, and we need to consider the effect of τ_0 on the filling time of the waveguide. The filling time is

$$t_F = \int_0^L \frac{dz}{v_g(z)} = \frac{Q}{\omega L}(1-e^{-2\tau_0})\int_0^L \frac{dz}{1-(z/L)(1-e^{-2\tau_0})} \ .$$

Carrying out the integration gives $t_F = \tau_0\frac{2Q}{\omega}$,

which is the same value as for the constant impedance structure.

The constant-gradient design was used at SLAC because of the uniform power loss and the lower average value for the peak surface electric field. To achieve this the structure radius is tapered from about b = 4.2 to 4.1 cm, and the disk radius is tapered from about 1.3 to 1.0 cm.

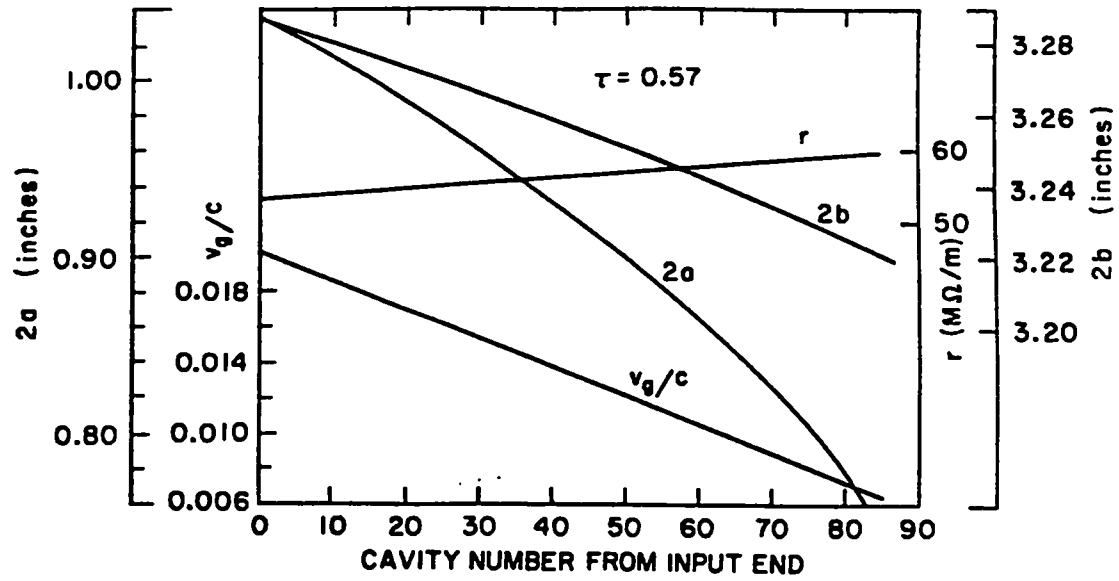

Fig. 4.30. Parameter variation as a function of cavity number along the SLAC 3.05 m constant gradient section with $t_0 = 0.230$ in. (taken from G. Loew and R Talman[15]).

4.7 Problems

4-1. Plot the transit-time factor for a π-mode two-gap cavity versus β/β_s in the range $0.5 < \beta/\beta_s < 3$. Assume a square-wave field distribution in the gaps, and assume $g/\beta\lambda = 1/4$. Is the transit-time factor maximum when $\beta = \beta_s$?

4-2. Suppose you want to accelerate deuterons (synchronously) in a drift-tube linac that has been designed and operated for protons in a $1\beta\lambda$ mode. Assume $m_D = 2\ m_P$, and assume the synchronous phase ϕ is unchanged. Calculate the required value of E_0T for the following two cases. (a) Use a $1\beta\lambda$ mode for the deuteron operation. If E_0 was already as high as you could reliably operate, is this solution practical? (b) Use a $2\beta\lambda$ mode for the deuteron operation. (c) Suppose the ratio of gap to cell length is 1/4. Calculate the transit-time factor for the $1\beta\lambda$ and $2\beta\lambda$ cases using the simple formula $T = (\sin x)/x$, where $x = \pi g/\beta\lambda$. What is the ratio of E_0 for the $2\beta\lambda$ deuteron case to that for proton operation?

4-3. Plot the dispersion relation (mode frequency $\Omega_q/2\pi$ versus phase advance per cavity $\pi q/N$) for $N + 1 = 5$ coupled cavities with uncoupled cavity frequency $\omega_0/2\pi = 400$ MHz and coupling constant $k = 0.05$.

4-4. Consider N+1 coupled cavities with an uncoupled cavity frequency ω_0 and coupling constant $k << 1$. (a) Write the expressions for the frequencies of the π mode and the mode closest to the π mode. (b) Calculate the fractional difference between the two mode frequencies. Obtain an approximation for this result when $N >> 1$. How does this depend on k and N? (c) If $k = 0.02$ and $N + 1 = 30$, calculate the fractional difference between the frequencies of the two modes. Compare this with the width of the π mode assuming the Q value for the π mode is 20,000. Are the two modes adequately separated?

4-5. Repeat parts (a), (b), and (c) of problem 3 for the $\pi/2$ mode of $N + 1$ coupled oscillators.

4–6. A coupled-cavity linac module that operates in a $\pi/2$ mode has 135 excited (accelerating) cells and 134 nominally unexcited coupling cells, and is driven in the central excited cell by a single klystron. The parameters are $Q_a = 20{,}000$ for the accelerating cells, $Q_c = 2000$ for the coupling cells, the frequency is 1280 MHz, and the coupling constant is $k = 0.05$. Assume the beam power is negligable. (a) Calculate the power-flow droop in the field excitation of the end cavities and sketch the field excitation along the module relative to the drive cell (for the accelerating cells only). (b) Calculate the power flow phase shift in the end cavities and sketch the power-flow phase shift

along the module (for the accelerating cells only), assuming the stop band is open by $\delta\omega/2\pi = 100$ kHz. (c) Calculate the field excitation of the two coupling cells adjacent to the drive cell relative to the drive cell amplitude. Sketch the excitation of the coupling cells along the module relative to the drive cell excitation.

4-7. Assume an RFQ cell has the following parameters: $\beta_S = 0.025$, $\lambda = 0.75$ m, a = 1.875 mm, and V = 50 kV. (a) Assume the vane-modulation parameter is m = 2. Calculate the focusing efficiency X, the characteristic radius r_0, the acceleration efficiency A, and the average axial field E_0. If the synchronous phase is $\phi = -30$ degrees, what is the energy gain of the synchronous particle in the cell? (b) Repeat part (a) assuming m = 1.

4-8. Assume the following parameters for SLAC, a constant-gradient traveling-wave linac: f = 2856 MHz, Q = 13,000, $r_L = 57$ MΩ/m, $\tau_0 = 0.57$, and 932 waveguide sections of length = 3.05 m each. (a) Show that the energy gain per section of an electron at the crest of the wave is $\Delta W(\text{MeV}) = 10.9\sqrt{P_0(\text{MW})}$. (b) Calculate the fill time of the waveguide and compare this with a pulse length of 1.6 μs. (c) Calculate the group velocity relative to the speed of light at both the input and output ends of a section. (d) If the peak input rf power per waveguide section is $P_0 = 16$ MW, what is the peak power at the end of a section. (This will be delivered to an external load). (e) If the peak input rf power per waveguide section is $P_0 = 16$ MW, calculate the energy gain per section using the formula of part (a), and calculate the total energy gain in the SLAC linac. What is the accelerating field E_0?

4-9. Resonant frequency errors in a coupled-cavity system that are small compared with the spacing of the normal modes might not seem to be serious, because the modes still remain well separated. But even small cavity-frequency errors can cause nonuniformity of the field distribution that may be unacceptable for accelerators. Consider the weakly coupled 3-cavity system operating in π mode, with an end-cell frequency error $\delta\omega_0/\omega_0 = 10^{-3}$ ($2\delta\omega_0$ is the frequency difference of the two end cells), a middle-cell frequency error $\delta\omega_1 = 0$ (middle cell has same frequency as the average of the end cells = ω_0), and coupling constant k = 0.01. (a) Ignoring the frequency error, calculate the frequency spacing of the three normal modes relative to $\omega_0/2\pi$. Is the cavity-frequency error small compared with the frequency spacing of the modes? (b) Calculate the perturbed π-mode field vector for this case. Describing the perturbed distribution as a linear field tilt, what is the fractional end-to-end field tilt? (c) Calculate the perturbed π/2-mode field vector. If only the end cells are used for acceleration, would the π/2 mode give a field distribution that is more uniform in the presence of the same cavity frequency errors?

4-10. We consider the effects of power losses in the coupled 3-cavity system. Assume there are no frequency errors ($\delta\omega_0 = \delta\omega_1 = 0$), a coupling constant k = 0.01, and $Q = 10^4$ for each mode. Assume the rf drive is located in one end cell. (a) Calculate the field vector for the 0, π/2, and π modes. (b) Calculate the power-flow phase shift in the end cell without the drive for the 0, π/2 and π modes. Calculate the π/2-mode power-flow droop in the end cell without the drive. (c) Assume beam loading causes $Q = 10^3$, and repeat part (b).

5 BEAM DYNAMICS

5.1 Longitudinal Dynamics

5.1.1 Introduction

Longitudinal focusing occurs for a synchronous phase that corresponds to a field that is rising in time (see Fig. 5.1). (For a traveling wave this occurs at the front of the wave, before the crest.)

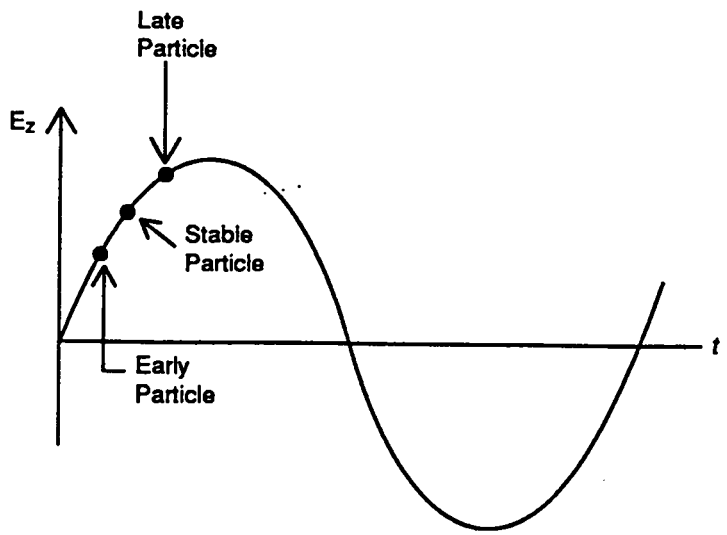

Fig. 5.1. Stable phase.

The early particles experience a lower field, and the late particles a higher field, than the synchronous particle. Consequently, the beam is formed into a sequence of stable bunches consisting of captured particles that are accelerated. Some particles are not captured, do not experience a net acceleration and fall behind in phase. Often these particles are lost radially before they arrive at the end of the linac.

To develop these ideas, we consider an array of standing-wave accelerating cells, designed in the nth cell for a particle with synchronous phase ϕ_{sn}, synchronous energy W_{sn}, and synchronous velocity β_{sn}. We express the phase, energy, and velocity of an arbitrary particle in the nth cell as ϕ_n, W_n, and β_n. The particle phase is defined as the phase of the field when the particle is at the center of the nth cell (center of the gap), and the particle energy is the value at the end of the nth cell.

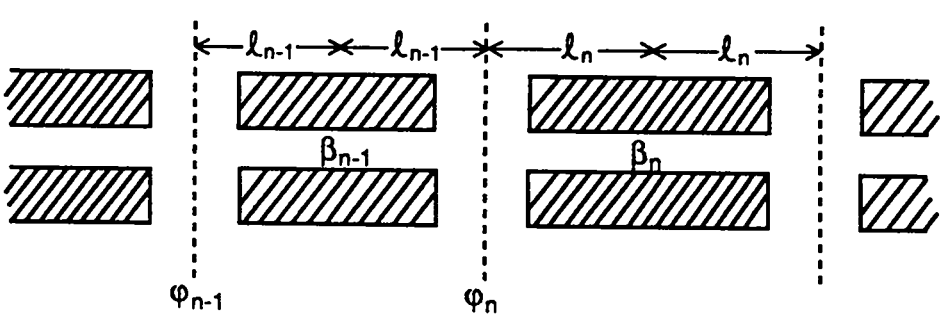

Fig. 5.2. Accelerating cells for deriving the difference equations of longitudinal motion.

We will assume that the velocities of the particles are close enough to the synchronous velocity that all particles have the same transit-time factor. The cell lengths have been chosen so that the synchronous particle always arrives at each succeeding gap at the correct phase. We now ask whether a particle that is close in phase and energy is accelerated to approximately the same energy as the synchronous particle, or whether its energy and phase deviations will grow.

5.1.2 Difference Equations of Longitudinal Motion for Standing-Wave Linacs

We now derive difference equations of motion by considering the motion through each cell to consist of a drift between gap centers and acceleration at the center of the gaps. From gap n−1 to gap n, the particle has a constant velocity β_{n-1}, as indicated in Fig. 5.2. The rf phase advance of the particle as it advances through the cell is

$$\phi_n = \phi_{n-1} + \omega \frac{2\ell_{n-1}}{\beta_{n-1}c},$$

where $\ell_{n-1} = N\beta_{s,n-1}\lambda/2$, where $N = \begin{Bmatrix} \frac{1}{2} \text{ for CCL} \\ 1 \text{ for DTL} \end{Bmatrix}$.

For synchronism the cell length must be $L_n = N(\beta_{s,n-1} + \beta_{s,n})\lambda/2$.

For an arbitrary particle $\phi_n = \phi_{n-1} + 2\pi N \frac{\beta_{s,n-1}}{\beta_{n-1}}$,

and for the synchronous particle $\phi_{s,n} = \phi_{s,n-1} + 2\pi N$.

The phase change of the particle through a cell relative to the synchronous particle is given by the difference equation

$$\Delta(\phi - \phi_s)_n = \Delta\phi_n - \Delta\phi_{s,n} = 2\pi N\beta_{s,n-1}\left[\frac{1}{\beta_{n-1}} - \frac{1}{\beta_{s,n-1}}\right].$$

Using the Taylor expansion we write

$$\frac{1}{\beta} - \frac{1}{\beta_s} = \frac{1}{\beta_s + \delta\beta} - \frac{1}{\beta_s} \cong -\frac{\delta\beta}{\beta_s^2}, \text{ for } \delta\beta << 1.$$

The relationship between δW and $\delta\beta$ is $\delta\beta = \frac{\delta W}{mc^2\gamma_s^3\beta_s}$,

and, when this is substituted for $\delta\beta$, we obtain the difference equation

$$\Delta(\phi-\phi_s)_n = -2\pi N\frac{(W_{n-1}-W_{s,n-1})}{mc^2\gamma_{s,n-1}^3\beta_{s,n-1}^2}.$$

Now we derive a difference equation for energy gain. For simplicity we restrict the discussion to particles on the axis. The energy gain for an arbitrary particle in the nth cell is

$$\Delta W_n = W_n - W_{n-1} = qE_0TL_n\cos\varphi_n.$$

For the synchronous particle

$$\Delta W_{s,n} = W_{s,n} - W_{s,n-1} = qE_0TL_n\cos\varphi_{s,n}.$$

The energy gain in cell n relative to that of the synchronous particle is given by the difference equation

$$\Delta(W-W_s)_n = \Delta W_n - \Delta W_{s,n} = qE_0TL_n(\cos\varphi_n - \cos\varphi_{s,n}).$$

To summarize, the difference equations for relative phase and energy are

$$\Delta(\phi-\phi_s)_n = -2\pi N\frac{(W_{n-1}-W_{s,n-1})}{mc^2\gamma_{s,n-1}^3\beta_{s,n-1}^2},$$

$$\Delta(W-W_s)_n = qE_0TL_n(\cos\varphi_n - \cos\varphi_{s,n}).$$

These can be solved numerically for the motion in $\Delta\phi$-ΔW space, known as longitudinal phase space.

5.1.3 Differential Equations of Longitudinal Motion

To study the stability of the motion, it is convenient to convert the difference equations to differential equations. In this approximation we replace the discrete action of the standing-wave fields by a continuous field. We let

$$\Delta(\phi-\phi_s) \rightarrow \frac{d(\phi-\phi_s)}{dn}, \text{ and } \Delta(W-W_s) \rightarrow \frac{d(W-W_s)}{dn},$$

where n is the cell number, now treated as a continuous variable. We can change variables from n to the axial distance s, using $n = s/(N\beta_s\lambda)$. The differential equations are

$$\gamma_s^3\beta_s^3\frac{d(\phi-\phi_s)}{ds} = -2\pi\frac{(W-W_s)}{mc^2\lambda}, \text{ and } \frac{d(W-W_s)}{ds} = qE_0T(\cos\phi - \cos\phi_s).$$

We now show that the two first-order differential equations of motion that have just been derived are the same as if we had considered acceleration of a particle by the space-harmonic component that is the synchronous traveling wave. The field of the synchronous wave is

$$E_z = E_0 T I_0\left[\frac{2\pi r}{\beta_s \gamma_s \lambda}\right]\cos\phi_s.$$

The energy gain, relative to the synchronous particle, of a particle of phase ϕ traveling on the axis over a distance ds is

$$d(W - W_s) = qE_0T(\cos\phi - \cos\phi_s)ds.$$

Thus $\dfrac{d(W - W_s)}{ds} = qE_0T(\cos\phi - \cos\phi_s)$.

This is the same as the energy equation just derived for the standing-wave case.

The phase change, relative to the synchronous particle, of a particle of phase ϕ traveling over a distance ds is

$$d(\phi - \phi_s) = \left[\frac{2\pi}{\beta\lambda} - \frac{2\pi}{\beta_s\lambda}\right]ds.$$

As above, this can be converted to $\gamma_s^3\beta_s^3\dfrac{d(\phi - \phi_s)}{ds} = -2\pi\dfrac{(W - W_s)}{mc^2\lambda}$.

Again, this equation for the relative phase is the same as that derived for a particle in a standing-wave field. Therefore, the action of the standing-wave field may be replaced with that of an equivalent traveling wave (the synchronous space harmonic).

5.1.4 Longitudinal Motion when Acceleration Rate is Small

The two first-order differential equations are

$$\gamma_s^3\beta_s^3\frac{d(\phi - \phi_s)}{ds} = -2\pi\frac{(W - W_s)}{mc^2\lambda}, \text{ and } \frac{d(W - W_s)}{ds} = qE_0T(\cos\phi - \cos\phi_s).$$

We can differentiate the first equation and substitute the second to obtain a second-order differential equation:

$$\frac{d}{ds}\left[\gamma_s^3\beta_s^3\frac{d(\phi - \phi_s)}{ds}\right] = -2\pi\frac{qE_0T}{mc^2\lambda}(\cos\phi - \cos\phi_s).$$

This can also be written as

$$\gamma_s^3\beta_s^3\frac{d^2(\phi - \phi_s)}{ds^2} + 3\gamma_s^2\beta_s^2\left[\frac{d}{ds}(\gamma_s\beta_s)\right]\left[\frac{d(\phi - \phi_s)}{ds}\right] + 2\pi\frac{qE_0T}{mc^2\lambda}(\cos\phi - \cos\phi_s) = 0.$$

This is a nonlinear second-order differential equation for the phase motion. It is not easy to write a

general solution, but we can expect the solution to be periodic with damping from the second term. Before we investigate the properties of the solution, we comment that, because phase is proportional to time, the more negative the phase, the earlier the particle. The phase difference $\phi-\phi_s$ between a particle and the synchronous particle is proportional to a spatial separation

$$z - z_s = -\frac{\beta_s \lambda}{2\pi}(\phi - \phi_s).$$

Now, we assume that the acceleration rate is small and ignore the damping term, and we also assume E_0T and ϕ_s are constant. Before solving the differential equations we first simplify the notation by making the following definitions:

$$w \equiv \delta\gamma = \frac{W - W_s}{mc^2}, \; A \equiv \frac{2\pi}{\beta_s^3 \gamma_s^3 \lambda}, \text{ and } B \equiv \frac{qE_0T}{mc^2}.$$

The differential equations are

$$w' \equiv dw/ds = B(\cos\phi - \cos\phi_s),$$

$$\phi' \equiv d\phi/ds = -Aw, \text{ and } \phi'' \equiv d^2\phi/ds^2 = -AB(\cos\phi - \cos\phi_s), \text{ where } AB = 2\pi qE_0T/(mc^2\beta_s^3\gamma_s^3\lambda).$$

The equations for ϕ' and w' show that the fixed points occur for $w = 0$, $\phi = -\phi_s$ and $w = 0$, $\phi = +\phi_s$. Now, integrate the second-order differential equation, which gives

$$d\phi' = -AB(\cos\phi - \cos\phi_s)ds.$$

Using $ds = d\phi/\phi'$ gives $\phi' d\phi' = -AB(\cos\phi - \cos\phi_s)d\phi$.

Now integrate both sides, and substitute $\phi' = -Aw$. This gives

$$\frac{Aw^2}{2} + B(\sin\phi - \phi\cos\phi_s) = H_\phi.$$

The quantity H_ϕ is a constant of integration, and this result is a statement of energy conservation for the longitudinal motion. We will identify H_ϕ as the Hamiltonian. The first term is the kinetic energy term, and the second is the potential energy. The value of H_ϕ depends on the initial coordinates of the particle. The potential energy term V_ϕ is

$$V_\phi = B(\sin\phi - \phi\cos\phi_s).$$

Plotting the potential energy versus ϕ shows that there is a potential well when $-\pi < \phi_s < 0$ as shown in Fig. 5.3. The particles that lie within the potential well will perform stable oscillations about the synchronous particle. We recall that there is acceleration for $-\pi/2 \le \phi_s \le \pi/2$.Then simultaneous acceleration with a potential well occurs when $-\pi/2 \le \phi_s \le 0$. One finds a stability limit for the phase motion, which extends from $\phi_2 < \phi < -\phi_s$. There is no simple formula for the

lower limit ϕ_2 . It can be obtained numerically from $H_\phi(\phi_2) = H_\phi(-\phi_s)$.

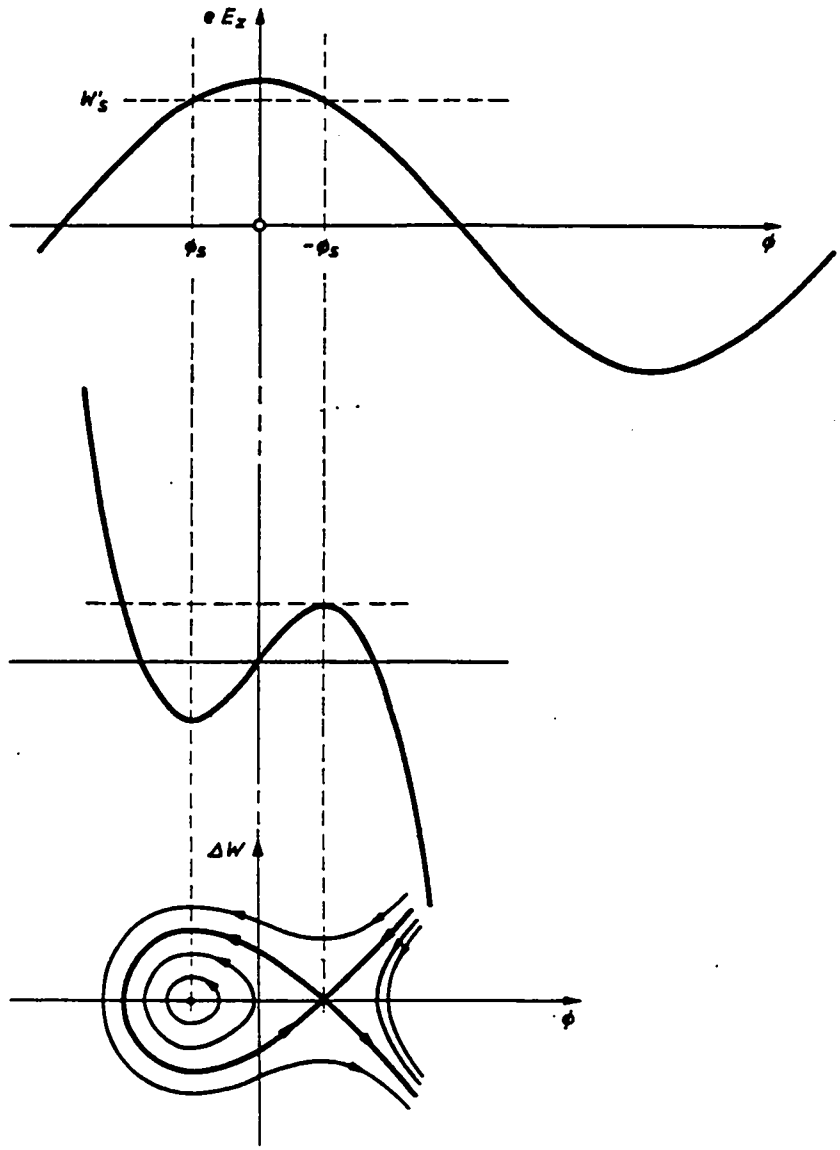

Fig. 5.3. At the top, the accelerating field as function of phase, the synchronous energy gain W's shown as a broken line. Next, the effective potential well, and at bottom, phase-plane trajectories for such a potential, including the separatrix. Taken from Hereward in Linear Accelerators, edited P. Lapostolle.

The limiting stable trajectory is called the separatrix. The parameters characterizing the separatrix limits are shown in Fig. 5. 5. At the potential maximum, where $\phi = -\phi_s$, we have $\dot{\phi} = 0$ and therefore $w = 0$. Then at $\phi = -\phi_s$

$$B\left(\sin(-\phi_s) - (-\phi_s \cos\phi_s)\right) = H_\phi .$$

This determines the constant H_ϕ, and the general result at the separatrix is

$$\frac{Aw^2}{2} + B(\sin\phi - \phi\cos\phi_s) = -B(\sin\phi_s - \phi_s\cos\phi_s).$$

It is useful to plot the separatrix curve in longitudinal phase space (Fig. 5.4) which is usually defined as ϕ versus ΔW, where ϕ is defined over the interval $-270° < \phi \leq 90°$. The separatrix is a closed curve in this space, which defines the area within which the trajectories are stable, and it can be plotted if the constants A and B are given. The separatrix is also called the fish, and the stable area is sometimes called the bucket. There are two solutions for w = 0, which determine the maximum phase width of the separatrix. One solution is $\phi_1 = -\phi_s$, which is a positive number because ϕ_s is negative. We recall that this is also a fixed point, and now we know that it is also an unstable fixed point. This is the maximum phase for stable motion. The minimum value at $\phi = \phi_2$ and w = 0 is the other solution. The equation for the separatrix for this case becomes

$$\sin\phi_2 - \phi_2\cos\varphi_s = \phi_s\cos\varphi_s - \sin\phi_s.$$

This can be solved numerically for ϕ_2.

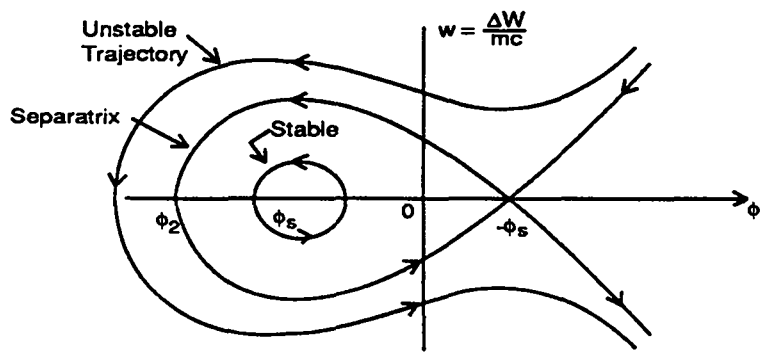

Fig. 5.4. Longitudinal separatrix.

To estimate ϕ_2, we first derive an expression for the total phase width of the separatrix. The total phase width is

$$\Psi = |\phi_s| + |\phi_2| = -\phi_s - \phi_2.$$

Then

$$\sin\phi_2 = -\sin(\phi_s + \Psi) = -[\sin\phi_s\cos\Psi + \sin\Psi\cos\phi_s].$$

Now we substitute this into the separatrix equation for ϕ_2, and solve an equation for tan ϕ_s:

$$\tan\phi_s = \frac{\sin\Psi - \Psi}{1 - \cos\Psi}.$$

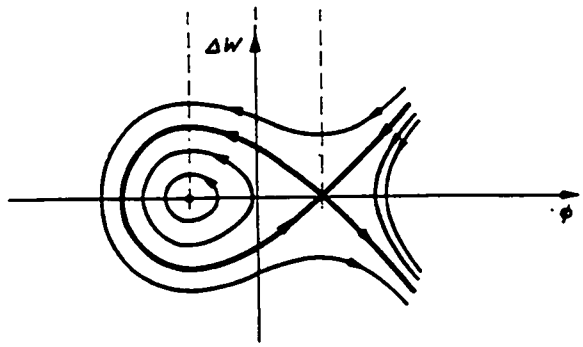

Fig. 5.5. Separatrix limits are shown by the thicker line.

When $\psi << 1$ and $\phi_s << 1$, $\sin\psi = \psi - \psi^3/6 + ...$ and $\cos\psi = 1 - \psi^2/2 + ...$, and we obtain

$$\tan\phi_s = \frac{\sin\Psi - \Psi}{1 - \cos\Psi} \cong -\frac{\Psi}{3}.$$

Then with $\tan\phi_s \cong \phi_s$, we have $\Psi \cong 3|\phi_s|$.

Therefore, in the small-angle approximation $\phi_2 = 2\phi_s$.

This is actually a good approximation for $|\phi_s| < 60°$. Beyond this value the stable phase interval is larger than $3|\phi_s|$. At $\phi_s = -90°$ the phase acceptance is maximum, extending over the full 360° as shown in Fig. 5.6. At 0 ° the phase acceptance vanishes.

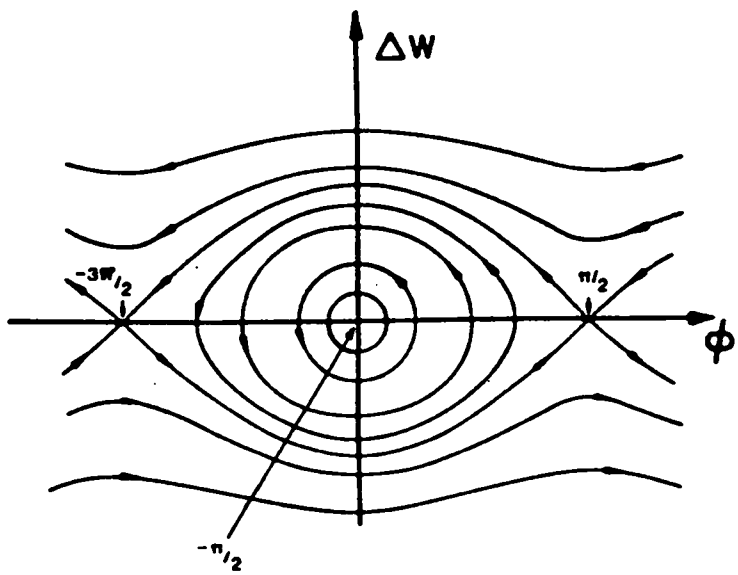

Fig. 5.6. Separatrix for $\phi_s = -90°$ (no acceleration).

The linac is designed to provide an acceleration rate given by $dW_s/ds = q\,(E_0T)_{design} \cos\phi_s$ to maintain synchronism. If the actual accelerating field E_0T is different from the design value, a different particle phase satisfies the synchronism condition and there is a new synchronous particle at that field. The new synchronous phase is given by $\cos\phi = \cos\phi_s\,(E_0T)_{design} / E_0T$. At $\phi = 0$ the phase acceptance vanishes, and the corresponding accelerating field is the threshold for forming a stable bucket for synchronous acceleration. Therefore

$$(E_0T)_{threshold} = (E_0T)_{design} \cos\phi_s.$$

Next we find the energy half width of the separatrix. It can be shown that $w = w_{max}$ occurs for $\phi = \phi_s$. Solving the separatrix equation for $w = w_{max}$,

$$w_{max} = \frac{\Delta W_{max}}{mc^2} = \sqrt{\frac{2qE_0T\beta_s^3\gamma_s^3\lambda}{\pi mc^2}(\varphi_s\cos\varphi_s - \sin\varphi_s)}.$$

5.1.5 Hamiltonian and Liouville's Theorem

The equation of motion can be written in Hamiltonian form. To demonstrate this we identify the energy invariant as the Hamiltonian

$$H_\phi = \frac{Aw^2}{2} + B(\sin\phi - \phi\cos\phi_s).$$

The canonically conjugate variables are ϕ and $p_\phi = -w = -(W - W_s)/mc^2$, and the second-order differential equation of motion is derived from Hamilton's Equations

$$p'_\phi = -\partial H_\phi / \partial\phi, \text{ and } \phi' = \partial H_\phi / \partial p_\phi.$$

It can be proven that the area in phase space occupied by the particles is constant for a system described by a Hamiltonian that is independent of time. This is the statement of Liouville's theorem, and it is valid for systems with no dissipation that satisfy the continuity equation in phase space. In our treatment of the longitudinal motion we have ignored the dissipation term, which is present only when there is acceleration. When the acceleration occurs slowly, the parameters β_s and γ_s change adiabatically. The phase-space area can be shown to be an adiabatic invariant, and therefore is still approximately constant. If the beam is accelerated slowly, the shape of the area enclosed by the particle trajectories changes but the area remains constant. This is usually a good approximation except that at very low velocities, where the relative velocity increase in the cell is large, the nonadiabatic dynamics cause an increase in the phase-space area which improves the acceptance. The separatrix looks like a golf club rather than a fish, as shown on Fig. 5.7. We will use the phase-space area conservation later to calculate the change of the phase width of the beam during adiabatic acceleration.

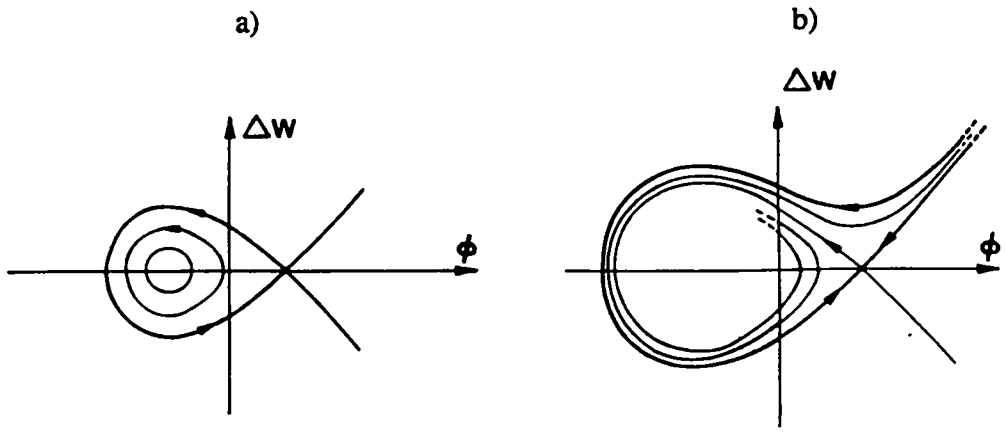

Fig. 5.7. Separatrix boundaries: (a) fish (ignoring acceleration), (b) golf club (including acceleration).

5.1.6 Small Oscillations

We return to the equation of motion

$$\phi'' \equiv \frac{d^2\phi}{ds^2} = -AB(\cos\phi - \cos\phi_s).$$

For small phase differences relative to the synchronous phase

$$\cos\phi \cong \cos\phi_s - (\phi - \phi_s)\sin\phi_s - \frac{(\phi-\phi_s)^2}{2}\cos\phi_s.$$

Then $\phi'' + k_{\ell 0}^2 \sin(-\phi_s)\left[(\phi-\phi_s) - \frac{(\phi-\phi_s)^2}{2\tan(-\phi_s)}\right] = 0,$

where $k_{\ell 0}^2 = AB\sin(-\phi_s) = \frac{2\pi q E_0 T \sin(-\phi_s)}{mc^2\beta_s^3\gamma_s^3\lambda}.$

When the quadratic term is small, we obtain the equation of small longitudinal oscillations. The quantity $k_{\ell 0}$ is the wave number of these oscillations. The period of the longitudinal oscillations is $L_\ell = 2\pi / k_{\ell 0}$, which can be compared with the rf period $\beta\lambda$. The corresponding angular frequency of small longitudinal oscillations is $\omega_{\ell 0} = k_{\ell 0}\beta_s c$, or

$$\left[\frac{\omega_{\ell 0}}{\omega}\right]^2 = \frac{qE_0 T\lambda \sin(-\phi_s)}{2\pi mc^2\gamma_s^3\beta_s},$$

where $\omega \doteq 2\pi c/\lambda$ is the rf angular frequency. The longitudinal oscillation frequency is typically <10% of the rf frequency. As the beam becomes relativistic, the longitudinal oscillations approach zero. The quadratic term in the differential equation for ϕ is the lowest-order nonlinear term. Because it is quadratic, it produces an asymmetric potential well, and the minus sign means that in the nonlinear part of the restoring force weakens the focusing.

Now we examine the trajectory of the small oscillations in longitudinal phase space. The general trajectory equation is

$$\frac{Aw^2}{2} + B(\sin\phi - \phi\cos\phi_s) = H_\phi.$$

In the approximation $|\phi - \phi_s| << 1$, we write

$$\sin\phi - \phi\cos\phi_s \cong \sin\phi_s - \phi_s\cos\phi_s - \frac{(\phi-\phi_s)^2}{2}\sin\phi_s.$$

Substituting this into the trajectory equation, we obtain

$$Aw^2 + B\sin(-\phi_s)(\phi - \varphi_s)^2 = C,$$

where C is a constant for the trajectory. Since ϕ_s is negative for stable motion, this is the equation for an ellipse in longitudinal phase space centered at $w = 0$, $\phi = \phi_s$. Therefore the fish-shaped phase-space trajectories near the separatrix become ellipses near the center of the fish. Define the maximum phase half-width as $\Delta\phi_0 = \phi_0 - \phi_s$, where ϕ_0 is the maximum phase. Because the point of maximum phase projection corresponds to a point on the ellipse with $w = 0$,

$$B\sin(-\phi_s)\Delta\phi_0^2 = C.$$

Then the equation for the ellipse can be written as

$$\frac{w^2}{w_0^2} + \frac{(\phi-\phi_s)^2}{\Delta\phi_0^2} = 1,$$

where $w_0 = \frac{(W - W_s)_0}{mc^2} = \sqrt{\frac{B}{A}\sin(-\phi_s)\Delta\varphi_0^2}$,

which is a point on the ellipse that corresponds to $\phi - \phi_s = 0$.

5.1.7 Phase Damping

For slow enough acceleration the parameters of the phase-space ellipses for small oscillations vary slowly. As discussed earlier, the area of the ellipses for the particles are adiabatic invariants. Therefore, during the acceleration, for each particle we may write

$$\text{Area} = \pi\Delta\phi_0\Delta W_0 = \pi\Delta\phi_0^2\sqrt{qE_0Tmc^2\beta_s^3\gamma_s^3\lambda\sin(-\phi_s)/2\pi} \ ,$$

or $\Delta\phi_0 = \frac{\text{constant}}{\left[qE_0Tmc^2\beta_s^3\gamma_s^3\lambda\sin(-\phi_s)/2\pi\right]^{1/4}}$, or $\Delta\phi_0 = \frac{\text{constant}}{(\beta_s\gamma_s)^{3/4}}$.

Because the phase space area is constant, we must have

$$\Delta W_0 = \text{constant}(\beta_s\gamma_s)^{3/4} \ .$$

This relation describes the decrease of the phase amplitude and the increase of the energy amplitude of phase oscillations during acceleration in a linac, an effect called phase damping (see Fig. 5.8). If the initial amplitude is $\Delta\phi_{0,i}$ at synchronous velocity β_{si}, the amplitude $\Delta\phi_0$ at some later point, where the synchronous velocity is β_s, is

$$\frac{\Delta\phi_0}{\Delta\phi_{0,i}} = \left[\frac{(\beta_s\gamma_s)_i}{\beta_s\gamma_s}\right]^{3/4} \ .$$

Likewise,

$$\frac{\Delta W_0}{\Delta W_{0,i}} = \left[\frac{\beta_s\gamma_s}{(\beta_s\gamma_s)_i}\right]^{3/4} \ .$$

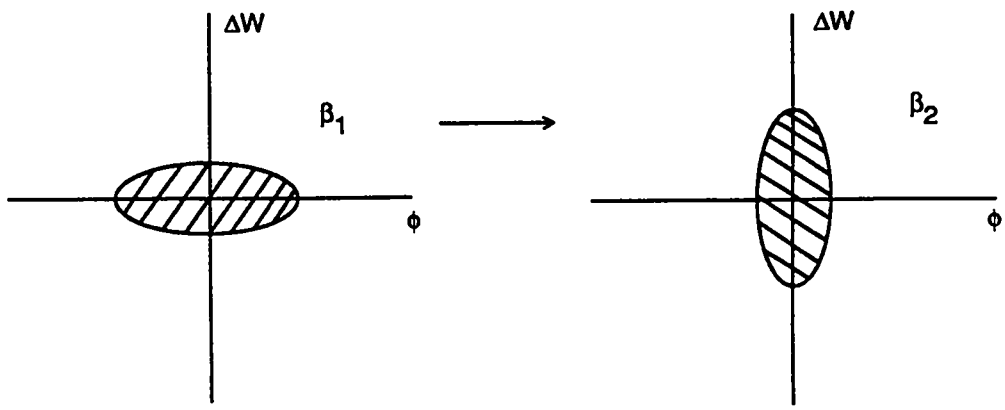

Fig. 5.8. Phase-damping of longitudinal beam ellipse caused by acceleration.

5.1.8 Longitudinal Dynamics of Ion Beams in Coupled-Cavity Linacs

In the high-energy sections of ion linacs, where the fractional velocity increase per tank is small, one can simplify the fabrication by designing each tank with a constant cell length for all cells in the tank. The length of each cell is $\beta_s\lambda/2$, where β_s is the design velocity. For each tank the β_s can be chosen to equal the velocity of the reference particle at the center of the tank. This construction changes the dynamics of the reference particle. Because all cell lengths in the tank are equal, the true synchronous phase is $\phi_s = -90°$, corresponding to no acceleration in the tank. The reference particle is not the synchronous particle, and the reference-particle phase varies as it passes through the tank. The energy gain of the particle in the tank is

$$\Delta W_r = qE_0T\cos\phi_r N_c\beta_s\lambda/2 \ ,$$

where N_c is the number of cells in the tank and ϕ_r is the mean value of the reference particle phase. This mean phase is sometimes (erroneously) called the synchronous phase because it functions in the energy gain expression as the synchronous phase would. It can therefore be called the effective synchronous phase. The reference particle is injected so that its phase increases in the first half of

the tank to a maximum value and then decreases in the second half of the tank, returning to the initial value at the end of the tank. Thus, the reference particle enters and exits the tank with the same phase. The total energy gain is the sum of the two equal contributions of the two halves of the tank.

The approximate maximum phase excursion of the reference particle can be calculated in the following way. We assume that the reference particle moves on the constant energy trajectory (Fig. 5.9), which we derived earlier by ignoring acceleration:

$$\frac{Aw^2}{2} + B(\sin\phi - \phi\cos\phi_s) = H_\phi .$$

The true synchronous phase is $\phi_s = -90°$. The tank-entrance coordinates are $\phi = \phi_1$, and $w = w_1 = -\Delta W_r/2mc^2$, where ΔW_r is the total energy gain of the reference particle in the tank. The trajectory equation becomes

$$\frac{Aw^2}{2} + B\sin\phi = \frac{Aw_1^2}{2} + B\sin\phi_1 .$$

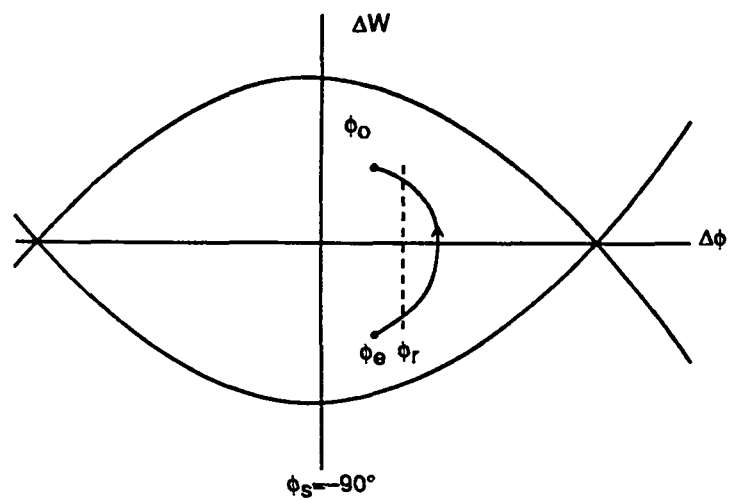

Fig. 5.9. Phase-space trajectory in a coupled-cavity linac structure with constant length cells.

The maximum phase excursion $\phi = \phi_0$ occurs for $w = 0$. Then,

$$\sin\phi_0 - \sin\phi_1 = \frac{A}{2B} w_1^2 .$$

If we expand the sine expressions about the mean phase of the reference particle, we have

$$\sin\phi_0 - \sin\phi_1 \cong \cos\phi_r(\phi_0 - \phi_1) .$$

To a first approximation we have used

$$\phi_r \cong \frac{\phi_0 + \phi_1}{2} .$$

Equating the two expressions for the difference of the sine expressions, we find the approximate phase excursion through the tank of the reference particle

$$\phi_0 - \phi_1 = \frac{\pi N_c}{8} \frac{\Delta W_r}{\gamma_s^3 \beta_s^2 mc^2} .$$

The reference particle moves from ϕ_1 to ϕ_0 in the first half of the tank and back to ϕ_1 in the second half. The phase excursion is usually no more than a few degrees. The motion of the other particles relative to the reference particle is given by the same equations derived earlier for the motion of particles relative to a synchronous reference particle.

5.1.9 Longitudinal Dynamics of Beams Injected into a v=c Linac

We discuss the physics of the capture, bunching, and acceleration of an injected beam with $v < c$ into a structure that supports a traveling wave, as shown in Fig. 5.10, with phase velocity $v = c$. The particle phase will slip on the wave, because the two velocities are different. The equation of motion of the particle is

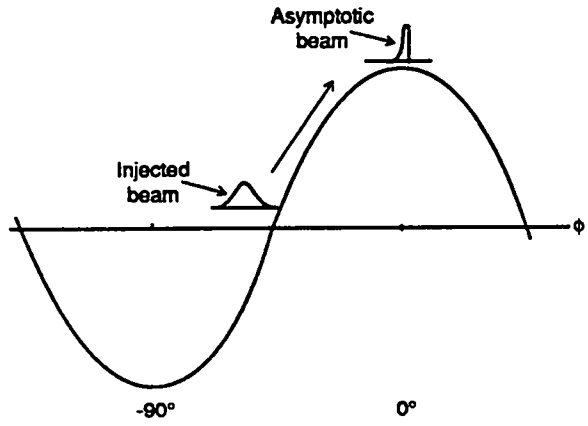

Fig. 5.10. Longitudinal dynamics in a v=c linac.

$$\frac{d}{dt} mc\beta\gamma = qE_0 \cos\phi.$$

The phase of the traveling wave at time t and position z is

$$\phi(z,t) = \omega t - 2\pi z / \lambda.$$

Suppose the particle has an initial coordinate z_i at time t_i. We write its initial phase on a wave, traveling at $v = c$, as

$$\phi_i = \omega t_i - 2\pi z_i / \lambda.$$

At a later time $t_i + dt$, the particle with velocity βc is at a position $z_i + \beta c\, dt$.
The new phase on the wave is

$$\phi = \omega(t_i + dt) - 2\pi(z_i + \beta c dt)/\lambda \quad \text{or} \quad \frac{d\phi}{dt} = \frac{2\pi c}{\lambda}(1-\beta).$$

Note that for $\beta < 1$, ϕ increases with time, which means the particle falls further behind the initial phase on the wave. Now we return to the equation of motion and change the independent variable from time to phase. We use $d(\gamma\beta) = \gamma^3\, d\beta$, and we write

$$\frac{d\beta}{dt} = \frac{d\beta}{d\phi}\frac{d\phi}{dt}.$$

Then we have $mc\gamma^3 \dfrac{d\beta}{d\phi}\dfrac{d\phi}{dt} = qE_0 \cos\phi.$

Then, substituting the equation for the rate of change of ϕ, we obtain

$$\frac{1}{(1+\beta)\sqrt{1-\beta^2}}\frac{d\beta}{d\phi} = \frac{qE_0\lambda}{2\pi mc^2}\cos\phi\,.$$

Now we integrate both sides from the initial values to the later values of β and ϕ. To carry out the integration we can use the substitution to the new variable α defined by $\beta = \cos\alpha$. We also need the integral

$$\int \frac{d\alpha}{1+\cos\alpha} = \tan\frac{\alpha}{2},$$

and the identity $\tan\dfrac{\alpha}{2} = \sqrt{\dfrac{1-\cos\alpha}{1+\cos\alpha}} = \sqrt{\dfrac{1-\beta}{1+\beta}}$.

We finally obtain $\sin\phi = \sin\phi_i + \dfrac{2\pi mc^2}{qE_0\lambda}\left[\sqrt{\dfrac{1-\beta_i}{1+\beta_i}} - \sqrt{\dfrac{1-\beta}{1+\beta}}\right]$.

First, we see that we do not have an oscillatory solution for this case. Also, because of acceleration $\beta > \beta_i$. Then the second term on the right is positive, which means $\sin\phi > \sin\phi_i$. Therefore the phase becomes more positive, as we expect. This means that if we want the particle to approach the crest, where $\phi = 0$, the particle must be injected at a negative phase. We see also that as β approaches $\beta = 1$, the phase ϕ approaches a constant asymptotic value, which is

$$\sin\phi_\infty = \sin\phi_i + \frac{2\pi mc^2}{qE_0\lambda}\sqrt{\frac{1-\beta_i}{1+\beta_i}}\,.$$

This discussion suggests that a good strategy for efficient acceleration is to start the initial phase at $-90° < \phi_i < 0°$ to allow for phase slip, and to choose the parameters so that the asymptotic phase is $\phi_\infty \approx 0$. To help the discussion let us define the second term as

$$F \equiv \frac{2\pi mc^2}{qE_0\lambda}\sqrt{\frac{1-\beta_i}{1+\beta_i}} .$$

We now consider an example that gives the maximum phase slip, which can be seen to allow capture of a given energy beam at the lowest field. Therefore, we choose $\phi_i \approx -90°$ (actually we must make it slightly more positive to insure acceleration) and $\sin\phi_i = -1$. For a solution with a physical asymptotic phase, we must have $F < 2$ (but $F = 2$ means $\phi_\infty = +90°$, which implies a very long linac). This implies a threshold for capture of

$$E_0 > \frac{\pi mc^2}{q\lambda}\sqrt{\frac{1-\beta_i}{1+\beta_i}} .$$

For efficient acceleration we need $F = 1$, which puts the asymptotic phase at the crest. This implies

$$E_0 = \frac{2\pi mc^2}{q\lambda}\sqrt{\frac{1-\beta_i}{1+\beta_i}} .$$

We can see that the smaller the initial velocity, the larger the accelerating field must be.

During the capture process, as the injected beam moves up to the crest, the beam is also bunched. This is due to velocity modulation caused by the early particles experiencing a lower accelerating field than later particles.

To estimate the magnitude of the bunching effect, we assume $\phi_i \approx -90°$ and $\phi_\infty \approx 0$. We suppose the initial phase width is $2\delta\phi_i$, with the initial centroid at $-\pi/2 + \delta\phi_i$. The relationships are

$$\sin\phi_\infty = \sin\phi_i + F, \quad \sin\phi_\infty = \phi_\infty, \text{ and } \sin\phi_i = \sin(-\pi/2 + \Delta) = -1 + \Delta^2/2 ,$$

where $\phi_i = -\pi/2 + \Delta, \quad \Delta << 1.$

We require the centroid to have an asymptotic phase at the crest, $\phi_\infty = 0$. Then, since $\phi_i = -\pi/2 + \delta\phi_i$, we find that

$$F = 1 - \frac{\delta\phi_i^2}{2} .$$

Then the earliest particle is asymptotically at $\phi_\infty = -\frac{\delta\phi_i^2}{2}$,

which is just earlier than the crest, and the latest particle is asymptotically at

$$\phi_\infty = \frac{3}{2}\delta\phi_i^2 .$$

The final half width of the beam is $\delta\phi_\infty = \delta\phi_i^2$.

Thus, if $\delta\phi_i = 15°$ is the initial half-width, the asymptotic half-width is about 3.9°.

In summary, if particles are injected into a structure whose phase velocity equals the velocity of light, they slip in phase, but if the accelerating field is chosen correctly, the particles will asymptotically approach the crest where they can be efficiently accelerated to high energies. This capture process can also result in significant bunching of the captured beam.

5.2 Transverse Dynamics

5.2.1 Introduction

The rf fields exert radial forces on off-axis particles as well as accelerating forces. As shown in Figs. 5.11 and 5.12, when the off-axis particles enter an accelerating gap and see a longitudinal accelerating field, they also see a radial electric field at the entrance that is directed inward (focusing), and one at the entrance that is outward (defocusing). The azimuthal magnetic field also acts on the particles to produce a radial force which is important only at high velocities. A net radial momentum impulse occurs if (1) the fields vary in time, (2) the displacement of the particle changes between the entrance and the exit, and (3) the particle velocity changes while the particle crosses the gap. For longitudinal stability we have seen that ϕ_s is negative, which means the field is rising when the synchronous particle is injected. This means the particles see higher defocusing than focusing fields. This is mechanism (1), and throughout most of a linac this effect usually is dominant and produces net radial defocusing.

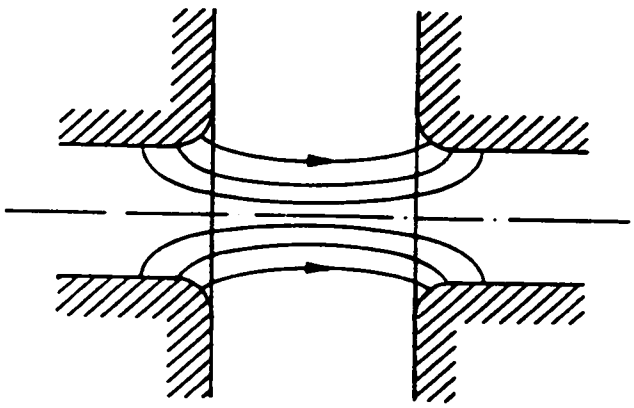

Fig. 5.11. Focusing and defocusing in an rf gap.

The condition for longitudinal focusing is that the field is increasing, but this is generally incompatible with radial focusing. This has been described as a consequence of Earnshaw's theorem, which is a more general principle that follows from Maxwell's equations. Earnshaw's theorem states that the electrostatic potential in free space cannot have a maximum or a minimum. Suppose a Lorentz transformation is made to the rest frame of the particle. In the rest frame the magnetic forces are zero, and only the electrostatic forces can act. If there is an electric potential minimum in one plane, there cannot be a minimum in all the other planes. This implies that simultaneous focusing electric forces cannot be applied in all three directions. If the longitudinal forces give focusing, the radial forces are defocusing, and conversely.

The net radial defocusing is due to a radially outward radial electric force and a radially inward magnetic force. For relativistic beams the forces cancel and there is no net radial force. For nonrelativistic beams focusing must be provided to compensate for this effect. We will see that there are exceptions, and there are circumstances for which the rf fields do provide a net focusing without violating these principles. At very low velocities, the velocity change in the gap is large, and the particles can be focused by mechanism (3). This is sometimes called electrostatic focusing because it is the mechanism at work for electrostatic lenses. Also for structures like the RFQ, the alternating-gradient focusing principle results in a net focusing force in all three planes, even

though at any point there is defocusing in one of the planes. Another configuration that provides net focusing in all three planes is known as alternating-phase focusing, where the accelerating gaps are arranged so that the synchronous phase alternates on the two sides of the crest.

Focusing is also needed for other reasons. The beam always has small transverse velocity components, which originate in the ion source for the random thermal motion and from beam optics aberrations in the ion- source extraction system. Space-charge forces also act to increase the transverse velocity components. Therefore focusing is necessary to confine the beam and provide high transmission.

The solution to this problem in the first proton linacs was to install conducting foils and later conducting grids in the exit drift tubes of each gap, which caused the electric field lines to terminate on these conductors. These approaches effectively removed the defocusing in the second half of the gap. But the discovery of the alternating-gradient focusing principle, led to the use of quadrupole lenses for focusing, which provided a much better solution, and higher beam currents became possible.

5.2.2 Radial Impulse from the Equivalent Traveling Wave

The easiest way to evaluate the radial forces is to use the fields of the equivalent traveling wave. The nonzero electric-field components of the equivalent traveling wave experienced by a particle of phase ϕ were derived in Section 3 as

$$E_z = E_0 T I_0(Kr)\cos\phi, \quad E_r = -\gamma_s E_0 T I_1(Kr)\sin\phi \ ,$$

and the azimuthal magnetic field was

$$B_\theta = -\frac{\gamma_s \beta_s}{c} E_0 T I_1(Kr)\sin\phi \ .$$

The radial Lorentz force component depends on both the radial electric field and the azimuthal magnetic field and is

$$\frac{dP_r}{dt} = q(E_r - \beta c B_\theta) = -q\gamma_s(1-\beta\beta_s)I_1(Kr)E_0 T\sin\phi \ .$$

This is the result we need to evaluate the effect of the radial fields, but we will put it into a more convenient form for discussion. The radial momentum can be written as $p_r = mc\gamma\beta r'$, where $r' = dr/dz$. The impulse over a length L will be

$$\Delta(\gamma\beta r') = \frac{1}{mc}\int_0^L -q\gamma_s(1-\beta\beta_s)E_0 T I_1(Kr)\sin\phi\frac{dz}{\beta c}$$

$$= -q\frac{\gamma_s(1-\beta\beta_s)}{mc^2\beta}E_0 T I_1(Kr)\sin\phi L.$$

If we make the (usually good) approximation that $\beta \approx \beta_s$ then

$$\Delta(\gamma\beta r') = -\frac{qE_0 T I_1(Kr)\sin\phi L}{mc^2\gamma_s\beta_s} \ .$$

For small Kr we have $I_1(Kr) \approx 1 + Kr/2$, and $\Delta(\gamma\beta\dot{r}) = -\frac{\pi q E_0 T \sin\phi L}{mc^2\gamma_s^2\beta_s^2\lambda} r$.

For longitudinal stability the sign of ϕ_s is negative, and on average all particles executing stable oscillations about the synchronous particle will also have negative phase. Therefore the radial impulse is positive, which means an outward or defocusing impulse. We see that the defocusing force vanishes in the extreme relativistic limit, where the attractive radial magnetic force cancels the repulsive electric force. The defocusing impulse is largest at low velocities and at $\phi = -90°$, where the field crosses zero.

5.2.3 Solution of Maxwell's Equations near Axis for TM Mode

For most cases the previous treatment using the equivalent traveling wave is sufficient. But for very low velocities, where the relative velocity change in the accelerating gap is large, we need to look at the problem again more carefully. Again, we assume that for the mode of interest E_z, E_r, and B_θ are the only nonzero field components (as is true for a uniform cylindrical cavity). The nonzero components of Maxwell's equations are the following.

$$(1)\quad \frac{1}{r}\frac{\partial(rE_r)}{\partial r} + \frac{\partial E_z}{\partial z} = 0 \quad \text{from}\left(\nabla\cdot\bar{E} = 0\right),$$

$$(2)\quad \frac{\partial E_r}{\partial z} - \frac{\partial E_z}{\partial r} = -\frac{\partial B_\theta}{\partial t} \quad \text{from}\left(\nabla x\bar{E}\right)_\theta = -\frac{\partial B_\theta}{\partial t},$$

$$(3)\quad -\frac{\partial B_\theta}{\partial z} = \frac{1}{c^2}\frac{\partial E_r}{\partial t} \quad \text{from}\left(\nabla x\bar{B}\right)_r = \frac{1}{c^2}\frac{\partial E_r}{\partial t},$$

$$(4)\quad \frac{1}{r}\frac{\partial(rB_\theta)}{\partial r} = \frac{1}{c^2}\frac{\partial E_z}{\partial T} \quad \text{from}\left(\nabla x\bar{B}\right)_z = \frac{1}{c^2}\frac{\partial E_z}{\partial t}.$$

We assume that near the axis E_z is independent of r. Then from Eq. (1)

$$rE_r = -\frac{\partial E_z}{\partial z}\int_0^r r dr, \quad \text{or} \quad E_r = -\frac{\partial E_z}{\partial z}\frac{r}{2}.$$

Differentiating with respect to r gives the related form

$$\frac{\partial E_r}{\partial r} = -\frac{1}{2}\frac{\partial E_z}{\partial z}.$$

From Eq. (3) $\frac{\partial B_\theta}{\partial z} = -\frac{1}{c^2}\frac{\partial E_r}{\partial t} = \frac{r}{2c^2}\frac{\partial}{\partial z}\frac{\partial E_z}{\partial t}.$

Integrating over z gives $B_\theta = \frac{r}{2c^2}\frac{\partial E_z}{\partial t}.$

Also $\frac{\partial B_\theta}{\partial r} = \frac{1}{2c^2}\frac{\partial E_z}{\partial t}.$

5.2.4 Radial Impulse from Standing-Wave Field in the Gap

Using the above results, we can derive expressions for the fields near the axis. We assume the standing-wave field solution for E_z near the axis looks like

$$E_z(r,z,t) = E_a(z)\cos(\omega t + \phi).$$

If we look at the shape of $E_a(z)$ in a typical accelerating gap, we see that when E_a is increasing with respect to z in the beginning of the gap, E_r is negative, which means radial focusing. When E_a is decreasing with respect to z at the end of the gap, E_r is positive, which means radial defocusing.

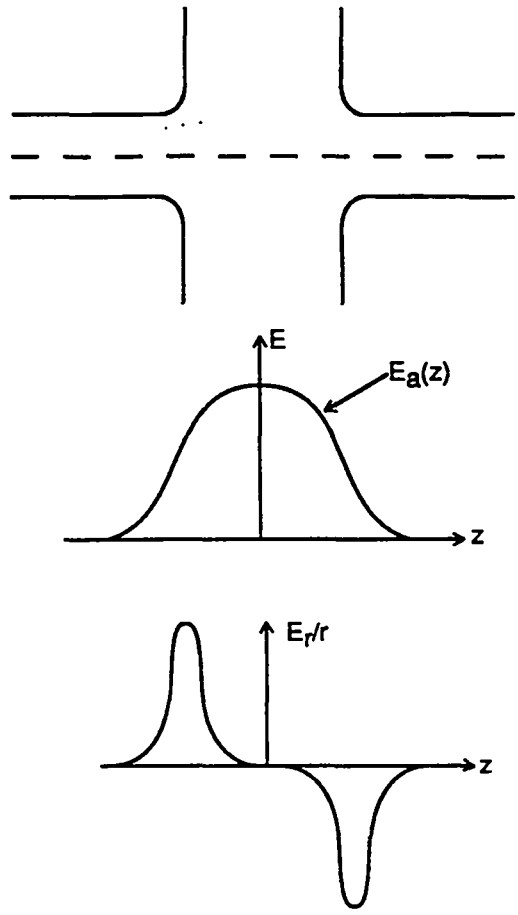

Fig. 5.12. Longitudinal and radial electric field in an rf gap.

Under what conditions can there be a net radial focusing? If the field is rising in time, as is necessary for longitudinal focusing, the defocusing field at the exit will be larger than the focusing field at the entrance. This effect usually dominates. But for very low velocities, when there are large velocity changes in the gap, the velocity increase in the gap means that the particle spends less time in the exit half of the gap than in the entrance half. This can give rise to a net focusing impulse. The momentum impulse near the axis is

$$\Delta p_r = q\int_{-L/2}^{L/2}\left(E_r - \beta c B_\theta\right)\frac{dz}{\beta c} = -\frac{q}{2}\int_{-L/2}^{L/2} r\left[\frac{\partial E_z}{\partial z} + \frac{\beta}{c}\frac{\partial E_z}{\partial t}\right]\frac{dz}{\beta c}.$$

First, examine the case where the velocity change and position change over the gap are small. The variation of these quantities gives rise to the electrostatic focusing effect, to which we will return. To simplify the above integral it is convenient to use

$$\frac{dE_z}{dz} = \frac{\partial E_z}{\partial z} + \frac{1}{\beta c}\frac{\partial E_z}{\partial t} ,$$

which expresses the fact that the total rate at which the field varies for a moving particle is the sum of the change at the new position plus the change in time. This substitution is useful because it will allow us to combine terms after integration. We use this to eliminate the partial derivative with respect to space, and we have

$$\Delta p_r = -\frac{qr}{2\beta c}\int_{-L/2}^{L/2}\left[\frac{dE_z}{dz} - \frac{1}{\beta c} + \frac{\beta}{c}\frac{\partial E_z}{\partial t}\right]dz.$$

The integral over the total derivative vanishes if the interval L extends into zero field at both ends, or if the field is periodic with period L.

$$\Delta p_r = \frac{qr\omega}{2\gamma^2\beta^2c^2}\int_{-L/2}^{L/2} E_z(z)\sin(\omega t + \phi)dz .$$

Consider a particle at the origin at time $t = 0$, so that $\omega t = kz$, where $k = 2\pi/\beta\lambda$.
We use the trigonometric relation

$$\sin(\omega t + \phi) = \sin\omega t\cos\phi + \cos\omega t\sin\phi ,$$

substitute $\omega t = kz$, and take the origin at the electrical center, as we did in Section 3 for the analysis of acceleration in a gap. Then

$$\Delta p_r = -\frac{qr\omega}{2\gamma^2\beta^2c^2}\sin\phi\int_{-L/2}^{L/2} E_z(z)\cos kz dz.$$

We use the definition of transit-time factor, and substitute $p_r = mc\gamma\beta r'$, to obtain

$$\Delta(\gamma\beta r') = -\frac{\pi q E_o T\sin\theta L}{mc^2\gamma^2\beta^2\lambda} r.$$

In the approximation that $\beta = \beta_s$, the result is the same as that obtained from the equivalent traveling wave.

5.2.5 Electrostatic Focusing Effect in the Gap

Now we return to the electrostatic focusing effect. Because this effect occurs at low velocity, we neglect the magnetic force. The radial momentum impulse is

$$\Delta p_r = q\int_{-L/2}^{L/2} E_r \frac{dz}{\beta c} = -\frac{q}{2\beta c}\int_{-L/2}^{L/2} r\frac{\partial E_z}{\partial z}dz.$$

For a specific example we consider the square-wave field defined by

$$E_z = \begin{Bmatrix} E_g\cos(\omega t+\phi), & |z| \le g/2 \\ 0, & |z| \ge g/2 \end{Bmatrix}.$$

Then $\frac{\partial E_z}{\partial z} = E_g\left[\delta\left(z+\frac{g}{2}\right)-\delta\left(z-\frac{g}{2}\right)\right]\cos(\omega t+\phi)$,

where δ is the Dirac delta function defined by $\int\delta(x)dx = 1$, and $\delta(x) = 0$ for $|x| > 0$. As before we calculate the momentum change of a particle with $z = \beta ct$, and we write

$$\Delta p_r = -\frac{q}{2}E_g\int\frac{r}{\beta c}\left[\delta\left(z+\frac{g}{2}\right)-\delta\left(z-\frac{g}{2}\right)\right]\cos\left(\frac{2\pi z}{\beta\lambda}+\phi\right)dz ,$$

$$\text{or } \Delta p_r = -\frac{q}{2c}E_g L\left[\frac{r_1}{\beta_1}\cos\left(\frac{\pi g}{\beta\lambda}-\phi\right)-\frac{r_2}{\beta_2}\cos\left(\frac{\pi g}{\beta\lambda}+\phi\right)\right],$$

where 1 and 2 refer to the entrance and exit planes of the gap. This form is sufficient to see the physics. Because of the acceleration $\beta_1 < \beta_2$. For ϕ near zero (near the crest), the overall sign will be negative, if the radius $r_1 > r_2$. The latter condition is expected, because the entrance field functions as a thin focusing lens and the exit lens as a thin defocusing lens. Really, three effects determine the lens strength: (1) More time is spent at the entrance (focusing) end than at the exit (defocusing) end. (2) The times at which the two kicks occur are not symmetrical about the time of passage past the center of the gap, an effect that helps the defocusing because the field is rising and is larger for longer gaps. (3) The beam has a smaller radius at the exit than at the entrance because of the focusing of the entrance and defocusing at the exit. This increases the net focusing.

5.2.6 Other Descriptions of Transverse Motion in the Gap

In the smooth approximation we replace the effect of the gap with an average force that acts continuously on the beam. We ignore the electrostatic focusing effect and make the identification

$$\frac{d\gamma\beta x'}{ds} = \frac{\Delta\gamma\beta x'}{L} = -\frac{\pi q E_0 T\sin\phi}{mc^2\lambda(\gamma\beta)^2}x, \text{ or } \frac{1}{\gamma\beta}\frac{d}{ds}\gamma\beta x' + \frac{\pi q E_0 T\sin\phi}{mc^2\lambda(\gamma\beta)^3}x = 0.$$

This can also be written as $\frac{1}{\gamma\beta}\frac{d}{ds}\gamma\beta x' - \frac{k_{\ell 0}^2}{2}x = 0,$

where $k_{\ell 0}^2 = \frac{2\pi q E_0 T\sin(-\phi)}{mc^2\lambda(\gamma\beta)^3}$ defines the longitudinal wavenumber, defined earlier in this section.

If the change of velocity in the gap is small, we can write

$$\Delta x' = \frac{\pi q E_0 T \sin(-\phi) L}{mc^2 \lambda (\gamma\beta)^3} x.$$

This suggests a simple thin-lens treatment. The effective thin-lens focal length is

$$\frac{1}{f_g} = \frac{Dx'}{x} = \frac{\pi q E_0 T \sin(-\phi) L}{mc^2 l (\gamma\beta)^3}.$$

When ϕ is negative to satisfy the longitudinal focusing requirement, the focal length is positive, corresponding to a defocusing lens. Then the effect of the gap can be represented by an entrance drift length to the center of the gap, the above thin-lens kick at the center of the gap, and a drift through the exit side of the gap.

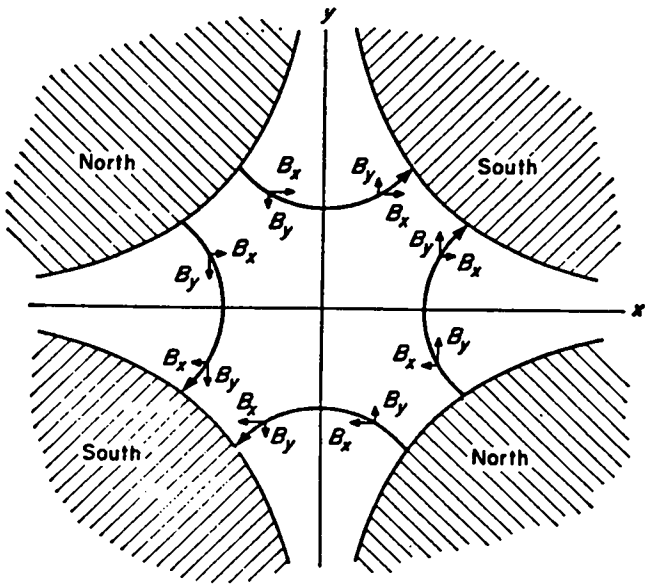

Fig. 5.13. Quadrupole magnet.

5.2.7 Quadrupole Focusing

For most linacs quadrupole focusing has been employed, since its discovery in the early 1950s. A cross section of a quadrupole magnet showing magnetic field lines is given in Fig. 5.13. The quadrupoles are installed within the drift tubes in drift-tube linacs, and are used between the tanks in coupled-cavity linacs. For a positive particle moving parallel to the beam axis, with velocity β and transverse coordinates x and y, the equations of motion for a perfect quadrupole lens with axial position s as the independent variable are

$$\frac{d^2x}{ds^2} + \kappa^2(s)x = 0, \text{ and } \frac{d^2y}{ds^2} - \kappa(s)y = 0,$$

where $\kappa^2(s) = \frac{qG(s)}{mc\gamma\beta}$.

The gradient is $G = B_x/y = B_y/x$. For a pole-tip of radius a_0 and pole-tip field B_0 the gradient is

$G = B_0/a_0$. With the polarity we have chosen, x is focusing and y is defocusing. Changing the polarity reverses the signs so that x would be defocusing and y would be focusing.

The effect of the rf defocusing in the gap may be approximately included as a continuous force from the equivalent traveling wave. The latter method gives

$$\frac{d^2x}{ds^2} + \kappa^2(s)x - \frac{k_{\ell 0}^2}{2}x = 0\,, \text{ and } \frac{d^2y}{ds^2} - \kappa^2(s)y - \frac{k_{\ell 0}^2}{2}y = 0,$$

where near the axis we have $k_{\ell 0}^2 = \dfrac{2\pi q E_0 T \sin(-\phi)}{mc^2\lambda(\gamma\beta)^3}$.

The quadrupoles are arranged in a regular lattice, which is either periodic or quasiperiodic to allow for the increasing cell lengths as the beam is accelerated. The most common lattice configuration (Fig. 5.14) is the FODO array (focusing-zero field-defocusing-zero field, etc). Because of the periodic force the equations of motion have the form of Hill's equation, for which the solutions are well known in the accelerator field (see Section 1).

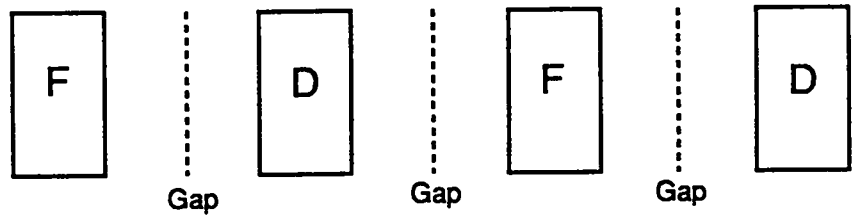

Figure 5.14 FODO Quadrupole lattice with accelerating gaps.

A useful method for studying the solution is to use the matrix formalism. The effect of the rf defocusing can be approximated by a thin-lens impulse at the center of the gap, and the quadrupoles can be treated as hard-edged elements with length equal to the effective length of the magnets. The properties of the solution are similar to those of the solutions to the Mathieu equation. This was studied by Smith and Gluckstern[16], and the results can be expressed in terms of a stability chart (Fig. 5.15). The stability chart is a plot of $\theta_0^2 = q\beta c G\lambda^2 / mc^2$ (dimensionless measure of the quadrupole focusing strength) as the ordinate, versus $\Delta = \pi q E_0 T\lambda \sin\phi / mc^2\beta$ (dimensionless measure of the rf impulse) as the abscissa. Any point in this space lies in either a stable or an unstable region. The lower boundary of the stability chart corresponds to a phase advance per focusing period of $\sigma = 0$, and the upper boundary has $\sigma = \pi$. There are an infinite number of passbands but the lowest passband is the only one that has sufficient bandwidth for a practical focusing system. The parameters can be chosen by using the stability chart to pick an operating trajectory as a function of particle energy so that all particles lie in the stable region.

An approximate formula for the phase advance per focusing period can be obtained by using the matrix method to form the transport matrix over one full period, and treating both the rf gaps and the quadrupole lenses as thin-lens impulses.

Keeping only the lowest-order terms results in a simple approximate formula. Recall that the focal length for the rf gap is given by

$$\frac{1}{f_g} = \frac{\Delta x'}{x} = \frac{\pi q E_0 T \sin(-\phi) L}{mc^2\lambda(\gamma\beta)^3}.$$

L is the length over which the rf impulse is integrated. The quadrupole focal length is given by

$$\frac{1}{f_Q} = \frac{\Delta x'}{x} = \pm \frac{qG\ell}{mc\gamma\beta}.$$

We obtain to lowest order

$$\sigma^2 \cong \left[\frac{L}{f_Q}\right]^2 - 4\frac{L}{f_g}\ ; \text{ or } \sigma^2 \cong \left[\frac{qG\ell L}{mc\gamma\beta}\right]^2 - \frac{4\pi qE_0 T\sin(-\phi)L^2}{mc^2\lambda(\gamma\beta)^3}\ .$$

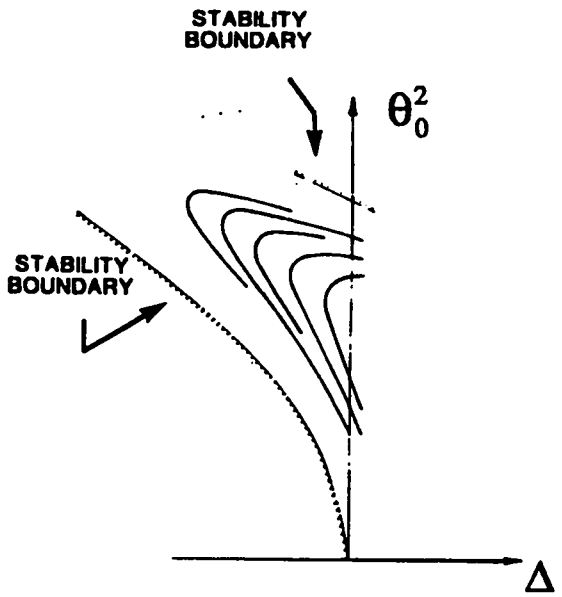

Fig. 5.15. Stability chart for transverse motion.

The length L is chosen to equal the spacing between lenses. Thus for the FODO lattice the period is 2L. The first term is the quadrupole term and the second is the rf impulse, which subtracts from the quadrupole term when ϕ is negative. This approximation is accurate to within about 10% for $\sigma < \pi/2$. For stability the quadrupole term must be larger than the rf defocusing term. We see that the rf defocusing term falls off with $\beta\gamma$ faster than the quadrupole term, so that the rf defocusing is more important at low velocities.

The phase advance per unit length $k = \sigma/2L$ is an effective wavenumber for transverse oscillations. In a smooth approximation the trajectory is sinusoidal, corresponding to simple harmonic motion, and the local effect of the individual lenses in the lattice is averaged out. Using the above approximation for σ, we have

$$k^2 = \left[\frac{\sigma}{2L}\right]^2 \cong \left[\frac{qG\ell}{2mc\gamma\beta}\right]^2 - \frac{\pi qE_0 T\sin(-\phi)}{mc^2\lambda(\gamma\beta)^3}\ .$$

This result shows that, to lowest order, the phase advance per unit length is independent of the lens spacing. But, as the lens spacing increases for fixed field strengths, s increases and reaches an upper limit for stability $\sigma < \pi$.

A smooth approximation formula for the Mathieu equation (see Bruck[17]) is useful for the nonrelativistic phase advance in the RFQ:

$$\sigma_{RFQ}^2 \cong \frac{1}{8\pi^2}\left[\frac{qV\lambda^2}{mc^2 r_0^2}\right]^2 - \frac{\pi q E_0 T \sin(-\phi)\lambda}{mc^2\beta} .$$

5.2.8 Radial Motion for Relativistic Beams

The radial rf force approaches zero for a relativistic beam because the magnetic force cancels the electric force. We now consider the radial trajectory for the particles that are being accelerated but experience no radial force. We let $\beta = 1$ and write

$$\frac{d}{dz}\left(\gamma\frac{dx}{dz}\right) = 0 \quad \rightarrow \gamma\frac{dx}{dz} = \gamma x' = \text{constant} .$$

This is a statement of transverse momentum conservation. We assume the injected beam at $z = 0$ is relativistic and has $\gamma = \gamma_0$ and an initial divergence $x' = x_0'$. Therefore transverse momentum conservation gives $\gamma x' = \gamma_0 x_0'$. Assuming the energy increases linearly with z, we write

$$\gamma = \gamma' z + \gamma_0 .$$

We now integrate a second time and obtain the total displacement at the end of the machine caused by an initial divergence at injection:

$$\Delta x = \int_0^z x' dz = \gamma_0 x_0' \int_0^z \frac{dz}{\gamma} = \frac{\gamma_0 x_0'}{\gamma'} \ln\left[\frac{\gamma}{\gamma_0}\right] = x_0' z \frac{W_0}{W - W_0} \ln\left[\frac{W}{W_0}\right] .$$

The trajectory is logarithmic rather than linear (see Fig. 5.16). This is because transverse momentum is conserved and the relativistic mass is increasing, which implies the divergence angle must decrease. One finds that for z = 3000 m, (the length of the SLAC accelerator), and for a maximum divergence of 0.25 mrad at an initial energy $W_0 = 40$ MeV, the displacement at a final energy of W = 40 GeV is only $\Delta x = 5$ mm. This is a remarkably small displacement, and it shows that for the relativistic case not much focusing is required.

Additional insight into explaining the very small displacement is obtained by seeing what the accelerator looks like in the frame moving with the same longitudinal velocity as the beam. Because of Lorentz contraction, if dz is a longitudinal element of length in the laboratory frame, where the accelerator is at rest, the element in the moving frame dz_m is

$$dz_m = dz / \gamma(z) .$$

The length of the accelerator ℓ_m in the moving frame is given in terms of the length ℓ in the laboratory frame by

$$\ell_m = \int_0^{\ell_m} dz_m = \int_0^{\ell} \frac{dz}{\gamma' z + \gamma_0} = \frac{mc^2 \ell}{W - W_0} \ln\left[\frac{W}{W_0}\right] .$$

For the SLAC linac using $\ell = 3000\,\text{m}$, $W_0 = 40$ MeV, and W = 40 GeV, we find $\ell_m = 0.27$ m. Because the accelerator appears so short in the moving frame, it is not as surprising that the displacement of the particles is so small.

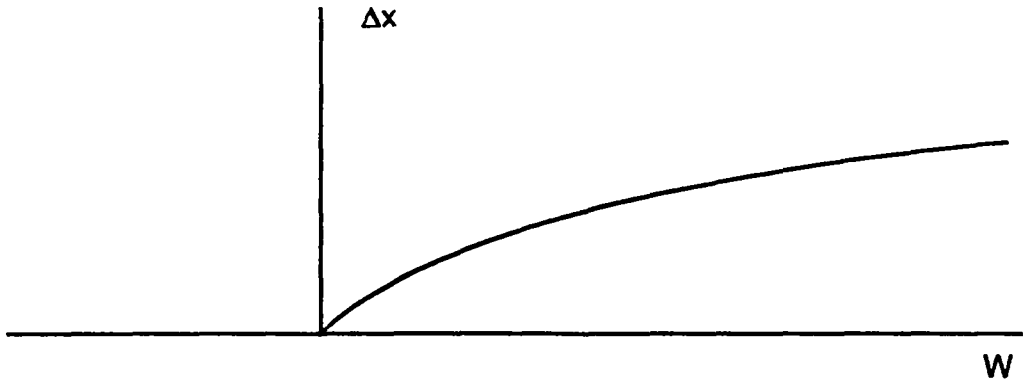

Fig. 5.16. Transverse deflection versus energy for an accelerated relativistic beam.

5.3 Problems

5-1. The parameters of a 400-MHz proton drift-tube linac at the injection energy of 2.5 MeV are $E_0T = 2$ MV/m and $\phi_s = -30$ degrees. What is the ratio of the energy acceptance (full height of the initial separatrix) to the injection energy?

5-2. For the drift-tube linac of problem 1, what is $(E_0T)_{threshold}$ for forming an initial bucket for synchronous acceleration?

5-3. The drift tube linac of problem 1, with constant $E_0T = 2$ MV/m and $\phi_s = -30$ degrees, accelerates a proton beam from 2.5 to 25 MeV. (a) Calculate the longitudinal phase advance per unit length k_ℓ in radians per meter at the injection energy of 2.5 MeV. Neglecting the increase of β from acceleration, how many rf periods are in one longitudinal oscillation at injection? (b) Repeat part (a) at the output energy of 25 MeV.

5-4. A 1284-MHz coupled-cavity linac accelerates a proton beam from 70 to 600 MeV. Ignore the effects of space charge.(a) If the maximum phase amplitude $\Delta\phi_0$ of the longitudinal oscillations is 10° at injection, what is its value at 600 MeV? (b) If the energy amplitude ΔW_0 of the longitudinal oscillations is 0.2 MeV at injection, what is its value at 600 MeV? Does the fractional energy spread increase or decrease? (c) Calculate the phase width ψ and the energy half-width ΔW_{max} of the separatrix at 70 and 600 MeV, assuming $E_0T = 7$ MV/m and $\phi_s = -25°$. How do the changes in the maximum dimensions of the separatrix between 70 and 600 MeV compare with the changes in the beam?

5-5. Suppose a coupled-cavity linac is composed of 1284-MHz tanks with 16 cells each, and has the parameters $E_0T = 7$ MV/m and an effective synchronous phase of $\phi_s = -25$ degrees (this is really the mean phase of the reference particle in each tank). At 100 MeV what is the phase excursion of the reference particle as it travels through the tank, and what is an approximate value of the injection phase?

5-6. A 0.25-MeV electron beam is injected into a 3-GHz accelerating structure that supports a traveling wave with phase velocity equal to the velocity of light. (a) What accelerating field is required to capture a beam injected at a phase near $\phi_i = -90$ degrees and to reach an asymptotic phase at the crest. (b) What is the asymptotic phase width of the beam if the initial phase width is 30°?

5-7. A FODO array of permanent-magnet quadrupole lenses with gradient G = 100 T/m and effective length $\ell = 3$ cm is used to focus a low-current proton beam in a 400-MHz drift-tube linac. Assume the array is periodic with lens spacing equal to $\beta\lambda$ (quadrupoles in every drift tube) at the injection energy of 2.5 MeV. (a) Use the smooth approximation formula in Section 5.2.7 for transverse phase advance per focusing period σ to calculate σ for the quadrupoles alone (as if $E_0T = 0$). (b) Calculate σ when $E_0T = 1$ MV/m and $\phi = -30$ degrees. Are the particles stable transversely? (c) For the same −30 degree phase and the same quadrupole array, what is the maximum accelerating field E_0T for transverse stability?

6 MULTIPARTICLE BEAM EFFECTS

6.1 Beam Ellipse and Emittance

6.1.1 Beam Quality, Phase Space, and Emittance

A beam in a linear accelerator generally consists of a collection of particles with the same electric charge, moving in approximately the same direction, with approximately the same position, phase, and energy. To maintain these conditions over a long distance, we have already seen that focusing is generally required. The term "beam quality" is sometimes used to describe the coherence of the beam; i.e. the degree to which the beam particles have nearly the same coordinates as the reference particle, which travels on the axis with a specified energy and phase. By this view the highest quality beam would consist of particles whose coordinates and momenta are all the same.

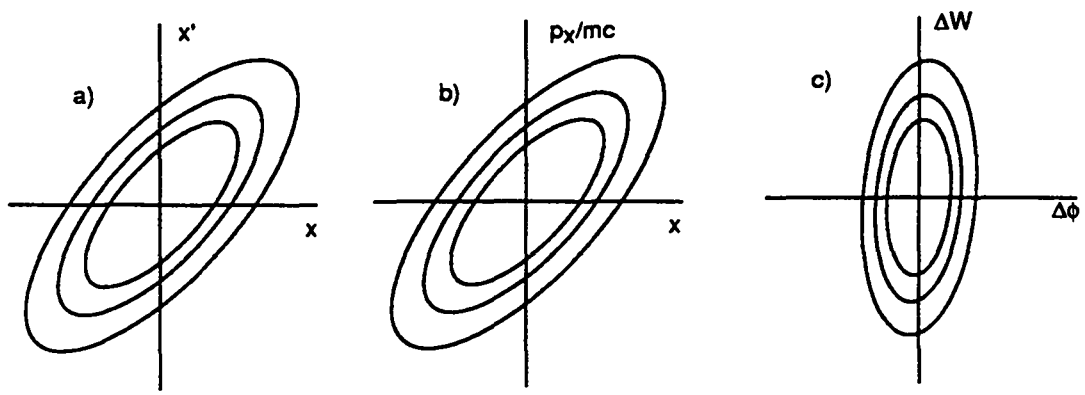

Fig. 6.1 Isodensity contours of the beam in (a) unnormalized transverse phase space, (b) normalized transverse phase space, and (c) longitudinal phase space. The emittance associated with any elliptical contour is the area of that contour divided by π.

To make the concept of beam quality more quantitative, we will define the beam emittances, figures of merit proportional to the two-dimensional phase-space areas, which decrease with increasing beam quality. Unfortunately, there are several definitions of emittance, and this leads to much confusion. We will present the definitions that are most common in the linear-accelerator field and point out areas of ambiguity. It is necessary to introduce the definitions of phase space, phase-space area of the beam, and eventually the emittance. We recognize that every particle can be described by its three Cartesian coordinates and three momentum components, or by six equivalent variables. For example, we may represent each particle in a linac by a single point in a six-dimensional phase space, defined by the two transverse coordinates, x and y, the divergence angles, dx/ds and dy/ds, and the longitudinal phase and energy variables ϕ and ΔW. It is also useful to refer to three orthogonal projections of the six-dimensional phase space called the two-dimensional phase-space projections: x-dx/ds, y-dy/ds, and ϕ-ΔW. In a linac one also refers to the transverse phase spaces x-p_x/mc and y-p_y/mc, where p_x and p_y are the normalized transverse momentum components. In either case the beam can be assigned areas in each of the two-dimensional phase-space projections, as shown in Fig. 6.1.

We will define a quantity proportional to the area, called the emittance, which is generally quoted as the figure of merit of *decreasing* beam quality. In defining the emittance, we first need to recognize the special significance of elliptical phase-space distributions. The beam-phase-space contours in a linac often have the approximate shape of an ellipse. One reason for this shape is the predominance of linear focusing forces. (By linearity we refer to the linear dependence of the restoring forces with respect to the displacement from the design particle.) With linear focusing, the trajectory of each particle in phase space lies on an ellipse. In general, a beam is said to be matched when the isodensity contours of the beam in phase space are concentric and similar to the trajectory ellipses. Therefore matched beams have elliptical contours. Furthermore, with linear focusing, elliptical distributions in phase space, even for unmatched beams, remain elliptical. Because of the tendency of beams to exhibit elliptical phase-space distributions, and because the area of an ellipse is π times the product of the semi-axes, it has become conventional to define, for each two-dimensional projection, a quantity called the emittance of the beam, which corresponds to the product of the semiaxes of an ellipse. The general equation for an ellipse can be written as

$$\gamma x^2 + 2\alpha x x' + \beta x'^2 = \varepsilon,$$

where $\gamma\beta - \alpha^2 = 1$, and the area of the ellipse is $\pi\varepsilon$. The definition of the emittance ε for any two-dimensional phase-space area (transverse or longitudinal) is

$$\varepsilon = \text{Area} / \pi .$$

Even when the phase-space area is not really elliptical, an effective ellipse is usually assumed. The ideal beam with maximum beam quality is the zero-emittance beam — called a laminar beam because it exhibits laminar-like flow. Laminar beams represent the ideal of a highly ordered and coherent beam, which, however, is never achieved in practice. Real beams have nonzero emittances at the source, due to the finite temperature of the source and to aberrations in the extraction optics.

Having defined the emittance in terms of an elliptical area of two-dimensional phase space, we return to the question of which phase-space area to select to characterize a real beam. If the beam distribution in phase space had a well-defined boundary, its emittance would be defined simply by the area within that boundary. However, real beams do not have well-defined boundaries. One method for assigning the phase-space area is to identify contours of equal phase-space density. A specific contour, such as one at 50% or 90% or 95% of the maximum density, might be used as a characteristic measure of the emittance. It can be shown that under certain conditions, namely (1) when Liouville's theorem is satisfied in the six-dimensional phase-space, and (2) when the forces in the three orthogonal directions are uncoupled, this definition also leads to conservation of the two-dimensional phase-space projected areas, and the emittances. The conditions under which Liouville's theorem is satisfied are (1) no dissipative forces such as radiation or multiple scattering, (2) no particles lost or created, and (3) absence of small-impact-parameter binary Coulomb collisions between particles (as opposed to smooth collective space-charge forces). When these conditions hold, the volume of six-dimensional phase space defined by any fixed-density contour of the beam is invariant. The emittances are defined in terms of the two-dimensional projections as described earlier, and the additional assumption of no coupling of the forces in different directions is necessary for emittance conservation.

6.1.2 RMS Beam Ellipse and RMS Emittance

Unfortunately, the presence of nonlinear forces can produce considerable distortion of the phase-space contours even when the areas are conserved. This distortion causes an effective growth, resulting from a filamentation process in six-dimensional phase space, in which the original beam-density distribution encloses regions that are rarified, and the average phase-space coordinates increase. Furthermore, forces that couple the motion between the three directions can cause real growth in the two-dimensional projected areas even though the six-dimensional volume is constant. Consequently it becomes useful to introduce another definition for the effective emittance, based on mean-square values or second moments of the coordinates and momenta. This definition is more relevant because it applies to arbitrary particle distributions and it is determined by the rms beam characteristics of the beam distribution.

The definition of rms emittance follows from the description of an arbitrary phase-space distribution by a characteristic rms ellipse (see Fig. 6.2). The general form of the rms ellipse is defined by Courant-Snyder parameters α_r, β_r, and γ_r, and an rms emittance ε_r that are defined in terms of the second moments of the particle distribution. To be specific we will describe the definitions for an unnormalized transverse emittance in x-x' space. For simplicity let us assume that the centroid of the beam lies on the axis. The point (x, x') lies on the rms ellipse if

$$\gamma_r x^2 + 2\alpha_r x x' + \beta_r x'^2 = \varepsilon_r \ ,$$

where $\gamma_r\beta_r - \alpha_r^2 = 1$. We define the ellipse parameters in the following manner. First, we require that the ellipse projections on the x and x' axes are equal to the rms values. Thus, we require

$$\overline{x^2} = \beta_r \varepsilon_r \quad \text{and} \quad \overline{x'^2} = \gamma_r \varepsilon_r \ .$$

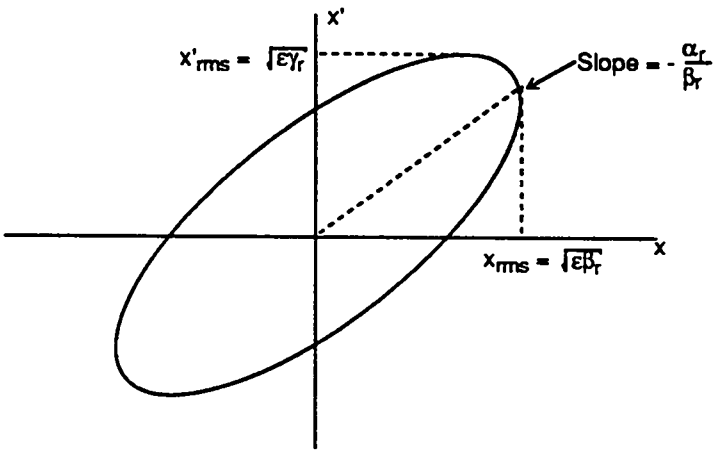

Fig. 6.2 The rms ellipse.

Furthermore, for the case of a matched beam with linear focusing, where the isodensity contours of the beam are concentric and similar to the trajectory ellipses, we will require that the rms ellipse also be concentric and similar. Thus, because the trajectory ellipses relate α and β by $\alpha = -\beta'/2$, we also require the same relationship

for α_r and β_r. Thus, we define

$$\alpha_r = -\frac{\beta_r'}{2} = -\frac{1}{2\varepsilon_r}\frac{d\overline{x^2}}{ds} = -\frac{\overline{xx'}}{\varepsilon_r} ,$$

where we have equated the derivative of the average over the particle distribution to the average of the derivative, and we assume that the emittance of the matched beam is constant. Therefore, the ellipse parameters have been defined in terms of the second moments of the distribution as

$$\beta_r = \frac{\overline{x^2}}{\varepsilon_r} , \quad \gamma_r = \frac{\overline{x'^2}}{\varepsilon_r} , \quad \text{and} \quad \alpha_r = -\frac{\overline{xx'}}{\varepsilon_r} .$$

We recall that the ellipse parameters are not independent, but are related by $\gamma_r\beta_r - \alpha_r^2 = 1$. The rms emittance as a function of the second moments is obtained by substituting the definitions of the ellipse parameters into this relationship. Thus,

$$1 = \beta_r\gamma_r - \alpha_r^2 = \frac{\overline{x^2x'^2}}{\varepsilon_r^2} - \frac{\overline{xx'}^2}{\varepsilon_r^2} ,$$

or, the rms emittance is $\varepsilon_r = \sqrt{\overline{x^2x'^2} - \overline{xx'}^2}$.

A simple exercise may be helpful in understanding the main characteristics of the rms emittance. Consider a particle distribution in phase space (see Fig. 6.3) that lies on a line (curved in general) that passes through the origin. This represents an idealized zero-emittance beam. Assume that, for any x, the divergence x' of the particles is given by

$$x' = Cx^n , \quad n \geq 1 ,$$

where C is a constant. The second moments of this distribution are

$$\overline{x^2} , \quad \overline{x'^2} = C^2\overline{x^{2n}} , \quad \text{and} \quad \overline{xx'} = C\overline{x^{n+1}} .$$

The (squared) rms emittance is given by

$$\varepsilon_r^2 = \overline{x^2x'^2} - \overline{xx'}^2 = C^2\left[\overline{x^2x^{2n}} - \overline{x^{n+1}}^2\right] .$$

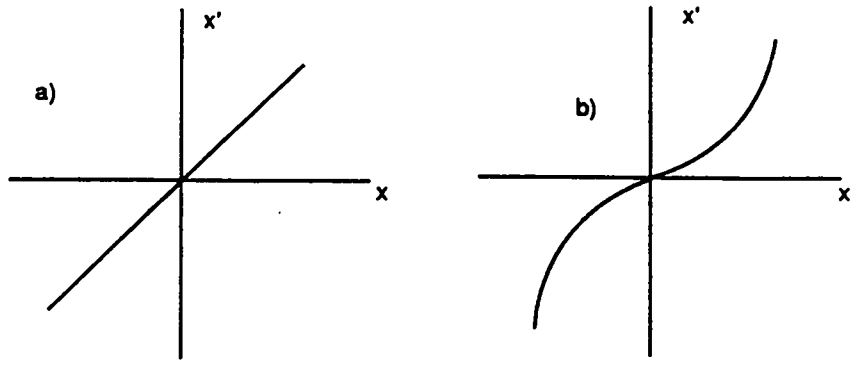

Fig. 6.3 The rms emittance ε_r for two distributions with zero area: (a) a straight line where $\varepsilon_r = 0$, (b) a curved line where $\varepsilon_r \neq 0$.

When n > 1, the relationship is nonlinear, the line in phase space is curved, and the rms emittance is in general not zero. When n = 1, the line is straight and the rms emittance is

$$\varepsilon_r^2 = C^2\left[\overline{x^2}^2 - \overline{x^2}^2\right] = 0, \quad n = 1.$$

Because this distribution is a line it has zero area for any n value. Thus the "true" emittance, which is the area/π that contains all the particles, is zero.

Therefore, we conclude that, even when the "true" emittance is zero, if the distribution lies on a curved line, its rms emittance is not zero. The rms emittance depends not only on the true area occupied by the beam in phase space but also on the distortions that produce an average curvature in the distribution. Such distortions are caused by nonlinear forces.

6.1.3 Transverse Emittance

Transverse emittance can be determined experimentally by making measurements of the particle distribution as a function of displacement and divergence. This distribution determines what is called the unnormalized emittance. For an upright ellipse, with semiaxes Δx and $\Delta x'$, the unnormalized emittance is

$$\varepsilon = \Delta x \Delta x' \ .$$

For an accelerator it is convenient to define what is called the normalized emittance, for which the dimensionless transverse momentum variable $\Delta p_x/mc$ is used instead of the divergence. Thus, for an upright ellipse the normalized emittance is

$$\varepsilon_n = \Delta x \Delta p_x / mc = \Delta x \Delta x' \beta\gamma \ ,$$

where we have assumed the paraxial approximation to write

$$p_x = \gamma m v_x = \gamma m v x' = p x' \ .$$

The normalized and unnormalized emittances are related by

$$\varepsilon_n = \varepsilon\beta\gamma \ .$$

The reason for introducing a normalized emittance is that, in an accelerator, the longitudinal momentum increases, and the average transverse momentum is constant. Therefore, the transverse momenta of the particles are unaffected by acceleration, but the divergence of the particles is reduced during acceleration because $x' = p_x/p$. Thus, the acceleration reduces the unnormalized emittance but does not affect the normalized emittance. The unnormalized emittance is not a useful figure of merit of beam quality when emittances at different energies are compared.

The typical units of either unnormalized or normalized emittance are meter-radians or centimeter-milliradians or millimeter-milliradians. Typical normalized rms emittance values range from a few tenths to a few millimeter-milliradians.

6.1.4 Longitudinal Emittance

The variables for longitudinal emittance can be chosen in several ways. We may write a normalized longitudinal emittance in the same way as we write the normalized transverse emittance,

$$\varepsilon_{n\ell} = \frac{\Delta z \Delta p}{mc} = \frac{\Delta t \Delta W}{mc} = \frac{\Delta\phi\Delta W}{\omega mc} \ ,$$

where we used the relationships $v\Delta p = \Delta W$, $\Delta z = v\Delta t$, and $\Delta\phi = \omega\Delta t$. This emittance has units of length; it can be expressed in the same units as transverse emittance and then compared with the transverse emittance values. However, phase difference $\Delta\phi$ and energy difference ΔW are more natural longitudinal units in a linac. Therefore, a very common form for longitudinal emittance is

$$\varepsilon_\ell = \Delta\phi\Delta W.$$

The units are usually expressed in degrees-MeV or degrees-keV. This emittance does not change because of acceleration, but it does change if there is a change of frequency along the accelerator. For example, if the frequency of the accelerator structure doubles at a certain energy, the emittance ε_ℓ also doubles. For a linac with a frequency transition, the emittance form $\Delta t\Delta W$ may be more useful, because it does not change when the frequency changes.

6.1.5 Emittance Conventions

Unfortunately, a lack of agreement on emittance conventions has led to much confusion. One ambiguity is whether emittance is defined as area/π (as we have done) or as area. This has led to one convention in the literature, namely, to express the emittance value as the numerical value of area/π times π: for example, $\varepsilon = 1\ \pi$ mm-mrad. This expresses the area, showing a factor π. For those who interpret the emittance as area/π, the value in this example is 1 mm-mrad. Another way to express emittance, defined as area/π, is to keep the symbol ε for area/π, by showing an explicit π on each side of the equation. Thus, in the above example, we would write

$$\varepsilon\pi = 1\pi \text{ mm} - \text{mrad} \ .$$

This convention is more consistent with our definitions, but does not have very widespread use.

The rms emittance has other areas of confusion. Some people multiply the rms emittance that we have defined (Sacherer[18] convention) by 4, and call this the rms emittance. This is the Lapostolle[19] convention, and it is useful because it gives the total emittance of an equivalent uniform beam (for continuous beams). Also, for almost all other real beams, the value of $4\times$ the rms emittance is very close to the emittance containing 90% of the beam, which is a common measure of an effective emittance that contains most of the beam. Use of the Lapostolle convention becomes confusing only when it is also called the rms emittance. One way to avoid confusion is to call this the 4-rms emittance. Some have found it convenient to quote an emittance of $6\times$ the rms emittance. This contains 95% of the beam for Gaussian beams. If this is called the 6-rms emittance instead of the rms emittance, it should lead to no confusion. Because of the lack of a convention for defining and expressing emittance, the reader of accelerator literature must beware, especially if the authors have not carefully defined the emittance they quote.

A useful result relates the total emittance to the rms emittance for uniform hyperellipsoids in n-dimensional space. The rms emittance for uniform hyperellipsoids is

$$\varepsilon_r = \frac{\varepsilon_{total}}{n+2} ,$$

and the rms size is related to the total size of the semiaxes R by

$$a = \frac{R}{\sqrt{n+2}} .$$

If a beam is uniform in 6-D space (6-D Waterbag distribution), $n = 6$. If the beam is uniform in 4-D space (4-D Waterbag distribution), $n = 4$. If the beam is uniform in all 3-D projections, $n = 3$, and for uniform beams in all 2–D projections (Kapchinskiy-Vladimirskiy distribution), $n = 2$.

6.1.6 Ellipse Transformations

Earlier, we used the transfer-matrix formalism to transport particle coordinates between two points in an accelerator. The formalism is valid when the forces acting on the beam are linear, i.e. depend linearly on the displacement from the on-axis reference particle. We now show how this can be extended to transport the beam ellipses between two locations, as shown in Fig. 6.4. The general equation of an ellipse in x-x' phase space is

$$\gamma x^2 + 2\alpha x x' + \beta x'^2 = \varepsilon ,$$

where $\gamma\beta - \alpha^2 = 1$.

It is convenient to express this equation in matrix form as

$$X^T \sigma^{-1} X = \varepsilon ,$$

where $X = \begin{bmatrix} x \\ x' \end{bmatrix}$, $X^T = [x\,x']$ is the transpose matrix, and $\sigma^{-1} = \begin{bmatrix} \gamma & \alpha \\ \alpha & \beta \end{bmatrix}$.

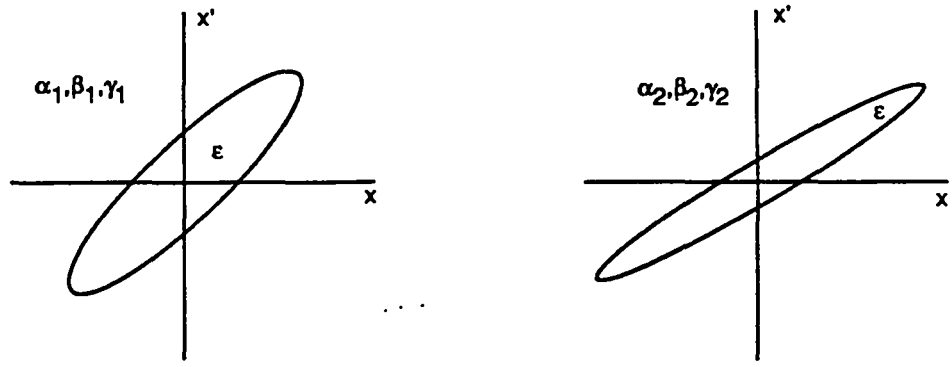

Fig. 6.4 Phase-space ellipse transformation between two locations.

This result can be easily verified by carrying out the matrix multiplication. The reason for defining the matrix as σ^{-1} instead of σ will become evident later. The inverse matrix is

$$\sigma = \begin{bmatrix} \beta & -\alpha \\ -\alpha & \gamma \end{bmatrix}.$$

Now suppose the coordinates at position 1 are transformed to new coordinates at position 2 by the action of linear forces. The transformation can be expressed in the form of a 2×2 transfer matrix R such that

$$X_2 = RX_1 .$$

The equation for the ellipse at location 1 is $X_1^T \sigma_1^{-1} X_1 = \varepsilon$.

The equation for the ellipse at location 2 is $X_2^T \sigma_2^{-1} X_2 = \varepsilon$.

where, because of the linear transformation, the ellipse emittance is assumed to be unchanged. We now obtain an expression for the σ matrix at location 2. Thus,

$$\varepsilon = X_1^T \sigma_1^{-1} X_1 = X_1^T R^T \left(R^T\right)^{-1} \sigma_1^{-1} R^{-1} R X_1 ,$$

or since $X_1^T R^T = (R\,X_1)^T$, we have

$$\varepsilon = (RX_1)^T \left[\left(R^T\right)^{-1} \sigma_1^{-1} R^{-1}\right] (RX_1) .$$

Then, the ellipse equation at location 2 is identified as

$$X_2^T \sigma_2^{-1} X_2 = \varepsilon \ ,$$

where $\sigma_2^{-1} = \left(R^T\right)^{-1} \sigma_1^{-1} R^{-1} = \left(R\sigma_1 R^T\right)^{-1}$, or $\sigma_2 = R\sigma_1 R^T$.

An equivalent expression is obtained by carrying out the above matrix multiplication, and is sometimes found to be more convenient.

$$\begin{bmatrix} \beta_2 \\ \alpha_2 \\ \gamma_2 \end{bmatrix} = \begin{bmatrix} R_{11}^2 & -2R_{11}R_{12} & R_{12}^2 \\ -R_{11}R_{21} & 1+2R_{12}R_{21} & -R_{12}R_{22} \\ R_{21}^2 & -2R_{21}R_{22} & R_{22}^2 \end{bmatrix} \begin{bmatrix} \beta_1 \\ \alpha_1 \\ \gamma_1 \end{bmatrix} .$$

The last two equations give the transformation of the ellipse parameters between locations 1 and 2. Thus, if the transport matrix R is given between two points, the ellipse transformation is obtained. This result is very useful for designing the matching optics to inject a matched beam ellipse into an accelerator with periodic focusing. It is valid even in the presence of space-charge forces, as long as those forces are linear.

6.2 Space Charge

6.2.1 Introduction

With increasing beam intensity the interaction between the like charges of the particles becomes more important. The charges produce mutually repulsive electric Coulomb fields that act in opposition to the focusing forces and reduce the stability of the beam. The Coulomb field at a distance r from a particle of charge q is

$$\vec{E}_r = \frac{q\hat{r}}{4\pi\varepsilon_0 r^2} \ .$$

In principle the total Coulomb field experienced by any particle is the sum of the fields due to all the other particles in the beam. Thus, if there are N particles in the beam, the electric field at the nth particle is

$$\vec{E}_r = \sum_{i \neq n}^{N} \frac{q\hat{r}_i}{4\pi\varepsilon_0 r_i^2} \ .$$

For linac beams with the order of 10^9 or more particles per bunch, the method of directly summing the fields from this many particles does not provide a practical solution to the calculation of the forces.

To develop a practical method for such a calculation, one may classify the electric self-interaction of the particles into two catagories: (1) the collisional regime, where the total self field is dominated by a few nearby particles that interact through small-impact-parameter binary collisions, and (2) the space-charge regime, where the total self-field is dominated by the majority of the particles producing a collective field that can be approximated by a smooth function of space and time. The collective space-charge regime occurs when nearby particles can move to shield the fluctuations of the other particles, a phenomenon known in plasma physics as Debye shielding. Ignoring the

effect of a finite-sized beam, the criterion for Debye shielding and collective behavior for a beam of number density n is that the number of particles N_D in a Debye sphere (a sphere of radius equal to the beam-Debye length λ_D) is

$$N_D = n\frac{4\pi\lambda_D^3}{3} >> 1 .$$

For accelerator beams this criterion is usually easily met and the collective space-charge force dominates; the effect of small-impact-parameter binary collisions can be neglected. However, for computer simulation of beams the bunch is represented by much fewer particles, typically 10^4, with a relatively large charge per particle. For this case, the binary collisions will be important unless the Coulomb forces are smoothed. Two common methods for doing this include (1) replacing the point charges by finite-sized charges, and (2) particle-in-cell codes where the charges are distributed at discrete locations on a mesh of points for the purpose of calculating the space-charge fields.

As the previous discussion suggests, space-charge-dominated beams behave in some respects like plasmas. Similarities include (1) particle redistribution to provide shielding from the effects of density fluctuations and external focusing fields as described above, and (2) density oscillations at the beam-plasma frequency. It may at first seem surprising that a single-charge-species beam can exhibit plasma oscillations, which are characteristic of plasmas composed of two charge species. But the effect of the external focusing force can play the role of the other charge species to provide the necessary restoring force that is the cause of such oscillations.

It is important to bear in mind that beams in linacs are also different from plasmas in some important respects. Perhaps the most important is that beam lifetimes in the linac, which are generally no more than a few microseconds, are too short for the beam to reach thermal equilibrium, even when the average external focusing forces are nearly constant. For this reason, and because Liouville's theorem and phase-space conservation often are a good approximation, the phase-space volume of the beam is a more important parameter than the beam temperature.

The space-charge fields can be separated into linear and nonlinear terms as a function of the displacement from the centroid. The linear space-charge term defocuses the beam and leads to an increase in the beam size. The nonlinear space-charge terms produce these same effects but also reduce the beam quality by further increasing the spread of the displacements, divergences, and energy.

Although the electric Coulomb force is independent of velocity, the space-charge forces in a linac depend on the velocity. First, one must account not only for the electric force between the particles but also for a magnetic force associated with the motion of the charges in the beam. While the electric force causes defocusing, the magnetic force causes attraction. This can be seen by considering the example of a long cylinder of beam charge with azimuthal symmetry and charge density qn(r) moving at velocity v. The electric field is directed radially outward, as shown in Fig. 6.5, and from Gauss's law is

$$E_r = \frac{q}{\varepsilon_0 r}\int^r n(r)rdr .$$

From Ampere's law the magnetic field is azimuthally directed and is

$$B_\theta = \frac{qv\mu_0}{r}\int^r n(r)rdr \ .$$

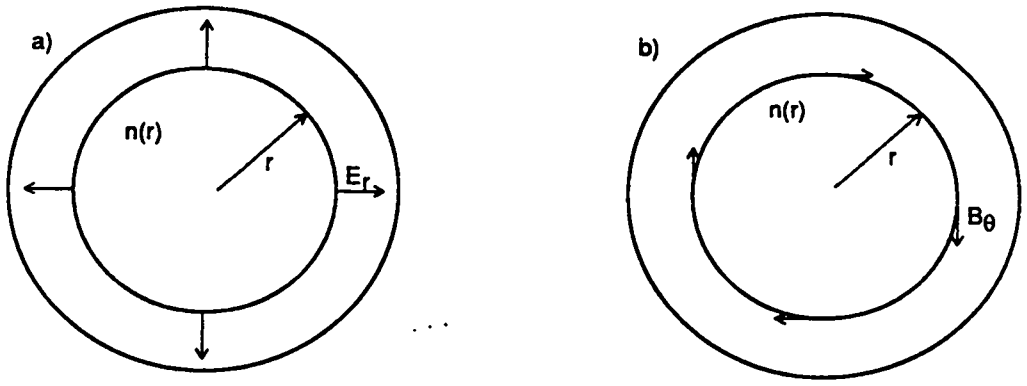

Fig. 6.5 Self-fields from a cylinder of charge with density n(r) moving with velocity v into the page: (a) self-electric-field from Gauss's law, and (b) self-magnetic field from Ampere's law.

The Lorentz force is $F_r = q(E_r - vB_\theta) = qE_r(1-\beta^2) = qE_r/\gamma^2$. Thus the attractive magnetic force, which becomes significant at high velocities, tends to compensate for the repulsive electric force. Therefore space-charge defocusing is primarily a nonrelativistic effect. It is of great concern for intense low-velocity ion beams and for electron beams at injection into a linac, but not for relativistic electron beams where $\beta \approx 1$. We will discuss this again in the next section.

The space-charge force in proton linacs is also reduced by an additional effect. When E_0 and ϕ_s are constant, the bunch length gradually increases with energy during the adiabatic acceleration, which reduces the peak current.

6.2.2 Relativistic Mass and Self-Magnetic-Field Corrections

The relativistic equations of motion are $F_i = mc\dfrac{d(\gamma\beta)_i}{dt}$, $\quad i = x, y, z.$

In the paraxial approximation we assume that $\beta_x << \beta_z$ and $\beta_y << \beta_z$. Then

$$\gamma = \left(1-\beta_x^2-\beta_y^2-\beta_z^2\right)^{-1/2} \approx \left(1-\beta_z^2\right)^{-1/2} \approx \left(1-\beta^2\right)^{-1/2} \ .$$

The longitudinal equation of motion is

$$F_z = mc\frac{d(\gamma\beta)}{dt} = mc\left(\dot{\gamma}\beta+\dot{\beta}\gamma\right) = mc\left(\dot{\beta}\gamma^3\beta^2+\dot{\beta}\gamma\right), \qquad F_z = \gamma^3 mc\dot{\beta} \ .$$

The longitudinal equation of motion has the same form as that of classical mechanics with the mass replaced by γ^3.

The transverse equation of motion will be written in a coasting-beam approximation, where we ignore acceleration. Thus

$$F_x = mc\frac{d(\gamma\beta)}{dt} = \gamma mc\dot{\beta}_x .$$

The transverse equation of motion has the same form as that of classical mechanics with the mass replaced by γ.

In Section 6.2.1 we investigated the effect of the self-magnetic-fields in the special case of a long cylindrical beam. To determine the effect of these fields in the more general case, it is convenient to Lorentz-transform the fields from the laboratory frame, where the accelerator is at rest, to the frame of reference moving with the beam, which we will call the beam frame. First, we consider the transverse fields. The field transformation is

$$E_x^\ell = \gamma\left(E_x^b - \beta c B_y^b\right); \quad \text{and} \quad \beta_y^\ell = \gamma\left(B_y^b - \frac{\beta}{c}E_x^b\right),$$

where the ℓ and b superscripts correspond to the laboratory and beam frames. We assume that the relative velocities in the beam frame can be ignored, so that the beam-frame magnetic fields are negligable. Therefore we set $B_x^b = B_y^b = 0$, and we eliminate E_x^b from the two equations. This yields

$$B_y^\ell = -\frac{\beta}{c}E_x^\ell .$$

The transverse Lorentz force is

$$F_x^\ell = q\left(E_x^\ell + \beta c B_y^\ell\right) = q\,(E_x^\ell - \frac{\beta}{c}E_x^\ell) = \frac{q}{\gamma^2}E_x^\ell .$$

Therefore the effect of the self-magnetic field can be accounted for by dividing the electric field by $1/\gamma^2$. Combining this with the transverse relativistic mass γm gives, for the effect of the self-fields, the relativistic transverse equation of motion

$$\dot{\beta}_x c = \frac{d^2x}{dt^2} = \frac{qE_x}{\gamma^3 m} .$$

The transverse velocities in the laboratory are negligable compared to the longitudinal velocities. Therefore the longitudinal magnetic field in the laboratory is also negligable. The longitudinal equation of motion is affected only by the relativistic longitudinal mass $\gamma^3 m$. Therefore, we have

$$\frac{d^2z}{dt^2} = \frac{qE_z}{\gamma^3 m} .$$

The γ^3 factor appears in all three components of the equation of motion, but for different reasons.

6.2.3 RMS Envelope Equation with Space Charge

We consider a distribution of particles in a beam moving in the s direction, where the particles satisfy the equation of transverse motion

$$x'' + \kappa(s)x - F_s = 0 \ ,$$

where the linear external force term is given by $-\kappa(s)x$ and F_s is the space-charge force term, which in general is nonlinear and includes the self-electric repulsive force and the self-magnetic attractive force. The quantity F_s is related to the space-charge electric field by $F_s = qE_s/\gamma^3 mv^2$. For simplicity we assume that the mean displacement and divergence are zero. We are interested in finding an equation of motion for the rms beam size. First, we write the equations of motion of the second moments of the distribution. Thus,

$$\frac{d\overline{x^2}}{ds} = 2\overline{xx'} \ , \quad \frac{d\overline{xx'}}{ds} = \overline{x'^2} + \overline{xx''} = \overline{x'^2} - \kappa(s)\overline{x^2} + \overline{xF_s} \ , \quad \text{and}$$

$$\frac{d\overline{x'^2}}{ds} = 2\overline{x'x''} = -2\kappa(s)\overline{xx'} + 2\overline{x'F_s} \ .$$

The averages are taken over the particle distribution. We now show that the first two equations lead to the equation of motion for the rms beam size. First, we write the rms beam size as

$$a \equiv \sqrt{\overline{x'^2}} \ .$$

Then, using the first of the above moment equations, we have

$$aa' = \overline{xx'} \ .$$

Differentiating this, and using the second of the moment equations gives

$$aa'' + a'^2 = \overline{x'^2} + \overline{xx''} \ , \quad \text{or} \quad aa'' - \frac{\overline{x^2}\,\overline{x'^2} - \overline{xx'}^2}{a^3} - \frac{\overline{xx''}}{a} \ .$$

The numerator of the second term will be recognized as the square of the rms emittance. Then, substituting the forces for x" gives

$$a'' + \kappa(s)a - \frac{\varepsilon_r^2}{a^3} - \frac{\overline{xF_s}}{a} = 0 \ .$$

This is called the rms envelope equation, and it gives the equation of motion of the rms beam size. The second term is the focusing term. The third term is the emittance term, and because it is negative it represents a repulsive pressure on the rms beam size, which depends on the emittance. The last term is the repulsive space-charge term. The equation of motion for the rms beam size looks like the single-particle equation of motion, except for the presence of the additional emittance term.

The third moment equation has not been used in this derivation. It can be shown that this equation affects the growth of rms emittance, and to obtain a time-dependent solution one would need to determine independently the evolution of the beam distribution. However, it can be shown that a useful energy-conservation principle can be derived from this equation, which leads to a useful upper limit to the emittance growth.

To carry this further we need to know the form of the particle distribution so that we can evaluate the space-charge term. We now evaluate the envelope equation for three simple examples.

Example 1: Continuous uniform cylindrical beam of radius R

From Gauss's law the electric field of a cylindrical beam of particles with charge q and velocity v, and with number density n(r), is

$$E(r) = \frac{q}{\varepsilon_o r}\int_0^r n(r) r dr \ .$$

If the current is $I = qN_\ell v$, where N_ℓ is the number of particles per unit length, the density for the uniform distribution of radius R is $n = N_\ell/\pi R^2 = I/q\pi R^2 v$. The space-charge electric field is

$$E(r) = \frac{Ir}{2\pi\varepsilon_0 R^2 v} \ .$$

For cylindrical symmetry we obtain $\overline{r^2} = \overline{x^2} + \overline{y^2} = \frac{\overline{x^2}}{2}$.

The mean square beam size in x is $\overline{x^2} = \frac{1}{2N_\ell}\int_0^R nr^2 2\pi r dr = \frac{R^2}{4}$.

Therefore the radius is related to the rms beam size in x by R = 2a. Other distributions have different ratios of R/a. The space-charge term in the rms envelope equation has the factor

$$\overline{xF_s} = \frac{q}{\gamma^3 m v^2}\overline{E_{sx} x} = \frac{qI\overline{x^2}}{2\pi\varepsilon_0\gamma^3 v^3 m R^2} = \frac{qI}{8\pi\varepsilon_0\gamma^3 v^3 m} \ .$$

Therefore the rms-envelope equation in x (or y) is

$$a'' + \kappa(s)a - \frac{\varepsilon_r^2}{a^3} - \frac{K}{4a} = 0 \ .$$

. . .

where K is a space-charge parameter called the generalized perveance given by

$$K = \frac{qI}{2\pi\varepsilon_0\gamma^3 v^3 ma} \ .$$

Example 2: Continuous Gaussian cylindrical beam

The number density is $n(r) = \frac{N_\ell}{2\pi a_r^2} \exp\left[\frac{-r^2}{2a_r^2}\right]$.

The electric field is obtained from Gauss's law as

$$E(r) = \frac{q}{\varepsilon_0 r}\int_0^r n(r) r dr = \frac{qN_\ell}{4\pi\varepsilon_0 a_r^2 r}\int_0^{r^2} \exp\left[\frac{-r^2}{2a_r^2}\right] dr^2 = \frac{qN_\ell}{2\pi\varepsilon_o r}\left[1 - \exp\left[\frac{-r^2}{2a_r^2}\right]\right].$$

To evaluate $\overline{x\,E_x}$ we use $\overline{rE_r} = \overline{xE_x} + \overline{yE_y} = 2\overline{xE_x}$.

Then

$$\overline{xF_s} = \frac{q}{\gamma^3 m v^2}\overline{E_{sx}x} = \frac{qI}{8\pi\varepsilon_0\gamma^3 v^3 m a_r^2}\int_0^{r^2}\left[1 - \exp\left[\frac{r^2}{2a_r^2}\right]\right]\exp\left[\frac{r^2}{2a_r^2}\right] dr^2 = \frac{qI}{8\pi\varepsilon_0\gamma^3 v^3 m}.$$

This is the same result as that obtained for the uniform distribution. Surprisingly, the space-charge term in the rms envelope equation is the same as that found for the uniform distribution. Then the rms envelope equation has the same form for the uniform and the Gaussian distributions.

$$a'' + \kappa(s)a - \frac{\varepsilon_r^2}{a^3} - \frac{K}{4a} = 0,$$

where K is the generalized perveance, defined earlier. We will see that the space charge term is exactly independent of the distribution for some cases, and is approximately independent of the distribution for all practical cases. This result will lead to the principle of the equivalent uniform beam for the description of the average behavior of beams with space charge.

Example 3: Uniform spherical bunch

From Gauss's law the electric field of a spherical bunch is radially outward and is given by

$$E(r) = \frac{q}{\varepsilon_0 r^2}\int_0^r n(r) r^2 dr.$$

For a uniform density over a radius R, the particle density is $3N/4\pi R^3$, where N is the number of particles in the bunch. The average current over an rf period is $I = qNc/\lambda$, where λ is the rf wavelength and c is the speed of light. The electric field is

$$E(r) = \frac{I\lambda}{c}\frac{r}{4\pi\varepsilon_o R^3}.$$

The mean-square radius is

$$\overline{r^2} = \frac{1}{N}\int_0^R r^2 n(r) 4\pi r^2 dr = \frac{3}{5}R^2 \ .$$

We use the result $\overline{r^2} = \overline{x^2} + \overline{y^2} + \overline{z^2} = 3\,\overline{x^2}$, to give $R^2 = 5\,\overline{x^2}$.

Also $\overline{rE} = \frac{I\lambda}{c}\frac{\overline{r^2}}{4\pi\varepsilon_0 R^3} = \frac{I\lambda}{c}\frac{3\overline{x^2}}{4\pi\varepsilon_0 R^3}$.

We can write $\overline{E\,r} = \overline{E_x x} + \overline{E_y y} + \overline{E_z z} = 3\,\overline{E_x x}$,

and therefore $\overline{xE_x} = \frac{I\lambda}{c}\frac{\overline{x^2}}{4\pi\varepsilon_0 R^3} = \frac{I\lambda}{c}\frac{1}{20\sqrt{5}\pi\varepsilon_0 a}$,

where $a = \sqrt{\overline{x^2}} = R/\sqrt{5}$.

The space-charge term in the envelope equation is

$$\overline{xF_s} = \frac{q\overline{xE_x}}{\gamma^3 m v^2} = \frac{qI\lambda}{20\sqrt{5}\pi\varepsilon_0 mc\gamma^3 v^2 a} \ .$$

The rms envelope equation in x (or y or z) is $a'' + \kappa(s)a - \frac{\varepsilon_r^2}{a^3} - \frac{K_3}{a^2} = 0$,

where K_s is a space-charge parameter given by $K_3 = \frac{qI\lambda}{20\sqrt{5}\pi\varepsilon_0 mc^3\gamma^3\beta^2}$

6.2.4 Envelope Equation for Continuous Elliptical Beams

Sacherer[18] and Lapostolle[19] derived envelope equations for continuous beams of arbitrary particle distribution with elliptical symmetry in x-y space (Fig. 6.6). The electric field components for the uniform distribution are

$$E_{sx} = \frac{I}{\pi\varepsilon_0 v(r_x + r_y)}\frac{x}{r_x}, \quad \text{and} \quad E_{sy} = \frac{I}{\pi\varepsilon_0 v(r_x + r_y)}\frac{y}{r_x},$$

where r_x and r_y are the semiaxes of the ellipse, related to the rms beam sizes by $r_x = 2\,a_x$, and $r_y = 2\,a_y$. The rms envelope equations apply to all distributions with elliptical symmetry; they are

$$a_x'' + \kappa_x(s)a_x - \frac{\varepsilon_{rx}^2}{a_x^3} - \frac{K}{2(a_x + a_y)} = 0, \quad \text{and} \quad a_y'' + \kappa_y(s)a_y - \frac{\varepsilon_{ry}^2}{a_y^3} - \frac{K}{2(a_x + a_y)} = 0 \ .$$

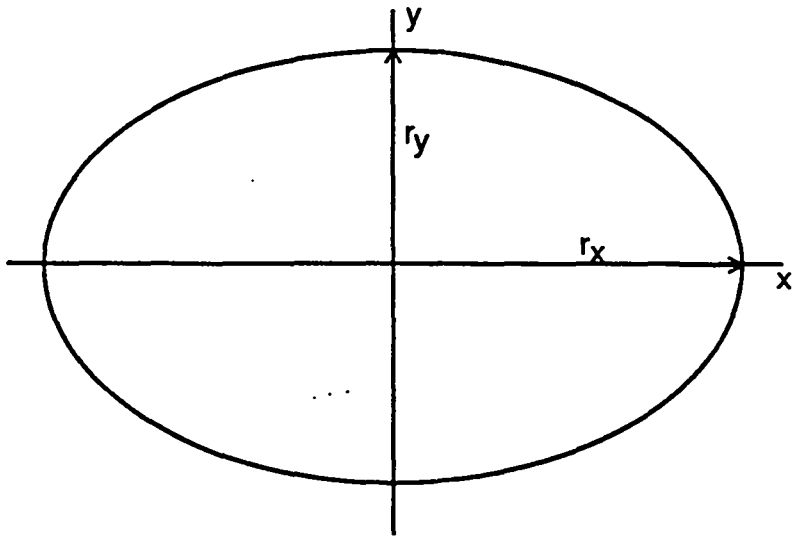

Figure 6.6 Cross section of continuous elliptical beam with semiaxes r_x and r_y.

These equations were first derived by Kapchinskiy and Vladimirskiy[20] for a stationary uniform beam (called the K-V distribution) in a quadrupole-focusing channel, and are known as the K-V envelope equations. Examples 1 and 2 above have circular symmetry in x-y space, which is a special case of elliptical symmetry. Indeed, we obtained the same space-charge term and the same rms envelope equation in those two examples.

6.2.5 Envelope Equation for 3-D Ellipsoidal Bunched Beams

The electric-field components for the three-dimensional (3-D) uniform ellipsoid (Fig. 6.7) are linear and uncoupled and are given by

$$E_{sx} = \frac{3I\lambda(1-f)}{4\pi\varepsilon_0 c(r_x + r_y)r_z}\frac{x}{r_x}, \quad E_{sy} = \frac{3I\lambda(1-f)}{4\pi\varepsilon_0 c(r_x + r_y)r_z}\frac{y}{r_y}, \quad E_{sz} = \frac{3I\lambda f}{4\pi\varepsilon_0 c r_x r_y}\frac{z}{r_z},$$

where r_x, r_y, and r_z are the semiaxes of the ellipsoid, I is the average current over an rf period, and λ is the rf wavelength.

The semiaxes are related to the rms beam sizes by $r_i = \sqrt{5}a_i, i = x,y,z$. The displacements x, y, and z are relative to the centroid of the bunch. The quantity f is an ellipsoid form factor and is a function of the parameter

$$p = \frac{\gamma r_z}{\sqrt{r_x r_y}}.$$

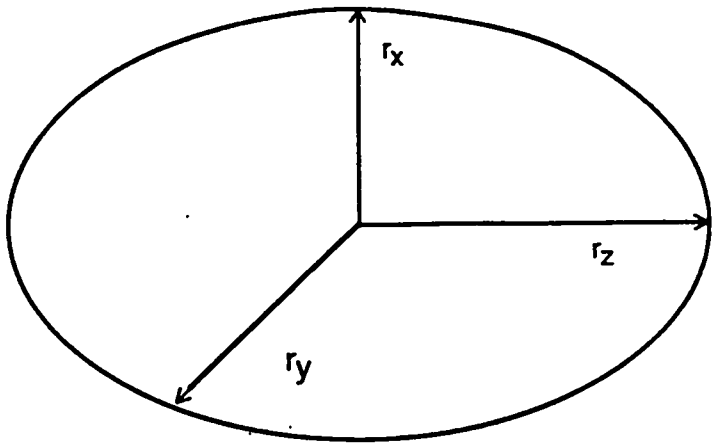

Fig. 6.7 Uniform 3-D ellipsoidal beam bunch with semiaxes r_x, r_y, and r_z.

Values of f(p) for p < 1 and f(1/p) for p > 1 can be obtained from Fig. 6.8. For a nearly spherical bunch (0.8 < p < 5), a useful approximate form is f=1/(3p). The rms envelope equations are

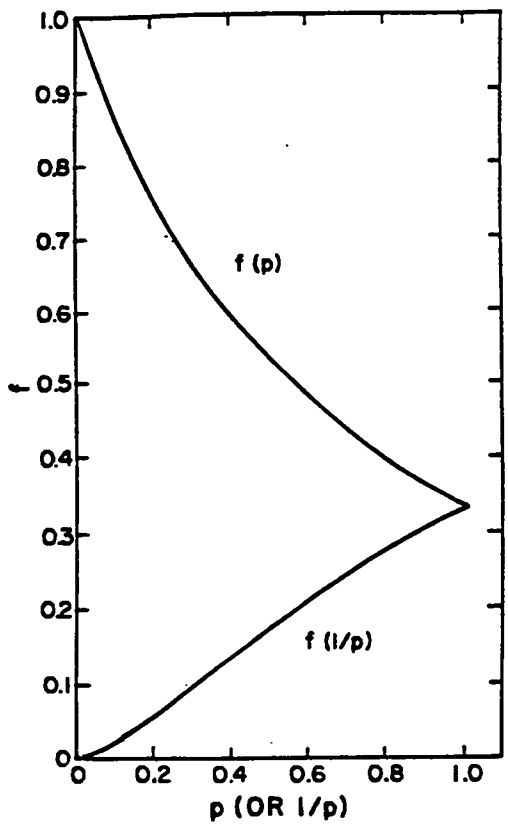

Fig. 6.8 Ellipsoid form factor f(p) vs p for p < 1 and f(1/p) for p > 1.

$$a_x'' + \kappa_x(s)a_x - \frac{\varepsilon_{r,x}^2}{a_x^3} - \frac{3K_3(1-f)}{(a_x+a_y)a_z} = 0, \quad a_y'' + \kappa_y(s)a_y - \frac{\varepsilon_{r,y}^2}{a_y^3} - \frac{3K_3(1-f)}{(a_x+a_y)a_z} = 0,$$

$$a_z'' + \kappa_z(s)a_z - \frac{\varepsilon_{r,x}^2}{a_z^3} - \frac{3K_3 f}{a_x a_y} = 0.$$

We have defined a 3-D space-charge parameter

$$K_3 = \frac{qI\lambda}{20\sqrt{5}\pi\varepsilon_0 mc^3\gamma^3\beta^2} .$$

Unlike that in the 2-D ellipsoidal case discussed above, the space-charge term is found to depend on the shape of the distribution for other distributions with ellipsoidal symmetry. However the dependence is very weak; the dependence of the space-charge term on the distribution is at the level of only a few percent.

6.2.6 Equivalent Uniform Beams

The form of the envelope equation is (nearly) independent of the distribution. If we assume that the emittances are constant, we can draw an important conclusion from this result. To calculate the rms beam trajectories, even in the presence of space-charge forces, we can replace the actual beam distribution (which may not be known) with an equivalent uniform beam having the same current and the same second moments as the real beam. It is convenient to identify an equivalent uniform beam because, as we have seen, the space-charge field of a uniform beam, with elliptical or ellipsoidal symmetry, is easily calculated and is linear.

The rms emittance is generally not constant, however, and its variation depends on the particle distribution through the third of the moment equations (see Section 6.2.3). Without knowing how the emittance varies, we can solve the envelope equation in the approximation that the emittance variation is ignored. Thus, the rms envelope equation is accurate only for distances over which the emittance growth is small. It is mainly useful for calculating the focusing properties of (short) beam-matching systems between acclererators in the presence of space-charge forces.

An advantage of the linearity of the space-charge fields in the uniform distribution is that the matrix formalism for ellipse transport, developed earlier, can be applied to problems with space charge. The matrix equation,

$$\sigma_2 = R\sigma_1 R^T ,$$

gives the transport of the ellipse parameters α, β, and γ between points 1 and 2. These parameters are elements of the σ matrix, and in linear systems the above equation can be solved by matrix multiplication if the transfer R matrix is given. The R matrix has been given earlier for common elements such as the quadrupole lens, thin lens, and drift space. To account for linear space-charge forces, we must use the space-charge electric fields given above. These fields depend on the rms beam size, which varies in the manner given by the ellipse β parameter, an element of the σ matrix. To account for space charge, we can take smaller integration steps through each element, and treat the space-charge impulse as a thin lens, which imparts a momentum impulse to each

particle given by

$$\Delta p_i = qE_{si}\frac{\Delta s}{v}\ , \quad i = x,y,z,$$

where E_i is the space-charge field component, and Δs is the step size over which the field acts. This treatment is the basis of envelope-equation codes such as TRACE and TRACE3D.

The equivalent uniform beam is also used to characterize an effective overall focusing strength in the presence of space charge. This can be done in a periodic focusing system by calculating the phase advance per focusing period including space charge, σ, and comparing this to the phase advance per focusing period with zero space charge, σ_0. For nonuniform charge densities σ_0 is the same as for the uniform beam, but, because the space-charge force is nonlinear, a unique phase advance parameter σ across the beam cannot be defined. For a uniform density the beam quantities σ and σ_0 can be obtained from the transfer matrix through one period, with and without space charge. The procedure assumes the beam is matched, so that the beam ellipse is the same as the machine ellipse (with space charge), and it must be periodic with the same period as the focusing lattice. The solution with space charge must be obtained by iteration because the beam size profile for the matched beam with space charge is not known. The ratio σ/σ_0 is a common measure of the importance of the space-charge force in a given direction. This ratio, which is always in the range $0 \le \sigma/\sigma_0 \le 1$, is called the tune depression or the tune-depression ratio. When $\sigma/\sigma_0 \approx 1$ the beam is relatively unaffected by space charge, and is said to be emittance dominated. When $\sigma/\sigma_0 \approx 0$, the beam is space-charge dominated.

6.2.7 Longitudinal Dynamics Including Space Charge

An accurate determination of the longitudinal dynamics of a beam with space charge must be obtained by numerical calculation. We will derive an expression for the longitudinal current limit by using the 3-D uniform ellipsoid model for the space-charge force. We begin with the equation of longitudinal motion, derived in Section 5.1.4,

$$\phi'' + AB(\cos\phi - \cos\phi_s)\ ,$$

where ϕ is the particle phase, ϕ_s is the synchronous phase, $A = 2\pi/\beta_s^3\gamma_s^3\lambda$, and $B = qE_0T/mc^2$. This led to the equation for the longitudinal potential, also derived in Section 5.1.4,

$$V_\phi = B(\sin\phi - \phi\cos\phi_s)\,.$$

For phases near the synchronous phase we have

$$\sin\phi \cong \sin\phi_s + (\phi-\phi_s)\cos\phi_s - \frac{(\phi-\phi_s)^2}{2}\sin\phi_s - \frac{(\phi-\phi_s)^3}{6}\cos\phi_s + \ldots\,.$$

The equation of motion becomes $\phi'' + k_{\ell 0}^2\left[(\phi-\phi_s) - \frac{(\phi-\phi_s)^2}{2\tan(-\phi_s)}\right]$,

where $k_{\ell 0}^2 = AB\sin(-\phi_s)$.

The potential becomes

$$V_\phi \equiv \left[\sin\phi_s - \phi_s\cos\phi_s + \sin(-\phi_s)\left\{\frac{(\phi-\phi_s)^2}{2} - \frac{(\phi-\phi_s)^3}{6\tan(-\phi_s)}\right\}\right] .$$

The first two terms are independent of the particle phase and can be treated as a constant shift in the reference point of the potential. The variation of the potential with phase is given by the second two terms. This approximation to the potential has a minimum at $\phi = \phi_s$, and a maximum at $\phi = -2\tan(\phi_s)$. The latter represents the stability limit on the right side of the potential well. The limit on the left side is the value of ϕ that gives the same value of the potential, and is at $\phi = -\tan(-\phi_s)$. For small relative angles, the angle is approximately equal to the tangent, and the phase width of the stability region is $\Delta\phi = 3|\phi_s|$. These results are consistent with the general results that were derived in Section 5.14.

Now we evaluate the effect of the space-charge forces, using the 3-D uniform ellipsoid model for the charge density, and assuming that the beam centroid is at ϕ_s, which is the bottom of the potential when there is no space charge. Then the single-particle equation of motion including space charge is

$$\phi'' + k_{\ell 0}^2\left[(\phi-\phi_s) - \frac{(\phi-\phi_s)^2}{2\tan(-\phi_s)}\right] - \frac{3qI\lambda f(\phi-\phi_s)}{4\pi\gamma^3\beta^2 mc^2 r_x r_y r_z} = 0 ,$$

where the semiaxes of the uniform ellipsoid are related to the rms sizes by $r_i = \sqrt{5}\,a_i$, $i = x,y,z$. We will define μ_ℓ as the ratio of the longitudinal space-charge force to the linear part of the longitudinal focusing force. Then

$$\phi'' + k_{\ell 0}^2\left[(1-\mu_\ell)(\phi-\phi_s) - \frac{(\phi-\phi_s)^2}{2\tan(-\phi_s)}\right] = 0 ,$$

where

$$\mu_\ell \equiv \frac{3qI\lambda f}{4\pi\varepsilon_0\gamma^3\beta^2 mc^3 r_x r_y r_z k_{\ell 0}^2} .$$

We can write the equation of motion as

$$\phi'' + k_{\ell 0}^2(1-\mu_\ell)\left[(\phi-\phi_s) - \frac{(\phi-\phi_s)^2}{2(1-\mu_\ell)\tan(-\phi_s)}\right] = 0 .$$

If we define the phase advance per unit length with space charge as

$$k_\ell^2 = k_{\ell 0}^2(1-\mu_\ell) ,$$

the linear equation of motion (ignoring the quadratic term) is

$$\phi'' + k_\ell^2(\phi - \phi_s) = 0 \ .$$

Another common figure of merit for evaluating the importance of the linear space-charge force is the longitudinal tune-depression ratio, defined as $k_\ell / k_{\ell 0}$. This is

$$\left[\frac{k}{k_{\ell 0}}\right]^2 = 1 - \mu_\ell = \frac{3qI\lambda f}{4\pi\varepsilon_0\gamma^3\beta^2 mc^3 r_x r_y r_z k_{\ell 0}^2} \ ,$$

and the ratio of linear space-charge to focusing force μ_ℓ can be expressed as

$$\mu_\ell = 1 - \frac{k_\ell^2}{k_{\ell 0}^2} \ .$$

6.2.8 Longitudinal Current Limit

We saw in Section 5.1.4 that, when the particles are accelerated by a field that is rising in time, longitudinal focusing forces act on the beam and a stable bucket is formed in which the particles can be captured and accelerated to high energies. As the beam current increases, the repulsive space-charge forces will reduce the size and depth of the longitudinal potential well that defines this bucket. For a given synchronous phase and a given accelerating field, there will be some value of the current at which the space-charge force is just equal to the focusing force and the potential well vanishes. This limiting current defines the longitudinal space-charge limit, or the longitudinal current limit for that given accelerator.

The beam-current limit corresponds to that current for which μ_ℓ and the phase width of the beam are maximum. We might assume that the maximum for μ_ℓ is 1, the value where the space-charge force is just balanced by the focusing force. This is certainly an upper limit, but the nonlinear nature of the longitudinal focusing force might establish a more conservative limit. Furthermore, we need to consider the nonlinear part of the force to evaluate the maximum phase width.

To investigate the limits, we evaluate the effect of space charge on the size of the phase-stable region. For small ϕ_s, $\tan(-\phi_s) \cong -\phi_s$, and the equation of motion with space charge has the same form as that without space charge, if we substitute

$$k_{\ell 0}^2 \to k_{\ell 0}^2(1 - \mu_\ell) \ , \qquad |\phi_s| \to |\phi_s|(1 - \mu_\ell) \ .$$

Then the phase width of the separatrix changes from $-|\phi_s| \le \phi \le 2|\phi_s|$ to

$$-|\phi_s|(1 - \mu_\ell) \le \phi \le 2|\phi_s|(1 - \mu_\ell) \ .$$

The energy half-width of the separatrix, calculated in Section 5.1.4, is also reduced according to

$$\frac{\Delta W_{max}}{mc^2} = \sqrt{\frac{2qE_0T\beta^3\gamma^3\lambda}{\pi mc^2}(\phi_s\cos\phi_s - \sin\phi_s)(1-\mu_\ell)} \ .$$

Now we return to the definition for μ_ℓ given above and solve it for the current; we obtain

$$I = \mu_\ell \frac{8\pi^2\varepsilon_0 c r_x r_y r_z E_0 T \sin(-\phi_s)}{3\beta\lambda^2 f} \ .$$

To determine the current limit resulting from the reduced bucket size, let us assume that the beam occupies the full phase width of the separatrix with space charge, so that

$$r_z = 3|\phi_s|(1-\mu_\ell)(\beta\lambda/2\pi)/2 \ ,$$

ignoring the earlier assumption that the beam centroid is at ϕ_s. Using the approximation for the ellipsoid form factor f given earlier, we obtain an expression for the current when the beam occupies the full width of the separatrix,

$$I = \frac{9}{2}\mu_\ell(1-\mu_\ell)^2\varepsilon_0 c\gamma\beta\sqrt{r_x r_y}E_0T\sin(-\phi_s)|\phi_s|^2 \ .$$

The maximum current occurs for $\mu_\ell = 1/3$, and gives a current limit

$$I_{\ell,max} = \frac{2}{3}\varepsilon_0 c\gamma\beta\sqrt{r_x r_y}E_0T\sin(-\phi_s)|\phi_s|^2 \ .$$

This calculation has been found to underestimate the maximum currents obtained from numerical simulation studies, but to give an accurate description of the dependence of the longitudinal limit with respect to the parameters. The maximum total bunch width is found to be about $2|\phi_s|$ and, when particles outside the core of the bunch are included, the maximum effective $\mu_\ell \approx 1$. With use of these values, a longitudinal current limit consistent with numerical simulation studies could be calculated approximately from

$$I_{\ell,max} = 2\varepsilon_0 c\gamma\beta\sqrt{r_x r_y}E_0T\sin(-\phi_s)|\phi_s|^2 \ .$$

We see that the longitudinal current limit increases with increasing beam size, and increasing accelerating field, and, for small angles where $\sin(-\phi_s) \approx -\phi_s$, it increases as the cube of the synchronous phase. Therefore, small increases in the synchronous phase can cause large increases in the current limit.

6.2.9 Transverse Dynamics with Space Charge

We will use an approximate treatment based on the smooth approximation for a periodic quadrupole focusing array, introduced in Section 5.2.7. The equation of transverse x motion in the smooth approximation has the form of an equivalent harmonic oscillator. Thus

$$\frac{d^2x}{ds^2}+\left[\frac{\sigma_0}{P}\right]^2 x-\frac{qE_{sx}}{\gamma^3\beta^2 mc^2}=0 \ ,$$

where σ_0 is the zero-current transverse phase advance per focusing period P, and E_{sx} is the space-charge electric field. Assuming a 3-D uniform ellipsoid, the electric field is linear; it is

$$E_{sx}=\frac{3I\lambda(1-f)x}{4\pi\varepsilon_0(r_x+r_y)r_x r_z} \ .$$

We define σ, the phase-advance per focusing period including space charge, so that

$$\left[\frac{\sigma}{P}\right]^2 \equiv \left[\frac{\sigma_0}{P}\right]^2-\frac{3qI\lambda(1-f)}{4\pi\varepsilon_0\gamma^3\beta^2 mc^3(r_x+r_y)r_x r_z} \ .$$

We substitute this field and solve for the transverse tune-depression ratio,

$$\left[\frac{\sigma}{\sigma_0}\right]^2=1-\frac{3qI\lambda(1-f)}{4\pi\varepsilon_0 mc^3\gamma^3\beta^2(r_x+r_y)r_x r_z}\left[\frac{P}{\sigma_0}\right]^2 \ .$$

Solving for the current, we obtain

$$I=\mu_T\frac{4\pi\varepsilon_0\gamma^3\beta^2 mc^3(r_x+r_y)r_x r_z}{q\lambda(1-f)}\left[\frac{\sigma_0}{P}\right]^2 \ ,$$

where μ_T is the ratio of space-charge to focusing force given by

$$\mu_T=1-\frac{\sigma^2}{\sigma_0^2} \ .$$

We recall from Section 5.2.7 that, for a magnetic quadrupole focusing channel, the zero-current phase advance per focusing period in a FODO channel is given in the smooth approximation by

$$\sigma_0^2 \cong \left[\frac{qG\ell P}{2mc\gamma\beta}\right]^2+\frac{\pi qE_0 T\sin(-\phi)P^2}{mc^2\lambda(\gamma\beta)^3} \ .$$

6.2.10 Matched-Beam Relationships

In the smooth approximation the transverse envelope equation is

$$a_x'' + \left[\frac{\sigma_0}{P}\right]^2 a_x - \frac{\varepsilon_{r,x}^2}{a_x^3} - \frac{3K_3(1-f)}{(a_x + a_y)a_z} = 0 \ ,$$

where

$$K_3 = \frac{qI\lambda}{20\sqrt{5}\pi\varepsilon_0 mc^3\gamma^3\beta^2} \ .$$

For a matched beam the smoothed beam envelope is constant, so that $a'' = 0$. Then, the envelope equation yields

$$\frac{\varepsilon_{r,x}^2}{a_x^4} = \left[\frac{\sigma_0}{P}\right]^2 - \frac{3K_3(1-f)}{(a_x + a_y)a_z a_x} = \left[\frac{\sigma}{P}\right]^2 \ ,$$

with use of the definition for σ given above for the equivalent uniform beam. Then, the tune depression ratio is

$$\left[\frac{\sigma}{\sigma_0}\right] = \frac{\varepsilon_{r,x}P}{a_x^2\sigma_0} \ .$$

The space-charge to focusing force ratio is

$$\mu_T = 1 - \left[\frac{\sigma}{\sigma_0}\right]^2 = 1 - \left[\frac{\varepsilon_{r,x}P}{a_x^2\sigma_0}\right]^2 \ .$$

The maximum value of μ_T is limited by the value of the emittance.

6.2.11 Transverse Current Limit

With increasing beam current the beam size grows until it is equal to the aperture, and further increasing current results in beam loss. The transverse beam-current limit can be estimated from the expression above for the current derived from the 3-D uniform ellipsoid model:

$$I_{T,max} = \mu_{T,max}\left[\frac{4\pi\varepsilon_0\gamma^3\beta^2 mc^3(r_x + r_y)r_x r_z}{q\lambda(1-f)}\right]_{max}\left[\frac{\sigma_{0,max}}{P}\right]^2 \ .$$

The choice $\mu_T = 1$ is the largest value for which a (smooth) potential well exists; from the results in Section 6.2.10, this value can be approached for small emittance beams. We have discussed the limits on r_z in the previous section. The maximum values of the transverse beam semiaxes r_x and r_y are determined by the aperture. The maximum usable aperture values may be limited by the acceptable nonlinearities, usually dominated by the nonlinear rf defocusing force. The quantity σ_0 is limited to $\sigma_0 < 90°$ by an envelope instability associated with high-intensity beams in quadrupole channels.

However, it may be that the value of σ_0 is limited instead by the quadrupole focusing available. Then it is more convenient to substitute the expression for σ_0 as a function of the quadrupole parameters

$$I_{T,max} = \mu_{T,max}\left[\frac{4\pi\varepsilon_0\gamma^3\beta^2 mc^3(r_x + r_y)r_x r_z}{q\lambda(1-f)}\right]_{max}\left\{\left[\frac{qG\ell}{2mc\gamma\beta}\right]^2 + \frac{\pi q E_0 T\sin(-\phi)}{mc^2\lambda(\gamma\beta)^3}\right\}_{max} .$$

The transverse current limit increases with the $G\ell$ product of the focusing lenses, and decreases with increased rf defocusing.

6.2.12 Emittance Growth from Space Charge

Both the external forces and the self-forces are nonlinear and couple the degrees of freedom. These forces cause rms emittance growth because the transverse oscillation frequencies of the beam depend on amplitude (from nonlinearities), and on the coordinates of the other degrees of freedom (from coupling). A resulting decoherence of transverse oscillations for different particles causes a filamentation-type distortion of the initial phase space distribution, unless the distribution is already internally matched to these forces.

For high-current linacs we are concerned with emittance growth resulting directly from self-forces as the dominant effect. Although we will refer to these as space-charge forces, in general the self-forces include both the electric and the magnetic forces. We begin by discussing space-charge-induced emittance growth, with a qualitative discussion of beam matching into an accelerator channel. We distinguish between what we will call internal matching, and rms matching. Internal matching constrains the 6-D phase-space distribution so that the isodensity contours coincide with the particle phase-space trajectories. For an internally matched beam the distribution will be in equilibrium, and no emittance growth will occur, even in the presence of nonlinear forces. Such an equilibrium distribution is periodic for periodic focusing. Examples of equilibrium distributions have been studied for 2-D transport channels with linear uniform focusing.

Given a real beam that is not internally matched, we would like to be able to transform it into an internally matched, equilibrium distribution for the given accelerator channel, without increasing the rms emittance in the process. We do not know whether it is even possible in principle to perform such a transformation, without accompanying emittance growth. What can be done is to match the rms beam sizes in each degree of freedom. This is accomplished by providing a beam optics transformation so that the rms sizes are exactly right to balance the sum of the focusing, space-charge, and emittance terms in the rms envelope equations. In a uniform focusing channel the matched rms sizes are then constant. In a periodic channel the rms sizes will undergo a periodic flutter about their average values. An rms matched beam is generally not internally matched, the beam distribution is not in equilibrium, and the beam will evolve with the possibility of irreversible emittance growth. Nevertheless, rms matching is an important characteristic of an internally matched, equilibrium distribution, and injection of an rms-matched beam can be considered a first approximation to providing the desired internally matched beam.

After a high-current, low-emittance beam is injected into the accelerator, assuming that resonances, which may occur under certain conditions, are avoided, the emittance grows very rapidly as the charges redistribute to provide shielding of the external

focusing field. This mechanism occurs for beams that are rms matched but not internally matched, and has been called charge-redistribution emittance growth. This growth occurs in only one quarter plasma period and is the fastest known emittance growth mechanism. The energy for emittance growth comes from the field energy associated with the initial distribution. If the beam is not rms matched, additional energy is available for emittance growth from the excess potential energy associated with the force unbalance. This additional growth may be called mismatch growth. This is followed by a slower growth as the velocity distributions in the three different planes approach equalization (equipartitioning). The emittance grows in the planes that receive energy, and decreases in the planes that deliver energy. Finally, the periodic focusing structure can excite modes of density oscillation in the beam, which can give emittance growth from the nonlinear space-charge forces. To avoid these resonances in a linac it is necessary to keep $\sigma_0 < 90°$. This is more stringent than for the stability of a zero current beam, for which the requirement is $\sigma_0 < 180°$. The mechanisms described above are summarized in Table 6.1.

Table 6.1 Mechanisms of Emittance Growth Induced by Space-Charge Forces

	Charge redistribution	RMS mismatch	Thermal-energy transfer	Structure resonance
Free-energy source	Nonuniform field energy	Potential energy	Thermal energy in other plane	Directed energy
Time scale	$\sim \tau_{plasma}/4$	$\sim 10\ \tau_{plasma}$	$\sim 10\ \tau_{plasma}$	$\sim 2\ \tau_{betatron}$
Distribution function sensitivity	Strong	Weak	Weak	Strong
For minimum growth	Uniform density or internal match	RMS match	Equipartition	$\sigma_0 < 90°$

Numerical simulations of nonequilibrium linac beams, whether rms matched or not, show that such beams do evolve to quasi-equilibrium distributions, which vary only slowly as the beam is accelerated. When focusing is linear, the equilibrium spatial distribution in the extreme space-charge limit consists of an approximately uniform charge-density core of density n. The density falls to zero over a finite distance approximately equal to the Debye length.

It is observed that the emittance growth results in the formation of a halo of low-density particles in phase space, and that the phase-space volume of the core is increased only slightly. This halo is especially undesirable for high-duty-factor linacs because it results in particle loss on the accelerator walls, which produces radioactivation of the accelerator.

6.3 Wakefields and Emittance Growth in Electron Linacs

Because electrons are so light, the typical beam injection energy in electron linacs is about $\beta \approx 0.5$. Nonlinear space-charge forces can still cause significant emittance growth in the initial stage of the acceleration. This is often caused by the transverse space-charge forces at the ends of the bunch being different from those at the center.

At velocities near the speed of light the space-charge forces become small because of the near cancellation of the electric and magnetic forces. But the interactions of the electric and magnetic fields of the bunch with the charges in the conducting walls of beam pipes and cavities create fields that act back on the beam. At low velocities these fields are said to be caused by image charges, and are generally small compared to the direct space-charge fields. At high velocities the induced wall charges and currents produce wakefields that act on subsequent charges. These fields can be classified as (1) short-range and (2) long-range wakefields. The short-range wakefields generated by the particles at the head of the bunch that act on the particles in the tail of the bunch cause energy loss and transverse deflection of the tail. The long-range wakefields act on subsequent bunches and their most serious effect is usually to produce a deflection of the bunches that oscillates in time and causes growth of the effective emittance when averaged over time. If the effect is sufficiently large, the beam displacement grows and further excites the deflecting fields. The result is an instability known as the beam-breakup instability, and the beam is eventually lost on the walls.

In free space the electric field of a relativistic charged particle is compressed into a disk perpendicular to the direction of motion. The longitudinal electric field approaches zero. For a beam of relativistic particles the transverse magnetic force nearly cancels the transverse electric force on the beam. For a relativistic beam in a perfectly conducting pipe with no discontinuities, the electric fields are again only transverse, and they terminate on surface charges in the pipe. The effect of the surface charges on the beam is usually negligible, and no wakefield is produced behind the beam. Wakefields are produced when there are geometrical changes along the beam pipe, and are largest at cavities and other beam pipe discontinuities. Wakefields produced when a bunch passes by such a discontinuity appear as a damped, oscillatory electromagnetic excitation, composed of the sum of the resonant modes excited by the beam. The highest frequencies are not localized but will propagate down the pipe, if the frequency is higher than the cut-off frequency of the pipe. The lower-frequency modes below cutoff remain localized near the cavity structures in which they are born. The wakefield description is important for extremely relativistic beams, where particles interact with each other only through the wakefields generated by earlier particles.

The short-range wakefields have two important effects. Longitudinal wakefields produced by the particles at the head of the bunch act on those in the tail. This can cause significant energy loss for the particles in the tail, resulting in unwanted energy spread for the bunch. A reduction in the energy spread results from operating with the bunch earlier than the crest. Then the later particles experience a larger energy gain from the accelerating field, which can partly compensate for the deceleration from the wakefields. Also, a transverse (dipole) wakefield produced by the head causes deflection of the tail and results in transverse emittance growth. The deflection is reduced by applying strong transverse focusing forces. For relativistic electron beams, strong focusing is not needed to compensate for space-charge or rf-defocusing forces, as it is for low-velocity proton beams, but it does reduce the undesirable emittance growth caused by the wave fields.

The long-range wakefields generally consist of a few low-frequency modes. The most important effects are from the dipole modes, which produce the beam-breakup

instability. This instability generally limits the intensity of electron linacs, whereas for proton linacs space-charge forces limit the intensity. The dominant deflecting modes are the two TM_{110} modes, which have a frequency in the pillbox cavity of about 1.6 × that of the main TM_{010} accelerating mode. The magnetic field of these modes (see Fig. 6.9) is transverse to the cavity axis and acts on particles on and near the axis to cause a transverse deflection perpendicular to both the beam axis and the magnetic field direction. These two deflecting modes differ in the polarity of the transverse magnetic field; the magnetic field directions differ by 90°. These modes also have a longitudinal electric field, which reverses direction on the cavity axis, where its magnitude is zero. An off-axis beam can excite the modes. The excitation of the beam-breakup instability can be initiated by an off-axis beam or a transverse density perturbation, which excites the cavity at the frequency of the deflecting mode.

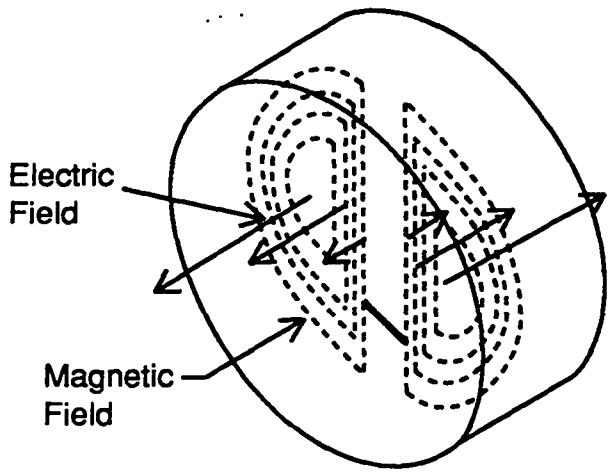

Fig. 6.9 Field pattern of a TM_{110} mode.

The two catagories of beam breakup are (1) regenerative and (2) cumulative. Regenerative beam breakup occurs in multicell coupled-cavity linac structures. The excited deflecting mode propagates along the structure together with the displaced beam. The longitudinal deflecting field of the mode decelerates the beam and feeds more energy into the mode. The transverse magnetic field of the mode further deflects the beam. Cumulative beam breakup occurs in linacs with independent cavities. The mode grows in the first cavity, resulting in a growing displacement of the subsequent beam bunches. The displaced bunches enter the next cavities, where, because of the larger initial displacements, the mode grows even more rapidly. The growth continues until the beam is lost on the walls. In cumulative beam-breakup there is no propagating wave from tank to tank, but the coupling of the effect from one cavity to the next is carried by the displaced beam. These beam breakup effects are particularly serious in their transient behavior, where the amplitudes can become very large.

There are several effective cures for beam breakup: (1) good beam alignment, (2) strong focusing, (3) stagger tuning of cavities to deliberately detune the deflecting mode frequencies from cell to cell, (4) choosing the accelerating gap so that the transit-time factor vanishes for the deflecting mode, thereby decoupling the deflecting mode from the beam, (5) choosing the aperture and the beam pipe large enough that deflecting modes can propagate away to an absorber.

6.4 Problems

6-1. Given the transfer matrix of a drift space, derive the results for the change in the ellipse parameters. Show that the ellipse parameter γ is invariant. What does this mean physically?

6-2. Given the transfer matrix of a thin lens, derive the results for the change in the ellipse parameters. Show that the ellipse parameter β is constant. Is this reasonable physically?

6-3. Measurements of transverse beam distribution for a proton beam with velocity $\beta = 0.06$ show an upright ellipse in the $x-x'$ plane, with an rms size $\Delta x_{rms} = 3$ mm and an rms divergence $\Delta x'_{rms} = 0.06$ mrad. (a) What is the rms unnormalized emittance? (b) What is the rms normalized emittance? (c) If the rms normalized emittance is conserved during acceleration to 100 MeV, what is the rms unnormalized emittance at 100 MeV?

6-4. Measurements of the longitudinal beam distribution result in an upright ellipse in the $\Delta\phi$-ΔW plane with rms values $\Delta\phi_{rms} = 1°$ and $\Delta W_{rms} = 100$ keV. (a) What is the longitudinal emittance in deg-MeV? (b) If the rf frequency is 800 MHz, what is the longitudinal emittance in sec-MeV?

6-5. Assume a bunched proton beam at 100 keV with an average current of 100 mA and a frequency of 400 MHz, having a uniform spherical density with radius 5 mm. (a) Calculate the particle density. (b) Calculate the electric field from space charge at the edge of the beam. (c) Calculate the space-charge parameter K_3. (d) Calculate the projected rms size in the x plane. (e) If the rms unnormalized emittance in the x plane is $\varepsilon_r\pi = 0.2\,\pi$ mm-mrad, what is the ratio of the space-charge term to the emittance term in the envelope equation? Is the beam space-charge or emittance dominated?

6-6. Consider a 100-mA proton beam at 5 MeV in a 200-MHz drift-tube linac with parameters $E_0T = 2$ MV/m, and synchronous phase $\phi_s = -25°$. Assume that the bunch is spherical and has an rms size of $\Delta x_{rms} = 2.24$ mm in all three planes. (a) Calculate $k_{\ell 0}$, the zero-current wave number of small longitudinal oscillations. (b) For the equivalent uniform beam, what is the longitudinal tune-depression ratio $k_\ell / k_{\ell 0}$, the wave number of small longitudinal oscillations k_ℓ including space charge, and the ratio of space-charge to focusing force μ_ℓ?

6-7. For the same beam as in problem 6-6, assume that the transverse focusing is provided by a FODO quadrupole array using quadrupoles with gradient-length product $G\ell = 3$ T-m placed in every drift tube. (a) What is the period of the focusing lattice at 5 MeV? (b) Using the smooth approximation formula given in Section 6.2.9, what is the zero-current phase advance per focusing period σ_0? Is it below the requirement $\sigma_0 < 90°$ to avoid the envelope instability? (c) For the equivalent uniform beam, what is the transverse tune-depression ratio σ/σ_0, the phase advance per focusing period σ, and the ratio of space-charge to focusing force μ_T?

REFERENCES

1. Particle Data Group, "Review of Particle Physics Properties," Physics Letters B239, (1990).
2. Feynman, R.P., R.B. Leighton, and M. Sands, *The Feynman Lectures on Physics,* (Addison Wesley Publishing Co., 1966).
3. Jackson, J.D., *Classical Electrodynamics,* (John Wiley & Sons, Inc., 1975).
4. Simon, Ramo, John R. Whinnery, and Theodore Van Duzer, *Fields and Waves in Communication Electronics,* (John Wiley & Sons, Inc., 1984).
5. Gandhi, Om P., *Microwave Engineering and Applications,* (Pergamon Press, 1987).
6. Piel, H., "Fundamental Features of Superconducting Cavities for High Energy Accelerators," CERN Accelerator School, CERN 87-03 (April 1987).
7. Moreno, Theodore, *Microwave Transmission Design Data,* (Dover Publications, 1948).
8. Courant, E.D. and H.S. Snyder, "Theory of the Alternating-Gradient Synchrotron," Ann. Phys. **3**, 1-48 (1958).
9. Brown, K.L., and R.V. Servranckx, "First and Second Order Charged Particle Optics," *AIP Conference Proceedings* **127,** American Institute of Physics, 62-130 (1985).
10. Nagel, D.E., E.A. Knapp, and B.C. Knapp, *Review of Scientific Instruments* **38,** 1583 (1963).
11. Wangler, T.P. "Calculations for Three Coupled Oscillators Including Eigenvalue Problem, Perturbation Theory and Losses," Los Alamos Group AT-1 memorandum AT-1:84-299, (August 29, 1984).
12. Knapp, E.A., B.C. Knapp, and J.M. Potter, *Review of Scientific Instruments* **39,** 979 (1968).
13. Kapchinskiy, I.M., and V.A. Teplyakov, *Prib. Tekh. Eksp.*, **2,** 19 (1970).
14. Neal, R.B., *The Stanford Two-Mile Accelerator,* (W.A. Benjamin Inc., 1968).
15. Loew, G. and R. Talman, "Elementary Principles of Linear Accelerators," *AIP Conference Proceedings* **105,** 1-91 (1983).
16. Smith, L., and R.L. Gluckstern, "Focusing in Linacs," *Review of Scientific Instruments* **26,** 220 (1955).
17. Bruck, Henri, *Circular Particle Accelerators,* Los Alamos Translation LA-TR-72-10 (1972).
18. Sacherer, F., "RMS Envelope Equation with Space Charge," *IEEE Transactions in Nuclear Science* **18,** 1105 (1971).
19. Lapostolle, P.M., "Possible Emittance Increase Through Filamentation Due to Space Charge in Continuous Beams," *IEEE Transactions in Nuclear Science* **18,** 1101 (1971).
20. Kapchinsky, I.M. and Vladimirsky, V. "Limitations of Proton Beam Current in a Strong Focusing Linear Accelerator Associated with the Beam Space Charge," Proceedings for the International Conference on High Energy Accelerators, CERN, p. 274 (1959).

BIBLIOGRAPHY

Alvarez, L. W., "The Design of a Proton Linear Accelerator," Phys. Rev. 70,799(1946).

Alvarez, L. W., H. Bradner, J. V. Franck, H. Gordon, J. D. Gow, L. C. Marshall, F. Oppenheimer, W. K. H. Panofsky, C. Richman, and J. R. Woodyard, "Berkeley Proton Linear Accelerator," Rev. Sci. Instrum. 26, 210-219(1955).

Bane, K. L. F., "Wakefield Effects in a Linear Collider", Physics of Particle Accelerators, AIP Conference Proceedings 153, Vol 1, 971 (1987).

Le Duff, J. "Beam Breakup", CERN Accelerator School, CERN 87-03(21 April, 1987) 610.

Boussard, D., "Beam Loading", CERN Accelerator School, CERN 87-03(21 April, 1987) 626.

Brau, Charles A., "Free Electron Lasers", Academic Press Inc.,(1990) Chapter 8 , RF Linacs.

Dome, Georges, "RF Systems: Waveguides and Cavities", Physics of Particle Accelerators, AIP Conference Proceedings 153, Vol 2, 1297 (1987).

D. A. Edwards and M. J. Syphers, "An Introduction to the Physics of Particle Accelerators", Physics of Particle Accelerators, AIP Conference Proceedings 184, Vol 1, 2(1989).

Ginzton, E. L., "Microwave Measurements",McGraw Hill (1957), Chapter 9 (Resonant Cavity Characteristics: Measurement of Q), Chapter 10 (Resonant Cavity Characteristics: Measurement of R_0/Q_0).

Gluckstern, R. L., "Radio-Frequency Systems: Electromagnetic Fields in RF Cavities and Cavity Chains", Physics of Particle Accelerators, AIP Conference Proceedings 127,344 (1985) .

Humphries, Stanley,Jr., "Principles of Charged Particle Acceleration",John Wiley & Sons(1986)Chapter 12 (Resonant Cavities and Waveguides), Chapter 13 (Phase Dynamics), and Chapter14 (Radio-Frequency Linear Accelerators).

Humphries, Stanley,Jr., "Charged Particle Beams",John Wiley & Sons(1990) Chapter13 (Introduction to Beam Emittance), and Chapter4 (Beam Emittance-Advanced Topics).

Kapchinskiy, I. M.,"Theory of Resonance Linear Accelerators", Harwood Academic Publishers(1985).

Kapchinskiy, I. M., "Particle Dynamics in Linear Resonance Accelerators", Atomizdat(1966) (English translation-Los Alamos report LA-TR-80-10.

Lapostolle, Pierre M., And Septier, Albert, ed., "Linear Accelerators", North Holland Publishing Company, and John Wiley & Sons(1970).

Lapostolle, Pierre M., "Proton Linear Accelerators: A Theoretical and Historical Introduction", Los Alamos Report LA-11601-MS, (July,1989).

Lawson, J. D., Physics of Charged Particle Beams, 2nd ed. (Clarendon Press, Oxford, 1987).

Le Duff, J. ,"Dynamics and Acceleration in Linear Structures", CERN Accelerator School, CERN 85-19,27 (November,1985) 144.

Le Duff, J. ,"Beam Breakup", CERN Accelerator School, CERN 87-03,21 (April, 1987) 610.

Le Duff, J. "High Field Electron Linacs", CERN Accelerator School, CERN 87-03,21 (April, 1987) 772.

Loew, G. A. , and Talman, R., "Lectures on the Elementary Principles of Linear Accelerators", Physics of Particle Accelerators, AIP Conference Proceedings 105,1 (1983) .

Neal, R. B. "The Stanford Two-Mile Accelerator", W. A Benjamin, Inc.(1968).

Piel, H., "Fundamental Features of Superconducting Cavities for High Energy Accelerators ", CERN Accelerator School, CERN 87-03,21 (April, 1987) 736.

Puglisi, M. ,"The Radiofrequency Quadrupole Linear Accelerator", CERN Accelerator School, CERN 87-03(21 April, 1987) 706.

Puglisi, M., "Radio-Frequency Acceleration", Physics of Particle Accelerators, AIP Conference Proceedings 184, Vol 2,1393(1989).

Ruth, Ronald D., "Progress on Next Generation Linear Colliders", Physics of Particle Accelerators, AIP Conference Proceedings 184, Vol 2,2208(1989).

Schempp, A. , "Principles and Technology of RFQs", Physics of Particle Accelerators, AIP Conference Proceedings 184, Vol 2,1477(1989).

Smith, Lloyd, "Linear Accelerators", Handbuch der Physik, Band XLIV (Springer, Berlin),344(1959) .

Smith, T. I., "Intense, Low Emittance Injectors for RF Electron Linacs", Physics of Particle Accelerators, AIP Conference Proceedings 184, Vol 2,1543(1989).

Stiening, R., "An Introduction to the Accelerator Physics of Linear Colliders of Linear Colliders", Physics of Particle Accelerators, AIP Conference Proceedings 105,281(1983) .

Stokes, Richard H., and T. P. Wangler, , "Radiofrequency Quadrupole Accelerators and Their Applications", Ann. Rev. Nucl. Part. Sci. , Vol 38 ,97-118(1988) .

Wilson, P. B., Griffin, J. E., Appendix, "High Energy Electron Linacs: Application to Storage Ring RF Systems and Linear Colliders", Physics of Particle Accelerators, AIP Conference Proceedings 87,450(1982) .

Wilson, P. B., "Introduction to Wake Fields and Wake Potentials", Physics of Particle Accelerators, AIP Conference Proceedings 184, Vol 1,525 (1989).

LOS ALAMOS NAT'L LAB.
IS-4 REPORT SECTION
RECEIVED

'93 OCT 21 AM 9 04